

Seismic probes of stellar mergers and magnetism

Thesis by
Nicholas Zhao Rui

In Partial Fulfillment of the Requirements for the
Degree of
Doctor of Philosophy

CALIFORNIA INSTITUTE OF TECHNOLOGY
Pasadena, California

2025
Defended April 29th, 2025

© 2025

Nicholas Zhao Rui
ORCID: 0000-0002-1884-3992

All rights reserved

People have stars, but they aren't the same. For travelers, the stars are guides. For other people, they're nothing but tiny lights. And for still others, for scholars, they're problems. For my businessman, they were gold. But all those stars are silent stars. You, though, you'll have stars like nobody else.

When you look up at the sky at night, since I'll be living on one of them, since I'll be laughing on one of them, for you it'll be as if all the stars are laughing. You'll have stars that can laugh!

And when you're consoled (everyone eventually is consoled), you'll be glad you've known me. You'll always be my friend. You'll feel like laughing with me. And you'll open your window sometimes just for the fun of it... And your friends will be amazed to see you laughing while you're looking up at the sky. Then you'll tell them, "Yes, it's the stars; they always make me laugh!" And they'll think you're crazy. It'll be a nasty trick I played on you...

And it'll be as if I had given you, instead of stars, a lot of tiny bells that know how to laugh...

Antoine de Saint-Exupéry, *The Little Prince*

ACKNOWLEDGEMENTS

To my advisor, *Jim Fuller*: thank you for listening to all of my bad ideas. Thank you for just the right combination of honest advice and unwavering support.

To my fellow group members: thank you for riding this wild wave with me. These include *Janosz Dewberry, Cat Felce, Nícolas Fernandes, Emily Hu, Connie Li, Linhao Ma, Stephon Qian, Yanlong Shi, Daichi Tsuna, Samantha Wu, and Guangyi Zhang*.

To my past mentors: thank you for having believed I could do science, even before it could be empirically tested. These are *Matt Hosek, Satcher Hsieh, Kyle Kremer, Jessica Lu, Fred Rasio, and Norman Yao*. And to my present mentors: thank you for continuing to believe I can do science, in spite of overwhelming scientific consensus. These include *Kareem El-Badry, Elias Most, Joel Ong, and Sterl Phinney*. You taught me what it means to do science.

To my friends, both in and out of the office: thank you for doing my bad ideas with me. These include *David Abramovitch, Sasha Alabugin, Guido Da Re, Shashank Dholakia, Shishir Dholakia, Ian Foo, Sarah Habib, Rae Holcomb, Elijah Kane, Yonna Kim, Yoonsoo Kim, Sergei Kliavinek, Taylor Knapp, Isaac Legred, Justin Mailom, Hannah Manetsch, Suchi Narayanan, Kyle Nelli, Orion Ning, Elina Sendonaris, Kiran Shila, Nadine Soliman, Dongze Sun, Hunter Thompson, Rhiannon Udall, and many, many others*.

To the Caltech Ballroom Swing Dance Club and Caltech Karate Club: thank you for keeping my sanity at exactly the right level and no higher.

To *JoAnn Boyd*: thank you for taking care of business while diligently keeping me informed about the location of snacks. To *Cameron Hummels*: thank you for giving me something to do and keeping me off the streets.

To my more inanimate supporters: thank you for making this PhD possible. These include the vibe shack, Kyle's minivan, Linhao's chair, JoAnn's couch, and the TAPIR coffee machine.

Most of all, to my parents *Eugene Rui* and *Lucy Zhao*, my sister *Carolynn Rui*, and *Muffin*: thank you for unconditionally loving and supporting me both during graduate school and throughout my life. You walked so I could sit at a desk and code all day.

ABSTRACT

Stellar pulsations can do what most other astrophysical observables cannot: directly probe internal stellar properties. This thesis consolidates work investigating how stellar oscillation modes are affected by two common but “noncanonical” pieces of stellar physics: mergers and magnetism.

The earlier chapters develop “seismic stellar merger genealogy,” the application of seismology to the discovery of stellar merger remnants. In **Chapter II**, I show that red giants which have engulfed close, main-sequence companions possess unusual gravity-mode period spacings, indicating their binary origin. I identify two dozen promising merger remnant candidates in archival *Kepler* data, roughly consistent with expected stellar merger rates. In **Chapter III**, I study the evolution and properties of the red-giant-like stars which result from coalescences of accreting helium-core white dwarf systems. These merger remnants display distinctive seismic and chemical properties, particularly during the core helium-burning phase as the result of an especially violent helium flash.

The later chapters develop “seismic stellar magnetometry,” the application of seismology to the measurement of stellar magnetic fields. In **Chapter IV**, I calculate the morphology of high-radial-order gravity modes under the influence of strong magnetic fields. The eigenfunctions exhibit two morphological features at which energy dissipation may be strong, in agreement with the suppressed dipole modes observed in many red giants. In **Chapter V**, I apply the same method to calculate the gravity-mode period spacing pattern under a strong magnetic field. The perturbative theory developed for weak fields underestimates the true frequency shifts to gravity modes caused by strong magnetic fields. In **Chapter VI**, I model the behavior of stochastic pulsators whose magnetic fields are strong enough to misalign their pulsations from the rotation axis. Even in the presence of stochasticity, the light curves of such oblique pulsators indefinitely retain some phase information in a way that can be used to identify them. In **Chapter VII**, I place upper bounds on the near-surface magnetic fields of a sample of white dwarfs based on the non-detection of magnetic features in their pulsation spectra. Although these constraints vary significantly with white dwarf structure and mode periods, they are consistently much stronger than the megagauss-scale magnetic fields to which spectroscopy is sensitive.

PUBLISHED CONTENT AND CONTRIBUTIONS

Rui, N. Z. and J. Fuller (2021). “Astroseismic fingerprints of stellar mergers.” In: *Monthly Notices of the Royal Astronomical Society* 508.2, pp. 1618–1631.
 doi: 10.1093/mnras/stab2528. arXiv: 2108.10322.
 —N.Z.R. contributed to the scientific premise, ran and analyzed simulations, and wrote the manuscript. This work has been adapted to **Chapter II**.

Rui, N. Z. and J. Fuller (2024). “Finding the unusual red giant remnants of cataclysmic variable mergers.” In: *Open Journal of Astrophysics*.
 doi: 10.33232/001c.123878. arXiv: 2404.14474.
 —N.Z.R. contributed to the scientific premise, ran and analyzed simulations, and wrote the manuscript. This work has been adapted to **Chapter III**.

Rui, N. Z. and J. Fuller (2023). “Gravity waves in strong magnetic fields.” In: *Monthly Notices of the Royal Astronomical Society* 523.1, pp. 582–602.
 doi: 10.1093/mnras/stad1424. arXiv: 2303.08147.
 —N.Z.R. contributed to the scientific premise, performed calculations, and wrote the manuscript. This work has been adapted to **Chapter IV**.

Rui, N. Z., J. M. J. Ong, and S. Mathis (2024). “Astroseismic g-mode period spacings in strongly magnetic rotating stars.” In: *Monthly Notices of the Royal Astronomical Society* 527.3, pp. 6346–6362.
 doi: 10.1093/mnras/stad3461. arXiv: 2310.19873.
 —N.Z.R. conceived of the scientific premise, performed calculations, ran simulations, and wrote the manuscript. This work has been adapted to **Chapter V**.

Rui, N. Z., J. Fuller, and J. M. J. Ong (2025). “It’s not just a phase: oblique pulsations in magnetic red giants and other stochastic oscillators.” In: *The Astrophysical Journal Letters* 985.2, L39.
 doi: 10.3847/2041-8213/add5e2. arXiv: 2505.03169.
 —N.Z.R. conceived of the scientific premise, performed calculations, ran simulations, and wrote the manuscript. This work has been adapted to **Chapter VI**.

Rui, N. Z., J. Fuller, and J. J. Hermes (2025). “Supersensitive Seismic Magnetometry of White Dwarfs.” In: *The Astrophysical Journal* 981.1, 72.
 doi: 10.3847/1538-4357/ada9e. arXiv: 2410.20557.
 —N.Z.R. conceived of the scientific premise, performed calculations, ran simulations, and wrote the manuscript. This work has been adapted to **Chapter VII**.

CONTENTS

Acknowledgements	iii
Abstract	iv
Published Content and Contributions	v
Contents	v
List of Figures	x
List of Tables	xiii
Chapter I: Introduction	1
1.1 Waves in stars	2
1.1.1 Production	2
1.1.2 Propagation	3
1.1.3 Oscillation modes	5
1.1.4 Taxonomy of stellar waves	6
1.2 Seismology as the hammer	8
1.2.1 Seismic stellar merger genealogy	8
1.2.2 Seismic stellar magnetometry	11
Chapter II: Asteroseismic fingerprints of stellar mergers	15
2.1 Introduction	16
2.2 Stellar models	18
2.2.1 Detailed oscillation mode calculations	19
2.3 Results	20
2.3.1 Heuristic description	20
2.3.2 ΔP_g is sensitive to mergers on the RGB	21
2.3.3 Pre-merger core degeneracy is key to merger identification	23
2.3.4 Mergers on the red clump are difficult to distinguish	25
2.4 Merger candidates	26
2.4.1 Promising candidates from ΔP_g	26
2.4.2 Recognizing merger remnants in the absence of ΔP_g	28
2.5 Discussion	30
2.5.1 Merger dynamics	30
2.5.2 Additional merger signals	31
2.5.3 Rates of stellar mergers	33
2.5.4 Mergers in dense stellar environments	34
2.6 Conclusion	34
2.A MESA simulation controls	35
Chapter III: Finding the unusual red giant remnants of cataclysmic variable mergers	40
3.1 Introduction	41
3.2 Stellar models	43
3.3 Red giant branch	46
3.3.1 More compact cores inflate the radius	48

3.3.2	Asteroseismic signatures on the red giant branch	49
3.3.3	Overbright tip of the RGB	52
3.4	Core helium-burning phase	54
3.4.1	Over-luminous red clump stars	57
3.4.2	Wider range of asteroseismic g-mode period spacings	60
3.4.3	Asteroseismic mixed-mode coupling	60
3.4.4	Abundance anomalies	62
3.4.5	Populating the horizontal branch with merger remnants	64
3.5	Candidate merger remnants	66
3.5.1	Undermassive red clump stars may be merger remnants	66
3.5.2	Zvrk: a possible post-dredge-up merger remnant?	68
3.5.3	Other potential post-dredge-up merger remnants	69
3.6	Discussion and future prospects	70
3.6.1	Progenitors and rates	70
3.6.2	Merger transients and mass retention	72
3.6.3	Rapid rotation	72
3.6.4	Non-asymptotic effects on pulsations	74
3.6.5	Broader progress in binary interaction asteroseismology	75
3.7	Summary	76
3.A	Dependence on the cooling age of the white dwarf	77
3.B	Thermal timescale of the core	78
3.C	Brunt–Väisälä frequency in degenerate helium cores	80
3.D	Post-helium flash composition profiles	82
Chapter IV: Gravity waves in strong magnetic fields		83
4.1	Introduction	84
4.2	Problem statement	87
4.2.1	Linearized fluid equations	88
4.2.2	Important frequency scales	89
4.2.3	Dipole geometry	91
4.3	Important features of the magnetogravity eigenproblem	93
4.3.1	Close analogy to the rotational problem	93
4.3.2	Sturm–Liouville problems with internal singularities	94
4.3.3	Power series expansion around singularity	96
4.4	Oscillation modes without dissipation	97
4.4.1	Zonal ($m = 0$) solutions	97
4.4.2	Tesseral and sectoral ($m \neq 0$) solutions	103
4.4.3	Alfvén wave solutions	106
4.5	Oscillation modes with dissipation	109
4.5.1	Numerical solutions of the evanescent branch	111
4.5.2	Numerical solutions of the propagating branch	114
4.6	Further remarks	116
4.6.1	Behavior of the wavefunctions near the equator and critical latitudes	116
4.6.2	The continuum spectrum and nonharmonic solutions	119
4.6.3	Magnetogravity waves in general geometries	120
4.6.4	Stable g modes in convective regions	122

Contents	viii
4.7 Summary	124
4.A Magnetogravity eigenproblems in other geometries	125
4.A.1 Fuller, Cantiello, et al. (2015): Uniform radial field model	125
4.A.2 Lecoanet, Vasil, et al. (2017): Multipole Cartesian geometry	126
4.B Numerically solving $\mathcal{L}_{\text{mag}}^{m,b}$	127
4.B.1 Numerical solution without dissipation	128
4.B.2 Numerical solution with dissipation	129
4.C Tightly confined equatorial magnetogravity waves	129
4.D Structure of Alfvén resonances including horizontal-field contributions to the magnetic tension	131
4.E Magnetic tangling-induced shear stress	132
Chapter V: Asteroseismic g-mode period spacings in strongly magnetic rotating stars	134
5.1 Introduction	135
5.2 Problem statement	137
5.2.1 The traditional approximation of rotation and magnetism (TARM) .	137
5.2.2 Assumptions, conventions, and scope	139
5.3 Analytic formulation	142
5.3.1 Fluid equations for gravity modes	142
5.3.2 Asymptotic period spacing	144
5.4 Numerical solutions of the horizontal problem	147
5.4.1 Numerical collocation scheme	147
5.5 Numerical solutions of the radial problem	150
5.5.1 Non-asymptotic numerical scheme	150
5.5.2 Stellar models	152
5.6 Results and discussion	154
5.6.1 Strong fields in red giant cores	154
5.6.2 Strong fields threading the envelopes of main-sequence pulsators .	163
5.6.3 Future prospects	171
5.7 Conclusion	173
Chapter VI: It's not just a phase: oblique pulsations in magnetic red giants and other stochastic oscillators	175
6.1 Introduction	176
6.2 Pulsation model	177
6.2.1 Rotationally aligned pulsations	178
6.2.2 Do two periodicities mean one mode or two?	180
6.2.3 Magnetic red giants: a theoretical case study	184
6.2.4 Simulated observations of oblique pulsations	187
6.3 Summary and prospects	189
6.A Transforming between the observer and corotating frames	191
6.B Amplitude evolution under stochastic driving	191
6.C Rotating and magnetic g-mode frequencies and eigenfunctions	193
Chapter VII: Supersensitive seismic magnetometry of white dwarfs	195
7.1 Introduction	196
7.2 Theoretical background	198
7.2.1 Seismic frequency shifts	199

7.2.2	Mode suppression	203
7.3	Methods	205
7.3.1	White dwarf models	205
7.3.2	Seismic field constraints	205
7.3.3	Dependence of magnetic sensitivity on white dwarf properties	207
7.4	Seismic field constraints in observed white dwarfs	209
7.4.1	Magnetic leaf diagrams	209
7.4.2	Carbon–oxygen white dwarfs	214
7.4.3	ELMVs: probing the stripped cores of red giants?	216
7.4.4	Caveats	219
7.5	Summary and future directions	220
7.A	Magnetic formalism	222
7.A.1	Magnetic frequency shifts of g-mode pulsations	222
7.A.2	Multiplet asymmetries due to magnetism	223
7.A.3	Asymmetry parameters for an inclined dipole	226
7.B	Correction for non-asymptotic effects	227
Chapter VIII: Conclusion		230
Bibliography		233

LIST OF FIGURES

<i>Number</i>	<i>Page</i>
1.1 Variable Hertzsprung–Russell diagram diagram	4
2.1 Cartoon comparing red giant–main-sequence merger remnants to single stars	17
2.2 Hertzsprung–Russell and asteroseismic propagation diagrams comparing merger remnants and single stars	19
2.3 Various asteroseismic observables as a function of the primary’s radius at merger	21
2.4 Propagation diagrams of merger remnants indistinguishable by asteroseismology	23
2.5 Differences in ΔP_g between merger remnants and single stars	24
2.6 Asteroseismic spacing diagram with candidate merger remnants indicated .	27
3.1 Cartoon showing the evolution of helium-core cataclysmic variable merger remnants	42
3.2 Summary of a possible formation channel of a merger remnant compared to the construction of the stellar model	44
3.3 Hertzsprung–Russell diagram showing the evolution of merger remnants .	47
3.4 Brunt–Väisälä frequency and temperature profiles for a merger remnant at various times	51
3.5 Propagation diagram showing the seismic properties of merger remnants .	52
3.6 Luminosities of merger remnants at the helium flash and various special masses	53
3.7 Kippenhahn diagrams for merger remnants at the helium flash and during core helium burning	55
3.8 Time evolution of various quantities during the core helium-burning phase of merger remnants	56
3.9 Asteroseismic propagation diagrams for core helium-burning merger remnants at various times	59
3.10 $\Delta\Pi$ and coupling factor for core helium-burning merger remnants	59
3.11 Surface abundances of merger remnants	63
3.12 Merger remnants on the horizontal branch	66
3.13 Merger remnants compared to observed undermassive red clump stars . . .	67
3.14 Possible progenitors of helium-core cataclysmic variable mergers	71

3.15	Effect of varying helium white dwarf luminosity on the evolution of the merger remnant	79
3.16	Composition profiles for selected merger remnant models at the beginning of core helium burning	81
4.1	Cartoon showing a refracted tesseral magnetogravity wave	87
4.2	a^{-1} for zonal magnetogravity waves	98
4.3	Eigenfunction for the $\ell = 5$ zonal magnetogravity mode for $b = 0.5$	99
4.4	Eigenfunction for the $\ell = 5$ zonal magnetogravity mode for $b = 1.3$	99
4.5	Radial group velocities of selected zonal magnetogravity waves	101
4.6	a^{-1} for tesseral/sectoral magnetogravity waves in the dissipationless problem	107
4.7	a^{-1} for tesseral/sectoral magnetogravity waves for real ω	109
4.8	Eigenfunction for the $\ell = 5$, $ m = 4$ tesseral magnetogravity mode for $\sqrt{\text{Re}(b^2)} = 1.3$	111
4.9	Eigenfunction for the $\ell = 5$, $ m = 4$ tesseral magnetogravity mode for $\sqrt{\text{Re}(b^2)} = 2.5$	113
4.10	a^{-1} for tesseral/sectoral magnetogravity waves for real $v_{p,r}$	115
5.1	Numerically computed eigenvalues appearing in the dispersion relation for gravity waves in rotating, magnetic stars	148
5.2	Important frequencies and non-perturbative frequency shifts for a red giant model	160
5.3	Relative error on the inferred magnetic field accrued when using applying perturbation theory	162
5.4	Important frequencies and non-perturbative frequency shifts for a young γ Doradus model	163
5.5	Important frequencies and non-perturbative frequency shifts for an evolved γ Doradus model	164
5.6	Important frequencies and non-perturbative frequency shifts for a young slowly pulsating B-type model	165
5.7	Important frequencies and non-perturbative frequency shifts for an evolved slowly pulsating B-type model	166
5.8	P_{crit} against P_{rot} for the dipole and quadrupole retrograde sectoral modes for a young slowly pulsating B-type model	169
6.1	Comparison between two double-periodicity stochastic pulsations	179
6.2	Magnetic g-mode frequency shifts due to an inclined dipolar magnetic field .	183
6.3	Phase diagram of pulsation regimes in magnetic field–rotation rate space .	186
6.4	Synthetic magnetically oblique g-mode triplet	188

7.1	Kiel diagram of magnetic and pulsating white dwarfs	198
7.2	White dwarf propagation diagram, magnetic weight function, and critical magnetic field	200
7.3	Dependence of seismic magnetic sensitivity on stellar and pulsational parameters	204
7.4	Seismic upper bounds on 24 white dwarfs	211
7.5	Magnetic leaf diagram for three DAV white dwarfs	212
7.6	Magnetic leaf diagram for three DBV white dwarfs	213
7.7	Seismic magnetic sensitivity for extremely low-mass white dwarfs	218
7.8	Magnetic leaf diagram for GD 278	219
7.9	Non-asymptotic correction to seismic magnetic sensitivity	228

LIST OF TABLES

<i>Number</i>	<i>Page</i>
2.1 Candidate merger remnants identified through asteroseismology	29
4.1 Values of selected dimensionless parameters at the critical depth and cutoff height for magnetogravity wave propagation	102
5.1 Summary of models for which magnetic, rotating g-mode frequencies are calculated	153
7.1 Summary of WD models	206
7.2 Observed and model spectroscopic/seismic properties and upper limits on the magnetic field of 24 WDs	210

Chapter 1

INTRODUCTION

A star is a fluid body which has relaxed into hydrostatic equilibrium, a state in which pressure forces exactly balance out gravity. In the absence of complicating effects such as rapid rotation or tidal effects from a close companion, this condition forces the star into a spherical shape obeying

$$\frac{dp}{dr} = -\rho g, \quad (1.1)$$

where p , ρ , and g respectively denote the pressure, density, and gravitational acceleration. It is also customary to assert that the star's interior sustain a significant amount of nuclear fusion. Defined this way, stars are a central subject of fascination in astronomy and astrophysics (the root *astro-* originates from the Ancient Greek ἀστρός, for star). Stars are also the hosts of planets, the luminous components of galaxies, and the progenitors of compact objects. Even in stories in which stars are not the protagonists, they are still central characters whose personalities must be understood.

Nature is known to create fusing fluid spheres satisfying Equation 1.1 within the mass range $10^{32} \text{ g} \lesssim M \lesssim 10^{35} \text{ g}$ ¹. In defiance of the simplicity of the problem statement, the structure and evolution of stars are extremely complicated and depend sensitively on the details of hydrodynamics, radiative transfer, and nuclear reactions evaluated at extreme pressures, temperatures, and densities. Yet stars defy experimentation: we cannot make stars in a laboratory², and we cannot travel to them³. All we can hope to do is observe them from afar.

Troublingly, stars are opaque to all wavelengths of light. Although photons propagate through stellar interiors, they scatter at such a high rate that their transport is diffusive. A photon only remembers information about its most recent interaction or so. The upshot is that an observer on earth effectively only measures blackbody radiation. This sort of radiation only depends on a single scalar, the temperature of the photosphere, the surface at which a photon is most likely to have last interacted before free-streaming through space. Departures from perfect blackbody behavior may be caused by, e.g., the influence of atomic transitions on the opacity, or emission from optically thin coronal regions, and

¹ $10.1 \lesssim M/M_{\odot} \lesssim 100$ when normalized to the mass M_{\odot} of the most well-known and well-understood such sphere.

²budget constraints.

³travel restrictions.

these departures may encode finer details about the stellar environment. However, in any case, photons are incapable of directly communicating any information to us from stellar interiors. This apparently curses our knowledge about the physics that goes in on these places to be forever model-dependent.

1.1 Waves in stars

This thesis concerns asteroseismology, the measurement of hydrodynamical waves in stars. Waves are evolving disturbances which result when a star is perturbed from hydrostatic equilibrium. When these perturbations are of low-enough amplitude, waves can be treated in linear theory. In this linear regime (assumed hereafter), waves obey superposition and evolve according to the linearized equations of stellar structure (e.g., Unno, Osaki, Ando, Saio, et al., 1989). When they reach the surface, waves perturb the surface flux and fluid displacement pattern to which photometry and spectroscopy are respectively sensitive.

In a maximally broad interpretation, hydrodynamical waves are carriers of information with unique characteristics. To drive home this point: the last decade preceding the time of writing has seen the rapid rise and high fashion of “multimessenger astronomy,” a phrase which describes observations of the same astrophysical source delivered by multiple “messengers” (e.g., gravitational waves, neutrinos, and different categories of electromagnetic radiation). Physically, each messenger probes different substructures within the source (possibly at different times), owing to the unique conditions governing the messenger’s production and propagation. In what follows, I summarize hydrodynamical waves’ characteristics as “messengers” with respect to these two fronts, and describe further essential physics.

1.1.1 Production

In order to exist, hydrodynamical waves must be produced. Fortunately, many things can excite them. The most well-observed pulsating star is the Sun, which possesses solar-like oscillations (whose nomenclature is self-evident). Solar-like oscillations are both turbulently excited and turbulently damped by near-surface convection (see, e.g., Houdek, Balmforth, et al., 1999) and occur in stars with deep outer convective zones (e.g., Sun-like stars, subgiants, red giants). Other excitation mechanisms include the κ - (opacity, e.g., Cox, 1963) and ϵ - (nuclear burning, e.g., Kawaler, 1988) mechanisms, convective flux blocking (Guzik, Kaye, Bradley, Cox, and Neuforge, 2000), and strange-mode instabilities (Glatzel, 1994). These processes often (but do not always) involve a heat-engine-like process which operates when the partial ionization zone of a certain species (e.g., helium) produces a thin convective zone sufficiently close to the stellar surface. Affected modes are sometimes called *self-excited*, *unstable*, or *overstable*, since they possess positive growth rates which

cause them to quickly and spontaneously grow to saturation amplitudes set by nonlinear effects. Modes can also be excited by tides raised by the gravitational fields of close companions (e.g., Fuller, 2017).

The diversity of stellar pulsations is worth emphasis—pulsators occur in the main-sequence, giant, and compact phases, and sample the heterogeneity of stars themselves. To visualize this, it is a traditional pastime of aficionados of stellar oscillations (and other variability) to plot various species of pulsator on a Hertzsprung–Russell diagram. A diagram showing the variability across such variable diagrams is shown in Figure 1.1. While excitation of oscillation modes is prerequisite to performing asteroseismology, nature often provides such means.

1.1.2 Propagation

Although stellar interiors are opaque to light, they are often transparent (or at least translucent) to hydrodynamical waves. The latter are therefore capable of delivering information from a star’s interior to its surface, at which point light can transmit the information the rest of the way to the observer. This is the real power of asteroseismology: it allows us to directly see into the stellar interior in a way that traditional methods cannot⁴.

It is mathematically convenient to decompose a given wave into components whose shape does not evolve in time. Components obeying this condition are eigenfunctions of the time derivative operator:

$$\partial/\partial_t \sim i\omega, \quad (1.2)$$

where ω is the angular frequency. It is also common to also make the identification

$$\nabla \sim -i\vec{k}, \quad (1.3)$$

where the components of the wavenumber \vec{k} can be interpreted as inverse reduced wavelengths: $k_i = 2\pi/\lambda_i$. This substitution is particularly justified when the eigenfunction varies rapidly enough in space to closely resemble a plane wave (Deubner and Gough, 1984). Heuristically, the linearized equations of stellar structure then relate ∂/∂_t to the spatial derivative ∇ , relative to their action on the fluid variables. These equations fix the local relationship between ω and \vec{k} —the *dispersion relation*—which determine the propagative behavior of the wave.

⁴As we have now definitively established asteroseismology to be a category of multimessenger astronomy ipso facto, it is of the author’s present opinion that this field should receive a proportionate amount of attention and funding.

1.1. Waves in stars

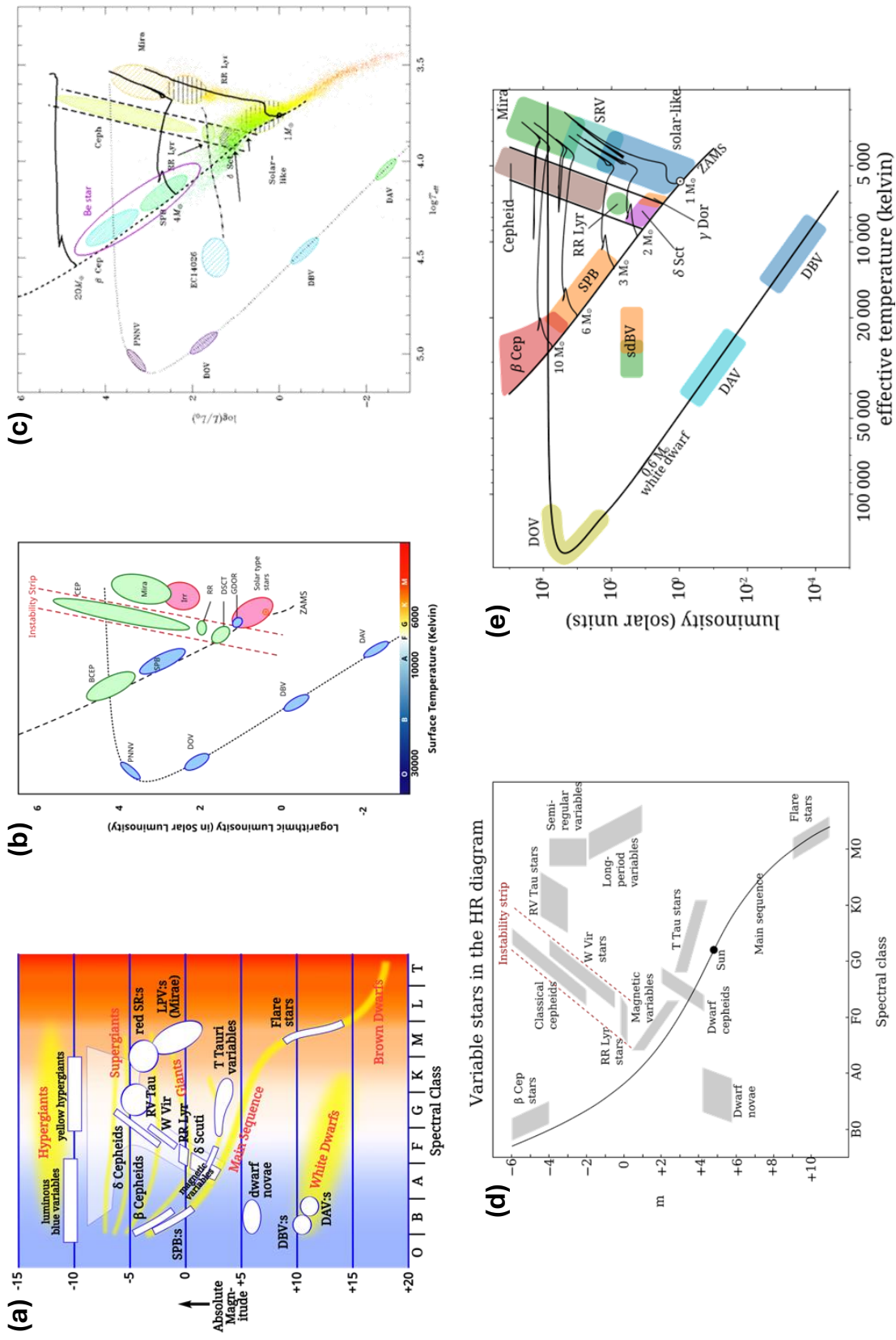


Figure 1.1: A representative sample of variable Hertzsprung–Russell diagrams, reproduced from Wikimedia Commons (for which copyright licenses were the most lenient). There is a diversity of diagrams designed to illustrate the diversity of variable stars. Diagrams are reproduced in compliance with copyright from the following references, with relevant licenses in the parentheticals: (a) Rursus (2008, CC BY-SA 3.0), (b) Pascal57 (2019, public domain), (c) Observatoire de Paris (2006, CC BY-SA 3.0), (d) Vallastro (2022, CC BY-SA 4.0), and (e) Warrickball (2023, CC BY-SA 4.0). Diagrams are reproduced as-is, in particular, panel (e) accidentally switches the labels of the DAV and DBV instability regions.

1.1.3 Oscillation modes

In stars, hydrodynamical waves often propagate across the star faster than they can be damped. When this occurs, waves “feel” the global stellar structure in which they propagate. In particular, the boundary conditions of the eigenvalue problem overdetermine ω and force it to take one of only a discrete set of values. The resulting eigenfunctions take the form of standing waves, called *modes*. Due to this quantization of ω , modes manifest in time series data as sinusoidal signals with sharply defined frequencies whose measurement enables the detailed extraction of stellar properties. In short, asteroseismology is a precision science—modern surveys can measure mode frequencies with minuscule uncertainties down to $\delta\nu \simeq 1/T \simeq 10^{-2} \mu\text{Hz}$ (set by the time baseline, e.g., $T = 4 \text{ yr}$ for the main mission of *Kepler*; Borucki et al., 2010).

The quantization introduced by boundary conditions allows modes to be indexed by three integer quantum numbers, one for each spatial dimension. In the simple, spherically symmetric case, the horizontal wavenumber k_h is quantized according to the appearance of the Laplacian operator in the linearized equations:

$$\nabla_h^2 \equiv \frac{1}{r^2 \sin \theta} \frac{\partial}{\partial \theta} \left(\sin \theta \frac{\partial}{\partial \theta} \right) + \frac{1}{r^2 \sin^2 \theta} \frac{\partial^2}{\partial \phi^2} \sim -\frac{\ell(\ell+1)}{r^2} \equiv -k_h^2, \quad (1.4)$$

i.e., $k_h = \sqrt{\ell(\ell+1)}/r$, where $\ell = 0, 1, 2, \dots$ is the angular degree, familiar from quantum mechanics. Here, θ and ϕ are spherical coordinates with respect to a (so far arbitrarily chosen) polar axis. It is convenient to further enforce $\partial/\partial\phi \sim im$ where $-\ell \leq m \leq \ell$. The angular dependence of the eigenfunctions are therefore given by the complex spherical harmonics $Y_{\ell m}$, quantized by the periodic domain of the unit sphere.

It remains to understand the dependence of the eigenfunction on radius. We hereafter work in the *asymptotic approximation*, which truncates the Jeffreys–Wentzel–Kramers–Brillouin (JWKB) expansion and heuristically amounts to assuming that the eigenfunction varies quickly in radius (e.g., Section 7.2 of Christensen-Dalsgaard, 2008). The radial quantization on the mode frequencies then imposes

$$\int k_r \, dr = \pi(n + \epsilon), \quad (1.5)$$

where the integral is over the mode cavity. By writing Equation 1.5, we assume that the wave is trapped underneath the stellar surface so that an outer boundary condition is indeed imposed, eliding a nuance related to the acoustic cutoff frequency (but see Deubner and Gough, 1984).

The spacing between successive modes can be found by taking a derivative:

$$\Delta\omega = \frac{\partial\omega}{\partial n}\Delta n = \left(\frac{\partial n}{\partial\omega}\right)^{-1} = \pi \left(\int \frac{\partial k_r}{\partial\omega} dr\right)^{-1}, \quad (1.6)$$

which can be rewritten as

$$\Delta\omega = \frac{\pi}{\int dr/v_{g,r}}, \quad (1.7)$$

where $v_{g,r} \equiv \partial\omega/\partial k_r$ is the radial component of the group velocity. The spacing between mode frequencies is therefore comparable to the inverse wave crossing time across the cavity.

1.1.4 Taxonomy of stellar waves

Multiple different species of waves propagate through stellar interiors, classified primarily by the force which is responsible for restoring fluid parcels back to the equilibrium. Further in the spirit of simplicity, we neglect spatial derivatives of the equilibrium stellar structure as well as perturbations to the gravitational potential (the *Cowling approximation*). The linearized hydrodynamical equations become

$$\frac{\partial\rho'}{\partial t} + \rho_0 \nabla \cdot \vec{u} = 0 \quad (1.8a)$$

$$\rho_0 \frac{\partial\vec{u}}{\partial t} = -\nabla p' - \rho' g \hat{r} \quad (1.8b)$$

$$\partial_t \rho' = \rho_0 N^2 \hat{r} \cdot \vec{u} / g + \partial_t p / c_s^2, \quad (1.8c)$$

where ρ' , p' , and \vec{u} are perturbed variables, ρ_0 is the unperturbed density profile, c_s is the speed of sound, and N is the Brunt–Väisälä (buoyancy) frequency.

The dispersion relation produced by Equations 1.8 is approximately

$$k_r^2 = \frac{1}{\omega^2 c_s^2} \left(\omega^2 - N^2 \right) \left(\omega^2 - S_\ell^2 \right), \quad (1.9)$$

where $S_\ell = k_h c_s$ is the Lamb frequency of degree ℓ . Equation 1.9 admits three qualitatively different behaviors.

When both $\omega^2 > S_\ell^2$ and $\omega^2 > N^2$, the dispersion relation is approximately

$$\omega^2 = k^2 c_s^2 \approx k_r^2 c_s^2. \quad (1.10)$$

This is the regime of *pressure waves*, whose restoring force is the pressure backreaction caused by fluid compression, i.e., the tendency of a fluid to resist being squeezed. Equation 1.10 asserts that, for high-radial-order pressure waves, c_s (with dimensions L/T) defines

the natural scale for converting between ω and k_r . A standing pressure wave is called a *pressure mode*, or *p mode*. By Equation 1.7, p modes are approximately spaced evenly in frequency by

$$\Delta\nu = \frac{\Delta\omega}{2\pi} = \left(2 \int dr/c_s\right)^{-1}, \quad (1.11)$$

called the *large frequency separation* (in contrast to the *small frequency separation*, e.g., Chaplin and Miglio, 2013).

In the opposite regime in which both $\omega^2 < S_\ell^2$ and $\omega^2 < N^2$, the dispersion relation instead takes on a very different form, approximately

$$\omega^2 = \frac{k_h^2}{k^2} N^2 \approx \frac{k_h^2}{k_r^2} N^2. \quad (1.12)$$

This is the regime of *gravity waves*, whose restoring force is buoyancy, i.e., the tendency of dense fluid to sink. Equation 1.12 asserts that, for high-radial-order gravity waves, Nk_h (with dimensions L·T) defines the natural scale for converting between ω and k_r . Moreover, Equation 1.12 implies that gravity waves must be nonradial ($\ell \neq 0$) and can only propagate in stably stratified regions ($N^2 > 0$). A standing gravity wave is called a *gravity mode*, or *g mode*. By Equation 1.7, g modes are approximately spaced evenly in period (*not* frequency) by

$$\Delta\Pi_\ell = \frac{2\pi\Delta\omega}{\omega^2} = \frac{2\pi^2}{\sqrt{\ell(\ell+1)}} \left(\int \frac{N}{r} dr \right)^{-1}, \quad (1.13)$$

called the *period spacing*. Algebraically, the spacing is even in period and not frequency due to the different dimensions of Nk_h and c_s .

Finally, when ω^2 lies between S_ℓ^2 and N^2 in either order, $k_r^2 < 0$, i.e., k_r is imaginary. Under these conditions, the eigenfunction grows or decays exponentially in space and is called *evanescent*.

The dispersion relation in Equation 1.9 describes most behaviors relevant to high-radial-order waves in stellar interiors. However, the introduction of additional forces can both modify the propagation of existing branches of waves as well as introduce new types. For example, in rotating stars, the Coriolis force modifies gravity waves to gravito-inertial waves (e.g., Dintrans, Rieutord, and Valdettaro, 1999). It also introduces inertial waves, for which the Coriolis force is the main restoring force (e.g., Rieutord and Valdettaro, 1997). Stars can also sustain modes which arise out of sharp discontinuities in the stellar profile, e.g., fundamental and interfacial modes, which are also not captured by Equation 1.9.

Red giants (RGs) are a central focus of this work. Like the Sun itself, RGs are solar-like oscillators whose pulsations are both excited and damped by turbulent processes associated

with near-surface convection. This stochastic driving is broadband and can excite up to dozens of modes to visible amplitudes, producing asteroseismic treasure troves. Unlike the Sun, however, RGs exhibit extreme density contrasts owing to their core–envelope structure. In particular, the high densities in the core push the allowed range of g-mode frequencies up to those which are driven by convection. RGs which are on the lower red giant branch or in the red clump display dipole modes which behave as p modes in the envelope and p modes in the core, with significant amplitude in each region, i.e., the cavities are significantly coupled. The resulting *mixed modes* constitute valuable seismic windows into the deep interior of the star. This combination of nice properties makes RGs excellent asteroseismic laboratories on which to push the frontier of our understanding.

1.2 Seismology as the hammer

This thesis investigates the observational properties of stars with histories of stellar mergers (**Chapters II–III**) and magnetic fields (**Chapters IV–VII**). Both topics are considered “noncanonical” components of stellar physics—they are traditionally ignored in the “standard model” of isolated, non-magnetic stellar evolution. This is not because stellar mergers or magnetic fields are rare but rather because each individually introduces additional, extremely complex phenomenologies which are often wise to ignore on a first pass.

In what follows, I treat stellar mergers and magnetism as nails for which seismology is the hammer. To organize the workspace, I summarize the recent literature in application of seismology to each of these pieces of physics, and place the core chapters of this thesis in their appropriate context.

1.2.1 Seismic stellar merger genealogy

For the most part, all of the properties of a single star are determined by two parameters: its initial mass M and current age t . In this simplified picture, a population of single stars thus populates a two-dimensional manifold in any parameter space within which they are placed. In contrast, the space of post-interaction stars is very high-dimensional. Mass transfer events and stellar mergers are messy maps from extremely diverse initial conditions (the progenitors’ structures and pre-interaction binary configuration) to the remnant star’s structure. Therefore, stellar merger remnants usually have combinations of stellar properties which position them off of the “single-star manifold.” This basic observation about the dimensionality of a stellar population generalizes when adding secondary (but deterministic) effects due to, e.g., metallicity.

Star clusters are an instructive example. It is common to assume that stars within the same cluster were born at the same time, and thus that the resulting population is coeval (i.e.,

t is a constant within the population). Single stars within a star cluster must therefore lie on a one-dimensional sequence within any parameter space. This is the basic reason why stars in any star cluster form an approximately one-dimensional sequence (isochrone) when plotted on a Hertzsprung–Russell diagram (luminosity L versus effective temperature T_{eff}). However, observed star clusters also possess objects which lie off of the isochrone in the Hertzsprung–Russell diagram. Their “outlier” status flag them as *prima facie* unusual, even without necessarily identifying them as post-interaction stars such as blue stragglers or hot subdwarfs (or photometric binaries, which are not post-interaction but nevertheless not captured by models of isolated stars).

Of course, it is still possible for a post-interaction star to closely resemble a single star. For instance, the remnant of a merger between two main-sequence stars is expected to closely resemble another isolated (but more massive) main-sequence star. This is because main-sequence stars (especially young ones) are made of more-or-less unprocessed hydrogen-rich material, as are the remnants of the mergers between them. Merger remnants may be particularly hard to discern if only their surface properties have been observed. Observational placement on an Hertzsprung–Russell, for example, only directly constrains the outer boundary condition satisfied by a solution of the stellar structure equations. Many different such solutions may exist.

In contrast, adding seismic observables allows stars to be placed in a space in which those with exclusively unusual *interiors* are also outliers. Framed this way, the seismic identification of stellar merger remnants can be framed as internal structure-informed anomaly detection, where the “anomalies” occur at the few-percent level in stars with Sun-like masses (e.g., Price-Whelan et al., 2020).

The initial chapters of this thesis focus on the seismic properties of two classes of RG-like merger remnants. For such merger remnants, the tools and intuition developed for the seismology of normal RGs can be straightforwardly adapted. **Chapter II** (Rui and Fuller, 2021a) considers RGs which have ingested close main-sequence companions during their ascension up the red giant branch. This engulfment endows the merger remnant with unusually overmassive envelopes to which seismology is sensitive. **Chapter III** (Rui and Fuller, 2024) considers the remnants of coalescences of accreting helium-core white dwarf systems. The resulting object possesses an abnormally low-entropy core which affects the remnant’s seismic properties and subsequent evolution.

In recent years, seismology has rapidly gained recognition as a probe of stellar interaction histories. Closely following Rui and Fuller (2021a), Deheuvels, Ballot, Gehan, et al. (2022) discovered roughly four dozen red giant branch stars in the scatter below the degenerate

sequence in the seismic $\Delta\nu$ – $\Delta\Pi_1$ diagram (see also Li, Deheuvels, and Ballot, 2024). Their positions on the seismic spacing diagram indicate that their total masses and degrees of core degeneracy are inconsistent with isolated stellar evolution, implying that they likely gained mass from a stellar interaction.

In the red clump (core helium-burning phase), Li, Bedding, Murphy, et al. (2022) identify two classes of unusual stars in the seismic mass–radius plane. The “very low-mass” stars have masses $\lesssim 0.8M_\odot$ implying main-sequence lifetimes longer than the age of the universe, and the “underluminous” stars have unusually low radii but otherwise normal masses. Both very-low-mass and underluminous stars have lost an unusually large amount of mass during the course of their evolution, likely due to a close binary interaction. These classes are distinguished from each other by whether the initial helium ignition was degenerate (very-low-mass) or non-degenerate (underluminous). Matteuzzi et al. (2023) further investigate three members within the very low-mass class of RGs (termed in that work as “red horizontal branch” stars), finding extremely high degrees of mixed-mode coupling consistent with model predictions for their evanescent wave regions.

Seismology can also effectively synergize with other observational techniques to identify systems of likely binary origin. By measuring $\Delta\Pi_1$, Hon, Huber, Rui, et al. (2023) seismically identified the star 8 UMi (Baekdu) as a core helium-burning star. However, 8 UMi is also the host of a close ($a \approx 0.5$ AU) giant planet which, in the single-star scenario, should have been engulfed during 8 UMi’s preceding red giant branch phase. The system can, however, be explained as the outcome of a merger between a RG and a helium-core white dwarf. Such a merger could have ignited 8 UMi’s helium without requiring it to ascend all the way to the tip of the red giant branch (e.g., Zhang and Jeffery, 2013). The lithium-richness of 8 UMi seems to lend credence to this binary hypothesis.

Rapid rotation in RGs is also a strong indicator for past stellar interactions. This is because the envelopes of isolated RGs spin extremely slowly, owing to angular momentum conservation on the red giant branch. In consequence, any detection of a substantial rotation rate in the envelope implies some kind of spin-up due to a stellar or tidal interaction (e.g., Carlberg, Majewski, et al., 2011; Tayar, Ceillier, et al., 2015; Ceillier et al., 2017). While surface rotation rates can be measured by other methods (e.g., photometric modulation, rotational broadening), rapid envelope rotation can also be corroborated by p-mode rotational splittings (see, e.g., Tayar, Moyano, et al., 2022; Ong, Hon, et al., 2024). Furthermore, unlike those other methods, seismology is also capable of measuring the rotation rates of the *cores* of RGs. Leveraging this sensitivity to differential rotation, (Ong, 2025) show that

the envelope and core of Kepler-56 rotate around different axes, consistent with either the past engulfment of or ongoing tidal realignment by a planet.

1.2.2 Seismic stellar magnetometry

Stellar magnetic fields are largely a consequence of the fact that electrically conductive fluids, common throughout the universe, conserve magnetic flux as they deform. In consequence, when a progenitor molecular cloud collapses and contracts manyfold into stars, even tiny magnetic fields can translate to large magnetic fields. Flux freezing also allows stars with complex motions (e.g., differential rotation, instabilities) to amplify small seed magnetic fields into large ones by “stretching” them out (the realm of dynamo theory, e.g., Elsasser, 1956). These processes offer a compelling post hoc explanation not only for the basic existence of stellar magnetic fields in general but also their observed diversity. Magnetic fields are also crucial actors in the rotational evolution of stars via magnetic braking (Mestel, 1968) and angular momentum transport (Aerts, Mathis, et al., 2019).

Magnetic fields influence the propagation of hydrodynamical waves as an additional restorative force and a damping effect. In high-radial-order g modes (such as those in the radiative cores of RGs), the wavenumber is primarily radial and the fluid motions are primarily horizontal. These properties make such modes primarily sensitive to the magnetic tension associated with the radial component of the magnetic field. The degree to which a magnetic field affects the propagation of a g mode is given by its strength relative to a critical field strength:

$$B_{r,\text{crit}} \propto \sqrt{\rho\omega^2}r/N, \quad (1.14)$$

typically hundreds of kilogauss in RG cores (Fuller, Cantiello, et al., 2015). At this field strength, the Alfvén frequency becomes comparable to the frequency of a g mode with angular frequency ω (e.g., Cantiello et al., 2016). Gravity waves propagating in regions with $B_r > B_{r,\text{crit}}$ are predicted to be strongly damped.

Magnetic g-mode suppression was first invoked by Fuller, Cantiello, et al. (2015) to explain the depressed amplitudes of dipole modes in $\simeq 20\%$ of observed RGs (García, Pérez Hernández, et al., 2014; Stello, Cantiello, Fuller, Huber, et al., 2016). The implication from Equation 1.14 that low-frequency modes are preferentially suppressed appears to be validated by the suppression of only the low-frequency g modes in a RG (KIC 6975038; Deheuvels, Li, et al., 2023) as well as in a B-type star with a strong surface magnetic field (HD 43317; Lecocanet, Bowman, et al., 2022). In this basic picture, observation of g-mode suppression places a lower bound on the magnetic field, and non-observation places an upper bound. However, an analysis by Mosser, Belkacem, et al. (2017) argues that dipole

modes in affected RGs still retain some g-mode-like character (see also Arentoft et al., 2017). This observation seems to contradict the supposition by Fuller, Cantiello, et al. (2015) that magnetic fields $> B_{r,\text{crit}}$ result in near-total suppression of g-mode energy.

Recent studies have greatly advanced our theoretical understanding of magnetogravity wave propagation. In a original schematic calculation, Fuller, Cantiello, et al. (2015) show that magnetogravity waves become spatially evanescent ($k_r^2 < 0$) when $B_r > B_{r,\text{crit}}$, and speculate that the resulting wave contain higher- ℓ content which is both efficiently damped and difficult to see due to geometric cancellation. Performing a deeper analysis of zonal magnetogravity waves under a realistic multipolar field geometry, Lecoanet, Vasil, et al. (2017) show that refracted magnetogravity waves approach zero wavelength at a finite “cutoff” height, suggesting a natural avenue for wave dissipation. Motivated by this progress, **Chapter IV** (Rui and Fuller, 2023) introduces a formalism for calculating the morphology of a g mode under the influence of a strong gravitational field. The radial–horizontal decomposition applied in this study is justified by the high radial orders characterizing g modes in typical RGs and intermediate-mass main-sequence stars. I find that, for $B_r > B_{r,\text{crit}}$, non-zonal modes develop sharp features at critical latitudes where the mode satisfies a resonance condition with the Alfvén frequency. These sharp features were also observed in the numerical calculations of Lecoanet, Bowman, et al. (2022), and provide an additional mechanism for g-mode dissipation. However, ray-tracing calculations by Loi (2020c) and Müller et al. (2025) show that some wave power may yet escape magnetic suppression and be observed, at least for high- ℓ modes. Analyses such as these are likely to help reconcile our theoretical picture of magnetic suppression with the residual g-mode character of suppressed-dipole modes reported by Mosser, Belkacem, et al. (2017) and Arentoft et al. (2017).

Magnetic fields weaker than $B_{r,\text{crit}}$ can still measurably influence g-mode frequencies, even if they are too weak to suppress g modes. When included as an additional restorative force, the Lorentz force always has the effect of increasing their frequencies (“stiffening” them). Most theoretical analyses calculate magnetic shifts to g-mode frequencies by performing perturbation theory with $B_r/B_{r,\text{crit}}$ as the small quantity (Gomes and Lopes, 2020; Bugnet, 2022; Li, Deheuvels, Ballot, and Lignières, 2022; Mathis and Bugnet, 2023; Das et al., 2024). It is usually further assumed that the magnetic field is still subdominant compared to the Coriolis force, such that the pulsations are aligned with the rotation axis.

Magnetic g-mode shifts were first discovered several years ago by Li, Deheuvels, Ballot, and Lignières (2022) in the dipole modes of three RGs. In particular, the study made use of the fact that magnetic shifts generally depend on m . This dependence causes the rotational

triplets of RGs to depart from uniform spacing in frequency (the frequency shift due to rotation is proportional to m), producing measurable “asymmetries.” Of particular intrigue has been the sensitivity of the asymmetry of the triplet to the *geometry* of the magnetic field. Later studies have expanded the sample of RGs with measured magnetic asymmetries to several dozen (Li, Deheuvels, Li, et al., 2023; Hatt et al., 2024). In RGs with stronger core magnetic fields (but still less than $B_{r,\text{crit}}$, so that suppression does not occur), magnetic frequency shifts can even be high enough to produce a measurable departure from the period-uniformity of g modes (Deheuvels, Li, et al., 2023).

Two chapters of these thesis address the calculation of magnetic g-mode frequency shifts when certain conventional assumptions are relaxed. **Chapter V** (Rui, Ong, et al., 2024) generalizes the method developed in Chapter IV to include rotation and uses it to predict g-mode frequency shifts under strong magnetic fields for which perturbation theory is inapplicable ($B_r \sim B_{r,\text{crit}}$). I emphasize a strong analogy to the traditional approximation of rotation, the standard approach for computing the effects of a strong Coriolis force (e.g., Hough, 1898a; Bildsten, Ushomirsky, et al., 1996; Lee and Saio, 1997). This *traditional approximation of rotation and magnetism* may help bridge the observational gap between RGs with dipole-suppression and those with magnetic asymmetries (interpreted with the perturbative theory). **Chapter VI** (Rui, Fuller, and Ong, 2025), in contrast, works in the perturbative weak-field limit, but allows the magnetic field to exceed the Coriolis force in strength. When this occurs, the g modes become oblique, and the one-to-one mapping between modes and power spectral peaks is broken. This is a well-known phenomenon afflicting the spectra of roAp stars, which are known to harbor strong surface magnetic fields (e.g., Kurtz, 1982; Dziembowski and Goode, 1996). I show that stochastic oblique pulsators (such as magnetic RGs or Sun-like stars) should possess frequency components whose relative phases and amplitudes are fixed, even as stochasticity erases absolute phase information. This perfect relative coherence may be the key to detecting oblique magnetic pulsators in RGs and Sun-like stars for the first time.

Finally, though most of the discussion about magnetogravity waves in this thesis occurs in the context of RGs, the vast majority of the formalism assumes little more than high-radial-order g-mode pulsation. In fact, although seismic magnetometry in RGs is recent, the idea of seismic magnetometry in white dwarfs dates back to a calculation by (Jones et al., 1989) showing that even weak magnetic fields (< 1 MG) can produce measurable frequency shifts. This was soon followed by the putative detection of asymmetric rotational triplets in the prototype DBV pulsator GD 358 (Winget, Nather, et al., 1994). **Chapter VII** (Rui, Fuller, and Hermes, 2025) uses non-detections of magnetic g-mode suppression and asymmetries

in rotational triplets/quintuplets to place order-of-magnitude upper limits on the magnetic fields in white dwarfs. It is found that seismology can place strong upper bounds on the near-surface magnetic fields of white dwarfs. These upper bounds are typically $\sim 1\text{--}10$ kG, but occasionally much more stringent ($\sim 1\text{--}100$ G).

Chapter VIII concludes with my perspective on possible future directions. This thesis in sum: most of what we know about stars comes from looking at them—I argue that we should also listen.

Chapter 2

ASTEROSEISMIC FINGERPRINTS OF STELLAR MERGERS

Rui, N. Z. and J. Fuller (2021). “Astroseismic fingerprints of stellar mergers.” In: *Monthly Notices of the Royal Astronomical Society* 508.2, pp. 1618–1631. doi: 10.1093/mnras/stab2528. arXiv: 2108.10322.

Stellar mergers are important processes in stellar evolution, dynamics, and transient science. However, it is difficult to identify merger remnant stars because they cannot easily be distinguished from single stars based on their surface properties. We demonstrate that merger remnants can potentially be identified through asteroseismology of red giant stars using measurements of the gravity mode period spacing together with the asteroseismic mass. For mergers that occur after the formation of a degenerate core, remnant stars have over-massive envelopes relative to their cores, which is manifested asteroseismically by a g-mode period spacing smaller than expected for the star’s mass. Remnants of mergers which occur when the primary is still on the main sequence or whose total mass is less than $\approx 2 M_{\odot}$ are much harder to distinguish from single stars. Using the red giant asteroseismic catalogs of Vrard, Mosser, et al. (2016) and Yu et al. (2018), we identify 24 promising candidates for merger remnant stars. In some cases, merger remnants could also be detectable using only their temperature, luminosity, and asteroseismic mass, a technique that could be applied to a larger population of red giants without a reliable period spacing measurement.

This work was inspired by discussions at the 2019 Scialog Meeting. We thank Dan Huber, Carl Melis, Sébastien Deheuvels, Fred Rasio, Jamie Lombardi, Tuguldur Sukhbold, and Pablo Marchant for insightful discussions and advice both scientific and technical. N.Z.R. acknowledges support from the Dominic Orr Graduate Fellowship at Caltech. J.F. is thankful for support through an Innovator Grant from The Rose Hills Foundation, and the Sloan Foundation through grant FG-2018-10515. This research has made use of the SIMBAD database, operated at CDS, Strasbourg, France. We thank the anonymous referee for their useful suggestions.

2.1 Introduction

Stellar mergers are physically complex processes with broad implications across astrophysics. Kochanek et al. (2014) find that galactic mergers occur at a high rate of $\sim 0.2 \text{ yr}^{-1}$, and Mink et al. (2014) further show that merger products comprise $\approx 30\%$ of high-mass main sequence stars. Mergers are a common endpoint of binary stellar evolution (Paczynski, 1976), and they are believed to be the origin of astrophysical transients such as luminous red novae (Tylenda and Soker, 2006; Soker and Tylenda, 2006; Ivanova, Justham, Nandez, et al., 2013; Pejcha et al., 2016; Metzger and Pejcha, 2017). Collisions between stars are also expected to occur at high rates in dense stellar environments such as globular clusters, where they are believed to be an important formation channel for blue stragglers (Bailyn, 1995), some of which have exotic properties suggestive of this origin (e.g., Schneider, Ohlmann, Podsiadlowski, Röpke, Balbus, Pakmor, and Springel, 2019). In these environments, they have been recently proposed as one possible explanation for multiple stellar populations (Mastrobuono-Battisti et al., 2019; Wang, Kroupa, et al., 2020).

While millions of merger remnants are expected to exist in the Galaxy, identifying the surviving stars in the field is challenging. Detailed asteroseismic characterization of red giant (RG) stars offers a new hope, because the oscillations of RGs are particularly rich in information for two reasons. First, the close values of the Brunt–Väisälä and Lamb frequencies create a narrow evanescent region within the star, coupling the observable p modes at their surfaces to the g modes within their radiative cores. Second, the frequencies occupied by these “mixed modes” are serendipitously excited by stochastic driving from convective motions in their envelopes. The intimate coupling between interior and surface oscillations allow for detailed asteroseismic constraints on their core structures, allowing for the determination of evolutionary states (Bedding et al., 2011; Bildsten, Paxton, et al., 2011; Mosser, Benomar, et al., 2014; Cunha, Stello, et al., 2015; Elsworth et al., 2017), internal rotation rates (Beck et al., 2012; Mosser, Goupil, Belkacem, Marques, Beck, Bloemen, De Ridder, Barban, Deheuvels, Elsworth, et al., 2012b; Klion and Quataert, 2017; Gehan et al., 2018; Ahlborn et al., 2020; Deheuvels, Ballot, Eggenberger, et al., 2020), and core magnetic fields (Fuller, Cantiello, et al., 2015; Stello, Cantiello, Fuller, Garcia, et al., 2016; Cantiello et al., 2016; Mosser, Belkacem, et al., 2017; Loi, 2020a).

Therefore, in addition to encoding stellar masses and radii in the large frequency spacing $\Delta\nu$ and the frequency of maximum power ν_{\max} (Kallinger, Weiss, et al., 2010), asteroseismology is also a probe of the core structures of RGs through the mixed mode period spacing ΔP_g

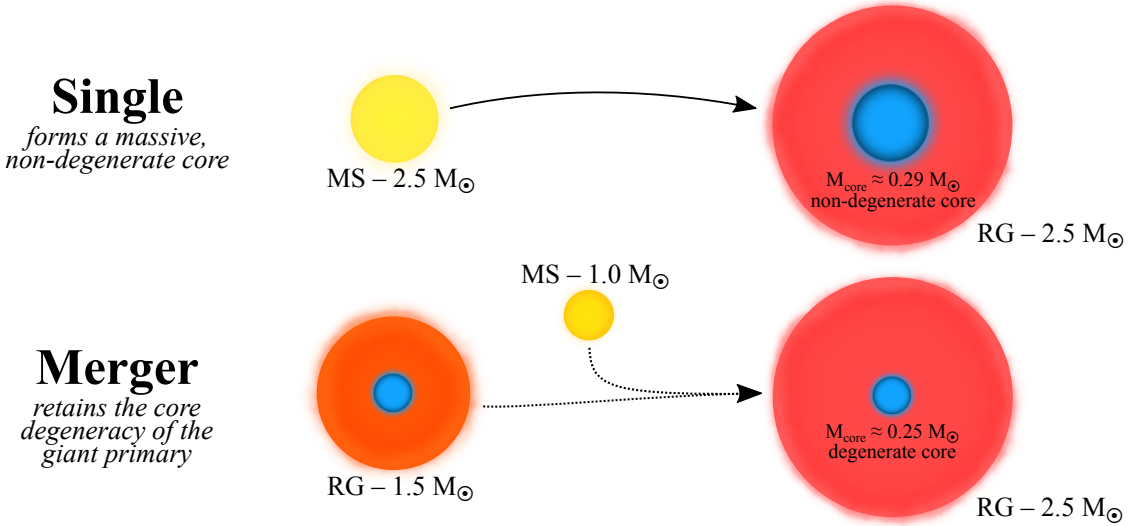


Figure 2.1: A cartoon comparing a $2.5 M_{\odot}$ RG formed as an isolated, single star with one formed in a merger where the primary has already entered the RG phase and the secondary remains on the MS. If the RG primary is in the mass range where it forms a degenerate core (e.g., $M = 1.5 M_{\odot}$), the merger product will generally retain it, even if a single star of the same mass would have been expected to produce a more massive, non-degenerate core on the RGB.

in the dipole ($\ell = 1$) mode peaks of approximately

$$\Delta P_g = \sqrt{2}\pi^2 \left(\int_{\mathcal{R}} \frac{N}{r} dr \right)^{-1}. \quad (2.1)$$

Here, N is the Brunt–Väisälä frequency and \mathcal{R} denotes the portion of the star’s central radiative region where $\nu_{\max} < N$ (Chaplin and Miglio, 2013). Intuitively, this dipole splitting results from the coupling of a given p mode to multiple, distinct g modes, hence the sensitive dependence of ΔP_g on the Brunt–Väisälä frequency in the central regions of the star. For a typical RG, ΔP_g is typically on the order of minutes, large enough to be measured by prominent surveys such as *CoRoT* (Mosser, Barban, et al., 2011) and *Kepler* (Stello, Huber, et al., 2013; Vrard, Mosser, et al., 2016). The value of ΔP_g is primarily determined by the mass and evolutionary state of the star’s helium core, and comparison of measured values to models provides an excellent test of stellar evolution theories.

In this work, we demonstrate that RGs which have a merger in their histories can be identified via asteroseismology, provided that the merger occurs after the primary has left the main sequence (MS) and the secondary remains a MS star. Asteroseismology will be effective at identifying a merger when the original RG develops a small, degenerate core that the final RG would not otherwise be expected to have. The difference in core structure

between such a merger product and an equal-mass RG forming via single star evolution manifests in a different gravity mode structure and, in turn, different period spacings of their dipole modes. We sketch this picture heuristically in Figure 2.1, which shows our fiducial comparison between a single $2.5 M_{\odot}$ RG and the product of a $1.5 + 1.0 M_{\odot}$ RG+MS merger.

2.2 Stellar models

In order to obtain physically realistic stellar models, we employ Modules for Experiments in Stellar Astrophysics (**MESA**, version r12778; Paxton, Bildsten, et al., 2010; Paxton, Cantiello, et al., 2013; Paxton, Marchant, et al., 2015; Paxton, Schwab, et al., 2018; Paxton, Smolec, et al., 2019), an open-source one-dimensional stellar evolution code. We first initialize a grid of single star models from $0.75 M_{\odot}$ from $2.75 M_{\odot}$, which are integrated through the MS and RGB, for the purpose of (1) providing initial conditions for binary merger models and (2) computing asteroseismic observables in single stars. The stellar models are taken to be non-rotating and solar-metallicity, with reasonable values for convective overshoot. Model details and inlists are provided in Appendix 2.A.

We then model mergers as rapid accretion events with a rate $\dot{M} = 10^{-5} M_{\odot} \text{ yr}^{-1}$ at the surface of the star. The original star starts off on the main sequence with solar composition, and at a specified age, it accretes material with the same composition as its surface (which is also close to solar composition). While this cannot be expected to capture the transient structure of the star immediately after the merger, it should provide a reasonable model of the star after thermal relaxation, i.e., a few thermal times after merger. While the adopted accretion rate is less than what is expected during a real merger, it should approximate a real merger event well because the accretion time scale $t_{\text{ac}} = M/\dot{M} \sim 10^5 \text{ yr}$ is much shorter than a thermal time scale, hence the accretion is still in the rapid (adiabatic) regime. We run a number of “merger” models, beginning with a fine grid of $1.5 + 1.0 M_{\odot}$ models where we vary the time of merger (Section 2.3.2). Next, we run a pair of grids where we vary the initial and final stellar masses, one in which the merger occurs when the primary is on the RGB, and the second when it is on the MS (Section 2.3.3). We then relax the convergence conditions required to run a $1.5 + 1.0 M_{\odot}$ model through helium burning, and we examine the behavior of the period spacing on the red clump (Section 2.3.4).

While in reality the secondary star may be expected to penetrate deeply into the star’s envelope before being disrupted and mixed into the star, modeling an RG+MS merger as a surface mass injection is sensible as long as the secondary mixes into the envelope before reaching the core. We can use the approximation of Eggleton (1983) to compute an effective Roche lobe radius for a secondary during a common envelope phase, taking as the mass

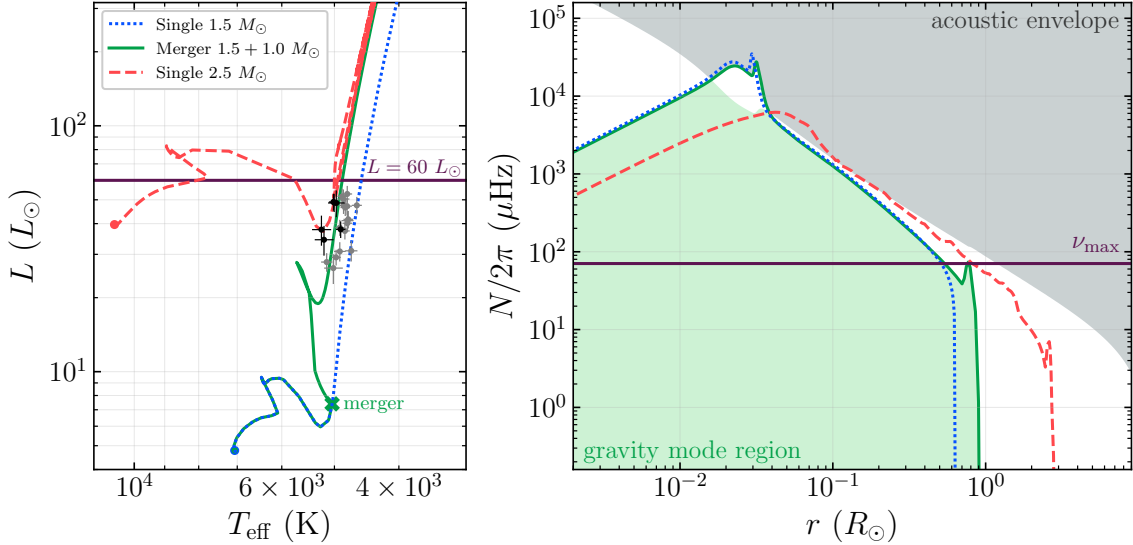


Figure 2.2: *Left:* Hertzsprung-Russell diagram of a single $1.5 M_{\odot}$ star (blue dotted line), a $1.5 + 1.0 M_{\odot}$ RG+MS merger product (solid green line), and a single $2.5 M_{\odot}$ star (dashed red line). Circular points indicate merger remnant candidates discussed in Section 2.4.1, with black points showing the best candidates. *Right:* Propagation diagrams at $L = 60 L_{\odot}$ for these three models. We also show the the gravity mode region (green), as well as the acoustic mode region (gray) and ν_{\max} (purple), for the merger model, although the latter two are similar between all three models. Despite the merger, the Brunt–Väisälä frequency of the merger product most closely resembles that of a non-merged star of the original mass, rather than that of a non-merged star of the present-day mass.

ratio $q = M_2/M_{1,\text{enc}}(r)$, the ratio of the mass of the secondary to the mass of the primary enclosed by the orbit. For the $1.5 + 1.0 M_{\odot}$ merger shown in Figure 2.2, we find that the MS secondary is expected to disrupt and mix into the primary’s convective envelope at $r \approx 2.8 R_{\odot}$ in our models, very close to the surface of the primary and far outside of the helium core ($r_{\text{core}} \approx 0.04 R_{\odot}$ on the lower RGB).

2.2.1 Detailed oscillation mode calculations

While the period spacing between modes of the same gravity mode degree generally lie quite close to the asymptotic period spacing ΔP_g , they may deviate somewhat from this value, particularly when the mode has a large mixed character. Since mixed modes are the most easily detected, it is critical to correct for this phenomenon when extracting the asymptotic period spacing from observations (e.g., Vrard, Mosser, et al., 2016).

In order to confirm that the asymptotic period spacing ΔP_g as defined by Equation 2.1 lies close to the actual gravity mode spacing of our stellar profiles, we employ `GYRE`, a shooting code which computes stellar oscillation modes given one-dimensional stellar

profiles (Townsend and Teitler, 2013). Working in the adiabatic limit, we first calculate all oscillation modes with $\ell = 0$ or 1 lying within a factor of 2 of ν_{\max} (computed from our MESA models using the scaling relation in Equation 2.3) for single $1.5 M_{\odot}$ and $2.5 M_{\odot}$ RGs. We next compute these modes for the product of a $1.5 + 1.0 M_{\odot}$ merger that occurs soon after the main sequence when the primary’s radius reaches $R = 1.25R_{\text{TAMS}}$. Here, R_{TAMS} is the radius of the star at the terminal age main sequence (TAMS), defined to be the earliest time that $X = 0$ in the core. Within each acoustic mode order, we calculate the difference in period between adjacent $\ell = 1$ modes (which differ in gravity mode order), finding them to be very close to ΔP_g in almost all cases except when the character of the mode was very mixed. Therefore, moving forwards, we center our discussion around ΔP_g (as defined in Equation 2.1), with the knowledge that (1) it is a good approximation to the actual, generally frequency-dependent period spacing, and (2) is typically reported in observations after accounting for this frequency dependence.

2.3 Results

2.3.1 Heuristic description

RGs comprise a large convective envelope surrounding a compact, high density core which primarily governs the star’s evolution. With the premise that a stellar merger between a RG with a degenerate core and a MS star mainly increases the RG’s envelope mass while leaving its core intact, the core mass and structure of the RG is nearly unaffected by the merger. Already compact and degenerate cores have higher Brunt–Väisälä frequencies in the core and thus a smaller ΔP_g , relative to the less compact and less degenerate cores arising from more massive stars. This gives rise to a robust observational signature of mergers of this type, provided that the core structure of the post-merger star is significantly different than that of a single RG star with the same mass as the merger product.

Figure 2.2 shows the Brunt–Väisälä frequency profiles of our fiducial models, where it is apparent that the RG merger product largely retains the core gravity mode structure of its RG progenitor. Whereas the $1.5 M_{\odot}$ single star model has a more compact gravity mode region characterized by a larger value of N in its degenerate core, the $2.5 M_{\odot}$ single star model has a more radially extended gravity mode region in its non-degenerate core whose N peaks at a lower frequency. Importantly, for an $1.5 + 1.0 M_{\odot}$ RG+MS merger, the Brunt–Väisälä frequency profile more closely resembles that of the original $1.5 M_{\odot}$ RG. As ν_{\max} and $\Delta\nu$ (together with T_{eff}) provide an independent asteroseismic measurement of the mass, ΔP_g can be used to distinguish a merger product from a single star via their different gravity mode regions. Specifically, merger remnants are expected to have a smaller ΔP_g (similar to that of the progenitor) relative to single stars of the same mass, when evaluated at the same

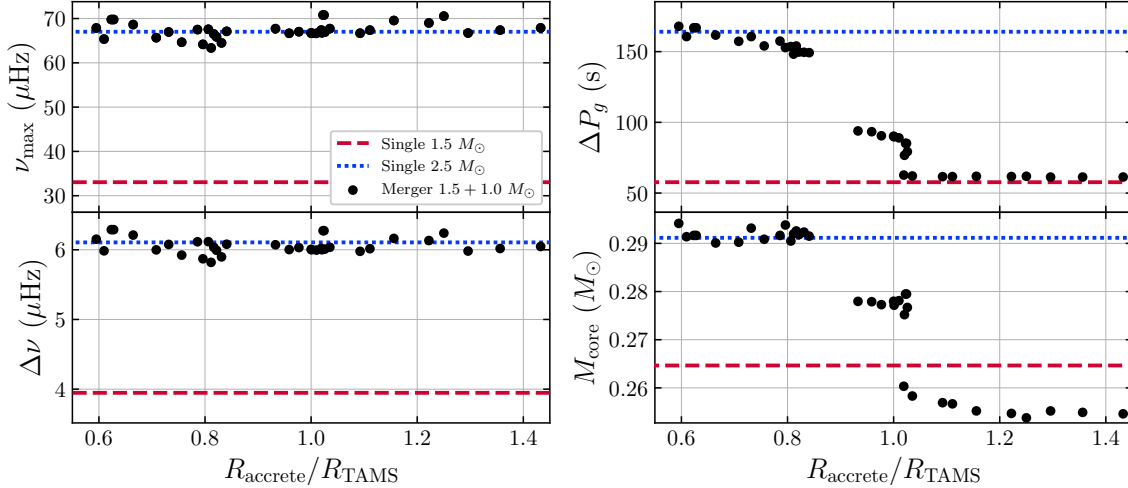


Figure 2.3: The frequency of maximum power ν_{\max} (top left), large frequency spacing $\Delta\nu$ (bottom left), asymptotic period spacing ΔP_g (top right), and helium core mass (bottom right) of the merger product of a $1.5 M_{\odot}$ primary with a $1.0 M_{\odot}$ secondary. The x -axis is the radius of the merging primary relative to its radius at the TAMS, so post-MS mergers occur when $R_{\text{accrete}}/R_{\text{TAMS}} > 1$. The asteroseismic quantities are evaluated when the merger remnant reaches $L = 60 L_{\odot}$ on the RGB. The red and blue lines show the analogous values for single $1.5 M_{\odot}$ and $2.5 M_{\odot}$ RG models of the same luminosity.

luminosity. In the model in Figure 2.2 at $L = 60 L_{\odot}$, the merger remnant has $\Delta P_g = 61.9$ s, very close to that of the original $1.5 M_{\odot}$ star ($\Delta P_g = 57.7$ s) but very far from that of a single star $2.5 M_{\odot}$ ($\Delta P_g = 164.0$ s).

The following sections elaborate on the point that ΔP_g reveals the fingerprint of a stellar merger, but only when the merger occurs after the primary has already left the MS (Section 2.3.2), and only when the merger brings an RG with a degenerate core into a mass regime where single star evolution does not produce degenerate cores (Section 2.3.3).

2.3.2 ΔP_g is sensitive to mergers on the RGB

We run a series of $1.5 + 1.0 M_{\odot}$ merger models where we vary the time of merger from the main sequence to the lower RGB. When the merger product reaches $60 L_{\odot}$ during its ascent up the RGB, we calculate ΔP_g —this luminosity is chosen because RGs at $L = 60 L_{\odot}$ lie just below the bump at a value of $\Delta\nu$ where mixed modes are still observable, but well above the base of the RGB where the merger occurs.

We also calculate the large acoustic frequency spacing $\Delta\nu$ and peak oscillation frequency ν_{\max} (Brown, Gilliland, et al., 1991):

$$\Delta\nu = \left(2 \int_0^R \frac{dr}{c_s}\right)^{-1} \quad (2.2)$$

$$\nu_{\max} = 3100 \mu\text{Hz} \left(\frac{M}{M_\odot}\right) \left(\frac{R_\odot}{R}\right)^2 \left(\frac{T_{\text{eff},\odot}}{T_{\text{eff}}}\right)^{1/2}. \quad (2.3)$$

When combined with the surface temperature, these two quantities trace the total mass and radius of the star. Independent of the time of merger, ν_{\max} and $\Delta\nu$ are unsurprisingly very close to their values for an equal-mass single RG, as the total mass and radius of the resulting RG will be almost identical to a non-merged analogy, when measured at the same luminosity.

Even though $\Delta\nu$ and ν_{\max} are only sensitive to the total mass and radius, ΔP_g traces the core structure and retains information about the star's evolutionary history which can be used to identify merger remnants. Figure 2.3 demonstrates that for mergers occurring after the TAMS, ΔP_g of the merger product more closely resembles that of the $1.5 M_\odot$ progenitor as if it had never merged. Physically, this is due to the pre-merger core already being high density and degenerate, such that its structure is insensitive to the overlying layers. In other words, mergers which occur after the TAMS barely affect the underlying core structure of the progenitor.

For mergers which occur when the primary is still on the MS, Figure 2.3 shows that ΔP_g is essentially the same as that for a single star of the same total mass. The reason for this is revealed in Figure 2.4, whose left-hand panel shows the propagation diagrams of an “early” $1.5 + 1.0 M_\odot$ merger which occurs at $t = 0.5 t_{\text{TAMS}}$, when the primary is on the MS. We see that, in contrast to the “late merger” case (right panel, Figure 2.2), the Brunt–Väisälä frequency profile of the “early” merger model is indistinguishable from a single star of the same mass. This occurs because the main sequence core is not degenerate and is sensitive to the mass of the overlying material, so the core readjusts to be nearly identical to that of a star that was born at $2.5 M_\odot$. As an additional note, we find that, if the merger occurs very close to the TAMS, ΔP_g plateaus to an intermediate value between what is expected for $1.5 M_\odot$ and $2.5 M_\odot$ single stars (Figure 2.3). However, due to the short time window for this merger occur, it is unlikely that this case will be frequently observed.

In principle, a MS merger model may require more sophisticated simulations of the hydrodynamical mixing associated with such a traumatic event. In such mergers, there may be a greater degree of mixing between the two stars, with material from both stars extending throughout the remnant in general. However, as the evolution of a MS star of a given

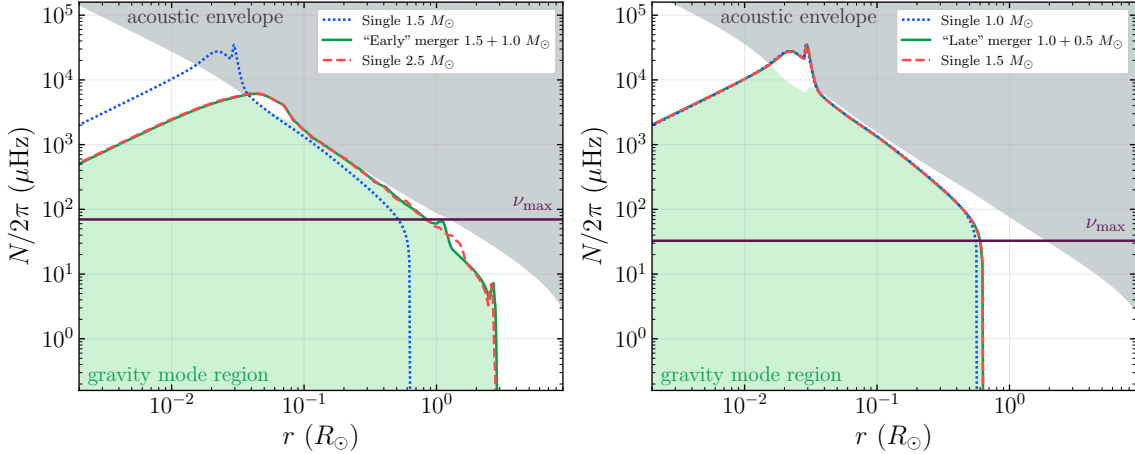


Figure 2.4: *Left:* Propagation diagrams at $L = 60 L_\odot$ for a single $1.5 M_\odot$ star (blue dotted line), a $1.5 + 1.0 M_\odot$ MS+MS merger product (green solid line), and a single $2.5 M_\odot$ star (red dashed line). When the merger occurs while the primary is still on the MS, the merger product will be nearly indistinguishable via ΔP_g from an equal-mass single star. *Right:* Propagation diagrams at $L = 60 L_\odot$ for a single $1.0 M_\odot$ star (blue dotted line), a $1.0 + 0.5 M_\odot$ RG+MS merger product (green solid line), and a single $1.5 M_\odot$ star (red dashed line). As single stars below $M \lesssim 2 M_\odot$ all share similar degenerate core structures, ΔP_g cannot distinguish between a lower mass merger product and equal-mass single star.

composition is essentially determined by its mass, we expect our simple surface accretion approximation to capture the most important effect. To confirm this, we use `MESA`'s native entropy sorting procedure (accessible as `create_merger_model`) to model a $1.5 + 1.0$ MS+MS merger, and confirm that the resulting gravity mode structure at $L = 60 L_\odot$ is virtually identical to the surface accretion merger model.

2.3.3 Pre-merger core degeneracy is key to merger identification

To understand the parameter space where merger products can be asteroseismically identified, we run two grids of merger models. The grids have primary mass in the range $M_{\text{primary}} \in [0.75, 2.50] M_\odot$ and post-merger mass in the range $M_{\text{product}} \in [1.00, 2.75] M_\odot$, spaced by $0.25 M_\odot$ in each dimension. We consider both the case where the merger occurs on the lower RGB (when the primary's radius reaches 1.25 times its value at TAMS) as well as the case where the merger occurs on the MS (when the primary reaches half of its TAMS age). Figure 2.5 compares the period spacings of merger products at $60 L_\odot$ to non-merged stars of equal masses. It is clear that the period spacing is substantially different for high enough product masses when the merger occurs on the RGB, but it is practically indistinguishable when the merger occurs on the MS. While ΔP_g could conceivably be reasonably discriminating for M_{product} as low as $\approx 1.75 M_\odot$ in the RG+MS case, the effect is especially pronounced for

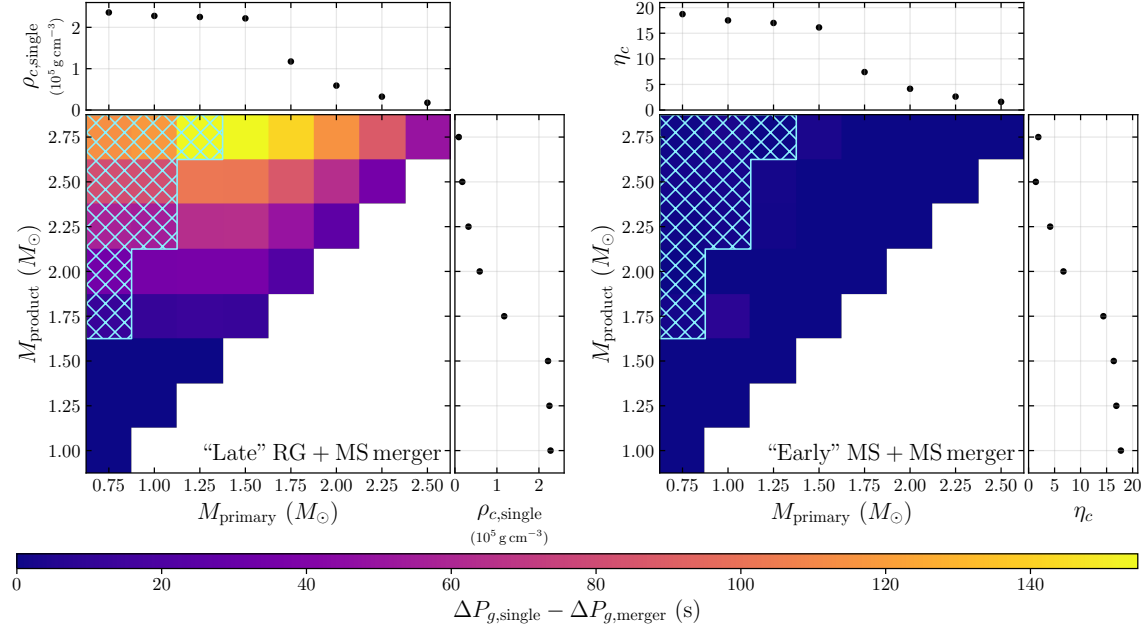


Figure 2.5: The difference between the period spacings of a single star and an RG+MS merger product of the same total mass, for a merger which occurs when the primary is on the lower RGB (*left*) or on the MS (*right*). In each panel, the period spacing difference is evaluated at a luminosity of $L = 60 L_{\odot}$. The side panels show the central density $\rho_{c,\text{single}}$ and central degeneracy parameter η_c for single stars at $L = 60 L_{\odot}$. Mergers resulting in stars with $M \gtrsim 2 M_{\odot}$ are distinguishable from their non-merged counterparts via ΔP_g , but only when the primary has already left the MS by the time the merger occurs. The hatching covers unphysical mergers where $M_{\text{product}} > 2M_{\text{primary}}$.

$\gtrsim 2 M_{\odot}$, corresponding approximately to the mass below which a star would be expected to develop a degenerate core.

In RGs with high core degeneracy, core properties such as the temperature, density, and Brunt–Väisälä frequency are primarily functions of the core mass, and they are largely independent of the properties of the surrounding envelope. This is the origin of the famous luminosity–core mass relation for RGs (Kippenhahn, 1981). Hence, ΔP_g can be seen as a tracer for the core mass. Late-stage MS stars will develop helium cores which grow as hydrogen-shell burning progresses, developing into proper RGs when the core mass reaches the star’s Schönberg–Chandrasekhar limit (Schönberg and Chandrasekhar, 1942). For a star with $M \lesssim 2 M_{\odot}$, the core becomes degenerate before this limit is reached, and the star enters the RGB with a degenerate core (Cox and Giuli, 1968). In this case, a merger which occurs after a degenerate core has already been formed will leave ΔP_g nearly unchanged—such mergers will simply add mass to the envelope, and the small increased pressure will leave the core unaffected. The merger product will be distinguishable from a single star in the

case that the latter would otherwise be expected to form a more massive non-degenerate core, which would have a larger ΔP_g .

We note, however, that ΔP_g is insensitive to a merger in the case that a single star with the same mass as the product would have developed a degenerate core anyway—this can be seen in our models for $M_{\text{product}} \lesssim 2 M_{\odot}$ in Figure 2.5. This is also demonstrated in the right panel of Figure 2.4, which shows a propagation diagram for the result of a $1.0 + 0.5$ RG+MS merger. Since both 1.0 and $1.5 M_{\odot}$ single stars would be expected to develop degenerate cores through normal stellar evolution, their gravity mode structures are very similar when they evolve to the same point on the RGB, and ΔP_g cannot be used to distinguish them (or a merger bringing a $1.0 M_{\odot}$ RG to a $1.5 M_{\odot}$ RG).

2.3.4 Mergers on the red clump are difficult to distinguish

We have so far focused on first ascent giants, which manifest observationally as a roughly horizontal track at low ΔP_g tracing the star’s evolution through $\Delta\nu$. However, many, more evolved RGs have already exhausted their hydrogen supplies available for off-center burning and have entered the helium core burning phase, with most such stars having accumulated on the red clump. Red clump stars are also very apparent on a spacing diagram as a large cloud of points at low $\Delta\nu$ and high ΔP_g , which makes them straightforwardly distinguishable from RGB stars (Figure 2.6). It is natural to wonder whether measurements of ΔP_g can be used to distinguish red clump merger remnants from single stars, similar to the process described above for RGB stars.

In practice, identifying merger remnants on the clump will be difficult due to the very similar values of ΔP_g between low-mass and high-mass clump stars. The evolution of ΔP_g over time is similar for the single $1.5 M_{\odot}$ and merger $1.5 + 1.0 M_{\odot}$ models. However, because the merger model has a larger total mass relative to the single star model, it has a systematically larger $\Delta\nu \simeq \sqrt{G\rho}$. This manifests as a slight horizontal offset between the two models’ evolutionary tracks on a spacing diagram. While this effect also applies to first ascent RGs, it is less obvious since the trajectory of such RGs through a spacing diagram is shallower, i.e., $\Delta\nu$ evolves much more quickly for first ascent giants than clump stars, relative to ΔP_g . This small offset between the single $1.5 M_{\odot}$ and merger $1.5 + 1.0 M_{\odot}$ evolutionary tracks is comparable to both models’ offsets from the track of a single $2.5 M_{\odot}$ star. In general, the three models all coincide with each other at some point in their evolution, making them difficult to distinguish using asteroseismology. Therefore, although constraining the merger history using ΔP_g may be possible in some cases, we anticipate that it will be difficult for most clump stars.

2.4 Merger candidates

2.4.1 Promising candidates from ΔP_g

The evolutionary stage of RGs can be tracked on an asteroseismic period vs. frequency spacing diagram like that shown in Figure 2.6, where merger remnants will appear as outliers relative to the paths taken by single stars. When ascending the RGB, RGs first evolve from larger ΔP_g and $\Delta\nu$ to smaller ΔP_g and $\Delta\nu$, later accumulating at high ΔP_g and low $\Delta\nu$ once they reach the red clump. Stars of different mass take different paths through the diagram, and merger remnants take different paths from single stars of the same mass. Hence, combined with an asteroseismic mass estimate (which can be deduced via ν_{\max} , $\Delta\nu$, and T_{eff}), mergers that occur after the primary has left the MS can readily be apparent from ΔP_g . For stars with $M \gtrsim 2 M_{\odot}$, merger remnants will manifest as stars with a significantly lower ΔP_g than expected from their mass. In other words, merger remnants will lie near tracks corresponding to lower mass single stars.

Figure 2.6 also shows the measured ΔP_g versus $\Delta\nu$ for a sample of 6111 RGs in the *Kepler* field from the catalog of Vrard, Mosser, et al., 2016. Of these RGs, we coarsely classify these stars as first ascent giants (1995; $\Delta P_g < 125$ s) and red clump stars (4116; $\Delta P_g \geq 125$ s). We identify 24 stars in this sample on the first ascent RGB with $M \geq 2 M_{\odot}$ which, despite their ostensibly larger masses, appear to lie on the sequence of a less massive ($\approx 1.5 M_{\odot}$) star through this space. Of these, 9 are flagged as having aliases, although Deheuvels, Ballot, Gehan, et al. (2022) find that the extracted period spacings of “high-mass” ($M \gtrsim 1.6 M_{\odot}$) RGs within this sample are usually unaffected by these. Note that one of these stars (KIC 8517859) has been classified as a δ Scuti star in some catalogs Barceló Forteza et al. (e.g., 2018) which, if correct, would exclude it as a merger remnant candidate. The possibility that it is a δ Scuti–RGB binary system (similar to, e.g., the system reported by Murphy, Li, et al., 2021) is also intriguing.

However, Yu et al. (2018), who later revisited these asteroseismic mass measurements, found that 17 of these candidates have masses $< 2 M_{\odot}$ after applying a correction assuming that these stars are first ascent giants (with one candidate absent in their catalog). Nonetheless, 6 of these stars (KIC 12254159, KIC 2972876, KIC 7778197, KIC 8708536, KIC 9907511, and KIC 11465942) have $M > 2 M_{\odot}$ in both catalogs, and should be considered the strongest merger remnant candidates in the sample. These merger candidates are listed in Table 2.1. For some of these candidates, it is possible that their true masses lie a few σ below their reported values, in which case they are consistent with single stars with $M \simeq 1.8 M_{\odot}$ without any need to invoke a merger scenario. Another possible source of false positives is that the extracted period spacings underestimate the true value—such errors may be exacerbated

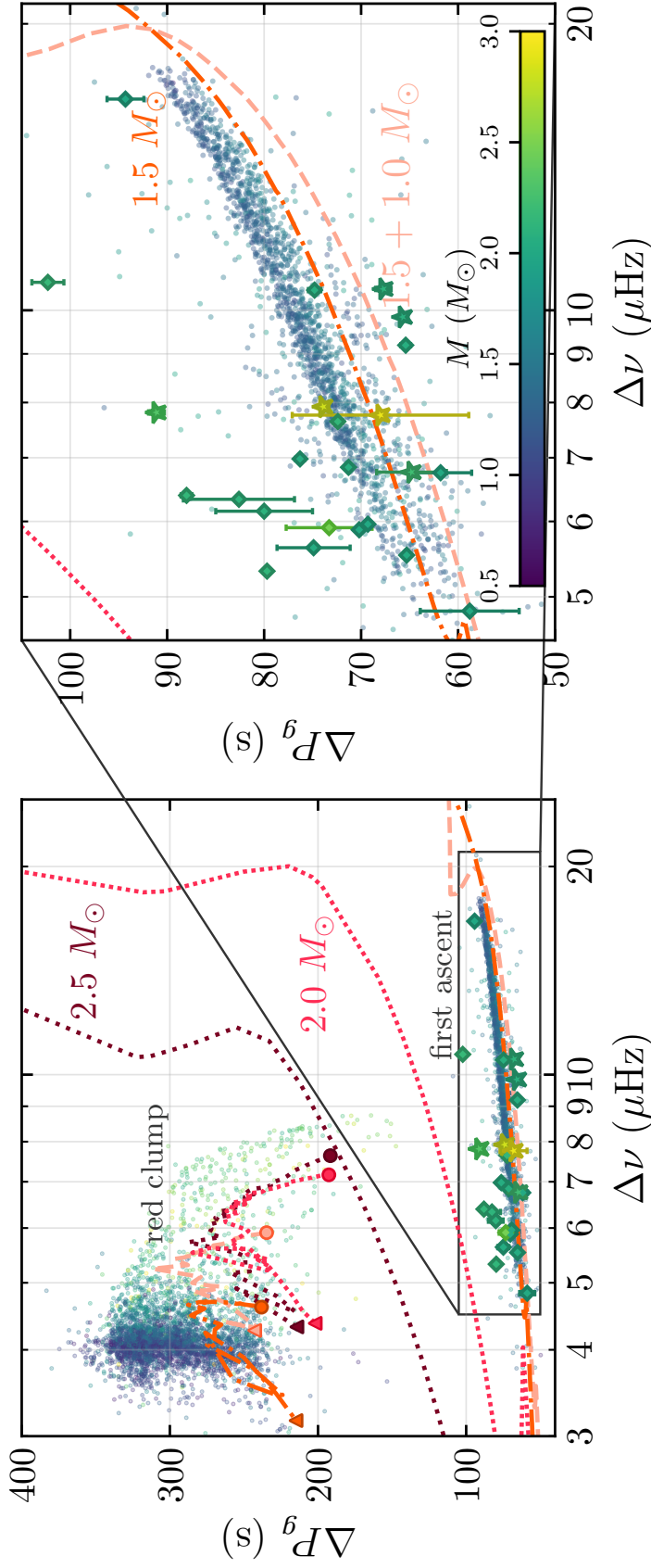


Figure 2.6: An asteroseismic frequency spacing diagram showing measurements of the g-mode period spacing ΔP_g as a function of the acoustic mode large frequency spacing $\Delta\nu$ from *Kepler* data (Vrard, Mosser, et al., 2016). Points are color coded by their measured asteroseismic mass, as shown by the color bar, overlaid on this plot are evolutionary tracks along the RGB for single stars of mass $1.5 M_\odot$ (dash-dotted orange line), $2.0 M_\odot$ (pink dense-dotted), and $2.5 M_\odot$ (maroon dotted), as well as a $1.5 + 1.0 M_\odot$ (salmon dashed) merger product. The cloud of points in the upper left are clump stars, with model tracks covering a central helium fraction of 90% (circle) to 1% (triangle). The right panel zooms in on the RGB track, where stars evolve from right to left. Merger remnant candidates are emphasized, with star symbols indicating first ascent masses $M \geq 2.0 M_\odot$ as reported by both Vrard, Mosser, et al. (2016) and Yu et al. (2018), and diamonds indicating those which have been reported to have $M \geq 2.0 M_\odot$ by Vrard, Mosser, et al. (2016) only. These stars are inconsistent with single star models but lie near our merger tracks and are good candidates to be merger products.

by suppressed dipole modes in some RGs (Mosser, Elsworth, et al., 2012; García, Pérez Hernández, et al., 2014; Fuller, Cantiello, et al., 2015; Stello, Cantiello, Fuller, Garcia, et al., 2016; Mosser, Belkacem, et al., 2017).

Note that our $1.5 M_{\odot}$ single star model track appears to run at slightly lower ΔP_g than the observed sample. Lower mass models come closer to the data points due to their smaller frequency spacings, as expected since a mass of $\approx 1.2 M_{\odot}$ is most common amongst *Kepler* RGs. It may also be possible that the models predict slightly too small ΔP_g (or conversely, slightly too large $\Delta\nu$) or that this difference is related to a correction applied in the Vrard, Mosser, et al. (2016) sample in the conversion between the uncorrected period spacing (which depends complexly on coupling to acoustic modes) and the asymptotic value.

Because RG evolution is primarily governed by core physics, we expect that the product of a $1.5 + 1.0 M_{\odot}$ merger after the TAMS to ascend the RGB at a rate similar to a single $1.5 M_{\odot}$ star, i.e., much more slowly than a single $2.5 M_{\odot}$ star. In our models, a $1.5 + 1.0 M_{\odot}$ merger remnant spends 37.8 Myr in the range $4 \mu\text{Hz} \leq \Delta\nu \leq 10 \mu\text{Hz}$ versus the much shorter 2.8 Myr for a single $2.5 M_{\odot}$ star. Hence, even though the single star evolutionary route is more common, merger products will be over-represented relative to single stars of the same mass within this range of frequency spacing.

Just before this paper was finalized, Deheuvels, Ballot, Gehan, et al. (2022) performed a similar study investigating the asteroseismic signatures of mass transfer. They also found that RGs which lie below the main RGB sequence in $\Delta\nu$ – ΔP_g space can be explained by stars that have accreted mass after developing a degenerate core. They propose that stars that lie below the main RGB sequence (especially those with $M \gtrsim 1.8 M_{\odot}$) have likely accreted mass, which increases their $\Delta\nu$ without modifying ΔP_g substantially. Indeed, our models predict the same behavior, which is why the merger model in Figure 2.6 lies to the right of the single star model. Using this asteroseismic signature, they identify ~ 30 RGs which may have experienced mass transfer in the past. Several of their mass transfer candidates do not appear in our list of candidates because they either have $M < 2 M_{\odot}$ or do not appear in the catalog of Vrard, Mosser, et al. (2016) but have separately measured period spacings. In turn, our candidate list contains stars which do not lie below the RGB period spacing sequence and therefore are not selected by their method.

2.4.2 Recognizing merger remnants in the absence of ΔP_g

While ΔP_g is a robust way to identify certain merger remnants on the basis of an apparently under-massive core, it may be possible to identify merger remnants without ΔP_g . Specifically, by using measurements of $\Delta\nu$, v_{max} , and T_{eff} , one can in principle constrain the stellar

Name	$M (M_{\odot})$	$\Delta\nu (\mu\text{Hz})$				$\Delta P_g (\text{s})$
		Vrard, Mosser, et al. (2016)	Yu et al. (2018)	Vrard, Mosser, et al. (2016)	Yu et al. (2018)	
KIC 2583386*	2.16 ± 0.17	1.92 ± 0.12	6.39	6.339 ± 0.032	88.0 ± 0.56	
KIC 2972876*	2.33 ± 0.25	2.15 ± 0.12	7.81	7.822 ± 0.020	91.1 ± 0.81	
KIC 5341131‡*	2.04 ± 0.10	1.82 ± 0.12	5.63	5.607 ± 0.018	74.9 ± 3.77	
KIC 5385518*	2.15 ± 0.15	1.89 ± 0.11	5.32	5.292 ± 0.014	79.7 ± 0.37	
KIC 5820672‡	2.08 ± 0.10	1.92 ± 0.14	10.50	10.431 ± 0.023	74.8 ± 0.64	
KIC 5857618*	2.13 ± 0.14	1.86 ± 0.10	6.33	6.334 ± 0.017	82.6 ± 5.73	
KIC 6118479	2.01 ± 0.14	1.60 ± 0.09	5.96	5.938 ± 0.019	69.3 ± 0.3	
KIC 6200178	2.06 ± 0.16	1.75 ± 0.09	6.98	6.953 ± 0.016	76.3 ± 0.46	
KIC 6437547	2.17 ± 0.02	1.90 ± 0.10	10.70	10.669 ± 0.023	102.3 ± 1.65	
KIC 7121674	2.02 ± 0.08	1.83 ± 0.10	5.88	5.844 ± 0.017	70.2 ± 0.31	
KIC 7457184	2.48 ± 0.17	1.96 ± 0.12	5.91	5.913 ± 0.017	73.3 ± 4.43	
KIC 7499531‡*	2.11 ± 0.13	1.99 ± 0.10	6.15	6.115 ± 0.014	80.0 ± 4.99	
KIC 7778197‡*	2.09 ± 0.12	2.21 ± 0.14	9.84	9.840 ± 0.018	65.7 ± 0.55	
KIC 8055108*	2.07 ± 0.13	1.84 ± 0.09	9.19	9.189 ± 0.014	65.4 ± 0.50	
KIC 8277879‡	2.16 ± 0.09	1.63 ± 0.09	7.64	7.901 ± 0.019	72.4 ± 0.48	
KIC 8364786	2.04 ± 0.07	1.79 ± 0.10	5.53	5.510 ± 0.013	65.3 ± 0.25	
KIC 8517859‡‡	2.00 ± 0.16	—	16.67	—	94.3 ± 1.9	
KIC 8558329‡	2.02 ± 0.18	1.65 ± 0.10	4.83	4.821 ± 0.013	58.8 ± 5.1	
KIC 8708536*	2.82 ± 0.15	2.71 ± 0.17	7.92	7.921 ± 0.031	73.9 ± 0.57	
KIC 9329200	2.07 ± 0.14	1.54 ± 0.09	6.84	6.823 ± 0.016	71.3 ± 0.38	
KIC 9784586*	2.01 ± 0.11	1.73 ± 0.09	6.75	6.728 ± 0.012	61.8 ± 3.20	
KIC 9907511‡*	2.12 ± 0.19	2.28 ± 0.15	10.53	10.488 ± 0.02	67.7 ± 0.80	
KIC 11465942*	2.92 ± 0.14	2.62 ± 0.21	7.76	7.762 ± 0.026	68.0 ± 9.1	
KIC 12254159*	2.23 ± 0.11	2.12 ± 0.13	6.76	6.732 ± 0.012	64.8 ± 3.6	

Table 2.1: Candidate merger products from Figure 2.6, identified as stars with period spacings consistent with low-mass RGB stars but with asteroseismic masses $\geq 2.0 M_{\odot}$ (Section 2.4.1). Asteroseismic properties are taken from the catalog of Vrard, Mosser, et al. (2016) and Yu et al. (2018)—for the latter, we have reported the corrected mass where the star has been assumed to be a first ascent RG.

* Stars where Yu et al. (2018) also find $M \geq 2.00 M_{\odot}$. These stars should be taken as the strongest merger remnant candidates.

† KIC 8517859 does not appear in the catalog of Yu et al. (2018). In addition, it has been classified as a δ Scuti variable in some catalogs, which would exclude it as a viable merger remnant candidate if true.

‡ Stars which are not present in the Gaulme, Jackiewicz, Spada, et al. (2020) catalog, which examined stars for surface activity.

* Stars whose observations are flagged as having aliases in the catalog of Vrard, Mosser, et al. (2016).

mass M , radius R , and luminosity L . The latter quantities can also be determined using *Gaia* parallax measurements, given a reliable T_{eff} . A merger remnant would then manifest as a giant which is less luminous and/or cooler than possible for a single star of mass M which is just beginning its ascent up the RGB.

For example, one could distinguish a $1.5 + 1.0 M_{\odot}$ merger remnant from a single $2.5 M_{\odot}$ star based on their location on the Hertzsprung-Russell diagram (HRD) in Figure 2.2. This is likely only possible if the remnant giant is young enough to be located at the base of the RGB such that its luminosity is smaller than that of a single $2.5 M_{\odot}$ model at the bottom of the RGB. In other words, at a given T_{eff} and mass M , merger remnants would be expected to have smaller luminosity (i.e., smaller R and larger $\Delta\nu$ and ν_{max}) than expected to be possible from the model track of a single star. As an example, four of our merger candidates from above lie below the $2.5 M_{\odot}$ track in Figure 2.2 and could potentially be identified using this method, if they were to have asteroseismic masses greater than $2.5 M_{\odot}$.

This method of identification is limited because it can only identify remnants young enough that they lie near the base of the RGB, and with masses where the minimum RGB luminosity is somewhat sensitive to mass. Additionally, the stellar track on a HRD is model-dependent and can vary with metallicity, further complicating this method (Basu et al., 2012). Nonetheless, this method does not require measurements of ΔP_g , so it may be applicable to a much larger number of stars for which only $\Delta\nu$ and ν_{max} can be measured, as expected for the bulk of red giants observed by *TESS*. We encourage follow-up work to investigate this technique in more detail.

2.5 Discussion

2.5.1 Merger dynamics

The RG+MS mergers described in this work may naturally be formed by binary coalescences when the primary in a close binary expands along the RGB and initiates unstable mass transfer (for a review, see Ivanova, Justham, Chen, et al., 2013). For conservative mass transfer, a mass ratio $q < 2/3$ (where q is the ratio of the donor to accretor mass) is required for stable mass transfer from a $n = 3/2$ polytrope. Hence mass transfer in standard coeval binaries (where an RG primary accretes onto a less massive secondary such that $q > 1$) is typically expected to be unstable, though we note a radiative core does enhance mass transfer stability (Soberman et al., 1997). In these unstable cases, stars are expected to eventually merge in a bright transient (“luminous red nova”; e.g., Ivanova, Justham, Nandez, et al., 2013). Moreover, on the lower RGB where the envelope binding energy is still large, mergers will occur more frequently relative to successful envelope ejections.

Hydrodynamical simulations (MacLeod et al., 2018) have shown that stellar coalescences are expected to produce a bipolar outflow structure which has been observed in follow-up radio observations of a number of luminous red novae (Kamiński, Steffen, et al., 2018). With observations taken using the Atacama Large Millimeter Array, Kamiński, Steffen, et al. (2018) estimate the ejecta mass of three red novae (V4332 Sgr, V1309 Sco, and V838 Mon) as varying dramatically between events, but characteristically on the level of a few percent of the total mass of the system. This is comparable to the prediction of Metzger and Pejcha, 2017 that the ejecta mass $M_{\text{ej}} \sim 0.1M$ is a relatively small fraction of the total mass of the system, such that the merger results in a single star with nearly the same total mass. The detection of similar outflow material around stars identified as merger products using asteroseismology could validate this method. In may cases, however, the merger ejecta may have already been expelled from the system. The lifetime of protoplanetary disks has been estimated to be on the order of 1 Myr (Mamajek, 2009; Cieza, 2015; Li and Xiao, 2016), whereas ΔP_g should be able to discern a merger remnant for approximately ≈ 40 Myr throughout its ascent up the lower RGB. Hence, circumstellar disks have most likely already been expelled from most asteroseismically detectable merger remnants.

Interestingly, V1309 Sco (Tylenda, Hajduk, et al., 2011) is thought to have arisen from a merger involving a primary of mass $M_1 \sim 1.5 M_{\odot}$ and radius $R_1 \sim 3.5 R_{\odot}$ (Metzger and Pejcha, 2017). The primary was thus on the sub-giant branch at the time of merger, at a time favorable for asteroseismic identification of the merger product. For a secondary of mass $M_2 \gtrsim 0.25 M_{\odot}$, the merger product would lie in the mass range favorable for asteroseismic identification, so V1309 Sco may be a perfect example of the type of stellar merger whose remnant can later be identified through asteroseismic techniques. Along similar lines, the *SPIRITS* survey recently identified a class of “eSPecially Red Intermediate-luminosity Transient Events” (“SPRITEs”; Kasliwal et al., 2017), characterized by luminosities between those of novae and supernovae, relatively red colors, and lack of any optical counterparts. (Metzger and Pejcha, 2017) suggest that these dustier SPRITE events may in fact be giant star mergers, in contrast to luminous red novae, which are more likely to be MS mergers.

2.5.2 Additional merger signals

To corroborate the merger candidates asteroseismically identified above, additional evidence for a previous merger event would be useful. Merger remnants are expected to initially be rapidly rotating, though they may spin down rapidly on a time scale of less than 1 Myr (Casey, Ho, Ness, Hogg, Rix, Angelou, Hekker, Tout, Lattanzio, Karakas, et al., 2019b). Some remnants may be expected to exhibit large magnetic fields generated during the merger (Schneider, Podsiadlowski, et al., 2016; Schneider, Ohlmann, Podsiadlowski, Röpke,

Balbus, Pakmor, and Springel, 2019) or sustained by a dynamo in the convective envelope due to the high post-merger rotation rate. The fields may be detected via spectropolarimetry (Aurière et al., 2015) or they may manifest in Ca II H&K emission (Medeiros and Mayor, 1999) or X-ray emission (Soker and Tylenda, 2007). A class of lithium-enriched giants has also emerged in the last few decades, some of which are also rapidly rotating (Charbonnel and Balachandran, 2000; Drake et al., 2002; Rebull et al., 2015; Martell et al., 2021a). Evidence has suggested tidal spin-up (Casey, Ho, Ness, Hogg, Rix, Angelou, Hekker, Tout, Lattanzio, Karakas, et al., 2019b), stellar mergers (Siess and Livio, 1999; Jura, 2003; Melis, 2020) and/or giant planet accretion (Denissenkov and Weiss, 2000; Sandquist et al., 2002; Reddy et al., 2002; Carlberg, Cunha, et al., 2012; Punzi et al., 2017; Soares-Furtado et al., 2021) as explanations for these lithium-enhanced, sometimes rapidly rotating stars. Asteroseismic merger candidates should be examined for these other signatures of a prior stellar merger. While there have been many surveys that have searched for lithium enhancement in RGs, many of them have been directed at a different field of view than the *Kepler* data set (Buder et al., 2018; Kumar, Reddy, Campbell, et al., 2020), not sufficiently photometrically deep (e.g., Kumar, Reddy, and Lambert, 2011), or restricted only to clump stars (e.g., Singh et al., 2021). The studies of Deepak and Lambert, 2021 and Yan et al., 2021 cross-referenced asteroseismic classifications with high lithium abundances via LAMOST data, but none of our merger candidates appear in their publicly available samples, suggesting they are likely not strongly lithium enhanced. While the catalog of Casey, Ho, Ness, Hogg, Rix, Angelou, Hekker, Tout, Lattanzio, Karakas, et al. (2019b) contains 23 lithium-rich giants which have also been asteroseismically observed by *Kepler*, only 2 of them have been identified to be on the RGB, and none of them coincide with any of our 24 merger remnant candidates. Additional spectroscopic study of our candidates may reveal more subtle, unusual compositional features which may be associated with a previous merger.

In addition, examining the light curves of *Kepler* RGs (and performing limited spectroscopic follow-up), Gaulme, Jackiewicz, Spada, et al. (2020) find a correspondence between surface activity, close binarity, and suppressed oscillations, consistent with previous work (García, Mathur, et al., 2010; Chaplin, Bedding, et al., 2011; Gaulme, Jackiewicz, Appourchaux, et al., 2014; Mathur et al., 2019). As discussed in Section 2.5.2, merger remnants may have elevated rotational rates and magnetic fields, suggesting that their oscillations may be preferentially suppressed. This may prevent a measurement of ΔP_g in some cases and may partially account for our relatively low fraction of remnant candidates (see Section 2.5.3). Of our 24 remnant candidates, 16 appear within the catalog of Gaulme, Jackiewicz, Spada, et al. (2020), who search for surface activity via rotational modulation in RG's light curves. However, they do not report surface activity in any of these candidates. In addition,

none of our candidates appear in the rotational catalog of Ceillier et al. (2017). While these non-detections do not provide additional support for the merger hypothesis, they may reflect an asteroseismic candidate selection bias due to the suppression of oscillations associated with stronger magnetic activity.

2.5.3 Rates of stellar mergers

For a circular orbit and mass ratio $q = 3/2$, Roche overflow will occur when $a = 2.4R_1$ (Eggleton, 1983). We calculate that a $1.5 M_\odot$ in a circular binary with a $1.0 M_\odot$ star will undergo Roche overflow on the lower RGB ($a \lesssim 30 R_\odot$) when the period $P \lesssim 12$ d, with weak dependence on the mass ratio. Such close binaries should account for $\approx 4\%$ of solar-type binaries (Raghavan et al., 2010). Price-Whelan et al. (2020) demonstrate a deficit of “close” binaries in red clump and asymptotic giant stars suggestive of stellar mergers on the RGB. Their observed decrease of close binaries approaching the red clump implies that $\approx 8\%$ of systems (singles and binaries) merge on the RGB, with $\approx 3\%$ of stars merging on the lower RGB where $\log g$ is higher than that of the clump but lower than that of the MS. Tracking transient events, Kochanek et al. (2014) additionally find that the rate of mergers in the Milky Way between an MS star and an evolved star is $\approx 0.045 \text{ yr}^{-1}$. Together with their star formation model ($3.5 M_\odot \text{ yr}^{-1}$ and the initial mass function of Kroupa and Weidner 2003) this merger rate implies that $\approx 7\%$ of red giants are merger remnants (although many of these mergers may occur higher up on the RGB). These observations consistently suggest that the fraction of lower RGB stars that are merger remnants (and which merged after the MS) is on the order of a few percent.

Within the Vrard, Mosser, et al. (2016) data set, we identify 24 candidate remnants (see Section 2.4.1), representing $\approx 1.2\%$ of the total number of RGB stars in their sample. A total of 6 ($\approx 0.3\%$) are found to be strong candidates using the asteroseismic mass measurements of both Vrard, Mosser, et al. (2016) and Yu et al. (2018). These fractions appear to fall somewhat short of our estimates above, but this is not unexpected. Our method is most sensitive to the subset of RG remnants with $M \gtrsim 2 M_\odot$ (corresponding to the identification criteria for candidate remnants), and also those which merge low enough on the RGB to produce a remnant which can still be probed effectively by asteroseismology. More detailed population synthesis would be needed to confirm whether our candidate fraction of $\sim 1\%$ is consistent with expectations of merger rates fulfilling the asteroseismic selection criteria.

2.5.4 Mergers in dense stellar environments

Dense stellar populations are clearly a natural setting for frequent stellar collisions as well as stellar-evolution mediated mergers in binaries hardened by scattering events. The high stellar densities associated with the core of globular clusters make them hotbeds for such mergers. Hills and Day (1976) estimate that as many as tens of percent of stars in some globular clusters may have suffered from at least one collision in their history, and Liu and Jiang (2021) find (assuming an initial binary fraction $f_b = 0.5$) that as many as 50% of RGs in a globular cluster may have undergone a binary interaction, with evolved blue straggler stars making up $\simeq 10\%$ of RGs. Unfortunately, owing to limited observing fields and stellar crowding, asteroseismic measurements of stars in star clusters is sparse—only four open clusters appear in the *Kepler* field, and only two of those have measured period spacings for non-clump giants (NGC 6791 and NGC 6819; Corsaro et al., 2012). Using these data, Brogaard et al. (2021) recently demonstrated the presence of overmassive giants in NGC 6791—these stars likely originate from mass transfer events or mergers which could potentially be encoded in the period spacing. In addition, while limited asteroseismology has been conducted on globular clusters (e.g., Stello and Gilliland, 2009; Miglio, Chaplin, et al., 2016), measurements of the period spacing for stars in these clusters still remain elusive.

Ultimately, future observational asteroseismology campaigns, especially those directed towards dense stellar regions (e.g., Miglio, Girardi, et al., 2021), appear lucrative for identifying a large sample of merger products as well as providing a direct measurement of the merger rate in these populations. Optimal observing targets for this type of merger remnant identification would have turn-off masses $\sim 1\text{--}2 M_\odot$, where stars with masses $\lesssim 2 M_\odot$ have entered the RGB but $M \gtrsim 2 M_\odot$ merger remnants can still form (although this threshold mass may decrease somewhat at lower metallicity). Such populations would place detectable merger remnants below the RG bump, where asteroseismology is most effective.

2.6 Conclusion

In this work, we investigated the asteroseismic signatures of stellar mergers, focusing on observable diagnostics in red giant merger remnants. Our main finding is that merger remnants can often be identified by the presence of an over-massive envelope relative to their cores, compared to what is expected for a single star. Merger remnants can be found amongst red giants, provided an asteroseismic measurement of the mass (via ν_{max} , $\Delta\nu$, and T_{eff}), in addition to a measurement of the mixed mode period spacing ΔP_g . Since the latter traces the core structure, it can be used to distinguish merger products from single stars under the following conditions:

- The merger occurs when the primary is on the RGB, so that it has already developed a dense core and the merger essentially only adds to the envelope of the star (Section 2.3.2).
- The additional mass contributed by the secondary brings the mass of the giant from $M \lesssim 2 M_{\odot}$ to $M \gtrsim 2 M_{\odot}$. This threshold corresponds roughly to the mass below which an RG would form a degenerate core, which would be distinguishable from the non-degenerate core of a more massive star formed via single star evolution (Section 2.3.3).

Mergers that occur when the primary is on the main sequence are difficult to identify because the merger remnant structure is nearly indistinguishable from a single star of the same mass. The same is true for a merger that does not bring the total mass above $\approx 2 M_{\odot}$.

In other words, ΔP_g can be used to identify a merger remnant in the situation where the primary in a RG+MS merger has already developed a dense and degenerate core that withstands the merger, which would not otherwise be produced by a single star with the mass of the merger product. At the same point on the HRD (or alternatively, at the same ν_{max} or $\Delta\nu$), a merger product is distinguished by a smaller period spacing relative to the expectations of a single star (Figure 2.6). Even without a ΔP_g measurement, mergers remnants can also potentially be identified as stars having a luminosity that is too low for their asteroseismically measured mass (see Section 2.4.2), and future work should examine this possibility in more detail.

Fortunately, the RG mass range where merger remnants can be identified is well-sampled in existing asteroseismic catalogs built primarily from *Kepler* data. Using the catalog of Vrard, Mosser, et al., 2016, we have identified 24 promising candidates in Section 2.4.1, and we encourage follow-up observations to search for additional hints of a prior merger such as rapid rotation, magnetic fields, unusual chemical abundances, or circumstellar gas and dust. These stars are a natural endpoint of close binary stellar evolution, and they are expected to be even more common in dense stellar environments. A further examination of the data and future observational surveys will provide illuminating constraints on the occurrence rates and outcomes of stellar mergers in the Milky Way.

2.A MESA simulation controls

The input `inlist_project` files for all of our MESA runs are very similar, with variations in specific parameters which control the initial mass of the star, as well as the mass accreted during the rapid merger period. Here, the parameters `x_ctrl(1)` and `x_ctrl(2)`

represent the mass accretion rate during the merger period (fixed at $\dot{M} = 10^{-5} M_{\odot} \text{ yr}^{-1}$) and the star age at which the merger occurs, respectively. We have also used the parameter `x_integer_ctrl(1)` to control profile write-out. This work is accompanied by a Zenodo repository containing inlists and selected output files associated with the simulations used in this work (Rui and Fuller, 2021b). We have included as a representative example the `inlist_project` file for the $1.5 + 1.0 M_{\odot}$ merger run, where the merger occurs when the radius of the primary reaches 125% of its value at TAMS:

```

&star_job
  pgstar_flag = .true.
/ ! end of star_job namelist

&controls
  !----- Write GYRE
  write_pulse_data_with_profile = .true.
  pulse_data_format = 'GYRE'

  x_integer_ctrl(1) = 10 ! Force write-out at log L close to integer values
  ↪ divided by this number

  !----- Manages accretion
  x_ctrl(1) = 1e-5 ! mass accretion rate
  x_ctrl(2) = 2614839409.7825627 ! time (yr) at which to start accretion (if
  ↪ 0, no accretion)

  mass_change = 0 ! initial accretion rate (modified dynamically)
  max_star_mass_for_gain = 2.50

  !----- MAIN
  initial_mass = 1.50
  initial_z = 0.02
  use_Type2_opacities = .true.
  Zbase = 2.d-2

  predictive_mix(1) = .true.
  predictive_superad_thresh(1) = 0.005
  predictive_avoid_reversal(1) = 'he4'
  predictive_zone_type(1) = 'any'
  predictive_zone_loc(1) = 'core'
  predictive_bdy_loc(1) = 'top'

  dX_div_X_limit_min_X = 3d-5
  dX_div_X_limit = 3d-1
  dX_nuc_drop_min_X_limit = 3d-5
  dX_nuc_drop_limit = 3d-2

  !----- WIND
  cool_wind_RGB_scheme = 'Reimers'
  cool_wind_AGB_scheme = 'Blocker'
  RGB_to_AGB_wind_switch = 1d-4

```

```
Reimers_scaling_factor = 0.2
Blocker_scaling_factor = 0.5

use_accreted_material_j = .true.
accreted_material_j = 0

!----- OVERSHOOTING
overshoot_scheme(1) = 'exponential'
overshoot_zone_type(1) = 'nonburn'
overshoot_zone_loc(1) = 'core'
overshoot_bdy_loc(1) = 'top'
overshoot_f(1) = 0.015
overshoot_f0(1) = 0.005

overshoot_scheme(2) = 'exponential'
overshoot_zone_type(2) = 'nonburn'
overshoot_zone_loc(2) = 'shell'
overshoot_bdy_loc(2) = 'any'
overshoot_f(2) = 0.015
overshoot_f0(2) = 0.005

overshoot_scheme(3) = 'exponential'
overshoot_zone_type(3) = 'burn_H'
overshoot_zone_loc(3) = 'core'
overshoot_bdy_loc(3) = 'top'
overshoot_f(3) = 0.015
overshoot_f0(3) = 0.005

overshoot_scheme(4) = 'exponential'
overshoot_zone_type(4) = 'burn_H'
overshoot_zone_loc(4) = 'shell'
overshoot_bdy_loc(4) = 'any'
overshoot_f(4) = 0.015
overshoot_f0(4) = 0.005

overshoot_scheme(5) = 'exponential'
overshoot_zone_type(5) = 'burn_He'
overshoot_zone_loc(5) = 'core'
overshoot_bdy_loc(5) = 'top'
overshoot_f(5) = 0.015
overshoot_f0(5) = 0.005

overshoot_scheme(6) = 'exponential'
overshoot_zone_type(6) = 'burn_He'
overshoot_zone_loc(6) = 'shell'
overshoot_bdy_loc(6) = 'any'
overshoot_f(6) = 0.015
overshoot_f0(6) = 0.005

set_min_D_mix = .true.
min_D_mix = 1d0
```

```

!----- MISC
photo_interval = 25
profile_interval = 50
max_num_profile_models = 3000
history_interval = 10
terminal_interval = 10
write_header_frequency = 10
max_number_backups = 500
max_number_retries = 3000
max_timestep = 3d15

!----- MISC
photo_interval = 25
profile_interval = 50
max_num_profile_models = 3000
history_interval = 10
terminal_interval = 10
write_header_frequency = 10
max_number_backups = 500
max_number_retries = 3000
max_timestep = 3d15

!----- MESH
mesh_delta_coeff = 1
varcontrol_target = 0.7d-3

/ ! end of controls namelist

&pgstar

```

The `run_star_extras.f` file accompanying this run takes the form of the default `standard_run_star_extras.inc` file, slightly modified to handle the merger and profile write-out. In particular, in the `extras_check_model` function, we add the following lines to initiate accretion at the proper time specified in the `inlist_project` file:

```

if (s% star_age >= s% x_ctrl(2) .and. s% x_ctrl(2) /= 0) then
    s% mass_change = s% x_ctrl(1)
end if

```

Additionally, in the function `extras_finish_step`, we add the following lines to force a write-out of the stellar profile at values of $\log L$ close to multiples of 0.1.

```

f = s% x_integer_ctrl(1)
s% xtra(1) = s% log_surface_luminosity

if ((floor(f * s% xtra_old(1)) - floor(f * s% xtra(1)) .ne. 0)) then
    s% need_to_update_history_now = .true.
    s% need_to_save_profiles_now = .true.
endif

```

In Section 2.3.2, we briefly discuss the usage of the `create_merger_model` feature to confirm the validity of modeling a MS+MS merger as a surface accretion event onto the primary. Specifically, we have included in `inlist_project` the option `write_model_with_profile = .true.` for the $M = 1.50 M_{\odot}$ and $M = 1.00 M_{\odot}$ models, and have passed the saved model files at the desired time of accretion to `saved_model_for_merger_1` and `saved_model_for_merger_2`.

In Section 2.3.4, we examine the period spacing for stars undergoing helium core burning on the red clump. As the helium flash is a very difficult stage of evolution to model numerically, we include the following two lines in the `&controls` section of `inlist_project` in order to prevent the timestep from becoming prohibitively small:

```
use_dedt_form_of_energy_eqn = .true.
convergence_ignore_eql_residuals = .true.
```

Chapter 3

FINDING THE UNUSUAL RED GIANT REMNANTS OF CATACLYSMIC VARIABLE MERGERS

Rui, N. Z. and J. Fuller (2024). “Finding the unusual red giant remnants of cataclysmic variable mergers.” In: *Open Journal of Astrophysics*. DOI: [10.33232/OJAS.123878](https://doi.org/10.33232/OJAS.123878). arXiv: [2404.14474](https://arxiv.org/abs/2404.14474).

Mergers between helium white dwarfs and main-sequence stars are likely common, producing red giant-like remnants making up roughly a few percent of all low-mass ($\lesssim 2M_{\odot}$) red giants. Through detailed modeling, we show that these merger remnants possess distinctive photometric, asteroseismic, and surface abundance signatures through which they may be identified. During hydrogen shell burning, merger remnants reach higher luminosities and possess pulsations which depart from the usual degenerate sequence on the asteroseismic $\Delta\nu$ – $\Delta\Pi$ diagram for red giant branch stars. For sufficiently massive helium white dwarfs, merger remnants undergo especially violent helium flashes which can dredge up a large amount of core material (up to $\sim 0.1M_{\odot}$) into the envelope. Such post-dredge-up remnants are more luminous than normal red clump stars, are surface carbon-, helium-, and possibly lithium-rich, and possess a wider range of asteroseismic g-mode period spacings and mixed-mode couplings. Recent asteroseismically determined low-mass ($\lesssim 0.8M_{\odot}$) red clump stars may be core helium-burning remnants of mergers involving lower-mass helium white dwarfs.

We thank Kareem El-Badry, Joel Ong, Marc Hon, and Yaguang Li for their insightful comments and thorough reading of the manuscript, as well as Lars Bildsten for useful discussions. We also acknowledge Masao Takata, Andrew Casey, Tim Bedding, and Ken Shen for their helpful remarks, as well as the anonymous referee whose report increased the clarity of the final manuscript. N.Z.R. acknowledges support from the National Science Foundation Graduate Research Fellowship under Grant No. DGE-1745301. All stellar evolution calculations were performed on the Wheeler cluster at Caltech, which was supported by the Sherman Fairchild Foundation and by Caltech.

3.1 Introduction

Growing evidence suggests that mergers between main-sequence (MS) stars and low-mass white dwarfs should be fairly common (Schreiber, Zorotovic, et al., 2015). The likely outcome of such a merger is to accrete the MS star onto the white dwarf, igniting hydrogen shell burning and creating an unusual red giant (RG) star. These RG remnants of those mergers should exist within the stellar population, and may be identifiable through a combination of their photometry, pulsations, and surface abundances.

Cataclysmic variables, or CVs, are stably mass-transferring systems with white dwarf (WD) accretors and MS donors. Typically, the progenitor binaries of CVs are post-common-envelope systems (Paczynski, 1976; Belczynski et al., 2005; Toonen and Nelemans, 2013; Camacho et al., 2014; Ablimit et al., 2016; Zorotovic and Schreiber, 2022) which have been tightened by magnetic braking and gravitational waves until the onset of Roche lobe overflow (Knigge, 2011).

For a while, the research field has been dogged by a *WD mass problem* (e.g., Zorotovic and Schreiber, 2020):

1. the typical accretor mass in CVs is $\simeq 0.8M_{\odot}$, greater than the typical observed mass of carbon–oxygen white dwarfs (CO WDs) $\simeq 0.6M_{\odot}$, and
2. only a small handful of helium(-core) white dwarf (hereafter He WD) accretors have ever been discovered in accreting systems, even though they should be frequent, observable outcomes of conventional binary stellar evolution (Zorotovic, Schreiber, and Gänsicke, 2011; Zorotovic and Schreiber, 2020; Pala et al., 2022).

Where are all of the low-mass CV accretors?

In the past decade, it was realized that the WD mass problem can naturally be solved by an extra, accretor mass-dependent angular momentum loss mechanism (Schreiber, Zorotovic, et al., 2015). This so-called *consequential angular momentum loss* would preferentially destabilize the mass transfer of CV-like systems with lower-mass white dwarfs, causing them to quickly merge before they can be observed (Belloni et al., 2018). Physically, this mechanism may be a frictional effect associated with nova events (Shen, 2015; Shen and Quataert, 2022), which are expected to be much longer-duration for lower-mass white dwarfs (Shara, Prialnik, et al., 1993) and may cause mergers to occur on the timescale of hours (Shen, 2015), although the subsequent analysis is agnostic to the details.

If CVs with low accretor masses are missing because they merge, it is obvious to ask whether their remnants can be observed and identified. In the case where the progenitor system is

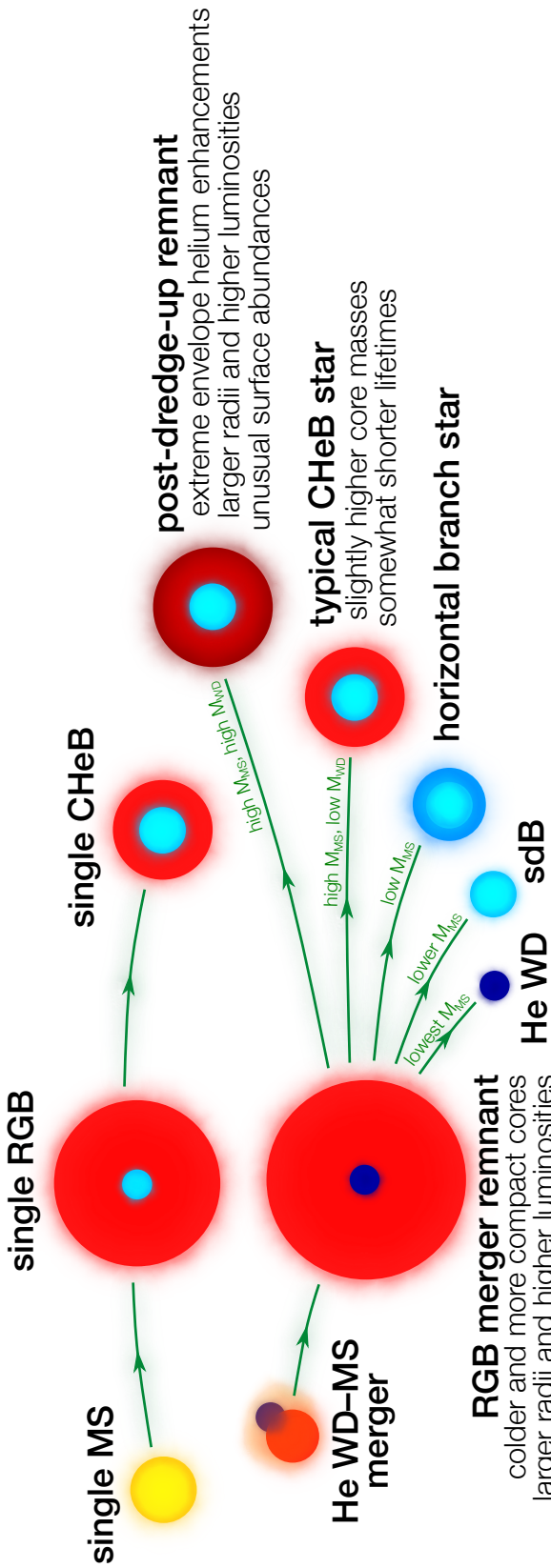


Figure 3.1: A summary diagram of the behavior of the He WD-MS merger remnants investigated in this work. On the RGB, merger remnants have cold and slightly more compact cores, which inflates their radii and changes the radiative structures of their cores to which asteroseismology is sensitive (Section 3.3). Merger remnants which are sufficiently massive enough to reach the tRGB ignite helium in abnormally energetic helium flashes. For massive enough progenitor He WDs, these events can dredge up significant amounts of helium into merger remnants' envelopes (Section 3.4), changing their surface abundances, and greatly modifying both their structure and evolution. In our models, such core dredge-up events occur when $M_{WD} \geq 0.27 M_{\odot}$, although the exact threshold depends on other factors such as the cooling age of the He WD (see Appendix 3.A). Less massive remnants become horizontal branch stars (Section 3.4.5), hot subdwarfs, or He WDs (not explored in this work).

a close He WD–MS binary (the scenario of focus in this study), the remnant is expected to evolve along highly modified versions of the red giant branch (RGB) and possibly core helium burning (CHeB, or the red clump) phases of isolated, low-mass ($M \lesssim 2M_{\odot}$) stars.

More recently, in only the last few years, the community has realized that stellar interactions may produce RGs with conspicuous and lasting asteroseismic signatures. Rui and Fuller (2021a) and Deheuvels, Ballot, Gehan, et al. (2022) show that many first-ascent RGs which gain hydrogen mass from companions (either through merger or stable mass transfer) possess unusually low gravity-mode period spacings. Li, Bedding, Murphy, et al. (2022) and Matteuzzi et al. (2023) similarly identify anomalously undermassive CHeB stars through asteroseismology. Because asteroseismology probes *internal* structures, it constrains separate information from traditional techniques which probe the surface properties of the star. It may thus play a critical role in identifying the remnants of cataclysmic variable mergers.

In this work, we investigate observable signatures of He WD–MS merger remnants. The physical picture we advance is shown schematically in Figure 3.1. We construct and evolve merger remnant models (described in Section 3.2), and demonstrate a significant number of telltale signs (photometric, asteroseismic, and surface compositional) which are complex downstream consequences of a highly cold and degenerate core during hydrogen shell burning. Sections 3.3 and 3.4 discuss merger remnants during hydrogen shell burning (RGB) and helium core burning (CHeB), respectively. In Section 2.4.1, we identify some merger remnant candidates in existing observations. Section 3.6 discusses other possible signatures, and contextualizes this work in the broader nascent field of binary interaction asteroseismology. Section 3.7 summarizes our key findings.

3.2 Stellar models

By the time of merger, the He WD component of a close He WD–MS binary has undergone an extended phase of radiative cooling lasting potentially up to gigayears. When the binary subsequently merges, the MS component (now the remnant’s envelope) quickly ignites hydrogen in a burning shell around the He WD (now the remnant’s core) and sets up thermal equilibrium on a short envelope thermal timescale:

$$\begin{aligned} \tau_{\text{th,env}} &= \frac{GM^2}{RL} \\ &\approx 0.1 \text{ Myr} \times \left(\frac{M}{M_{\odot}}\right)^2 \left(\frac{R}{10R_{\odot}}\right)^{-1} \left(\frac{L}{30L_{\odot}}\right)^{-1}. \end{aligned} \quad (3.1)$$

In contrast, the degenerate core only thermalizes (via electron-mediated conduction) with the hydrogen burning shell on a much longer timescale $\sim 10\text{--}100$ Myr comparable to the

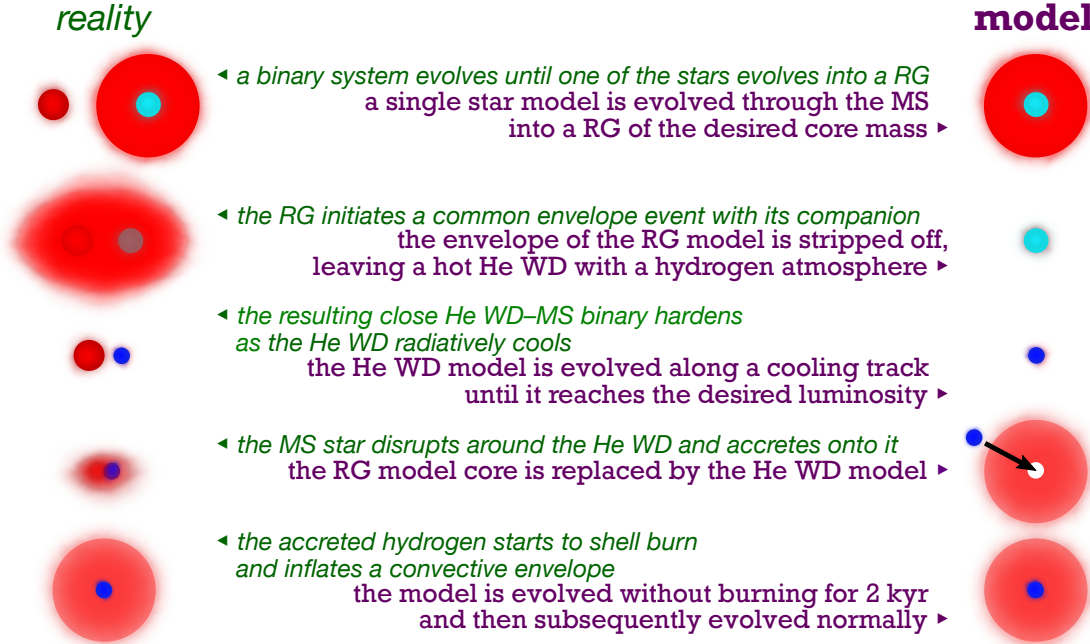


Figure 3.2: A summary of the evolution of one possible progenitor system of a He WD–MS merger remnant (left), juxtaposed against our procedure for constructing the stellar model of a merger remnant in MESA (right).

duration of the RGB phase (see Appendix 3.B). Therefore, as previously noticed by Zhang, Hall, et al. (2017), the low-entropy core can persist for long enough to influence the long-term evolution of the remnant.

Using Modules for Experiments in Stellar Astrophysics (MESA, version r10398; Paxton, Bildsten, et al., 2010; Paxton, Cantiello, et al., 2013; Paxton, Marchant, et al., 2015; Paxton, Schwab, et al., 2018), we create and evolve evolutionary models of merger remnants, consisting of cold helium cores surrounded by hydrogen envelopes¹.

We do this in the following stages (summarized in Figure 3.2):

1. An isolated star with $M = 1.2M_{\odot}$ is evolved through the MS and part of the RGB until it attains the desired initial core mass of the remnant, M_{WD} . This initial mass is chosen to be close to typical RG masses from *Kepler* (e.g., Yu et al., 2018). Because single RGs with $M \lesssim 2M_{\odot}$ all obey the same core mass–luminosity relation, the subsequent analysis is insensitive to this choice.

¹Inlists and other files required to reproduce our results can be found at the following Zenodo link: <https://zenodo.org/records/10828187>

2. The hydrogen envelope is removed by applying a high mass-loss rate (using `relax_initial_mass` with $|\dot{M}| = 10^{-3}M_{\odot} \text{ yr}^{-1}$). To simulate a realistic white dwarf atmosphere, we retain an additional $M_{\text{atm}} = 10^{-4}M_{\odot}$ of material from the base of the envelope, on top of the core mass M_{WD} .
3. The resulting object (which quickly relaxes into a He WD) is evolved through a cooling track to $\log(L_{\text{WD}}/L_{\odot}) = -4.0$.
4. To stellar-engineer the merger remnant, we start with a scaffold RG model with core mass M_{WD} . To build the scaffold model, we start with the original RG model from above, and remove envelope mass from the scaffold model via relaxation with $|\dot{M}| = 10^{-3}M_{\odot} \text{ yr}^{-1}$ with nuclear burning disabled, until the RG attains the desired final envelope mass M_{MS} (physically equal to the mass of the MS star participating in the merger, assuming no mass lost).

Next, we replace shells with mass coordinates $m \leq M_{\text{WD}}$ with the He WD model, excluding the He WD's atmosphere (shells where $X \geq 10^{-4}$). Because the modified RG model's core is now more compact, we recalculate the radial coordinate grid to be consistent with $dm = 4\pi r^2 \rho dr$. This produces a merger remnant with total mass $M_{\text{tot}} = M_{\text{MS}} + M_{\text{WD}}$.

For most merger remnant models in this work, we somewhat arbitrarily fix M_{MS} such that $M = 0.8M_{\odot}$, to resemble fairly typical low-mass RGs which may result from CV mergers.

5. To ensure numerical convergence, the resulting remnant is evolved for 2 kyr without burning and gold tolerances disabled. Nuclear reactions and gold tolerances are re-enabled at 2 kyr and 4 kyr, respectively. Although not initially so, the merger remnant model quickly reaches hydrostatic equilibrium. Evolution through the helium flash involves disabling gold tolerances again, and the models are terminated after helium-burning when the central helium fraction drops to $Y_c \leq 10^{-3}$.

In post-processing, we truncate the first 1 Myr (a few envelope thermal times) of our merger remnant models in order to avoid possibly unphysical transient behavior closely following the merger, which is not modelled accurately.

The relatively low He WD luminosity $L_{\text{WD}} = 10^{-4.0}L_{\odot}$ is chosen to highlight the effects of a highly degenerate core in the limiting case. In Appendix 3.A, we show that, once the core has thermalized sufficiently long on the RGB, the effect of increasing L_{WD} is very similar to that of decreasing M_{WD} . This is because these changes ultimately affect the entropy of

the merger remnants’ cores in the same direction, and subtler differences in the remnants’ core temperature profiles are erased by thermal conduction on the core’s thermal time (see Appendix 3.B).

Our models include the predictive mixing scheme described in Section 2.1 of Paxton, Schwab, et al. (2018) to account for near-core mixing, and to suppress numerical instability associated with definition of the convective core boundary, especially during the CHeB phase. We omit winds in order to avoid sensitivity to the wind prescription, which is highly uncertain. The effect of winds at the tip of the RGB (or mass loss during the merger itself) is primarily to increase the value of M_{MS} required for a given merger remnant mass during CHeB. Stellar models are initialized to solar metallicity, using the metal mass fractions given by Grevesse and Sauval (1998). We use the built-in `pp_cno_extras_o18_ne22` network for nuclear reactions.

When evolving the non-merged and merger remnant models, we run MESA in the hydrodynamical mode (evolving the radial velocity variable v_r explicitly), in order to stably evolve our models through the helium flash. We find that this is particularly necessary in the merger remnant models, where the helium flash is abnormally violent (see Section 3.4). We are able to model merger remnants involving He WD masses as high as $M_{\text{WD}} = 0.38M_{\odot}$. Higher He WD masses cause numerical problems during the He flash.

This scheme for producing He WD–MS merger remnants produces very similar models to those of Zhang, Hall, et al. (2017), who instead manually add the hydrogen envelope back onto the He WD using a large, time-dependent mass gain rate. We find that our method more reliably produces a model which MESA can evolve without case-by-case human intervention, and allows for the successful evolution of remnants with more degenerate cores.

In order to demonstrate the effects of the enhanced core degeneracy in our merger remnant models, we also run a model (hereafter the *non-merged* model) of a RG whose envelope has only partially been removed on the RGB (so that it has a total mass $M = 0.80M_{\odot}$). Besides having possibly a low-mass envelope, this model otherwise behaves like a normal RG and should be thought of as representing standard stellar evolution.

3.3 Red giant branch

Soon after merger, a merger remnant quickly relaxes into a RG which behaves similarly to a normal star on the RGB. Specifically, it is composed of an inert degenerate helium core surrounded by a tenuous hydrogen envelope which is inflated to a large radius by hydrogen burning in a thin shell at its base. However, merger remnants differ from single RGs because

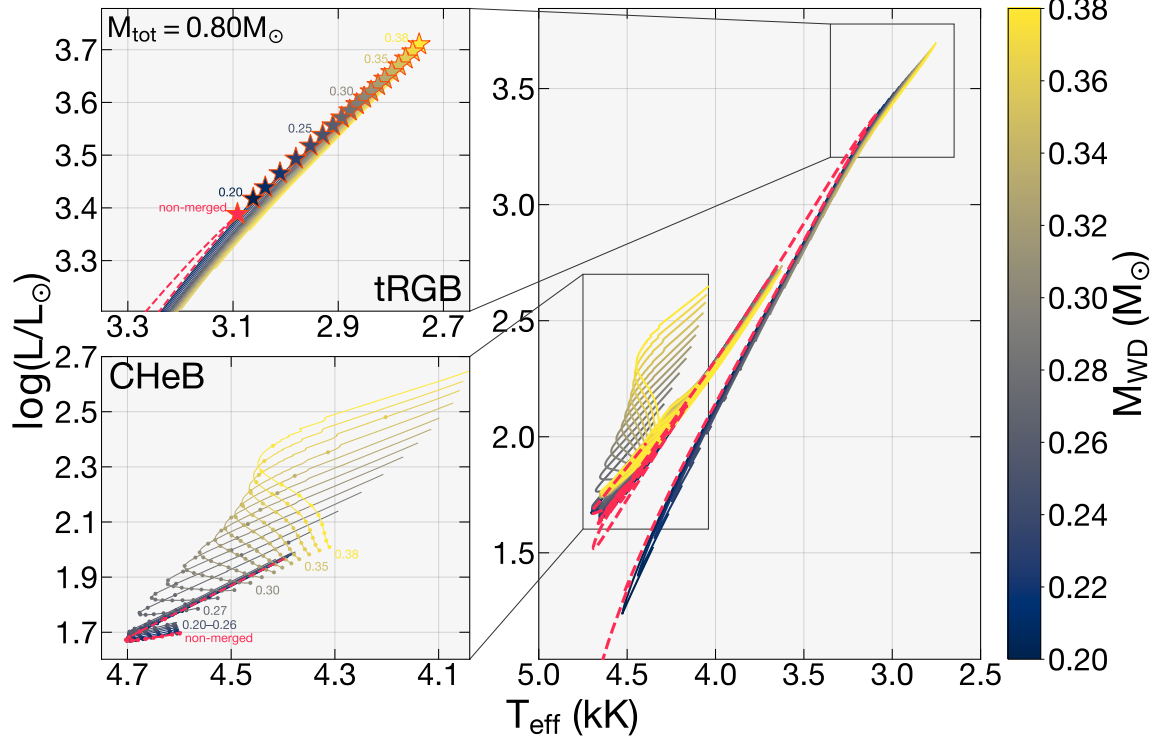


Figure 3.3: The trajectories on the Hertzsprung–Russell diagram of merger remnant models with varying He WD mass M_{WD} and total mass $M_{\text{tot}} = M_{\text{MS}} + M_{\text{WD}} = 0.80M_{\odot}$. The *red dashed* line indicates a non-merged model with $M = 0.80M_{\odot}$. The *top-left* and *bottom-left* panels zoom into the tRGB and CHeB stages, respectively. The *red-outlined* star symbols on the top-left panel indicate the location of the helium flash. On the *bottom-left* panel, only evolution $\gtrsim 5$ Myr following the helium flash is shown, and *points* are distributed 10 Myr apart. We have excised times near the helium flash, when the envelope sometimes becomes hydrodynamical.

their cores are cold (owing to the potentially long cooling phase of the progenitor He WD), rather than being almost isothermal with the burning shell.

Soon after their formation, merger remnants, especially those involving lower-mass He WDs, are out of thermal equilibrium and temporarily shrink in radius. The duration of this phase is a decreasing function with M_{WD} , lasting $\simeq 10$ Myr for $M_{\text{WD}} = 0.20M_{\odot}$ and dropping to $\lesssim 1$ Myr by $M_{\text{WD}} = 0.27M_{\odot}$. The degree of this secular dimming also drops off strongly with M_{WD} . However, after this short-lived period, the remnant evolves monotonically up a modified version of the RGB.

Overall, this cold core has three consequences on the RGB:

1. At fixed helium core mass, the star is brighter and has a larger radius (Section 3.3.1). Because the helium core of a remnant is colder and thus slightly more compact, the overlying hydrogen-burning shell has a significantly higher luminosity.
2. The degenerate core alters the structure of the gravity-mode (g-mode) cavity (Section 3.3.2), modifying the propagation of g modes in an observable way.
3. The helium flash, which occurs when some shell in the core reaches a sufficient temperature $T \simeq 10^8$ K, is slightly delayed (Section 3.3.3). This allows merger remnants to exceed the maximum luminosity attainable by a single RG at the tip of the RGB. Additionally, the more violent helium flash can have significant consequences for the CHeB stage (Section 3.4).

3.3.1 More compact cores inflate the radius

In a typical RG, the total luminosity L is essentially entirely determined by its core mass M_c (Refsdal and Weigert, 1970), with very little sensitivity to the mass of the envelope. This correspondence is called the *core mass–luminosity relation*. Photometrically, this means that single RGs with similar core masses will appear essentially indistinguishable on a Hertzsprung–Russell diagram, even if their envelopes differ significantly in mass. Asteroseismically, it results in a tight relationship between the large frequency spacing $\Delta\nu$ and the g-mode period spacing $\Delta\Pi$ (defined and interpreted below) for degenerate-core RGs with $M \lesssim 2M_\odot$ (e.g., Deheuvels, Ballot, Gehan, et al., 2022).

Crucial to this relation is that the radius of the burning shell (which is similar to the radius of the core, R_c) is a strict function of M_c (for a degenerate core, roughly $R_c \propto M_c^{-1/3}$). In merger remnants, the core is cooler than the hydrogen-burning shell and therefore slightly more compact (Althaus et al., 2005). In this case, the luminosity is no longer fixed by M_c alone, although it is still determined by the environment around the burning shell.

In addition to modifying its placement on the Hertzsprung–Russell diagram (Figure 3.3), the inflated radius significantly modifies the observable pressure (p) modes in the envelope. Asteroseismically, RGs are solar-like oscillators (Chaplin and Miglio, 2013), for which a frequency of maximum power ν_{\max} and large (p-mode) frequency spacing $\Delta\nu$ can be measured. These observables are approximately related to the mass M and radius R of the RG as

$$\nu_{\max} \propto g/T_{\text{eff}}^{1/2} \propto M R^{-2} T_{\text{eff}}^{-1/2} \quad (3.2)$$

and

$$\Delta\nu \simeq \sqrt{G\rho} \propto M^{1/2} R^{-3/2} \quad (3.3)$$

(Ulrich, 1986; Brown, Gilliland, et al., 1991).

In the absence of additional information, M_c and R_c are not known. While L , v_{\max} , and $\Delta\nu$ are all significantly different in merger remnants, this is only a direct consequence of their inflated radii. Therefore, these observables alone cannot distinguish merger remnants except near the tip of the RGB (Section 3.3.3). However, independent probes of the core, most notably the asteroseismic g-mode period spacing (Section 3.3.2) can help distinguish merger remnants from normal stars.

3.3.2 Asteroseismic signatures on the red giant branch

Asteroseismically, RGs which are sufficiently low on the RGB (roughly before the red bump; Pinçon, Goupil, et al., 2020) have strong enough mixed-mode coupling such that the g-mode period spacing $\Delta\Pi$ can be measured:

$$\Delta\Pi \approx \frac{\sqrt{2}\pi^2}{\int_{\mathcal{R}}(N/r) \, dr}, \quad (3.4)$$

defined here specifically for the dipole ($\ell = 1$) modes. This quantity probes the radiative core of the star. The integral in Equation 3.4 is taken over \mathcal{R} , the g-mode cavity of the RG, i.e., the region where $2\pi\nu_{\max} < N$, where N is the Brunt–Väisälä frequency. At present, $\Delta\Pi$ has been measured for a few thousand RGs (e.g., Vrard, Mosser, et al., 2016), observationally constraining the structures of their radiative cores.

By Equation 3.4, more stratified radiative zones with larger integrals over $N d \ln r$ have lower period spacings. In Appendix 3.C, we show that the Brunt–Väisälä frequency in the degenerate part of the radiative core is given by

$$N^2 \approx N_0^2 \frac{k_B T}{Z E_F} \left(1 - \frac{5}{2} \nabla\right) \propto \frac{T}{Z E_F} \left(1 - \frac{5}{2} \nabla\right), \quad (3.5)$$

where E_F is the Fermi energy of the core, $\nabla = d \ln T / d \ln P$, and the normalization N_0^2 is comparable to the dynamical frequency of the core, and is given by

$$N_0^2 = \frac{\rho g^2}{p} \sim \sqrt{GM_c/R_c^3}. \quad (3.6)$$

Both a typical RG core and cooling WD are approximately isothermal ($\nabla \ll 1$). Then, ignoring the temperature dependence of the stellar structure for the moment, we approximately expect

$$N \propto \sqrt{T}. \quad (3.7)$$

A “cold,” highly degenerate isothermal core will have a significantly smaller N , and therefore significantly larger $\Delta\Pi$, than a “warm” one (Bildsten and Cutler, 1995). However, if there is a temperature gradient, it may significantly affect $\Delta\Pi$.

The evolution of the buoyancy profile of a merger remnant with $M_{\text{WD}} = 0.25M_{\odot}$ and $M_{\text{MS}} = 0.55M_{\odot}$ (together with a non-merged model of equal mass) is shown in the top panels of Figure 3.4. In He WD–MS merger remnants, the period spacing is modified by two effects which act roughly in opposite directions with comparable magnitudes.

First, at early times (left panels of Figure 3.4), the core of a merger remnant is roughly isothermal at its initial temperature $T \ll T_{\text{shell}}$. In comparison, the core of a single RG is roughly isothermal with the hydrogen-burning shell ($T \approx T_{\text{shell}}$). During this time period, the Brunt–Väisälä frequency profile in the core is suppressed from that of a single star by a factor $\sqrt{T_{\text{shell}}/T}$. This effect tends to increase the period spacing. However, in a short time $< \tau_{\text{th,core}}$, electronic thermal conduction (approximately obeying the nonlinear law in Equation 3.18) sets up a temperature gradient ∇ . Curiously, we find that this temperature gradient happens to mostly cancel out the factor $\sqrt{T_{\text{shell}}/T}$ (see Equation 3.5) to cause the N profiles of the single and merger remnant models to be similar (*top center* panels of Figure 3.4). Equality between the Brunt–Väisälä frequency profiles occurs long before the interior of the core has thermalized to the shell temperature. Therefore, in the relatively short time that it takes heat conduction to set up a temperature gradient throughout the core, the lower temperature of the merger remnant core no longer works to increase $\Delta\Pi$. The reason for this “coincidental” cancellation remains mysterious, but may be related to some properties of long-lived pre-thermalized solutions of nonlinear heat diffusion. These solutions (called “intermediate asymptotics”; Barenblatt, 1996) exhibit self-similar behavior in many nonlinear heat diffusion problems (often in the context of diffusion in a porous medium), and have been studied extensively in applied mathematics (by, e.g., Witelski and Bernoff, 1998; Galaktionov et al., 2004; Hayek, 2014).

The second effect is that, because N scales with the dynamical frequency of the core, it is higher in a more compact core, and is therefore larger in a merger remnant’s core than in a single star’s core. In contrast with the first effect, the increased Brunt–Väisälä frequency due to this effect persists until the core heats up enough for the difference in R_c between the merger remnant and single stars to be erased (which occurs on the thermal timescale $\tau_{\text{th,core}}$). This effect tends to reduce $\Delta\Pi$ in the merger remnant compared to a single RG. As a merger remnant evolves, $\Delta\Pi$ typically evolves from being larger than that of a single star (at *fixed* M_c) to smaller (Figure 3.5), although it may not achieve the latter regime by the helium flash if the merger involves a sufficiently massive WD. In our models, departures of

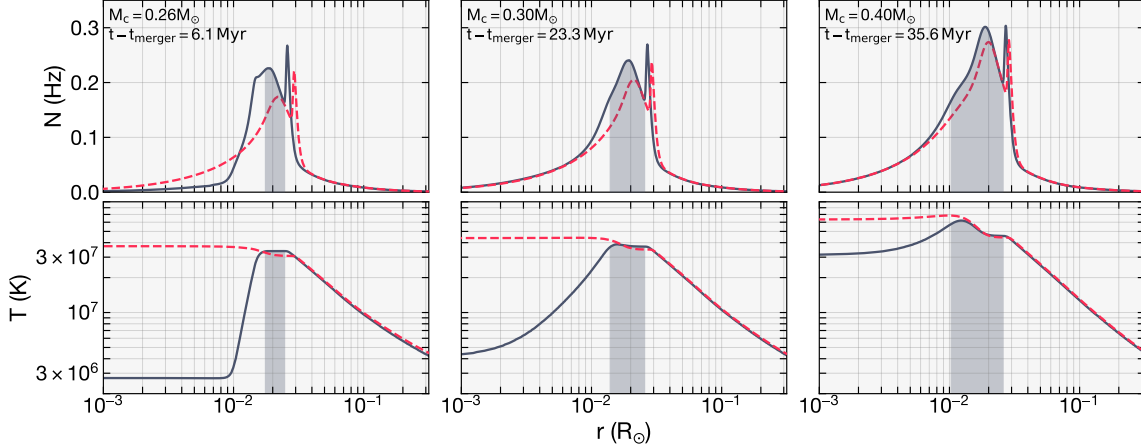


Figure 3.4: The Brunt–Väisälä frequency N (top) and temperature T (bottom) shown for the $M_{\text{MS}} = 0.55M_{\odot}$, $M_{\text{WD}} = 0.25M_{\odot}$ merger remnant (solid gray-blue) and non-merged model of $M = 0.80M_{\odot}$ (red dashed), at various stages of evolution. The two models are compared at equal core masses M_c . The shaded region denotes helium deposited onto the helium core of the merger remnant model by hydrogen burning during its evolution.

$\Delta\Pi$ from the non-merged case can reach up to ≈ 10 s at a given core mass. However, we again caution that M_c is not directly known, and diagnosis of a past merger requires another observable, such as the radius or $\Delta\nu$.

Asteroseismic measurements $\Delta\nu$ and $\Delta\Pi$ of RGs are typically represented on a spacing diagram as shown in Figure 3.5. Most stars on the RGB (zoomed in on the *bottom* panel) cluster around a tight sequence which ultimately arises from the core mass–luminosity relation (e.g., Deheuvels, Ballot, Gehan, et al., 2022). This is also essentially the path followed by our $M = 0.8M_{\odot}$ non-merged model, modulo a small order-unity factor owing to a weak dependence on total mass ($\Delta\nu \propto M^{1/2}$). In this space, it is clear merger remnants usually lie above the degenerate sequence, before slowly evolving back towards it. The position of merger remnants above that of normal RGB stars is dominated by the larger radii of these objects at the same core mass. Since $\Delta\nu \propto R^{-3/2}$, this shifts their positions on the diagram to the left. Merger remnants may also pass slightly below the degenerate sequence during their evolution (due to sufficiently small values of $\Delta\Pi$). This effect is however subtle. Stars in this region of $\Delta\nu$ – $\Delta\Pi$ space may more naturally be explained by RG–MS mergers (Deheuvels, Ballot, Gehan, et al., 2022), particularly if they lie far below the degenerate sequence.

The g-mode period spacing $\Delta\Pi$ is only observable for remnants sufficiently low on the RGB (i.e., below the RGB bump, which is the “hook” feature in Figure 3.5). For merger remnants in this regime, departure from the degenerate sequence is most prominent during

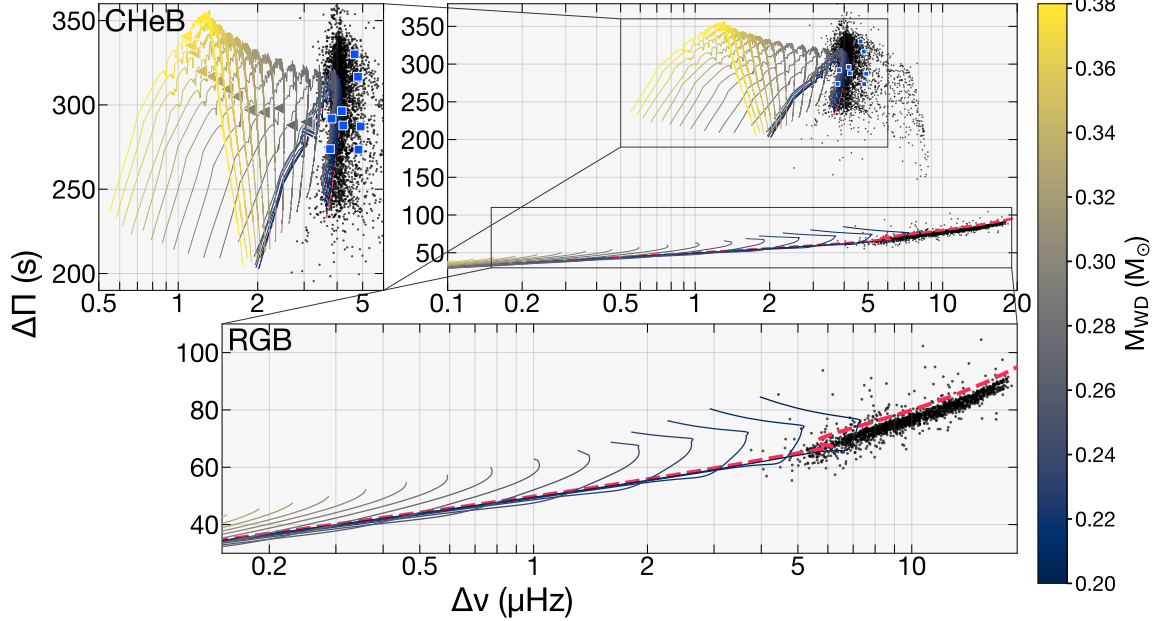


Figure 3.5: An asteroseismic spacing diagram ($\Delta\Pi$ versus $\Delta\nu$) showing merger remnant evolutionary sequences and a non-merged model (red dashed) all with $M = 0.80M_{\odot}$. The top-right panel shows the entire parameter space, and the left and bottom panels zoom in on CHeB stars and the RGB, respectively. Roughly speaking, both RGB and CHeB stars evolve from right to left on this diagram (i.e., towards decreasing $\Delta\nu$, or increasing R). The black points are observations taken from the catalog of Vrard, Mosser, et al. (2016) with stars flagged for possible aliases removed. In the top-left panel, colored triangles denote the last 5 Myr of the CHeB phase. The blue squares denote 8 stars from the very low-mass sample of Li, Bedding, Murphy, et al. (2022) which appear in the Vrard catalog.

the initial contraction phase after the formation of the remnant, although RGs which have passed this phase still lie above the degenerate sequence for an additional ~ 20 Myr. Hence, this particular asteroseismic diagnosis may only be possible for sufficiently recent mergers involving sufficiently low-mass He WDs.

3.3.3 Overbright tip of the RGB

During the RGB phase of a single star, the helium core grows in mass and contracts over time, as the envelope expands. Simultaneously, the core heats up gradually until the temperature is high enough for helium burning through the triple- α process ($\simeq 10^8$ K), at which time the star has reached the tip of the RGB (tRGB).

In our most extreme model with $M_{\text{WD}} = 0.38M_{\odot}$, the tRGB surface luminosity exceeds that of a single star by a factor of 2 (Figure 3.3). This factor is likely to be even larger for more massive values of M_{WD} than we can run (but which are still physical). At the tRGB,

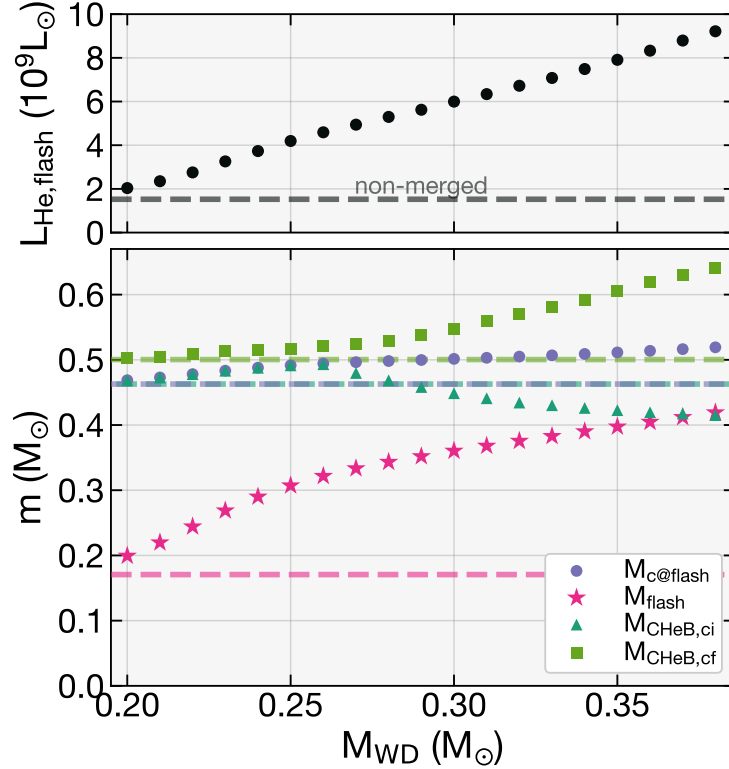


Figure 3.6: *Top*: The maximum helium-burning luminosities $L_{\text{He,flash}}$ attained during the helium flash in our merger remnant models with total mass $M_{\text{tot}} = M_{\text{MS}} + M_{\text{WD}} = 0.80M_{\odot}$. *Bottom*: For the merger remnant models, we show core masses $M_{\text{c}}@{\text{flash}}$ at the helium flash (purple circles), mass coordinates M_{flash} where the helium flash begins (magenta stars), and initial (turquoise triangles) and final (green squares) core masses $M_{\text{CHeB,ci}}$ and $M_{\text{CHeB,cf}}$ during the CHeB phase. In both panels, *dashed lines* denote values for the $M = 0.80M_{\odot}$ non-merged model.

our merger remnant models outshine the tRGB of the single star model for between 140 kyr ($M_{\text{WD}} = 0.20M_{\odot}$) and 1.8 Myr ($M_{\text{WD}} = 0.38M_{\odot}$). Since RG luminosities are essentially totally determined by near-core properties, even merger remnants of low mass (involving small values of M_{MS}) are still expected to outshine single RGs at the tRGB.

The ostensibly well-known luminosity of the tRGB is often leveraged to measure cosmological distances (Bellazzini, Ferraro, and Pancino, 2001; Bellazzini, Ferraro, Sollima, et al., 2004). We point out that overbright merger remnants near the tRGB may affect the tRGB of a stellar population’s role as a standard candle. However, this effect is probably minor, since merger remnants of this type likely make up no more than a few percent of all RGs.

3.4 Core helium-burning phase

When the core reaches a sufficient temperature, helium burning begins. In single RGs, it is well known that helium ignites off-center due to a slight temperature inversion caused by neutrino cooling (Thomas, 1967). The peak burning rate reached during the subsequent helium flash depends sensitively on the density where helium ignites (Salpeter, 1957), and therefore on the mass of the helium core. Subsequent intermittent burning events occur in a series of subflashes (Thomas, 1967). In a normal RG, these subflashes propagate inwards over the course of a few megayears until they reach the core, fully lifting the degeneracy of the helium core and burning $\approx 4\%$ of its mass into carbon. Once this occurs, RGs quickly contract on a thermal time until they have radii $\approx 11R_\odot$ (the CHeB phase), after which they are supported by a combination of helium core- and hydrogen shell burning, which generally contribute in comparable amounts to the stellar luminosity.

In merger remnants, the helium flash occurs similarly, although, as previously pointed out by Zhang, Hall, et al. (2017), the flash occurs farther off-center (Figure 3.6), since the core temperature inversion is now dominated by the low temperature of the WD progenitor rather than the weaker effect of neutrino cooling (compare the *dashed red* and *solid blue* curves of the *lower-right* panel of Figure 3.4). Additionally, the subflashes occur closer together in time, and are more energetic in general.

In our models, the maximum helium-burning luminosity attained by a merger remnant is roughly a linear function of M_{WD} , with the most extreme model attaining a factor of ≈ 5 higher helium-burning luminosity than attained by a non-merged star (see the *top* panel of Figure 3.6). The energy production rate can be a whopping $\approx 10^{10}L_\odot$ at the peak of the helium flash. Since mergers involving more massive WDs than those on our model grid are possible, even larger helium-burning luminosities may occur in nature. The most vigorous helium flash in our merger models also burns a larger fraction of the core into carbon, up to $\simeq 7\%$ by mass. We present the post-helium flash composition profiles of several of our models in Appendix 3.D.

We verify in our models that the helium flash, though abnormally energetic in merger remnants, still does not result in hydrodynamical burning (which might result in detonation). Specifically, following Shen, Kasen, et al. (2010), we verify that convection is always efficient enough to flatten temperature gradients created by helium burning, and also that the hierarchy $|v_r| \ll v_{\text{conv}} \ll c_s$ is maintained throughout the helium core (though not necessarily in the hydrogen envelope). The properties of this dredge-up concern physics in the helium core only, and is essentially independent of the envelope mass. Similar core

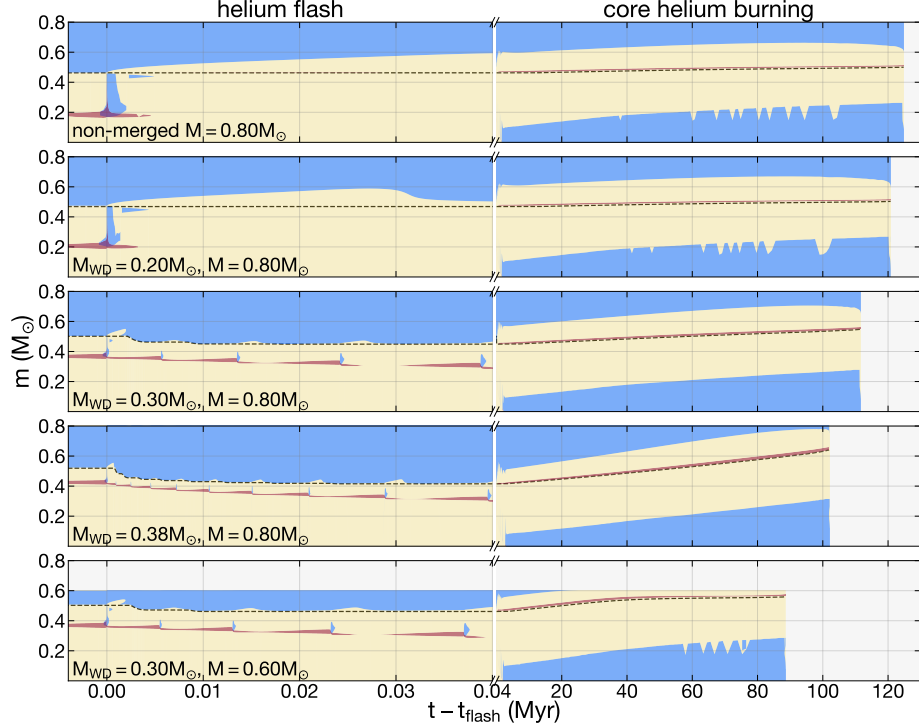


Figure 3.7: Kippenhahn diagrams for the non-merged $M = 0.80M_{\odot}$ and selected merger remnant models, during the helium flash (*left*) and CHeB phase (*right*). Convective (radiative) zones are shown in blue (yellow), and burning regions fusing more vigorously than $\epsilon = 10^3 \text{ erg g}^{-1} \text{ s}^{-1}$ are shown in red (at this scale, the CHeB region is highly localized to the center of the star and cannot be seen). The *black dashed line* indicates the helium core mass M_c . Merger remnant models with $M_{\text{WD}} \geq 0.27M_{\odot}$ experience core dredge-up events during the helium flash, and subsequently develop thinner convective envelopes by mass during CHeB. If M_{MS} is small enough, the convective envelope disappears entirely, and the star enters the horizontal branch.

dredge-up events during the helium flash have also been predicted in low-metallicity stars which have undergone extreme mass loss (Sweigart, 1997; Cassisi, Schlattl, et al., 2002).

The CHeB-phase evolution of our merger remnant models fits into two regimes, sorted by M_{WD} :

1. For $M_{\text{WD}} \leq 0.26M_{\odot}$, the flash is delayed slightly, and occurs when the core is slightly more massive. As a result, the CHeB phase of these remnants begins with a slightly higher helium core mass. Specifically, our single non-merged model ignites helium at a core mass $M_c \approx 0.46M_{\odot}$, and our merger remnant model with $M_{\text{WD}} = 0.26M_{\odot}$ undergoes its flash at a slightly higher core mass $M_c \approx 0.50M_{\odot}$.

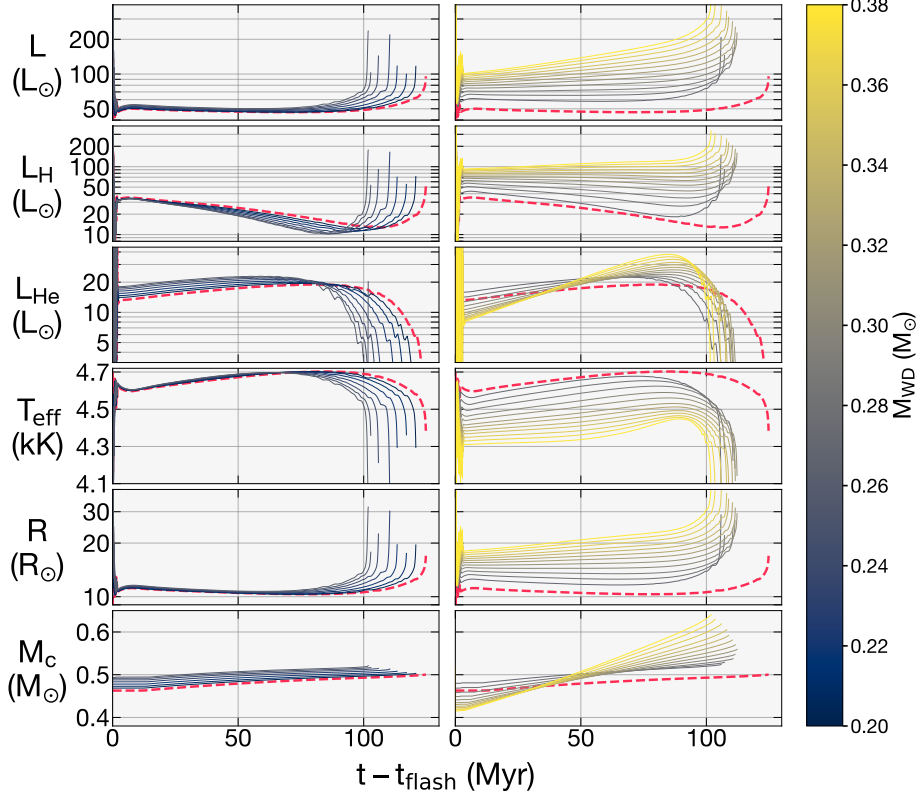


Figure 3.8: Time evolution of the CHeB-phase luminosity L , hydrogen- and helium-burning luminosities L_H and L_{He} , effective temperature T_{eff} , radius R , and helium core mass M_c for merger remnant models and a non-merged model (red dashed) all with $M = 0.80M_{\odot}$. The *left* and *right* panels show merger remnant models with $M_{\text{WD}} \leq 0.26M_{\odot}$ and $M_{\text{WD}} \geq 0.27M_{\odot}$, respectively. The latter models have helium flashes which are vigorous enough to dredge up some of the helium core into the envelope.

2. For $M_{\text{WD}} \geq 0.27M_{\odot}$, the flash produces so much heat that it causes the convective envelope to deepen significantly, dredging up both the hydrogen-burning shell and the outer layers of the helium core (see Figure 3.7). For our most extreme model ($M_{\text{WD}} = 0.38M_{\odot}$), $\approx 20\%$ of the core ($\approx 0.1M_{\odot}$ of helium) is dredged up into the envelope, significantly modifying its mean molecular weight.

As a result of this, merger remnants involving lower-mass He WDs $M_{\text{WD}} \leq 0.26M_{\odot}$ evolve very similarly to normal red clump stars, appearing almost identical to them in both photometric (*bottom-left* panel of Figure 3.3) and asteroseismic (*top-left* panel of Figure 3.5 and *left* panel of Figure 3.10) observables. One minor difference is that the merger remnants have systematically shorter CHeB lifetimes, by up to $\lesssim 20\%$.

In contrast, merger remnants involving more massive He WDs $M_{\text{WD}} \geq 0.27M_{\odot}$ evolve and appear very differently from their single counterparts. The following sections focus on observational signatures in this latter case (hereafter *post-dredge-up merger remnants*). The dredge-up event ultimately affects the luminosity (Section 3.4.1), asteroseismology (Sections 3.4.2 and 3.4.3), and surface abundances (Section 3.4.4) significantly.

3.4.1 Over-luminous red clump stars

During the CHeB phase, post-dredge-up remnants have significantly modified photometric properties:

1. They are brighter and slightly cooler, with the effect being stronger for higher values of M_{WD} (*bottom-left* panel of Figure 3.3 and *top-right* panel of Figure 3.8). For our most extreme model ($M_{\text{WD}} = 0.38M_{\odot}$), the luminosity is roughly tripled.
2. Their luminosities evolve much more significantly over the CHeB phase. Again, this effect is stronger for higher values of M_{WD} . In comparison, normal CHeB stars have essentially fixed luminosities for almost the entirety of the helium-burning phase.

As in normal CHeB stars, nuclear energy production has two main contributions:

1. *Core helium burning.* The now non-degenerate helium core burns helium through the triple- α process in a convective core. Structurally, the core is similar to normal, intermediate-mass MS stars in that they have convective core burning surrounded by a radiative envelope. Analogously, the helium-burning luminosity is essentially set by the helium core mass.
2. *Hydrogen shell burning.* Hydrogen continues to burn in a shell around the helium core through the CNO cycle. The luminosity of the hydrogen burning is a sensitive function of the environment around the burning shell.

The luminosities of these burning regions are highly coupled to each other. For example, the mass of the helium core determines the *helium-burning* luminosity and, thus, the radius of the core. This in turn strongly affects the *hydrogen-burning* luminosity and thus the total luminosity of the star. In turn, the luminosity of the hydrogen-burning shell determines the growth rate of the helium core, therefore feeding back onto the time dependence of *both* contributions to the luminosity.

As can be seen in the *right* panels of Figure 3.8, post-dredge-up merger remnants can have significantly larger hydrogen-burning luminosities L_{H} . While normal clump stars

have comparable hydrogen- and helium-burning luminosities ($\approx 20L_{\odot}$ in both cases), our most extreme merger remnant model with $M_{\text{WD}} = 0.38M_{\odot}$ has $L_{\text{H}} \simeq 100L_{\odot}$ (compared to $L_{\text{He}} \lesssim 40L_{\odot}$). The dominant factor setting L_{H} in a post-dredge-up remnant is the mean molecular weight μ at the hydrogen-burning shell, which is significantly enhanced by the helium dredge-up event. Single star models have a near-solar helium mass fraction $Y \approx 30\%$. In contrast, the $M_{\text{WD}} = 0.38M_{\odot}$ remnant model (with total mass $M = 0.80M_{\odot}$) has a much larger value $Y \approx 46\%$ owing to the $\approx 0.1M_{\odot}$ of helium added to a pre-existing, solar-composition envelope with mass $\approx 0.3M_{\odot}$. These values of Y correspond approximately to mean molecular weights $\mu \approx 0.62$ and $\mu \approx 0.70$, respectively. Refsdal and Weigert (1970) show that the hydrogen-burning luminosity exhibits a steep scaling with μ : $L \propto \mu^{7-8}$ for CNO-cycle burning, corresponding to increases in L_{H} by a factor $\simeq 2.5$, which is roughly consistent with the behavior of L_{H} in our models.

Because L_{H} is very sensitive to μ , the appearance and evolution of the remnant is now acutely sensitive to the initial envelope mass of the remnant. This is contrary to single stars, in which L and T_{eff} during the CHeB phase are nearly independent of the envelope mass. Since μ is set by the final mass fraction of the envelope after the dredge-up event, larger pre-existing envelopes dilute the added helium and reduce the mean molecular weight enhancement. We note in passing that structurally important increases in μ during a core dredge-up event also appear in some RG–He WD merger models of Zhang and Jeffery (2013).

As can be seen in Figure 3.8, the helium-burning luminosity L_{He} is also different in post-dredge-up models. L_{He} essentially tracks the helium core mass M_{c} until significant core helium depletion at the end of the CHeB phase. The high value of L_{H} translates to a fast-growing helium core, and, in turn, an up to a factor of a few increase in L_{He} over the CHeB phase. In sum, the higher L_{H} and L_{He} naturally translate to an overbright CHeB phase with significant time evolution in luminosity.

The increased luminosity causes merger remnants to have abnormally large radii, up to $R \approx 20R_{\odot}$ in our models (for $M_{\text{WD}} = 0.38M_{\odot}$). In addition to affecting the photometry, these large radii can also be directly measured asteroseismically via ν_{max} and $\Delta\nu$, together with the scaling relations in Equations 3.2 and 3.3. However, in order to distinguish merger remnants from ordinary stars beginning to ascend the asymptotic giant branch, it may also be necessary to measure mixed mode period spacings or surface abundances.

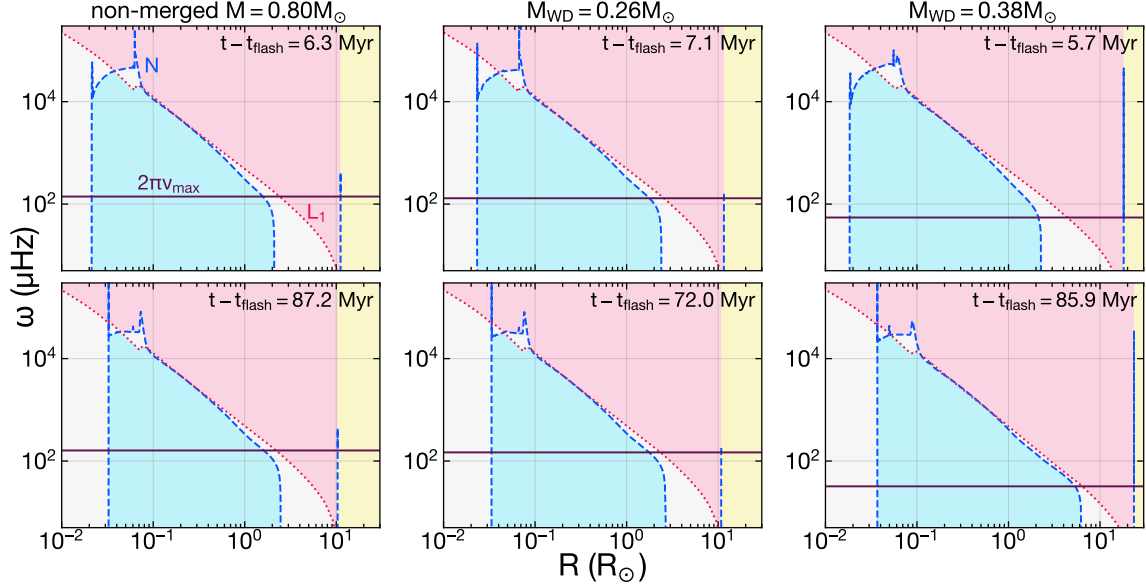


Figure 3.9: CHeB-phase asteroseismic propagation diagrams for a non-merged model (left) and merger remnants with $M_{\text{WD}} = 0.26M_{\odot}$ (center) and $M_{\text{WD}} = 0.38M_{\odot}$ (right). The Brunt–Väisälä (N), dipole Lamb (L_1), and maximum power ($2\pi\nu_{\text{max}}$) frequencies are shown as the *dashed blue*, *dotted red*, and *solid purple* curves, respectively. Color coding of areas denotes the p-mode propagating regions (pink), g-mode propagating regions (light blue), evanescent regions (white), and the exterior of the star (yellow). *Top* panels show propagation diagrams near the beginning of the CHeB phase, and *bottom* panels show the same farther along the CHeB phase, when the models attain maxima in the asteroseismic g-mode period spacing $\Delta\Pi$. All models have total mass $M = 0.80M_{\odot}$.

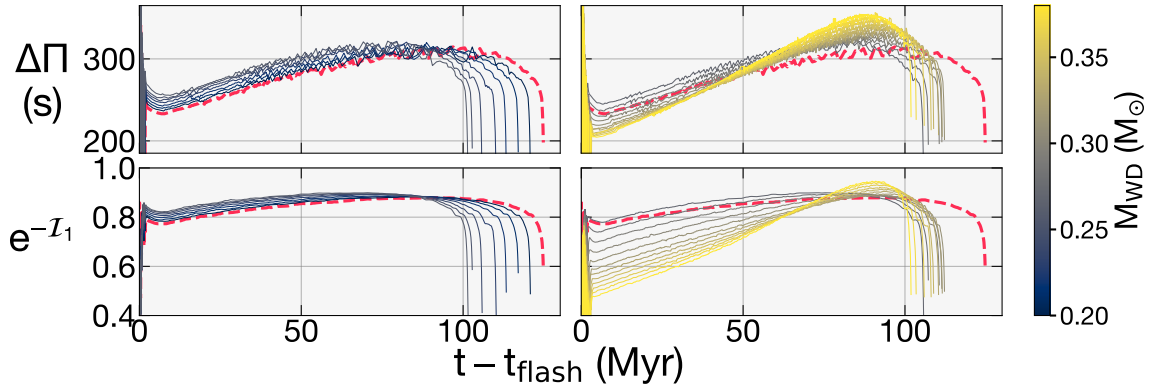


Figure 3.10: Time evolution of the CHeB-phase asteroseismic g-mode period spacing $\Delta\Pi$ (top), and e^{-I_1} (bottom), which is a simple proxy for the dipole mixed-mode coupling factor. We plot merger remnant models and a non-merged model (red dashed) all with $M = 0.80M_{\odot}$. As in Figure 3.8, the *left* and *right* panels show merger remnant models with $M_{\text{WD}} \leq 0.26M_{\odot}$ and $M_{\text{WD}} \geq 0.27M_{\odot}$, respectively.

3.4.2 Wider range of asteroseismic g-mode period spacings

During the CHeB phase, post-dredge-up mergers remnant models have substantially different structures which directly modify asteroseismic observables such as $\Delta\Pi$. This can be seen by comparing the *left* and *right* panels of Figure 3.9, which show the propagation diagrams of the non-merged and $M_{\text{WD}} = 0.38M_{\odot}$ merger remnant models at two selected times. On the other hand, merger remnants which do not experience significant dredge-up of the helium core ($M_{\text{WD}} \leq 0.26M_{\odot}$) have essentially identical structures (compare the *left* and *center* panels of Figure 3.9).

Because the nuclear burning luminosities are substantially modified in post-dredge-up models, the g-mode period spacing $\Delta\Pi$ of merger remnants spans a wider range of values over the CHeB phase (see the *top-right* panel of Figure 3.10, as well as the *top-left* panel of Figure 3.5). While $\Delta\Pi$ (Equation 3.4) depends on the integral of N within the radiative core, its value is dominated by the regions with the largest N . As can be seen in Figure 3.9, N is maximal underneath the hydrogen-burning shell (i.e., below the compositional spike in N at radii $\lesssim 0.1R_{\odot}$).

At the beginning of the CHeB phase (the *top* panels of Figure 3.9), post-dredge-up merger remnants have smaller helium core masses, resulting in smaller L_{He} . This results in a smaller convective core (slightly extending the bottom boundary of the g-mode cavity) as well as a slightly higher core dynamical frequency (resulting in slightly higher values of N overall). Both of these effects tend to decrease $\Delta\Pi$.

In contrast, near the end of CHeB (the *bottom* panels of Figure 3.9), the helium core of merger remnants has grown substantially due to the large hydrogen burning rate. They therefore evolve to have larger L_{He} , which ultimately results in an *increased* convective core size and overall lower N profile, and therefore larger $\Delta\Pi$. Because they also have inflated radii (Section 3.4.1), they have smaller values of $\Delta\nu$, and will occupy a region to the left of normal clump stars on a $\Delta\nu$ – $\Delta\Pi$ spacing diagram (*top* panels of Figure 3.5).

3.4.3 Asteroseismic mixed-mode coupling

In RGs, pulsations can probe not only the g-mode cavity (through $\Delta\Pi$) but also the evanescent zone between the p- and g-mode cavities. The extent of coupling between the two cavities is usually described by a coupling factor q (Unno, Osaki, Ando, Saio, et al., 1989). In addition to determining the visibility of mixed modes, q itself is an independent observable which probes a different internal structural feature than does $\Delta\Pi$ (Mosser, Pinçon, et al., 2017; Dhanpal et al., 2023). The recent discovery that low-mass or low-metallicity

RGs have preferentially high q (Matteuzzi et al., 2023; Kuszlewicz et al., 2023) has created revitalized demand for physical interpretations of q .

Computing q is mathematically nontrivial and involves detailed solution of a wave transmission problem (e.g., Takata, 2016a; Takata, 2016b; Takata, 2018) or fitting a model spectrum directly (e.g., Jiang and Christensen-Dalsgaard, 2014). Takata (2016a) show that the coupling factor is related to the transmission coefficient T by

$$q = \frac{1 - \sqrt{1 - T^2}}{1 + \sqrt{1 - T^2}}. \quad (3.8)$$

Takata (2016b) further write the transmission coefficient as

$$T = e^{-\pi(X_I + X_R)}. \quad (3.9)$$

Here, X_I is defined as an integral over the evanescent zone \mathcal{E} of the radial wavenumber with respect to the asymptotic dispersion relation, i.e., for dipole modes,

$$\begin{aligned} \mathcal{I}_1 \equiv \pi X_I &= \int_{\mathcal{E}} |k_r| \, dr \\ &= \int_{\mathcal{E}} \frac{\omega}{c_s} \sqrt{\left(1 - N^2/\omega^2\right) \left(L_1^2/\omega^2 - 1\right)} \, dr \end{aligned} \quad (3.10)$$

where, for simplicity, we have applied the Cowling approximation. X_R is a remainder term which can be specified analytically in the limit of a thin evanescent zone (Takata, 2016b), where it is most important.

We focus on the value of $e^{-\mathcal{I}_1}$ as a rough proxy for the mixed-mode coupling. Although CHeB stars typically have strong coupling such that X_R is likely to be important, calculation of this contribution requires more care (see, e.g., Rossem, 2023), and we therefore defer a detailed calculation of q in these merger remnants to a potential future investigation.

From the propagation diagrams (Figure 3.9), it can be seen that the evanescent zone evaluated at ν_{\max} is initially substantially wider in the $M_{\text{WD}} = 0.38M_{\odot}$ post-dredge-up merger remnant than in the non-merged model. This decreases the value of $e^{-\mathcal{I}_1}$ and, in turn, the g-mode coupling factor q at early phases of CHeB evolution.

However, late in the CHeB phase of post-dredge-up merger remnants involving especially massive He WDs with $M_{\text{WD}} \geq 0.33M_{\odot}$, the evanescent region becomes exceedingly small because of a larger radiative core. This temporarily causes $e^{-\mathcal{I}_1}$ and the mixed-mode coupling to become larger than in typical CHeB stars, giving their mixed modes high visibility.

In the last $\lesssim 20$ Myr, both $\Delta\Pi$ and e^{-I_1} dive sharply as the CHeB star begins to enter the asymptotic giant branch phase. During this time, the star expands especially quickly, and it will lie even farther to the left of most merger remnants on the asteroseismic spacing diagram in Figure 3.5.

3.4.4 Abundance anomalies

Merger remnants that experience a core dredge-up at the flash naturally display unusual surface abundances. While dredge-up of the helium core most obviously produces an enhancement in ^4He , direct spectroscopic measurement of helium abundance in late-type stars is likely infeasible. Fortunately, dredge-up probably enriches the surface with other elements that can be directly probed spectroscopically. Figure 3.11 shows surface abundances for selected species in terms of the index $A(X)$, defined for a given species X as

$$A(X) \equiv \log(n_X/n_{\text{H}}) + 12 \quad (3.11)$$

where n_X and n_{H} are the surface *number* densities of X and hydrogen, respectively.

We find that post-dredge-up remnants exhibit significant ^{12}C surface enrichment, up to $\simeq 1$ dex relative to hydrogen. This enhancement arises from dredge-up of core material which has been partially fused during the helium flash into carbon. Post-dredge-up remnants thus possess increased values of C/Fe and decreased values of $^{13}\text{C}/^{12}\text{C}$. Additionally, our post-dredge-up remnant models also possess significant surface enhancements (up to ~ 1.5 dex relative to hydrogen) in ^{18}O and ^{22}Ne , which are created by successive α captures of ^{14}N (e.g., Clayton, 2003) during the helium flash. As the surface abundance of ^{16}O in all of our merger remnant models is almost identical to that of our non-merged model, the surface abundance ratio $^{16}\text{O}/^{18}\text{O}$ is also decreased by up to ~ 1.5 dex in post-dredge-up remnants. While not included in our reaction network, it is also probable that a significant amount of ^{26}Mg is formed through α capture of ^{22}Ne in the abnormally hot helium flash (as in Shen, Blouin, et al., 2023). The surface abundance of ^{26}Mg is therefore also likely to be enhanced.

The lithium abundance is also important, because it can be created by the burning of ^3He or destroyed by burning at temperatures comparable to those required for hydrogen burning. Lithium-rich giants make up about 3% of all CHeB stars (Kumar, Reddy, Campbell, et al., 2020), and have previously been suggested to have formed via binary interactions or mergers (e.g., Zhang and Jeffery, 2013; Casey, Ho, Ness, Hogg, Rix, Angelou, Hekker, Tout, Lattanzio, Karakas, et al., 2019a). Our merger remnant models with high M_{WD} become highly lithium-rich very soon after merger, owing to a brief dredge-up event which occurs when hydrogen burning is first turned on (similar to the Cameron–Fowler mechanism;

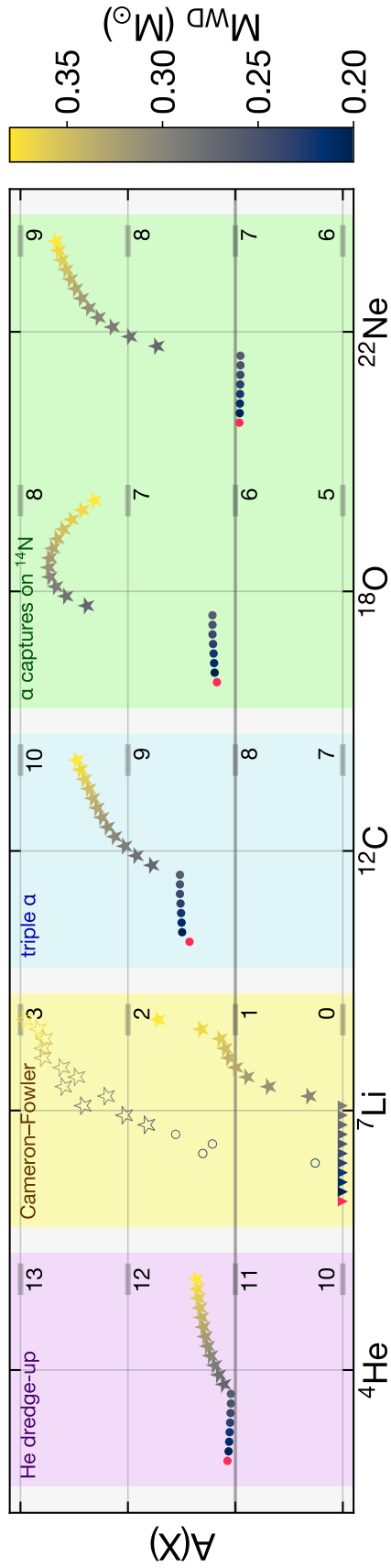


Figure 3.11: Selected surface abundances $A(X)$ (defined in Equation 3.11) during the CHeB phase. *Red points* denote the $M = 0.80M_{\odot}$ non-merged model, and *starred points* denote post-dredge-up merger remnants. For ^7Li , *filled symbols* denote lithium enrichment due to the helium flash only (described in Section 3.4.4), whereas *hollow symbols* denote lithium enrichment due to both the helium flash and merger itself (which may be inaccurately modelled). Note that the vast majority of CHeB stars have $A(\text{Li}) \lesssim 1.5$ (Kumar, Reddy, Campbell, et al., 2020), and the solar abundance is $A(\text{Li}) \approx 1.05$ (Asplund et al., 2009).

Cameron and Fowler, 1971). While such a merger-era lithium enhancement seems *plausible* (see, e.g., observations of lithium enrichment in luminous red novae; Kamiński, Schmidt, et al., 2023), our treatment of the merger process itself is highly artificial, and the evolution of the remnant is unreliable for post-merger ages younger than a thermal time, $\tau_{\text{th,env}}$. Modification to the surface abundances of other species during this (possibly artificial) dredge-up event are minor, since they primordially occur in much higher abundance than lithium.

If lithium is not enhanced during the merger, we investigate whether core dredge-up during the helium flash may be able to create lithium-rich giants anyway. To test this, we remove all of the lithium from our merger remnant models (with total $M = 0.8M_{\odot}$) just prior to the tRGB, and evolve them through the helium flash and CHeB phase. As shown in Figure 3.11, most models do not become lithium-rich according to the standard criterion $A(\text{Li}) \geq 1.5$ (e.g., Deepak and Lambert, 2021), with the exception of the $M_{\text{WD}} = 0.38M_{\odot}$ model. It is possible that merger remnants with higher values of M_{WD} or lower values of M_{MS} may attain stronger lithium enhancements. Moreover, extra mixing during the helium flash suggested by recent evidence may increase the amount of lithium surfaced (Kumar, Reddy, Campbell, et al., 2020; Martell et al., 2021b; Schwab, 2020). Overall, we conclude that, unless lithium enrichment occurs at merger or non-canonical mixing processes operate during the helium flash, He WD–MS merger remnants are unlikely to become lithium-rich.

3.4.5 Populating the horizontal branch with merger remnants

Neglecting mass loss during merger or through winds, M_{MS} sets the envelope mass of the merger remnant. In the preceding discussion, we have focused on varying M_{WD} and fixed M_{MS} so that the total mass of the merger remnant models is $M_{\text{tot}} = M_{\text{WD}} + M_{\text{MS}} = 0.80M_{\odot}$. However, in principle, M_{MS} could span a wide range of masses, including very small ones (if the hydrogen-rich component is a brown dwarf or if there is significant mass loss, e.g., Metzger, Zenati, et al. 2021), up to a few solar masses for mergers with intermediate-mass MS stars. In this section, we explore the behavior of merger remnants under varying M_{MS} .

Variation of M_{MS} may significantly change the behavior of the remnant in the following ways:

1. If M_{MS} is sufficiently small, merger remnants may only ignite helium with scant hydrogen envelopes (starting CHeB as subdwarf B-type stars; sdBs), or may fail to ignite helium altogether (fizzling out into He WDs). For reasons of scope, we do not investigate the He WD or sdB outcomes (but see the detailed modeling of Zhang, Hall, et al. 2017 and Zhang, Jeffery, Su, et al. 2023). Alternatively, if the envelope

mass drops below $M_{\text{env}} \simeq 0.1 M_{\odot}$ during CHeB but can still sustain hydrogen shell burning, the remnant can evolve onto the horizontal branch (Catelan, 2009).

2. In post-dredge-up remnants (where a helium flash mixes a fixed amount of core helium into the envelope), the helium fraction of the envelope during the CHeB phase is set by M_{MS} (larger hydrogen-rich envelopes during this stage more effectively dilute this additional helium). For merger remnants massive enough to enter a CHeB phase with a hydrogen-burning shell, this significantly affects their hydrogen-burning (and, thus, total) luminosity (as in Section 3.4).

Fixing $M_{\text{WD}} = 0.30 M_{\odot}$, we present in Figure 3.12 the CHeB-phase evolution of merger remnants with $M_{\text{MS}}/M_{\odot} \in [0.30, 0.35, 0.40, 0.50, 0.70]$. All of these models are massive enough to reach the tRGB and undergo a helium flash, which in this case is energetic enough to dredge up $\approx 0.06 M_{\odot}$ of helium. However, the envelopes of models with lower M_{MS} possess much more helium-enriched envelopes: envelope helium mass fractions during the CHeB phase for these models range from $Y = 0.36$ (for $M_{\text{MS}} = 0.70 M_{\odot}$) to $Y = 0.48$ (for $M_{\text{MS}} = 0.30 M_{\odot}$).

At the zero-age CHeB, all of these models possess a convective envelope. As expected, models with lower M_{MS} (and higher envelope Y) have higher hydrogen shell-burning luminosities at the beginning of the CHeB phase (as can be seen in the L_{H} panel in Figure 3.12). Models with higher $M_{\text{MS}} = 0.40, 0.50$, and $0.70 M_{\odot}$ retain these convective envelopes and behave similarly to the remnants discussed in Section 3.4.

The lower-mass $M_{\text{MS}} = 0.30$ and $0.35 M_{\odot}$ models display significantly different behavior. These models burn most of their remaining hydrogen during the CHeB phase such that their envelope mass drops below $0.1 M_{\odot}$. The outer layers of these models become completely radiative (at $t - t_{\text{flash}} \approx 25$ Myr and 55 Myr, respectively), and the remnants behave like horizontal branch stars. When this occurs, the stars become very blue, roughly reaching respective effective temperatures $T_{\text{eff}} \approx 20000$ K and ≈ 12000 K. While these models continue to sustain hydrogen-shell burning to some extent, L_{H} significantly drops during this horizontal branch stage (decreasing by factors $\simeq 10$ and $\gtrsim 2$ for the $M_{\text{MS}} = 0.30 M_{\odot}$ and $M_{\text{MS}} = 0.35 M_{\odot}$ models). In the $M_{\text{MS}} = 0.30 M_{\odot}$ model, this extreme drop in L_{H} precipitates a significantly lower total luminosity, which is readily apparent on a Hertzsprung–Russell diagram (*top-left* panel of Figure 3.12). We confirm for these two cases that the inclusion of gravitational settling does not change the results. A Reimers wind (Reimers, 1975; Reimers, 1977) scaled as in Reimers (1977) suggests that winds in these objects are small ($\dot{M} < 10^{-10} M_{\odot} \text{ yr}^{-1}$) and may be ignored.

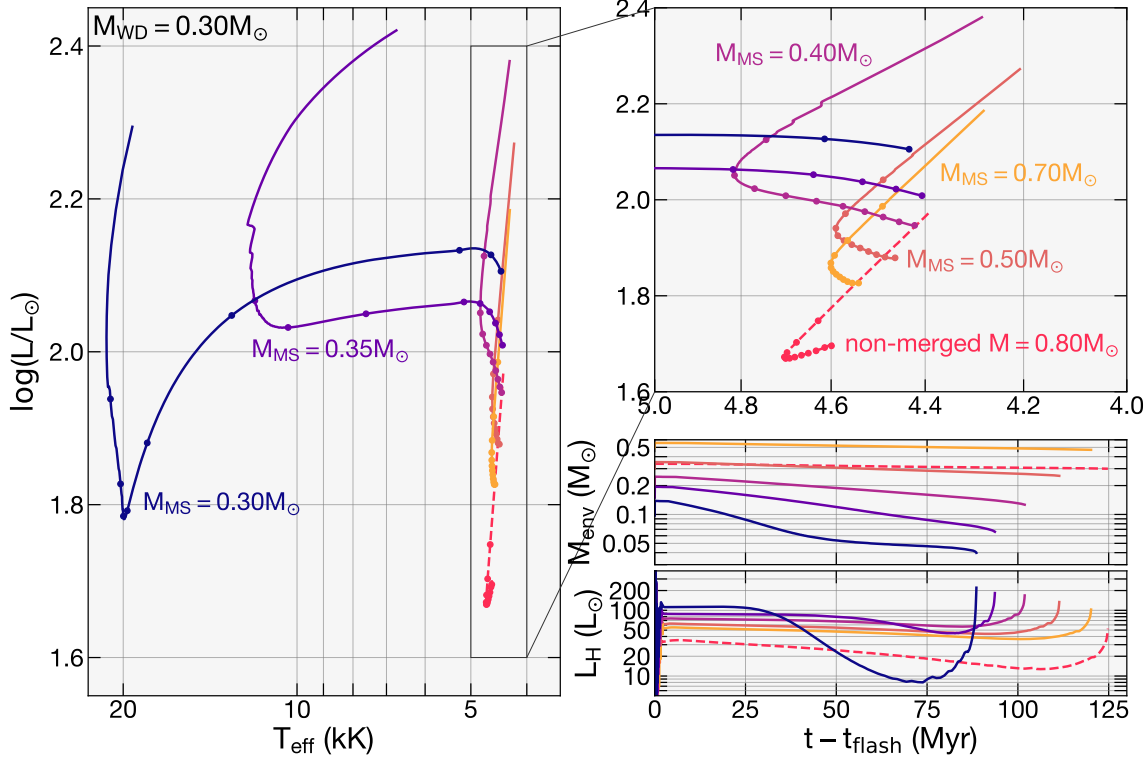


Figure 3.12: Evolution during the CHeB phase for merger remnants with $M_{\text{WD}} = 0.30 M_{\odot}$ but varying M_{MS} (Section 3.4.5). We plot a Hertzsprung–Russell diagram (left, with zoomed-in inset on the top right) and the time evolution of the hydrogen-rich mass $M_{\text{env}} = M - M_c$ and hydrogen shell-burning luminosity L_{H} (bottom right). A non-merged model with $M = 0.80 M_{\odot}$ is also shown for comparison (red dashed line).

3.5 Candidate merger remnants

3.5.1 Undermassive red clump stars may be merger remnants

Using asteroseismology, Li, Bedding, Murphy, et al. (2022) discovered a population of undermassive CHeB stars with masses $\lesssim 0.8 M_{\odot}$ (their “very low-mass” sample). Since single stars of these masses could not have evolved off of the MS in the age of the universe, these undermassive stars must have undergone non-standard evolution, such as stripping by a companion or binary assembly. Although Li, Bedding, Murphy, et al. (2022) argue that these undermassive giants are the product of partial envelope stripping by close companions, most of these objects do not exhibit the expected radial velocity variability between APOGEE and Gaia (Kareem El-Badry, private communication), disfavoring this formation channel. Matteuzzi et al. (2023) identify several more such objects (referred to as “red horizontal branch” stars), further demonstrating their extremely strong mixed-mode coupling. Figure 3.5 shows 8 members of the very low-mass sample of Li, Bedding, Murphy, et al. (2022) for which Vrard, Mosser, et al. (2016) reports g-mode period spacings. Despite their small

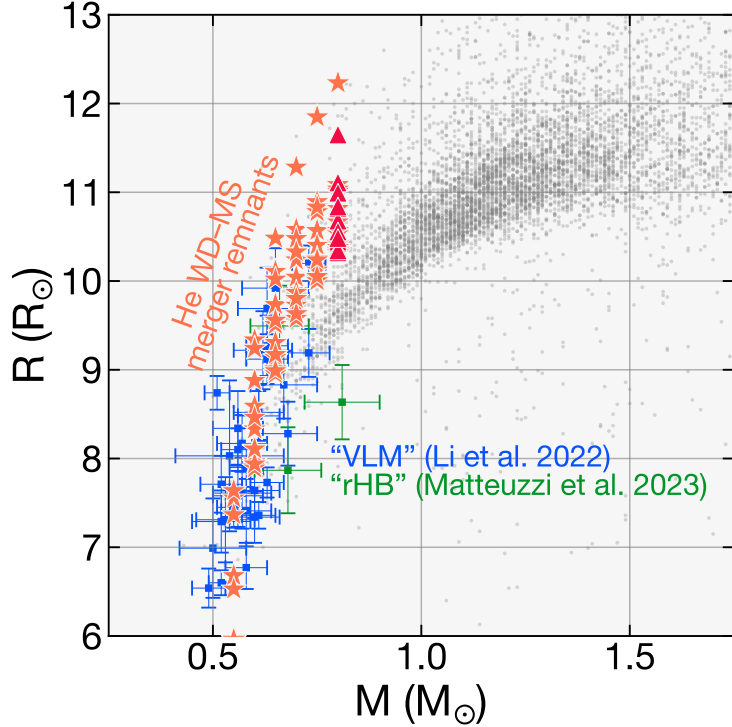


Figure 3.13: Measured masses and radii of observed CHeB stars, measured using asteroseismology. *Blue and green squares* denote the *very low-mass* (VLM) sample of Li, Bedding, Murphy, et al. (2022) and *red horizontal branch* (rHB) stars of Matteuzzi et al. (2023). *Gray data points* are taken from the catalog of Yu et al. (2018). *Orange stars* denote CHeB-phase merger remnant models with $M_{\text{WD}} = 0.20M_{\odot}$ and varying M_{MS} . *Red triangles* denote a CHeB-phase non-merged model with $M = 0.8M_{\odot}$, for comparison. Model track points are sampled 10 Myr apart.

masses, these very low-mass CHeB stars have typical values of $\Delta\Pi$ and, therefore, likely possess similar core structures to those of normal CHeB stars.

Observed undermassive clump stars likely have typical helium core masses and only stand out due to their low envelope masses. He WD-MS mergers naturally explain these objects: as long as M_{WD} is small enough that no dredge-up occurs at the helium flash, merger remnants have core masses which are basically normal. Furthermore, a merger remnant's envelope mass is simply set by M_{MS} (modulo merger or tRGB mass loss), which can be arbitrarily low. Finally, this binary scenario does not leave any companion behind, explaining why most undermassive CHeB stars are consistent with being single at present. While other mechanisms may exist for forming single undermassive CHeB stars (e.g., mass loss during failed common-envelope events), He WD-MS mergers appear to be highly promising.

To demonstrate this possibility, we run additional merger remnant models, fixing $M_{\text{WD}} = 0.20M_{\odot}$ and varying M_{MS} between $0.35M_{\odot}$ and $0.60M_{\odot}$ (total masses M between $0.55M_{\odot}$ and $0.80M_{\odot}$). Lower-mass merger remnant models have masses and radii which are consistent with the observed very low-mass sample of Li, Bedding, Murphy, et al. (2022) (Figure 3.13). Because the He WD–MS merger channel produces CHeB stars with essentially normal cores, our models behave almost identically to models performed by Li, Bedding, Murphy, et al. (2022) of normal CHeB stars with artificial envelope stripping to mimic mass loss from an initially standard RG.

3.5.2 Zvrk: a possible post-dredge-up merger remnant?

Using asteroseismology, Ong, Hon, et al. (2024) recently discovered a peculiar RG (“Zvrk”) with the following features:

1. The oscillation spectrum is complex, superficially resembling typical spectra of CHeB giants (which are dense due to their strong mixed-mode coupling, e.g., Mosser, Pinçon, et al., 2017; Dhanpal et al., 2023).
2. The asteroseismic scaling relations imply a radius $R \approx 24R_{\odot}$, a factor of two larger than that of a typical CHeB star.
3. The star is highly lithium-rich ($A(\text{Li}) > 3$), and also has a somewhat high [C/N] ratio relative to typical first-ascent RGs of the same mass, or indeed CHeB stars (e.g., Bufanda et al., 2023).
4. Photometric modulation and asteroseismic rotational splittings (assuming a pure p-mode spectrum) are consistent with a fast-spinning envelope with period $P \approx 100$ d.

Mainly on the basis of its radius, Ong, Hon, et al. (2024) conclude that Zvrk cannot be in the CHeB phase and must instead be a first-ascent RG. Because the expected mixed-mode coupling for an RG of this size would be weak, they argue that the spectrum is actually composed of pure p modes (rather than mixed modes), with the complexity of the spectrum instead coming from large rotational splittings from its fast rotation rate.

We suggest instead the possibility that Zvrk is a post-dredge-up He WD–MS merger remnant which is on the CHeB phase, *not* the RGB. This addresses the aforementioned observations in the following ways:

1. If Zvrk were a CHeB star, it would naturally have a large mixed-mode coupling and, thus, a CHeB-like spectrum (see also Section 3.4.3).

2. Our models of post-dredge-up CHeB remnants (Section 3.4.1), like Zvrk, have radii approximately twice as large as those of typical CHeB stars.
3. As demonstrated in Section 3.4.4, post-dredge-up remnants are expected to be carbon-rich, similar to Zvrk. While the core dredge-up event at the helium flash is unlikely to match the measured value of $A(Li)$, lithium enrichment may occur at merger (Kamiński, Schmidt, et al., 2023, as suggested by observations of luminous red novae). Although some of our merger remnant models become very lithium-rich soon after merger (as we describe in Section 3.4.4), future work should address whether this enhancement persists under more careful modeling.
4. As discussed in Section 3.6.3, merger remnants are likely rapidly rotating.

It is unclear at present whether He WD–MS mergers can reproduce these effects in the correct combination to match observations. The mass $M \approx 1.2M_{\odot}$ inferred by scaling relations is larger than those of our fiducial models ($M = 0.8M_{\odot}$), possibly requiring even stronger core dredge-ups which probably occur for larger values of M_{WD} than we can model. We point out that an extreme dredge-up event of this type probably modifies ν_{\max} (in a still-contested manner; Viani et al., 2017; Zhou et al., 2024) and, thus, the accuracy of scaling relation-based values of M and R . The similarly behaving remnants of RG–He WD mergers (e.g., Zhang and Jeffery, 2013) may also possibly reproduce the properties of Zvrk.

Further complicating the picture, Ong, Hon, et al. (2024) point out that a naïve identification of the double-ridged feature in Zvrk’s échelle diagram with the usual $\ell = 0$ and 2 degrees implies an unusually small p-mode offset $\epsilon_p \sim 0.25$. This is too low to be consistent with a low-mass RG of any canonical evolutionary state: none of the observed stars in Figure 10 of Kallinger, Hekker, et al. (2012) have $\epsilon_p < 0.4$ (though CHeB stars *do* have lower values of ϵ_p than do first-ascent RGs with comparable $\Delta\nu$). Of course, if Zvrk is a post-dredge-up remnant, it may well be possible that it attains an unusual value of ϵ_p . While not theoretically characterized in this work, ϵ_p may turn out to be another observational diagnostic for He WD–MS remnants.

While it is beyond the scope of the present work, we encourage a more detailed investigation to determine whether this hypothesis can explain Zvrk’s large radius, oscillation spectrum, surface abundances, and rapid rotation in a quantitative and self-consistent way.

3.5.3 Other potential post-dredge-up merger remnants

On the $\Delta\nu$ – $\Delta\Pi$ diagram, Mosser, Benomar, et al. (2014) identify several RGs which lie near, but slightly leftward, of the red clump (see their Figure 1). While Mosser, Benomar,

et al. (2014) argue that these stars have recently undergone helium subflashes, we suggest that they might be post-dredge-up remnants. As we show in Section 3.4.2, post-dredge-up remnants are also expected to have values of $\Delta\Pi$ comparable to those of normal CHeB stars, but smaller values of $\Delta\nu$ on account of their larger radii.

Recently, a small number of highly carbon-deficient red giants has been discovered and characterized as a distinct class with a few common properties (Bidelman and MacConnell, 1973; Bond, 2019; Maben et al., 2023). These objects are almost all in the CHeB phase (as implied by their g-mode period spacings), and many are also lithium-rich and overluminous compared to the usual red clump (Maben et al., 2023). However, the He WD–MS merger scenario predicts a carbon *enrichment* and thus fails to explain the abnormally *low* carbon abundances in these stars.

3.6 Discussion and future prospects

3.6.1 Progenitors and rates

While very few CVs with He WD accretors have been discovered (to our knowledge), CV progenitors (known as pre-CVs) *have* been, some shown in Figure 3.14. As their name suggests, such systems are expected to eventually initiate (possibly unstable) mass transfer after a combination of magnetic braking and gravitational radiation tighten their orbits sufficiently.

Zorotovic, Schreiber, and Gänsicke (2011) compile a catalog of post-common envelope binaries (PCEBs), WD–MS binary systems, some of which may contain He WD components, identified in this work as those with $M_{\text{WD}} < 0.5M_{\odot}$ (see Figure 3.14). Most of the MS components are of relatively low mass, with $M_{\text{MS}} \simeq 0.3M_{\odot}$. However, many of these systems contain fairly massive He WDs and could, upon merging, display fairly extreme versions of the asteroseismic and photometric merger remnant signatures we propose.

In later years, Maxted, Bloemen, et al. (2014) identified a separate class of close detached binaries involving AF-type MS stars orbiting low-mass ($\simeq 0.2M_{\odot}$) proto-He WDs, with Roestel et al. (2018) later measuring M_{WD} and M_{MS} for 36 such systems (see Figure 3.14). Due to the low masses of the proto-WD components, EL CVns are likely formed via stable mass transfer rather than common-envelope events (which would likely result in merger; Chen, Maxted, et al., 2017). The EL CVns in Figure 3.14 will likely merge when the stellar component is either a MS star or a subgiant (Lagos et al., 2020). In the He WD–subgiant case, the He WD is expected to merge with the subgiant core and produce a similar, low-entropy-core remnant as in the He WD–MS case explored in this work. However,

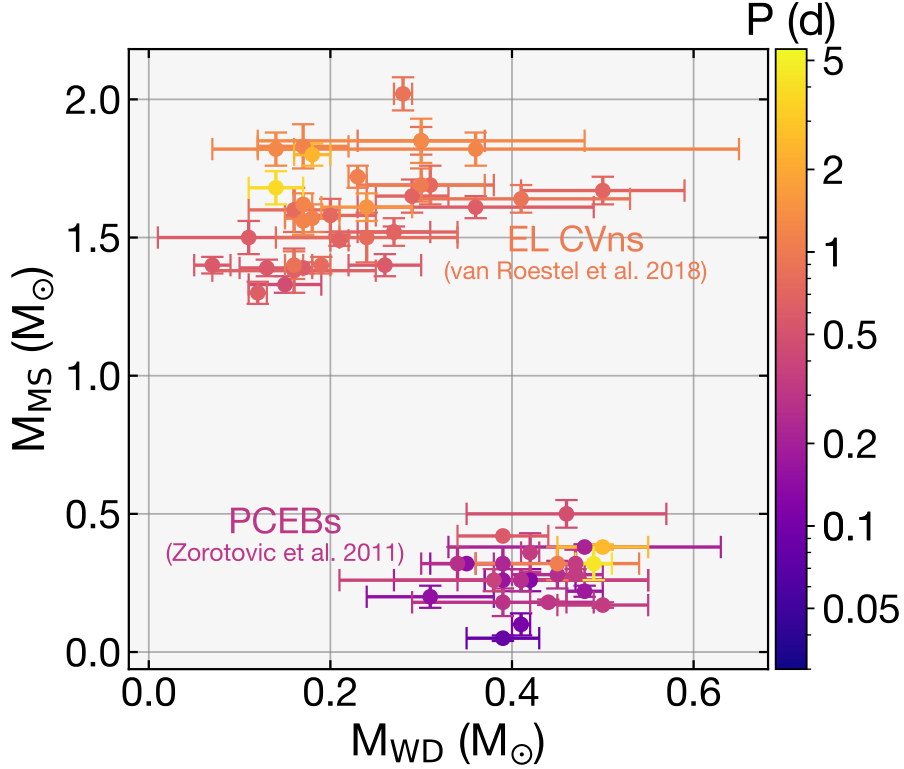


Figure 3.14: Parameters for a collection of known pre-CVs which may contain He WDs ($M_{\text{WD}} \leq 0.5M_{\odot}$) taken from Zorotovic, Schreiber, and Gänsicke (2011) for PCEBs and Roestel et al. (2018) for EL CVns. Color indicates the orbital periods of each system.

He WD–subgiant mergers may also have their own distinctive signatures, and a detailed investigation of the associated remnants is probably warranted.

Based on MESA models of merger remnants (Zhang, Hall, et al., 2017), Zhang, Hall, et al. (2018) perform a population synthesis calculation to determine how much these sorts of merger remnants contribute to the population of single He WDs, which are not a natural outcome of isolated stellar evolution (see also Zorotovic and Schreiber, 2017). Assuming a star-formation rate of $5M_{\odot} \text{ yr}^{-1}$, their calculation implies a Galactic formation rate of merger remnants $\sim 0.02 \text{ yr}^{-1}$ (about half of which fizzles out into He WDs before starting helium burning), with a factor-of-a-few uncertainty when the Reimers wind parameter is varied (Reimers, 1975; Reimers, 1977). If merger remnants continue to appear as RGs for $100T_{\text{m8}} \text{ Myr}$, the Milky Way should contain $\sim 2T_{\text{m8}} \times 10^6$ remnants at a given time. Put another way, for a Kroupa initial mass function (Kroupa, 2001), single low-mass RGs in the range $0.8M_{\odot}$ to $2.0M_{\odot}$ form at a rate $\sim 0.3M_{\odot} \text{ yr}^{-1}$. If isolated RGs have lifetimes

$100T_{\text{s8}}$ Myr, He WD–MS merger remnants should make up roughly $\sim 7\% \times (T_{\text{m8}}/T_{\text{s8}})$ of all low-mass RGs.

The present work has focused on the case where the compact component is a He WD. However, in principle, lower-mass CO WDs may also participate in mergers with MS stars for the same reasons. In such cases, the MS component is expected to disrupt around and accrete onto the carbon–oxygen core and initiate shell burning, and the merger remnant is therefore likely to resemble an asymptotic giant branch star with an unusually cold core. We defer a detailed investigation of this interesting possibility to a future work.

3.6.2 Merger transients and mass retention

The observable signatures of He WD–MS merger remnants described in this paper are applicable long (at least a thermal time) after the merger. However, the merger itself as well as any preceding novae events should produce observable transients and other emission, whose rates should be consistent with the population of merger remnants.

Metzger, Zenati, et al. (2021) show that the merger itself likely produces a dusty transient similar to a luminous red nova (e.g., Kulkarni, Ofek, et al., 2007) powered by recombination of the ejected material, and roughly estimate a Galactic rate $\sim 0.1 \text{ yr}^{-1}$. This is larger than the rate predicted by Zhang, Hall, et al. (2018) by a factor ~ 5 , although both estimates are subject to significant uncertainties. From this rate, they estimate that the Milky Way contains 10^3 – 10^4 remnants at the present day, which is much smaller than the $\sim 10^6$ we estimate in Section 3.6.1. The reason is that their models predict the merger remnant only retains a small fraction $\sim 10\%$ of the hydrogen supplied by an already low-mass MS star, rather than all of it. This implies a much shorter post-merger lifetime ~ 10 – 100 kyr.

However, Metzger, Zenati, et al., 2021 investigates cases where the MS star has a low mass, $M_{\text{MS}} \lesssim 0.5M_{\text{WD}}$. As they point out, higher-mass MS stars will likely produce gravitationally unstable disks that accrete much more efficiently onto the WD, closer to our assumption of conservative mass accretion. Ignition of hydrogen burning on the WD during the merger (not included in their simulations) may also cause the remnant to swell up and gain more mass from the disk. An independent constraint on the population of He WD–MS merger remnants in the Milky Way may help distinguish these scenarios.

3.6.3 Rapid rotation

While most RG envelopes rotate very slowly, spectroscopic (Carlberg, Majewski, et al., 2011) and photometric (Ceillier et al., 2017) studies have indicated that $\sim 2\%$ of RGs are rapidly rotating ($v \sin i \gtrsim 10 \text{ km s}^{-1}$, or $v/v_{\text{crit}} \gtrsim 7\%$ for typical values $M \sim M_{\odot}$ and

$R \sim 10R_{\odot}$), likely as a result of stellar interactions such as mergers. The He WD–MS merger remnants discussed in this work may also rotate rapidly enough for rotation measurements to serve as an orthogonal diagnosis for their binary origin.

The merger occurs when the MS component of the close binary overflows its Roche lobe. Very roughly, this occurs at a semimajor axis $a \sim 3R_{\text{MS}} \sim 3R_{\odot}(M_{\text{MS}}/M_{\odot})^{0.8}$, according to the traditional mass–radius scaling formula for the MS. At the time of merger, the total binary has an orbital angular momentum

$$L = M_{\text{MS}}M_{\text{WD}}\sqrt{\frac{Ga}{M}} \quad (3.12)$$

where $M_{\text{tot}} = M_{\text{MS}} + M_{\text{WD}}$ (and we have assumed a circular orbit). Then, assuming that no mass is lost during the merger, the final envelope spin rate of the resulting RG remnant is

$$\begin{aligned} \Omega_{\text{env}} \sim & 3.8 \mu\text{Hz} \times \left(\frac{\kappa}{0.2}\right)^{-1} \left(\frac{M_{\text{MS}}}{0.5M_{\odot}}\right)^{0.4} \left(\frac{M_{\text{WD}}}{0.3M_{\odot}}\right) \\ & \times \left(\frac{M}{0.8M_{\odot}}\right)^{-1/2} \left(\frac{R}{20R_{\odot}}\right)^{-2} \end{aligned} \quad (3.13)$$

where we have scaled the moment of inertia of the merger remnant’s envelope to $\kappa = I/M_{\text{MS}}R^2 = 0.2$ (as in, e.g., Bear and Soker, 2010).

This corresponds to rotation periods ~ 20 days, more than half the surface breakup frequency $\Omega_K = \sqrt{GM/R^3} \sim 6.2 \mu\text{Hz}$, depending on the inflated radius of the remnant. This is much faster than the rotation rate of typical RG stars at similar radii: rapid rotation (without associated radial velocity variability) and associated magnetic activity can therefore help distinguish merger remnants.

However, Equation 3.13 gives an estimate of the envelope rotation rate very soon (roughly a thermal time) after the merger. The subsequent evolution of the rotation profile is strongly dependent on the physics of magnetic braking (which saps angular momentum from the system) and angular momentum transport (which couples the core and envelope rotation rates). Both of these pieces of physics are not particularly well understood (especially in the context of fast-rotating RGs), and models which incorporate both of these effects are necessary for predicting the long-term evolution of core and envelope rotation rates of merger remnants (Qian et al., in preparation).

Throughout this work, we have neglected rotation-induced mixing processes (Zahn, 1994; Talon et al., 1997; Mathis and Zahn, 2004; Zahn, 2010; Park et al., 2020) which may be important in a rapidly rotating merger remnant. Our predictions for the amount of helium and other species mixed into the envelope and brought to the surface during a core dredge-up event should thus be considered lower limits.

3.6.4 Non-asymptotic effects on pulsations

Both Equations 3.3 and 3.4 for $\Delta\nu$ and $\Delta\Pi$ rely on the *asymptotic* approximation for stellar oscillations, i.e., that the radial wavelength of the oscillation is much smaller than the scale height of any structural variable. While the asymptotic approximation is well-justified for most RGs (see, e.g., the introductory discussion of Ong and Basu, 2020), merger remnants may possess sharp features in their profiles (glitches) which may cause departures from the asymptotic formulae. Indeed, such glitches are observed in a small fraction of CHeB red giants (Vrard, Cunha, et al., 2022a).

Although we eschew a comprehensive analysis of non-asymptotic effects in this work, we point out three possible glitches which may occur in He WD–MS merger remnants:

1. Soon after merger, the Brunt–Väisälä frequency rises sharply with radius at the interface between the He WD and hydrogen-burning shell. In intermediate-mass MS stars, a similar spike in N near the convective core can produce variations in $\Delta\Pi$ versus P whose “period” in this space is a function of the buoyancy coordinate of the glitch (Miglio, Montalbán, Noels, et al., 2008; Pedersen et al., 2018). Given the low-entropy state of the core and the short-lived nature of the entropy discontinuity, it remains to be seen whether this buoyancy feature is detectable.
2. In merger remnants, more intense helium flashes quickly burn larger fractions of helium into carbon. This enhances the composition gradient between helium flash-processed material and outer layers of the helium core. This may produce an abnormally strong compositional peak in N during the CHeB phase, which may manifest as an observable buoyancy glitch.
3. At the He I and He II ionization zones, the first adiabatic exponent dips abruptly, producing sharp features in the sound speed (e.g., Miglio, Montalbán, Carrier, et al., 2010). Notably, the amplitudes of these acoustic glitches increase with higher helium mass fraction Y (Houdek and Gough, 2007). During the CHeB phase of our models, Y can be enhanced to extreme degrees (Section 3.4), and it is possible that the effect of these acoustic glitches may be very strong.

Detailed mode calculations are likely required to determine whether these glitches are observable, what their characteristics are in the oscillation spectrum, and to what extent they can be used to identify and characterize merger remnants.

Our predictions for the large frequency spacing $\Delta\nu$ relies on the scaling relations in Equation 3.3, which is known to require corrections when the outer layers deviate from homology to

a calibration standard (Belkacem et al., 2013; Ong and Basu, 2019). This may be slightly modified in merger remnants by changes in surface composition or rapid rotation, and should be investigated in the future.

3.6.5 Broader progress in binary interaction asteroseismology

Due to the diversity of stellar interactions expected to occur in the field, other post-merger stellar structures and their asteroseismic signatures deserve future investigation, in particular:

- *RG–He WD mergers* likely produce unusual CHeB giants, which have been previously explored as a possible channel for producing certain classes of carbon stars (Izzard et al., 2007; Zhang and Jeffery, 2013; Zhang, Jeffery, Li, et al., 2020) and as possible progenitors of the 8 UMi planetary system (Hon, Huber, Rui, et al., 2023) and CK Vulpeculae, a historical transient observed in the year 1670 which is now a bipolar nebula (Tylenda, Kamiński, et al., 2024). The models of Zhang and Jeffery (2013) suggest that these merger remnants behave like overluminous CHeB stars, similar to those described in Section 3.4.1 for the He WD–MS scenario (compare their Figure 4 to our Figure 3.3).
- *CO WD–MS mergers* are likely to result from consequential angular momentum loss, particularly for lower-mass CO WDs. While existing modeling literature typically focuses on progenitor systems’ nova eruptions (Iben and Tutukov, 1996; Shara, Yaron, et al., 2010; Kato et al., 2017) or their role in producing Type Ia supernovae (Kovetz and Prialnik, 1994; Cassisi, Iben, et al., 1998; Newsham et al., 2014; Hillman et al., 2016; Wang, 2018), mergers of such remnants should become unusual asymptotic giant branch stars with highly degenerate cores (Cassisi, Iben, et al., 1998; Piersanti et al., 2000; Wolf et al., 2013), with possibly observable consequences.
- *CO WD–He WD mergers* are the likely progenitors of *R Coronae Borealis stars* (*R Cor Bor* stars), which are yellow supergiants consisting of a carbon–oxygen core surrounded by a helium envelope inflated by shell burning (Clayton et al., 2007; Menon et al., 2013). *R Cor Bor* stars are known to pulsate at periods between 40 and 100 d (Lawson and Kilkenny, 1996; Karambelkar et al., 2021), making asteroseismology a promising tool for probing their internal structures (Wong and Bildsten, 2024).
- Last year, Bellinger, Mink, et al. (2024) identified asteroseismology as a tool for testing the post-MS merger channel for producing *blue supergiants*, finding that the g-mode period spacing $\Delta\Pi$ constrains their formation channels. In a parallel

observational study using TESS, Ma, Johnston, et al. (2024) discovered a peculiar but universal low-frequency ($f \lesssim 2 \text{ d}^{-1}$) photometric power excess, although the physical nature of these oscillations remains unclear, and the authors were unable to observe individual modes or measure $\Delta\Pi$.

Binary interaction asteroseismology is a technique at its infancy, with likely many more fruitful directions.

3.7 Summary

In this work, we presented detailed models of merger remnants of He WD–MS mergers. Merger remnants quickly initiate hydrogen shell burning and become unusual giant stars which may hide inside the RG population. However, they exhibit a number of unique signatures which may be used to distinguish them. In summary, during hydrogen shell-burning (RGB), merger remnants:

1. are over-inflated at a given core mass.
2. depart from the standard degenerate sequence on the asteroseismic $\Delta\nu$ – $\Delta\Pi$ diagram. Asteroseismology can thus identify remnants whose mixed-mode coupling is sufficiently strong.
3. undergo delayed helium flashes, and attain higher luminosities at the tRGB than do single RGs.

During helium core burning (CHeB), remnants of mergers involving lower-mass He WDs:

1. attain core masses which are essentially typical for single CHeB stars.
2. are strong candidates for the undermassive red clump stars discovered by Li, Bedding, Murphy, et al. (2022) and Matteuzzi et al. (2023).

Remnants of mergers involving higher-mass He WDs dredge up a significant fraction (up to $\sim 0.1 M_\odot$) of helium into the envelope. During core helium burning, these post-dredge-up merger remnants:

1. have significantly larger radii and luminosities than single stars on the red clump.
2. exhibit a wider range of asteroseismic g-mode period spacings $\Delta\Pi$ than do typical stars on the red clump.

3. attain abnormally strong degrees of asteroseismic mixed-mode coupling towards the end of CHeB.
4. are enriched in ^{12}C , as well as ^{18}O and ^{22}Ne .
5. may already have been discovered. The rapidly rotating RG discovered by Ong, Hon, et al. (2024) (“Zvrk”) has many of the predicted properties of this type of merger remnant.

Observational probes of these merger remnants can constrain the He WD–MS merger process at the population level. In turn, this may provide additional confirmation of the consequential angular momentum loss hypothesis and white dwarf mass problem for CVs.

3.A Dependence on the cooling age of the white dwarf

Pre-merger, all of the merger models discussed in the main text use a He WD which has been cooled until it achieves a luminosity $L_{\text{WD}} = 10^{-4.0}L_{\odot}$. This relatively low luminosity is chosen to explore the limiting case of a very degenerate helium core. In our models, this luminosity corresponds to relatively long He WD cooling ages $5 \text{ Gyr} \lesssim t_{\text{cool}} \lesssim 7 \text{ Gyr}$, with a fixed L_{WD} corresponding to longer t_{cool} for He WDs with higher masses M_{WD} or more substantial atmospheres. For comparison, note that the merger remnant models of Zhang, Hall, et al. (2017) use $L_{\text{WD}} = 10^{-2.0}L_{\odot}$.

In this Appendix, we discuss the effect of varying $\log(L_{\text{WD}}/L_{\odot})$. Figure 3.15 shows the evolution of some selected selected quantities for four models (the first three of which also appear in the main text):

1. A non-merged model, which has a “normal” helium core on the RGB which is close to isothermal with the hydrogen-burning shell.
2. A merger remnant with $\log(L_{\text{WD}}/L_{\odot}) = -4.0$ and $M_{\text{WD}} = 0.30M_{\odot}$.
3. A merger remnant with $\log(L_{\text{WD}}/L_{\odot}) = -4.0$ and a *lower-mass* $M_{\text{WD}} = 0.27M_{\odot}$.
4. A merger remnant with a *higher pre-merger He WD luminosity* $\log(L_{\text{WD}}/L_{\odot}) = -2.5$ and $M_{\text{WD}} = 0.30M_{\odot}$. This value of $\log(L_{\text{WD}}/L_{\odot})$ corresponds to a He WD cooling age $t_{\text{cool}} \approx 550 \text{ Myr}$.

All models have total masses of $M = 0.80M_{\odot}$ and WD atmospheres of mass $10^{-4}M_{\odot}$, and respectively.

As described in Section 3.3, merger remnants during the RGB will start with initially low-entropy cores, but their entropies will gradually grow due to heat diffusion and deposition of higher-entropy helium resulting from hydrogen burning. The degree of entropy deficit in the core therefore results from a combination of the entropy of the original He WD as well as its mass, which determines its total heat capacity). Because increasing $\log(L_{\text{WD}}/L_{\odot})$ and decreasing M_{WD} affect this core entropy deficit in the same way, merger remnants should be affected by increases in $\log(L_{\text{WD}}/L_{\odot})$ and decreases in M_{WD} in similar ways.

Figure 3.15 shows the evolution of the models listed above. They all have comparable radii on the RGB, but $\Delta\Pi$ (reflecting the internal thermal structure of the core) varies somewhat between them. As can be seen on the *bottom left* panel of Figure 3.15, the core temperature T_c of the $M_{\text{WD}} = 0.27M_{\odot}$, $\log(L_{\text{WD}}/L_{\odot}) = -4.0$ model initially behaves very similarly to the $M_{\text{WD}} = 0.30M_{\odot}$, $\log(L_{\text{WD}}/L_{\odot}) = -4.0$ model, since not enough time has yet elapsed for conduction to significantly modify its temperature. Later on, T_c in the $M_{\text{WD}} = 0.27M_{\odot}$ model takes a sharp upturn to more closely resemble the warmer $M_{\text{WD}} = 0.30M_{\odot}$, $\log(L_{\text{WD}}/L_{\odot}) = -2.5$ model. By the helium flash, these two models have very similar $\Delta\Pi$ and temperature profiles.

Once the helium flash occurs, variations in the temperature profile due to a finite thermal conductivity in the core are erased entirely. During the CHeB phase, the $M_{\text{WD}} = 0.27M_{\odot}$, $\log(L_{\text{WD}}/L_{\odot}) = -4.0$ and $M_{\text{WD}} = 0.30M_{\odot}$, $\log(L_{\text{WD}}/L_{\odot}) = -2.5$ models are essentially identical (*right* panels of Figure 3.15). Both models evolve significantly differently than the $M_{\text{WD}} = 0.3M_{\odot}$, $\log(L_{\text{WD}}/L_{\odot}) = -4.0$ model (which had a larger entropy deficit on the RGB).

In summary, decreasing the cooling age of the merging He WD has a very similar effect to slightly decreasing its mass. Hence, the merger models in the main text are expected to behave similarly to merger models with younger and slightly more massive WDs.

3.B Thermal timescale of the core

In this Appendix, we estimate the timescale $\tau_{\text{th,core}}$ for a cold, highly degenerate remnant core to thermalize with a hot burning shell. In this environment, electron-mediated heat conduction is the dominant heat transport mechanism.

The resulting heat flux \vec{q} takes the form

$$\vec{q} = -\alpha_{\text{cond}}\rho T \nabla T \quad (3.14)$$

where

$$\alpha_{\text{cond}} \approx 2.44 \times 10^3 A Z^{-2} \text{ cm}^4 \text{ s}^{-3} \text{ K}^{-2}, \quad (3.15)$$

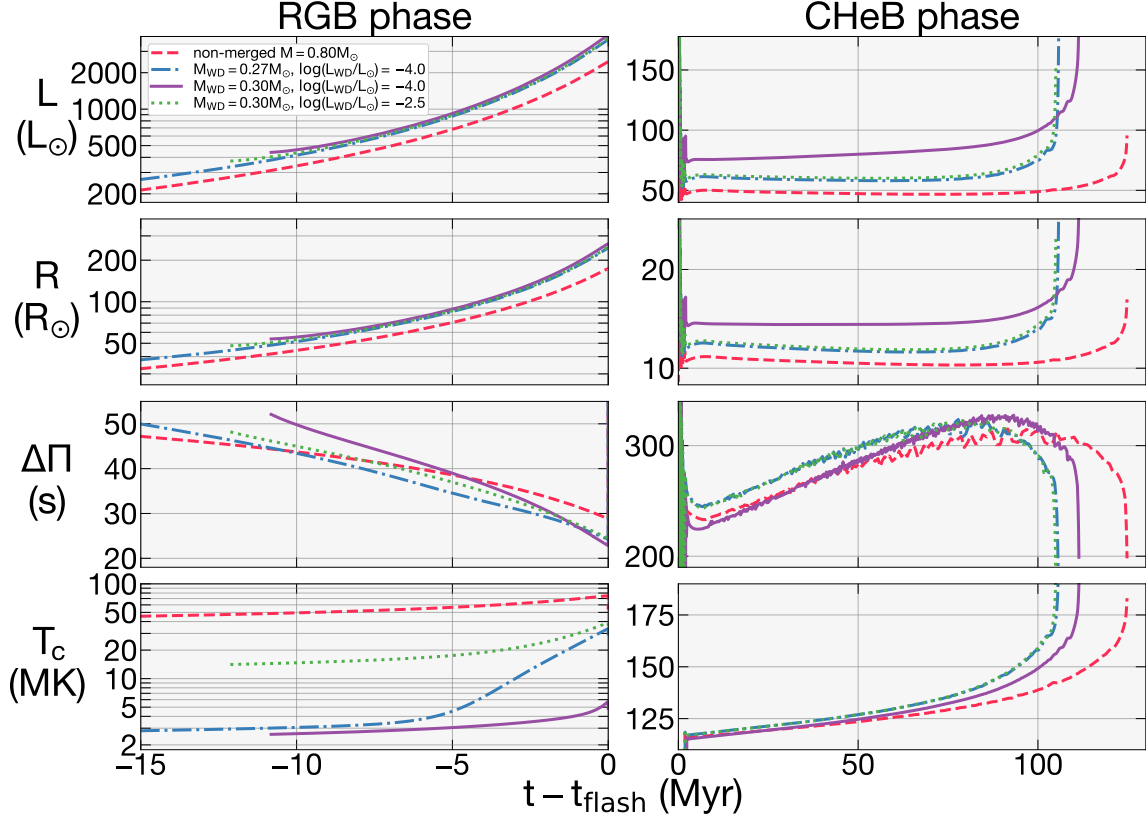


Figure 3.15: The total luminosity L , radius R , asteroseismic g -mode period spacing $\Delta\Pi$, and central temperature T_c for selected models during the RGB (*left*) and CHeB (*right*) phases. A model with $M_{\text{WD}} = 0.30M_{\odot}$ but a brighter He WD ($\log(L_{\text{WD}}/L_{\odot}) = -2.5$) is included.

see Mestel (1950). The heat capacity per unit volume is dominated by the non-degenerate ions:

$$c_v \approx \frac{\varepsilon}{T} \approx \frac{3\rho k_B}{2Am_p}. \quad (3.16)$$

In the absence of heat sources, the continuity equation for energy density ε within the interior of the WD is thus given by

$$\frac{\partial \varepsilon}{\partial t} = -\nabla \cdot \vec{q}. \quad (3.17)$$

Substituting Equations 3.14 and 3.16 into Equation 3.17 yields the following nonlinear heat diffusion equation:

$$\frac{\partial T}{\partial t} = \frac{\kappa}{r^2} \frac{\partial}{\partial r} \left(r^2 T \frac{\partial T}{\partial r} \right), \quad (3.18)$$

cf. Mestel (1952). In writing Equation 3.18, we have assumed spherical symmetry, and that ρ does not vary with temperature. The diffusion coefficient κ is given by

$$\kappa = \frac{2Am_p\alpha_{\text{cond}}}{3k_B}. \quad (3.19)$$

At early times, the core is essentially isothermal at a low temperature $T_0 \ll T_{\text{shell}} \simeq 3 \times 10^7$ K. Thermal contact with the hot hydrogen-burning shell at the outer boundary sets up a temperature gradient $\partial T / \partial r \sim T_{\text{shell}} / R_c$. The natural length scale of the problem is R_c . By Equation 3.18, the core therefore thermalizes on a timescale $\tau_{\text{th,core}}$ given roughly by

$$\frac{1}{\tau_{\text{th,core}}} \sim \frac{\kappa T_{\text{shell}}}{R_c^2} \quad (3.20)$$

or

$$\tau_{\text{th,core}} \sim \frac{3k_B}{2Am_p\alpha_{\text{cond}}} \frac{R_c^2}{T_{\text{shell}}} \approx 80 \text{ Myr} \times \left(\frac{R_c}{0.035R_\odot} \right)^2 \left(\frac{T_{\text{shell}}}{3 \times 10^7 \text{ K}} \right)^{-1} \left(\frac{Z}{2} \right)^2 \left(\frac{A}{4} \right)^{-2}. \quad (3.21)$$

A similar timescale to $\tau_{\text{th,core}}$ has been previously derived by Shen, Idan, et al. (2009). The scaling relation in Equation 3.21 is normalized to a typical He WD in thermal contact with a typical hydrogen-burning shell. This timescale is comparable to the length of the remnant’s RGB phase—the longest RGB phase leading to helium ignition in our merger remnant models lasts $\simeq 180$ Myr (for a He WD mass $M_{\text{WD}} = 0.20M_\odot$). Heat conduction thus cannot completely destroy the low-entropy state of the core quickly enough to erase its long-term effects on the appearance and evolution of the remnant, especially for higher values of M_{WD} .

3.C Brunt–Väisälä frequency in degenerate helium cores

In this Appendix, we derive the Brunt–Väisälä frequency N in the part of the g-mode cavity which lies within the helium core of a star on the RGB. This region is characterized by degenerate electrons which dominate the pressure support and non-degenerate ions which dominate the heat capacity.

Following Brassard, Fontaine, Wesemael, Kawaler, et al. (1991), in the absence of composition gradients, N can be written as

$$N^2 = N_0^2 \frac{\chi_T}{\chi_\rho} (\nabla_{\text{ad}} - \nabla) \quad (3.22)$$

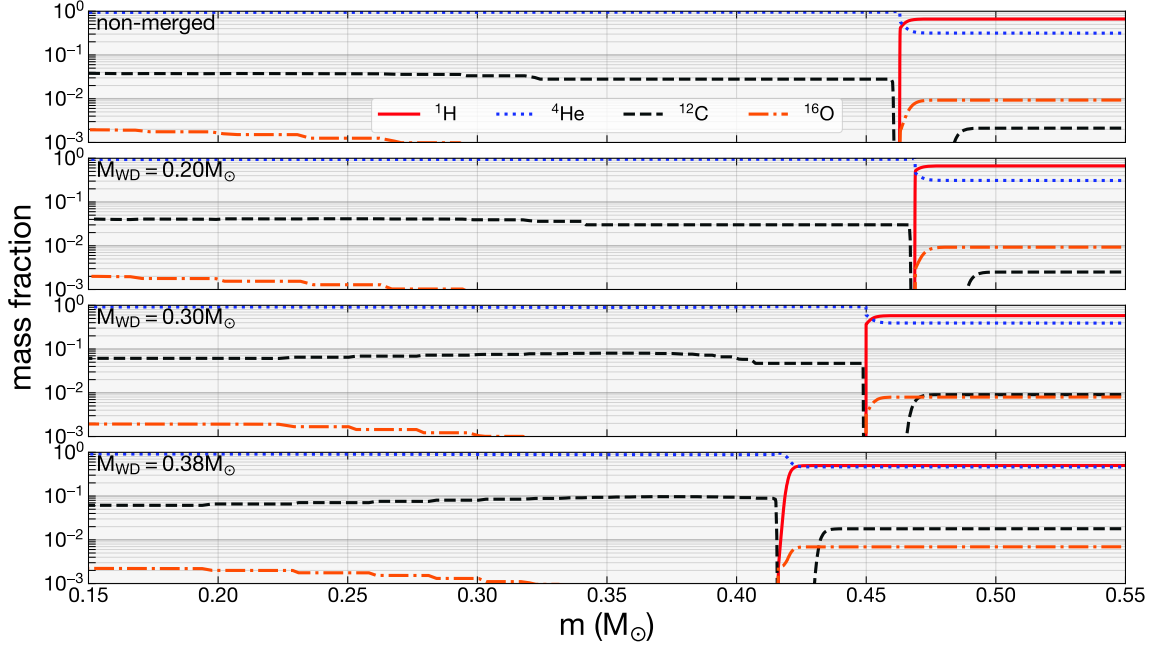


Figure 3.16: Composition profiles for the non-merged $M = 0.80M_{\odot}$ and selected merger remnant models at the beginning of CHeB (a few megayear after the helium flash).

where

$$\chi_T = \left(\frac{\partial \ln p}{\partial \ln T} \right)_{\rho} \quad (3.23a)$$

$$\chi_{\rho} = \left(\frac{\partial \ln p}{\partial \ln \rho} \right)_T \quad (3.23b)$$

$$\nabla_{\text{ad}} = \left(\frac{d \ln T}{d \ln p} \right)_{\text{ad}} \quad (3.23c)$$

$$\nabla = \frac{d \ln T}{d \ln p} \quad (3.23d)$$

and we have defined

$$N_0^2 = \frac{\rho g^2}{p} \quad (3.24)$$

where roughly $N_0 \simeq \sqrt{GM_c/R_c^3}$ is comparable to the dynamical frequency of the core.

In degeneracy-supported matter, $\chi_{\rho} \approx 5/3$ and $\nabla_{\text{ad}} \approx 0.4$ are basically constant. In WDs, the pressure has two contributions from the degenerate electrons (which dominate the total pressure) and non-degenerate ions (which carry the temperature dependence):

$$p = \frac{2}{5} n_e E_F + n_i k_B T \quad (3.25)$$

where $n_e = Z\rho/Am_p$ and $n_i = \rho/Am_p$ are the electron and ion number densities, respectively, and E_F is the electronic Fermi energy. Roughly

$$p \approx \frac{2}{5} \frac{Z\rho E_F}{Am_p} \quad (3.26a)$$

$$\left(\frac{\partial p}{\partial T} \right)_\rho \approx \frac{\rho k_B}{Am_p}. \quad (3.26b)$$

Then

$$\chi_T = \frac{T}{p} \left(\frac{\partial p}{\partial T} \right)_\rho = \frac{5}{2Z} \frac{k_B T}{E_F}. \quad (3.27)$$

Therefore, for mostly degenerate matter,

$$N^2 \approx N_0^2 \frac{k_B T}{Z E_F} \left(1 - \frac{5}{2} \nabla \right). \quad (3.28)$$

3.D Post-helium flash composition profiles

Figure 3.16 compares the composition profiles for various merger remnants at the beginning of CHeB, soon after the helium flash. As explained in Section 3.4, merger remnants involving more massive He WDs (higher M_{WD}) convert a larger fraction of their core helium into carbon during the helium flash. Moreover, our merger remnant models with $M_{WD} \geq 0.27M_\odot$ (e.g., the *bottom* two panels of Figure 3.16) undergo core dredge-up events which mix some of the helium core into the envelope. Such merger remnants therefore begin CHeB with lower core masses and possess envelopes which are dramatically enhanced in species such as helium and carbon (see Section 3.4.4).

Chapter 4

GRAVITY WAVES IN STRONG MAGNETIC FIELDS

Rui, N. Z. and J. Fuller (2023). “Gravity waves in strong magnetic fields.” In: *Monthly Notices of the Royal Astronomical Society* 523.1, pp. 582–602. doi: 10.1093/mnras/stad1424. arXiv: 2303.08147.

Strong magnetic fields in the cores of stars are expected to significantly modify the behavior of gravity waves: this is likely the origin of suppressed dipole modes observed in many red giants. However, a detailed understanding of how such fields alter the spectrum and spatial structure of magnetogravity waves has been elusive. For a dipole field, we analytically characterize the horizontal eigenfunctions of magnetogravity modes, assuming that the wavevector is primarily radial. For axisymmetric modes ($m = 0$), the magnetogravity wave eigenfunctions become Hough functions, and they have a radial turning point for sufficiently strong magnetic fields. For non-axisymmetric modes ($m \neq 0$), the interaction between the discrete g mode spectrum and a continuum of Alfvén waves produces nearly discontinuous features in the fluid displacements at critical latitudes associated with a singularity in the fluid equations. We find that magnetogravity modes cannot propagate in regions with sufficiently strong magnetic fields, instead becoming evanescent. When encountering strong magnetic fields, ingoing gravity waves are likely refracted into outgoing slow magnetic waves. These outgoing waves approach infinite radial wavenumbers, which are likely to be damped efficiently. However, it may be possible for a small fraction of the wave power to escape the stellar core as pure Alfvén waves or magnetogravity waves confined to a very narrow equatorial band. The artificially sharp features in the WKB-separated solutions suggest the need for global mode solutions which include small terms neglected in our analysis.

We thank Daniel Lecoanet, Yuri Levin, Sterl Phinney, Janosz Dewberry, Joel Ong, and Saul Teukolsky for their helpful advice and comments. N.Z.R. acknowledges support from the National Science Foundation Graduate Research Fellowship under Grant No. DGE-1745301. J.F. is thankful for support through an Innovator Grant from The Rose Hills Foundation, and the Sloan Foundation through grant FG-2018-10515. We thank the anonymous referee for their thorough review and helpful suggestions, which greatly improved the work.

4.1 Introduction

Stellar magnetism is a highly impactful, but often neglected, property of many main sequence stars (Ferrario, Pringle, et al., 2009; Vidotto et al., 2014), red giants (García, Hernández, et al., 2014; Stello, Cantiello, Fuller, Garcia, et al., 2016; Stello, Cantiello, Fuller, Huber, et al., 2016; Fuller, Cantiello, et al., 2015), white dwarfs (Angel, 1977; Wickramasinghe and Ferrario, 2000; Liebert et al., 2003), and neutron stars (Thompson and Duncan, 1993; Kulkarni and Thompson, 1998; Levin, 2006) alike. In stars, such magnetic fields are expected to originate from dynamo mechanisms (Baliunas et al., 1996; Spruit, 2002; Maeder and Meynet, 2005; Brun and Browning, 2017), as fossils leftover from the star’s formation (Braithwaite and Spruit, 2004; Dudorov and Khaibrakhmanov, 2015; Ferrario, Melatos, et al., 2015), or from stellar mergers (Ferrario, Pringle, et al., 2009; Tutukov and Fedorova, 2010; Wickramasinghe, Tout, et al., 2014; Schneider, Ohlmann, Podsiadlowski, Röpke, Balbus, Pakmor, and Springel, 2019). Despite the importance and ubiquity of strong stellar magnetism, our understanding of oscillations in such highly magnetized stars remains incomplete, even at the qualitative level.

Interest in the influence of magnetic fields on nonradial stellar oscillations has been reignited in the past few years by the discovery of suppressed dipole ($\ell = 1$) and quadrupole ($\ell = 2$) oscillation modes in a family of red giants (Mosser, Elsworth, et al., 2012; García, Hernández, et al., 2014; Stello, Cantiello, Fuller, Garcia, et al., 2016; Stello, Cantiello, Fuller, Huber, et al., 2016; Mosser, Belkacem, et al., 2017). It is largely believed that the origin of this phenomenon is magnetic in nature, with recent work suggesting that ingoing gravity waves can damp out after either being trapped inside the core (the “magnetic greenhouse effect,” Fuller, Cantiello, et al., 2015), refracted into high-wavenumber oscillations (Lecoanet, Vasil, et al., 2017), or dissipated by Alfvén waves (Loi and Papaloizou, 2017). In parallel, Li, Deheuvels, Ballot, and Lignières (2022) have made the first-ever constraints on the interior magnetic field *topology*—the recent development of such new powerful observational tools further demands proportionate advances in our theoretical understanding of internal magnetogravity waves.

Efforts to understand the impact of magnetic fields on stellar oscillation modes have taken many forms, but have been limited due to the difficulty of the problem. For example, early attempts to understand magnetic effects on non-radial oscillations involved introducing a magnetic field as a small perturbation (e.g., Goossens, 1972; Goossens et al., 1976; Goossens, 1976; Mathis, Bugnet, et al., 2021). Some of these perturbative calculations have promisingly suggested that core magnetic fields may leave imprints on the mixed-mode period spacing (Prat, Mathis, Buysschaert, et al., 2019; Prat, Mathis, Neiner, et al., 2020a;

Bugnet et al., 2021; Bugnet, 2022), in addition to their impact on dipole mode visibilities. However, magnetic mode splittings are often small except for fields large enough to strongly couple with Alfvén waves, where a perturbative treatment is largely inappropriate (Cantiello et al., 2016). While other analyses have assumed a purely horizontal field (Rogers and MacGregor, 2010; Mathis and De Brye, 2011; MacGregor and Rogers, 2011; Dhouib, Mathis, et al., 2022), such studies are not applicable to the general case where the radial component of the field dominates the interaction with the gravity waves. Fuller, Cantiello, et al. (2015) used a Wentzel–Kramers–Brillouin (WKB) approximation in both components of the wavenumber to show that magnetogravity waves are forced to be evanescent when the mode frequency lies below a characteristic frequency given by

$$\omega_B = \left(\frac{\ell(\ell+1)B_0^2 N^2}{\pi \rho_0 r^2} \right)^{1/4}, \quad (4.1)$$

where ℓ , B_0 , N , ρ_0 , and r are the angular degree, radial magnetic field, Brunt–Väisälä frequency, density, and radius, respectively. This result can also be recovered exactly when considering the coupling of gravity waves to an exactly uniform radial field geometry (see Section 4.62). However, while setting a useful scale for strong coupling between gravity waves and the magnetic field, this analysis relies on the assumption that the radial magnetic field is uniform at a given radius (which is not physical).

Other studies have probed the behavior of magnetogravity waves under arbitrarily complicated magnetic field geometries using a flexible ray-tracing method (Loi and Papaloizou, 2018; Loi, 2020c; Loi, 2020b). However, crucially, this method relies heavily upon the (WKB) approximation that both the radial *and* horizontal components of the wavenumber are large compared to the variation scales of the magnetic field and stellar structure. In reality, the horizontal wavenumber $k_h = \sqrt{\ell(\ell+1)}/r$ of the observable $\ell \lesssim 3$ modes likely has a comparable length scale to that of the magnetic field gradient. It is clear that a fuller understanding of magnetogravity waves must account for a magnetic field which is allowed to vary with latitude and longitude, without assuming an unrealistically large horizontal wavenumber.

Some progress on this front was made by Lecoanet, Vasil, et al. (2017), who solve for the eigenmodes of a two-dimensional Cartesian analogue of a multipole magnetic field geometry, demonstrating that modes in their model cannot propagate in regions whose magnetic field exceeds a critical strength (see Section 4.A.2) close to the estimate of Equation 4.1. However, since their analysis cannot capture modes which propagate horizontally relative to the field (i.e., non-axisymmetric modes), the possibility is left open that such non-axisymmetric modes may propagate deeper into a star. Later, Lecoanet, Bowman, et al.

(2022) extended this analysis numerically to more general tesseral/sectoral ($m \neq 0$) modes using the `DEDALUS` code in order to probe the interior field of a main sequence B-type star HD 43317. However, explanations for many qualitative properties of the solution have heretofore remained elusive. In this work, we analyze the horizontal structure of g modes under a strong magnetic field. We assume that the wavevector is primarily radial, and the radial wavelengths of the perturbations are much smaller than the stellar structure length scale (the radial WKB approximation), and numerically solve for the magnetogravity mode eigenfunctions. We find that such g modes contain sharp features in the fluid displacements at the locations of resonances with Alfvén waves (so-called “critical latitudes”), and that the general structure of their branches and eigenfunctions are sensitive to even vanishingly small amounts of dissipation. We also discuss the importance of the horizontal component of the field near these critical latitudes, as well as near the equator. Nevertheless, we still find that g modes cannot propagate arbitrarily deep in sufficiently magnetized stars, and are likely converted into outgoing slow magnetic waves that dissipate inside of the star. An outline of the solution described in this work is shown in Figure 4.1.

We organize this paper as follows. In Section 4.2, we describe the problem setup: a stably stratified, magnetized star obeying the incompressible MHD equations (Section 4.2.1), whose essential physics are governed by the relationship between the mode, Alfvén, and magnetogravity frequencies ω , ω_A , and ω_B (Section 4.2.2). For the majority of this work, we specialize to a dipole magnetic field (Section 4.2.3). In the WKB limit, the resulting differential eigenproblem contains singularities at critical latitudes corresponding to resonances with the Alfvén spectrum. We point out a close analogy with the rotational problem (Section 4.3.1), then comment on previous work on internally singular eigenproblems (Section 4.3.2), and lastly investigate the behavior of eigenfunctions around those critical latitudes (Section 4.3.3). In Section 4.4, we present zonal ($m = 0$; Section 4.4.1) and sectoral/tesseral ($m \neq 0$; Section 4.4.2) solutions to the problem. We then comment on the origin and behavior of the continuous Alfvén wave spectrum (Section 4.4.3). However, since vanishingly small dissipation can qualitatively affect the mode spectrum, we present numerical solutions of dissipative solutions in Section 4.5, first allowing for evanescent solutions (Section 4.5.1) and then constraining the radial phase velocity (Section 4.5.2). Finally, in Section 4.6, we discuss the importance of horizontal field terms near the critical latitudes and equator (Section 4.6.1), nonharmonic solutions of singular differential equations (Section 4.6.2), the effects of more general magnetic field geometries (Section 4.6.3), and the possibility of magnetically stabilized g modes in convective zones (Section 4.6.4). Section 4.7 concludes.

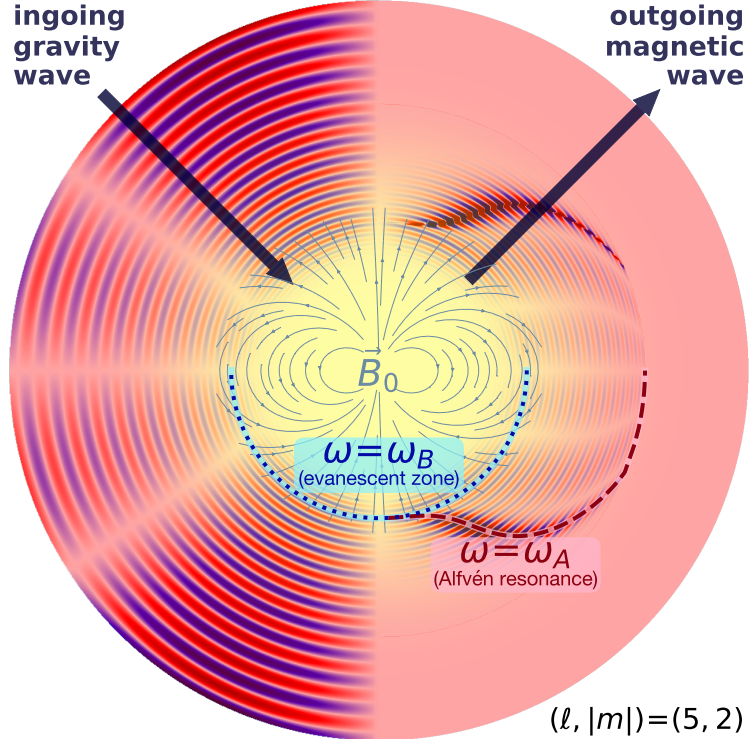


Figure 4.1: A meridional slice of the θ displacement ξ_θ for a magnetogravity mode with $(\ell, |m|) = (5, 2)$, with the left half showing an ingoing gravity wave and the right half showing an outgoing (slow) magnetic wave (calculated in Section 4.5.2), which approaches an infinite wavenumber at a cutoff radius (where it is dissipated). The eigenfunctions become large at the Alfvén resonance $\omega = \omega_A$ ($b \cos \theta = \pm 1$; red dashed line), and they become evanescent past the turning point $\omega = \omega_B$ ($a \sim 1$; blue dotted line), where the solutions are given in Section 4.5.1. This diagram is not to scale, as the stellar profile has been modified to better show the spatial structure of the magnetic wave.

4.2 Problem statement

In this work, we consider a spherically symmetric star in hydrostatic equilibrium, with a possibly large equilibrium magnetic field (which is not spherically symmetric). It is assumed that the magnetic field does not act on the background structure, i.e., it is not strong enough to introduce substantial departures from a spherically symmetric stellar profile. For simplicity, we ignore rotation and use the incompressible and Cowling approximations, such that buoyancy and magnetic forces dominate the dynamics. These forces are likely to dominate in, e.g., the slowly rotating radiative cores of red giants.

Throughout this work, we use the term “magnetogravity wave” to refer to the general phenomenon of a gravity wave propagating through a highly conductive, magnetized fluid. In sufficiently magnetized stars, ingoing magnetogravity waves are refracted outwards, and

(as we will show in Sections 4.4.1, 4.4.2, and 4.5.2) approach infinite radial wavenumber at a finite height—we refer to such waves as “slow magnetic waves.” Such branches are “slow” in the sense that their phase and group velocities approach zero as waves propagate outwards. This medium also sustains “Alfvén waves,” which are confined to magnetic field lines and appear as highly localized, linearly independent toroidal solutions to the fluid equations (see Section 4.4.3).

In this Section, we first introduce the linearized fluid equations (Section 4.2.1). We then identify the most important dimensionless parameters governing the physics (Section 4.2.2). Finally, we specialize to the case of a dipole magnetic field (Section 4.2.3), to which the majority of this work is dedicated.

4.2.1 Linearized fluid equations

The linearized incompressible MHD equations are

$$\nabla \cdot \vec{\xi} = 0 \quad (4.2a)$$

$$\rho_0 \partial_t^2 \vec{\xi} = -\nabla \left(p' + \frac{1}{4\pi} \vec{B}_0 \cdot \vec{B}' \right) - \rho' g \hat{r} + \frac{1}{4\pi} \left(\vec{B}_0 \cdot \nabla \right) \vec{B}' \quad (4.2b)$$

$$\rho' = \frac{\rho_0 N^2}{g} \xi_r \quad (4.2c)$$

$$\vec{B}' = \left(\vec{B}_0 \cdot \nabla \right) \vec{\xi} \quad (4.2d)$$

where $\vec{\xi}$ is the perturbed fluid displacement, while ρ' , p' , and \vec{B}' are the Eulerian density, pressure, and magnetic field perturbations, and 0 subscripts indicate non-perturbed quantities (Proctor and Weiss, 1982). Here, N is the Brunt–Väisälä frequency, and $g = g(r)$ is the inward gravitational acceleration. Here, we have assumed the WKB approximation in the radial direction *only*, and have made the Cowling approximation ($g' \approx 0$). Additionally, as implied by Equation 4.2c, we only consider adiabatic oscillations. Equation 4.2d is simply the induction equation in ideal magnetohydrodynamics, written in the WKB limit (for \vec{B}_0 varying radially on a length scale $\sim r$). Throughout this paper, we will focus on solving for oscillation modes with harmonic time dependence, i.e., those with $\propto e^{i\omega t}$ (although this assumption is discussed in Section 4.6.2).

Describing an incompressible fluid under ideal magnetohydrodynamics, these equations admit modes which are restored by buoyancy and magnetism (i.e., there are no acoustic waves). Gravity waves are expected to have large radial wavenumbers which are much larger than both their horizontal wavenumbers ($k_r/k_h \sim N/\omega \sim 10^2$ in typical red giant cores) and the star’s structural variation scale $1/H$. However, the horizontal wavenumber $k_h \simeq \sqrt{\ell(\ell+1)}/r$, so low- ℓ magnetogravity modes vary horizontally on similar length

scales to large-scale magnetic fields. Therefore, we have adopted a WKB approximation in the radial direction only (i.e., $\partial/\partial r \approx -ik_r$) such that k_r is assumed to be larger than any structural gradients.

We define the Alfvén frequency $\omega_A = \vec{k} \cdot \vec{v}_A$, where $\vec{v}_A = \vec{B}_0/\sqrt{4\pi\rho_0}$ is the Alfvén velocity. Then the assumption that $k_r \gg k_h$ entails that $\omega_A \propto (\vec{B} \cdot \vec{k}) = B_r k_r + B_h k_h \simeq B_r k_r$, such that the horizontal component of the magnetic field is unimportant as long as B_r and B_h are comparable. This approximation is made by Fuller, Cantiello, et al. (2015), and is very analogous to the “traditional approximation of rotation” (see Section 4.3.1). We discuss the importance of B_h terms in Section 4.6.1.

When a WKB approximation is made in both the vertical and horizontal directions (or if a monopolar field is considered; Appendix 4.A), the dispersion relation is given by

$$\omega^2 - \frac{k_h^2}{k_r^2} N^2 - k_r^2 v_A^2 = 0 \quad (4.3)$$

where $v_A = |v_{A,r}|$ is the radial component of the Alfvén velocity (Unno, Osaki, Ando, Saio, et al., 1989). If both buoyancy and magnetism are important, all three terms in Equation 4.3 are of the same order. This defines a hierarchy of variables: letting ϵ be a small quantity around which we implicitly expand, we see that, if $\omega, k_h \sim \mathcal{O}(1)$, then $N, k_r \sim \mathcal{O}(\epsilon^{-1})$ are “large” and $v_A \sim \mathcal{O}(\epsilon)$ is “small.” Hereafter, we only retain terms leading-order in ϵ , which is realistic as long as $k_r \gg k_h$.

4.2.2 Important frequency scales

To understand the nature of this magnetogravity problem, we can non-dimensionalize the relevant physics equations. All formulations of the magnetogravity problem (see, e.g., Appendix 4.A) that make similar assumptions to ours can be formulated as the following horizontal eigenproblem at a given radius (see Section 4.6.3):

$$\mathcal{L}^{k_r v_A / \omega} p' + \left(\frac{\omega^2}{N^2} r^2 k_r^2 \right) p' = 0 \quad (4.4)$$

where $\mathcal{L}^{k_r v_A / \omega}$ is some geometry-dependent differential operator that depends on the ratio of the Alfvén frequency $\omega_A \sim k_r v_A$ to the mode frequency ω . In Equation 4.4, v_A is a measure of the the Alfvén velocity at a given radius. Although the magnetic field strength clearly varies as a function of θ and ϕ , hereafter we use v_A to denote its *maximum* value at a given radius.

The Buckingham π theorem (Vaschy, 1892; Federman, 1911; Riabouchinsky, 1911; Buckingham, 1914) states that, for some equations depending on p dimensionful quantities in q

independent dimensions, those equations can be written in terms of $p - q$ dimensionless quantities which completely determine their behavior. In this particular problem, Equation 4.4 depends on the $p = 5$ dimensionful quantities ω , N , k_r , and r , and v_A over the $q = 2$ independent dimensions, length and time. Therefore, the essential behavior of the magnetogravity problem can be understood by understanding the interaction of $p - q = 3$ dimensionless quantities.

One natural dimensionless quantity to construct is rk_r , the radial wavenumber rescaled to the characteristic length scale of the star. Fortunately, because $rk_r \gg 1$ according to the radial WKB approximation, the non-dimensionalized version of Equation 4.4 will not actually depend on this quantity. Next, because $\mathcal{L}^{k_r v_A / \omega}$ depends only on the combination $k_r v_A / \omega$ (which describes the presence/location of resonances between modes and Alfvén waves), it is natural to choose this to be another dimensionless quantity:

$$b = \frac{k_r v_A}{\omega} \simeq \frac{\omega_A}{\omega}. \quad (4.5)$$

Finally, if one seeks to non-dimensionalize Equation 4.4 using a third quantity which does not depend on the spatial structure of the mode itself (i.e., independent of k_r), the remaining dimensionless quantity must depend solely on some “depth parameter” a , given by

$$a = \left(\frac{N}{\omega} \right) \left(\frac{v_A / r}{\omega} \right). \quad (4.6)$$

We refer to a as a depth parameter because N and v_A often increase with depth in stars such as red giants, so we expect a to increase with depth. It is possible that a could reach a maximum at some finite radius which would admit a weakly magnetized inner region. In practice, this inner region will be nearly decoupled from the rest of the star by an evanescent region and will be effectively unobservable, except for finely tuned frequencies. In a red giant, N^2 peaks near the H-burning shell, where the value of a will likely peak as well.

In the terminology of Fuller, Cantiello, et al. (2015), $a \sim \omega_B^2 / \omega^2$ where

$$\omega_B \sim \sqrt{N v_A / r} \quad (4.7)$$

is the magnetogravity frequency, below which modes cannot be spatially propagating. We thus argue that the frequency scale ω_B defining strong magnetogravity waves (identified by Fuller, Cantiello, et al. 2015 under some specific assumptions) arises as the most natural mode-independent frequency scale in the problem.

Adopting b and a as our dimensionless parameters, Equation 4.4 can be rewritten as

$$\mathcal{L}^b p' + \frac{b^2}{a^2} p' = 0. \quad (4.8)$$

For the hierarchy of variables adopted in Section 4.2.1, we see that both a and b are of order unity within the domain of interest, where magnetic forces and buoyancy forces are comparable. Consequently, when non-dimensionalizing the fluid equations, specifying a (which is independent of k_r) determines the spectrum of allowed b . For a fixed mode frequency ω , the resulting dispersion relation will therefore relate ω_B to the allowed $\omega_A \propto k_r$.

For the remainder of this, we will study the magnetogravity problem in terms of these two dimensionless quantities, which relate the mode (ω), Alfvén (ω_A), and magnetogravity (ω_B) frequencies to each other.

4.2.3 Dipole geometry

We give special attention to the case of a magnetic field whose radial component is dipolar,

$$\vec{B}_0 = B_0(r) \cos \theta \hat{r} + B_\theta(r, \theta, \phi) \hat{\theta} + B_\phi(r, \theta, \phi) \hat{\phi} \sim B_0(r) \cos \theta \hat{r}. \quad (4.9)$$

Because the wavenumbers of gravity waves are predominantly radial, the radial component of the field couples most efficiently to them (Fuller, Cantiello, et al., 2015), and the horizontal field components can be neglected at lowest order. This generic dipole angular dependence encompasses as special cases the force-free dipole ($B_0(r) \propto r^{-3}$) and uniform $B_0 \hat{z}$ ($B_0(r) = \text{const.}$) field geometries, as well as the mixed poloidal–toroidal field solution of Prendergast (1956).

For this special case, and adopting a radial WKB approximation, Equations 4.2 can be written in spherical polar coordinates as

$$ik_r \xi_r + \frac{1}{r} \frac{d}{d\mu} \left(\xi_\theta \sqrt{1 - \mu^2} \right) - \frac{im}{r\sqrt{1 - \mu^2}} \xi_\phi = 0 \quad (4.10a)$$

$$\rho_0 N^2 \xi_r = ik_r p' \quad (4.10b)$$

$$\rho_0 \omega^2 \xi_\theta = -\frac{\sqrt{1 - \mu^2}}{r} \frac{dp'}{d\mu} + \frac{1}{4\pi} k_r^2 B_0^2 \mu^2 \xi_\theta \quad (4.10c)$$

$$\rho_0 \omega^2 \xi_\phi = \frac{im}{r\sqrt{1 - \mu^2}} p' + \frac{1}{4\pi} k_r^2 B_0^2 \mu^2 \xi_\phi \quad (4.10d)$$

where we have substituted Equation 4.2c into the radial component of Equation 4.2a, Equation 4.2d into the horizontal components of Equation 4.2a, and kept only leading-order terms. Here, $\mu \equiv \cos \theta$, and the axisymmetry of this geometry entails eigenfunctions with $\partial/\partial\phi \rightarrow im$ for an integer m .

In terms of the pressure perturbation p' , the other perturbations become

$$\xi_r = \frac{ik_r}{\rho_0 N^2} p' = \frac{i}{\rho \omega^2 r} \left(\frac{\omega}{N} \right) \frac{b}{a} p' \quad (4.11a)$$

$$\xi_\theta = -\frac{\sqrt{1-\mu^2}}{\rho_0 \omega^2 r (1-b^2 \mu^2)} \frac{dp'}{d\mu} \quad (4.11b)$$

$$\xi_\phi = \frac{im}{\rho_0 \omega^2 r \sqrt{1-\mu^2} (1-b^2 \mu^2)} p' \quad (4.11c)$$

$$\rho' = \frac{ik_r}{g} p' \quad (4.11d)$$

and $\vec{B}' = -iB_0 \mu k_r \vec{\xi}$. When Equations 4.11a, 4.11b, and 4.11c for the displacements are substituted into the continuity equation (Equation 4.10a), we obtain

$$\mathcal{L}_{\text{mag}}^{m,b} p'(\mu) + \frac{b^2}{a^2} p'(\mu) = 0 \quad (4.12)$$

where

$$\mathcal{L}_{\text{mag}}^{m,b} p'(\mu) = \frac{d}{d\mu} \left(\frac{1-\mu^2}{1-b^2 \mu^2} \frac{dp'(\mu)}{d\mu} \right) - \frac{m^2}{(1-\mu^2)(1-b^2 \mu^2)} p'(\mu). \quad (4.13)$$

Equation 4.12 can be viewed as an eigenvalue equation for the unusual operator $\mathcal{L}_{\text{mag}}^{m,b}$. Letting λ be the (conventionally negative) eigenvalues of $\mathcal{L}_{\text{mag}}^{m,b}$, Equation 4.12 is

$$\mathcal{L}_{\text{mag}}^{m,b} p' + \lambda p' = 0 \quad (4.14)$$

with

$$\lambda = b^2/a^2 \quad (4.15)$$

constitutes the dispersion relation for magnetogravity waves.

In the limit of zero magnetic field, $\mathcal{L}_{\text{mag}}^{m,b}$ approaches the usual generalized Legendre operator (whose eigenfunctions are associated Legendre polynomials). Here, while a and b individually approach zero, the combination $\lambda = b^2/a^2 (= r^2 k_r^2 \omega^2/N^2)$ approaches $\ell(\ell+1)$, matching the zero-field result that $k_h = \sqrt{\ell(\ell+1)}/r$. In this case, Equation 4.15 approaches the unusual internal gravity wave dispersion relation $\omega/N = k_h/k_r$.

In this work, we index mode branches using ℓ and $|m|$, corresponding to the angular degree and order of the branch at zero field (note that modes of $+m$ and $-m$ have identical spectra). Hereafter, we refer to mode branches as an ordered pair $(\ell, |m|)$, e.g., the $(2, 1)$ branch corresponds to the branch which, at zero field, has a horizontal dependence of a spherical harmonic with $\ell = 2$ and $m = \pm 1$. However, note that the eigenvalue of $\mathcal{L}_{\text{mag}}^{m,b}$ does not equal $\lambda = \ell(\ell+1)$ except precisely in the $b = 0$ (zero-field) case, and the index ℓ is just used for indexing purposes.

4.3 Important features of the magnetogravity eigenproblem

4.3.1 Close analogy to the rotational problem

In the study of nonradial pulsations under uniform rotation, it is common to consider only the influence of the Coriolis force, which dominates the rotational effect for small Ω . Specializing further to the case where $k_r \gg k_h$, it is common also to ignore the horizontal component of the rotational vector $\vec{\Omega}$, since the product $\vec{k} \cdot \vec{\Omega} = k_r \Omega_r + k_h \Omega_h \approx k_r \Omega_r$ will be dominated by the radial term (see, e.g., Lee and Saio, 1997; Chen and Lü, 2009; Wang, Boyd, et al., 2016). Under this approximation (the “traditional approximation of rotation”), the radial and horizontal fluid equations become separable, and the following eigenproblem appears:

$$\mathcal{L}_{\text{rot}}^{m,\nu} p'(\mu) + \lambda p'(\mu) = 0 \quad (4.16)$$

where $\mathcal{L}_{\text{rot}}^{m,\nu}$ (called the “Laplace tidal operator”) is given by

$$\begin{aligned} \mathcal{L}_{\text{rot}}^{m,\nu} p'(\mu) &= \frac{d}{d\mu} \left(\frac{1 - \mu^2}{1 - \mu^2 \nu^2} \frac{dp'(\mu)}{d\mu} \right) - \frac{m^2}{(1 - \mu^2)(1 - \mu^2 \nu^2)} p'(\mu) \\ &\quad - \frac{m \nu (1 + \mu^2 \nu^2)}{(1 - \mu^2 \nu^2)^2} p'(\mu) \end{aligned} \quad (4.17)$$

where $\nu = 2\Omega/\omega$ describes the influence of rotation.

Comparing $\mathcal{L}_{\text{mag}}^{m,b}$ and $\mathcal{L}_{\text{rot}}^{m,\nu}$ suggests a close analogy—the latter is identical to the former (with ν playing the role of b) except for the presence of an extra term (the second term in Equation 4.17) which distinguishes prograde ($m\nu < 0$) and retrograde ($m\nu > 0$) modes (Lee and Saio, 1997). Because a dipole magnetic field does not privilege either clockwise or counterclockwise-propagating oscillations, the symmetries of the problem do not permit this term to exist in the magnetogravity problem.

The eigenfunctions of $\mathcal{L}_{\text{rot}}^{m,\nu}$ (whose eigenvalues we denote by $\lambda_{\ell m}^{\nu}$) are called Hough functions (Hough, 1898a; Hough, 1898b), and their properties have been widely studied, both analytically (Homer, 1990; Townsend, 2003; Townsend, 2020) and numerically (Bildsten, Ushomirsky, et al., 1996; Lee and Saio, 1997; Chen and Lü, 2009; Fuller and Lai, 2014; Wang, Boyd, et al., 2016). In Section 4.4.1, we show that the exact correspondence between $\mathcal{L}_{\text{mag}}^{m,b}$ and $\mathcal{L}_{\text{rot}}^{m,\nu}$ in the zonal ($m = 0$) case allows us to identify Hough functions as eigensolutions of the magnetogravity problem.

We note that, for $|\nu| > 1$, the coefficients in the Laplace tidal operator $\mathcal{L}_{\text{rot}}^{m,\nu}$ (Equation 4.17) switch signs on the domain, and Sturm–Liouville theory no longer guarantees that its eigenvalues are positive-definite (see Section 4.3.2), and indeed there are an infinite number of $\lambda_{\ell m}^{\nu} < 0$ branches occupying the range $|\nu| > 1$ which diverge to negative infinity as

$|\nu| = 1$ is approached (e.g., Lee and Saio, 1997). In the rotation problem, these negative $\lambda_{\ell m}^{\nu}$ branches correspond physically to oscillatory convective modes (e.g., Section 4.6.4). Notably, in the retrograde case for $|m| \neq 0$, some of these branches of eigenvalues actually rise above 0 and physically correspond to Rossby waves (Lee and Saio, 1997). In the magnetogravity problem, these negative eigenvalue branches are not directly relevant in radiative regions (see Section 4.4.1 for a discussion of this), although their existence may imply magnetically stabilized g modes in convective regions (see Section 4.6.4).

In the general m case (Section 4.4.2), $\mathcal{L}_{\text{mag}}^{m,b}$ and $\mathcal{L}_{\text{rot}}^{m,\nu}$ no longer coincide. However, the Laplace tidal equation can at least provide some basic expectations about the behavior of the magnetogravity eigenfunctions, although the latter are significantly more pathological.

4.3.2 Sturm–Liouville problems with internal singularities

The magnetogravity problem is dependent on the behavior of the eigenvalue problem stated in Equation 4.12, which contains a differential operator whose coefficients have singularities on the interior of the domain, at least, when ω and k_r are real (at $\mu = \pm 1/b$). To inform our procedure, we summarize in this Section the previous body of work on such Sturm–Liouville problems with internal singularities.

Consider the following general eigenvalue problem

$$(P(x)y'(x))' - Q(x)y(x) + \lambda y(x) \equiv \mathcal{L}y(x) + \lambda y(x) = 0 \quad (4.18)$$

where $P(x)$ and $Q(x)$ are real functions of x on the open range $x \in (a, b)$, and primes denote derivatives in x . If the value of $f(x)^*P(x)g'(x)$ matches at the endpoints $x = a$ and $x = b$ for any two functions $f(x)$ and $g(x)$ satisfying some boundary conditions, then the operator \mathcal{L} is Hermitian with respect to the inner product

$$\langle f, g \rangle = \int_a^b f(x)^* \mathcal{L}g(x) \, dx \quad (4.19)$$

for those boundary conditions. Standard Sturm–Liouville theory then implies that \mathcal{L} has a large number of “nice” properties such as an orthonormal basis of eigenfunctions with real eigenvalues (e.g., Al-Gwaiz, 2008). Specific properties held by $P(x)$ and $Q(x)$ often imply bounds on those eigenvalues. An important example is that, if $P(x), Q(x) > 0$ on (a, b) , then all of the eigenvalues λ must be positive. This can be seen by multiplying Equation

4.18 by $y(x)^*$, integrating over the domain, and solving for λ

$$\begin{aligned}\lambda &= \frac{-\int_a^b y(x)^* (P(x)y'(x))' dx + \int_a^b Q(x)y(x)^*y(x) dx}{\int_a^b y(x)^*y(x) dx} \\ &= \frac{\int_a^b P(x)|y'(x)|^2 dx + \int_a^b Q(x)|y(x)|^2 dx}{\int_a^b |y(x)|^2 dx}\end{aligned}\tag{4.20}$$

where in the second equality we have integrated by parts, applying our boundary condition to discard the boundary term. Equation 4.20 is called the Rayleigh quotient, and the fact that all of the integrands that appear are positive-definite implies that λ must be positive. We will apply this result in later sections.

While the differential operator $\mathcal{L}_{\text{mag}}^{m,b}$ (for real b) appears superficially similar to \mathcal{L} as written in Equation 4.18, the comparison is thwarted by the interior singularities which appear in P and Q at $\mu = \pm 1/b$ (for $|b| \leq 1$, Sturm–Liouville theory indeed applies). Although we show in Section 4.4.1 that solutions in the $m = 0$ case are Hough functions which are second-differentiable everywhere, solutions with $m \neq 0$ do not generally have this property, and have a number of unusual attributes (physically reflecting resonant interaction of gravity modes with Alfvén waves).

Motivated by problems in atmospheric physics (Boyd, 1976; Boyd, 1982), Boyd (1981) wrote down a prototypical eigenvalue problem with an interior singularity,

$$\frac{d^2y(x)}{dx^2} - \frac{1}{x}y(x) + \lambda y(x) = 0.\tag{4.21}$$

Equation 4.21 is called the Boyd problem, and its interesting mathematical properties have been the subject of some study (Boyd, 1981; Everitt et al., 1987; Gunson, 1987; Atkinson et al., 1988). The most interesting case is when it is considered over the domain $x \in (a, b)$ where $a < 0 < b$, so that there is an interior, non-integrable singularity at $x = 0$. It is common to consider this problem over the direct sum domain $x \in (a, 0) \cup (0, b)$, over which Everitt et al. (1987) show that Equation 4.21 possesses an orthonormal basis of discrete eigenfunctions with real λ . These eigenfunctions are continuous over the entire range $x \in (a, b)$ (including over the singularity), but not necessarily differentiable.

Boyd (1981) and Everitt et al. (1987) note that, for a given real λ , $y(x)$ has two linearly independent solutions defined in terms of the Whittaker functions, $M_{-\kappa,1/2}(-x/\kappa)$ and $W_{-\kappa,1/2}(-x/\kappa)$ (with $1/\kappa \equiv 2\sqrt{\lambda}$), themselves defined via confluent hypergeometric functions (Whittaker, 1903). While the former is analytic, the latter has a logarithmic divergence whose coefficient is proportional to $M_{-\kappa,1/2}(-x/\kappa)$. As we will show, these properties

are shared by the magnetogravity wave (analogous to $M_{-\kappa,1/2}(-x/\kappa)$; Section 4.4.2) and Alfvén wave (analogous to $W_{-\kappa,1/2}(-x/\kappa)$; Section 4.4.3) parts of the eigenfunctions of $\mathcal{L}_{\text{mag}}^{m,b}$. Notably, the former solution $M_{-\kappa,1/2}(-x/\kappa)$ *vanishes* at $x = 0$.

The Boyd problem shares many properties with the magnetogravity problem (Equation 4.12). In particular, the singularity in the Boyd problem appears in Q , and the singularity in Q in the magnetogravity is responsible for the unusual behavior of its eigenfunctions (as shown in Section 4.4.1, the magnetogravity problem is numerically well-behaved when $Q = 0$). We will see in Section 4.4.2 that p' eigenfunctions of the $m \neq 0$ eigenproblem also vanish at the critical latitudes. However, we shall also see that the displacements $\vec{\xi}$ are discontinuous for $m \neq 0$, even though p' is continuous, making the solutions unphysical.

4.3.3 Power series expansion around singularity

When $|b| > 1$ for real b , Equation 4.12 develops a singularity at the critical latitudes $\mu = \pm 1/b$ where the mode frequency exactly matches the Alfvén frequency, and in this case naïvely trying to numerically solve for these modes produces erratic behavior.

In order to characterize the behavior of Equation 4.12 in the $|b| > 1$ case, we can perform a Frobenius power series expansion of the form

$$p'(\mu) = (\mu - 1/b)^\alpha \sum_{n=0}^{\infty} c_n (\mu - 1/b)^n. \quad (4.22)$$

The leading-order term is the indicial equation, and can be solved to yield $\alpha = 0$ and $\alpha = 2$, implying either that the leading-order dependence of the eigenfunctions around the singularity must either be constant or quadratic. Enforcing equality at the next two lowest orders for $\alpha = 0$ (the constant case) yields

$$0 = \frac{(b^2 - 1)^3}{b^5} c_1 \quad (4.23a)$$

$$0 = \frac{b^2 - 1}{b^4} [(b^4 - 6b^2 + 5)c_1 + b^3 m^2 c_0] \quad (4.23b)$$

indicating that $c_1 = 0$ (the first derivative vanishes) and also $m^2 c_0 = 0$ (the value of the function also vanishes when $m \neq 0$). Therefore, the pressure perturbation of eigenfunctions which can be expanded in this way must vanish at the critical latitudes, as must their first derivatives. Note that, while the first derivative at $\mu = \pm 1/b$ must also vanish in the $m = 0$ case (consistent with numerical solutions in Section 4.4.1), the value of the pressure perturbation need not vanish.

This result may also be seen in a more straightforward fashion from Equation 4.12 by multiplying the singular factor to the numerator. One thereby obtains

$$\begin{aligned} & \left(1 - \mu^2\right) \left(1 - b^2\mu^2\right) \frac{d^2 p'(\mu)}{d\mu^2} + 2\mu \left(b^2 - 1\right) \frac{dp'(\mu)}{d\mu} \\ & + \left(\frac{b^2}{a^2} \left(1 - b^2\mu^2\right) - \frac{m^2}{1 - \mu^2}\right) \left(1 - b^2\mu^2\right) p'(\mu) = 0. \end{aligned} \quad (4.24)$$

If the pressure perturbation p' is everywhere finite, then Equation 4.24 implies that $dp'/d\mu = 0$ when $\mu = \pm 1/b$ (for any value of m).

To show that the value of the function must also vanish for $m = 0$, we require not just that the horizontal gradient of p' vanish in the direction across the critical latitude but the more general result that it vanish in all directions on this curve, i.e., that p' must be a constant on connected curves of $|b| = 1$. We will show this in Section 4.6.3 for magnetic fields which are more general functions of θ and ϕ). Then the only way to enforce both that $p' \propto e^{im\phi}$ and $p' = \text{const.}$ on a critical latitude is for p' itself to vanish. This result can be compared to the vanishing of the finite eigenfunctions of the Boyd equation around $x = 0$ (Section 4.3.2). In Section 4.4.2, we will demonstrate that this fact requires that the $m \neq 0$ solutions must be exactly confined to an equatorial band with width $\Delta\mu = 2/|b|$, in the sense of having exactly zero amplitude outside of it.

4.4 Oscillation modes without dissipation

In this Section, we give solutions for the zonal ($m = 0$; Section 4.4.1), tesseral/sectoral ($m \neq 0$; Section 4.4.2), and Alfvén continuum (Section 4.4.3) modes for the singular eigenvalue problem discussed in Section 4.3. The inclusion of viscous terms neutralizes the singularity and is discussed in Section 4.5. This is similar to the treatment given by authors such as Boyd (1981) and similar authors investigating internally singular eigenvalue problems (Section 4.3.2). We refer to the solutions obtained in this way as *dissipationless solutions*, and caution that this is distinct from the *limit* as the dissipation is taken to zero (*dissipative solutions*; Section 4.5). The $m = 0$ modes in the dissipationless solutions do not contain any discontinuous behavior at the critical latitude, and are exactly approached in the low-dissipation limit. However, as we show in Section 4.5, any nonzero dissipation implies important qualitative differences in the $m \neq 0$ modes, even in the very high Reynolds number, near-ideal magnetohydrodynamic flows in real stars.

4.4.1 Zonal ($m = 0$) solutions

In Section 4.3.1, we noted the correspondence between $\mathcal{L}_{\text{mag}}^{m,b}$ and the $\mathcal{L}_{\text{rot}}^{m,v}$ operator which appears in the rotational problem. The latter's eigenfunctions are the Hough functions

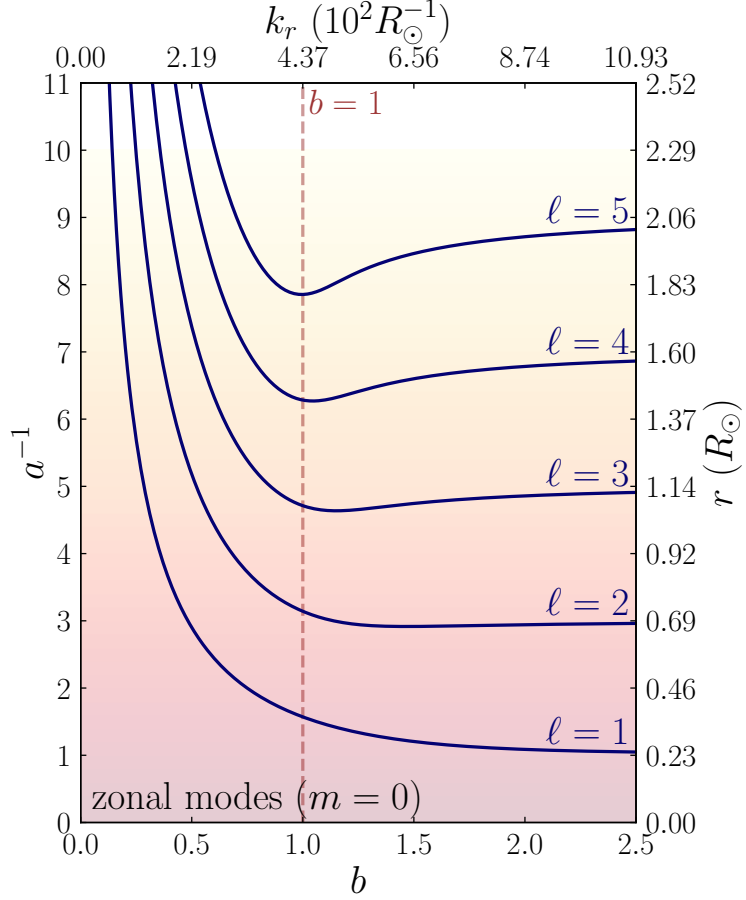


Figure 4.2: The inverse depth parameter a^{-1} plotted against b for zonal ($m = 0$) modes (Section 4.4.1). The quantities a^{-1} and b have been roughly translated to r and k_r using constant values $\omega = 2\pi \times 10^2 \mu\text{Hz}$, $N = 10^2\omega$, $v_A = 0.1 \text{ km s}^{-1}$, and $R = 10R_\odot$, reasonable parameters near the hydrogen burning shell in a first-ascent red giant. Ingoing gravity waves of different ℓ follow the tracks to the right, such that they never propagate back towards the surface of the star, and are converted to slow magnetic waves with high radial wavenumber.

$\Theta_{\ell m}^\nu(\mu)$ with eigenvalues $\lambda_{\ell m}^\nu$, where ℓ denotes the degree of associated Legendre polynomial obtained by following a given Hough function branch to $\nu = 0$. When $m = 0$, the correspondence becomes exact, and

$$\mathcal{L}_{\text{mag}}^{m,b} p'(\mu) = \mathcal{L}_{\text{rot}}^{m,b} p'(\mu) = \frac{d}{d\mu} \left(\frac{1 - \mu^2}{1 - b^2 \mu^2} \frac{dp'(\mu)}{d\mu} \right). \quad (4.25)$$

It can therefore be seen that the Hough functions $\Theta_{\ell m}^b(\mu)$ are also horizontal pressure $p'(\mu)$ eigenfunctions of the $m = 0$ case of the magnetic problem. Known properties of Hough functions thus greatly inform the behavior of these eigenfunctions. In particular, because (a real value of) b sets $1/|b|$ as a length scale with respect to μ in $\mathcal{L}_{\text{mag}}^{m,b}$, Hough functions become approximately confined to an equatorial band of width $\Delta\mu \approx 2/|b|$.

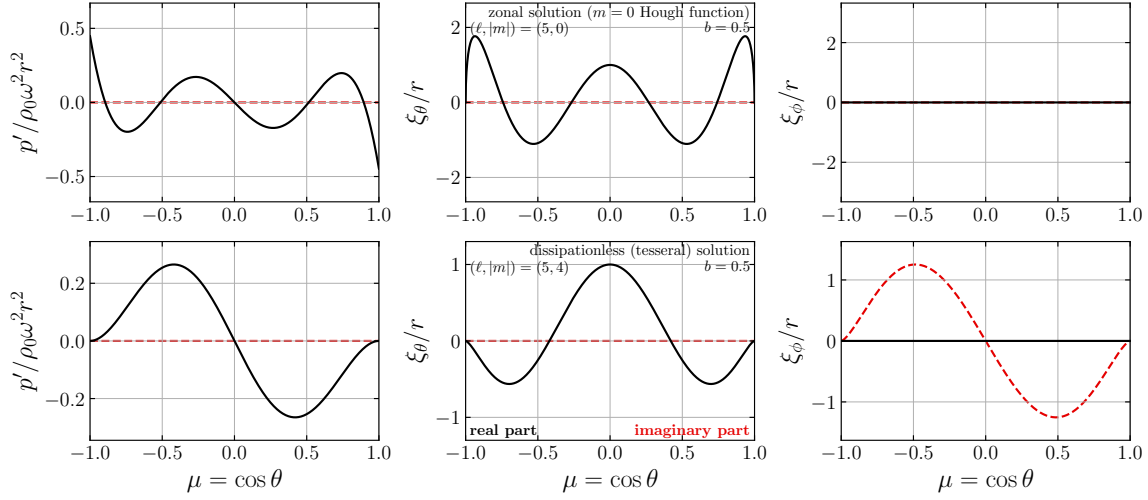


Figure 4.3: Fluid perturbations for the zonal $(\ell, |m|) = (5, 0)$ (top; Section 4.4.1) and tesseral $(5, 4)$ modes (bottom; Section 4.4.2) as a function of the latitude $\mu = \cos \theta$, for $b = k_r v_A / \omega = 0.5$. The left, center, and right columns are the non-dimensionalized p' , ξ_θ , and ξ_ϕ perturbations, respectively, with black solid lines representing the real part and red dashed lines representing the imaginary part. For low b , the eigenfunctions are close to spherical harmonics.

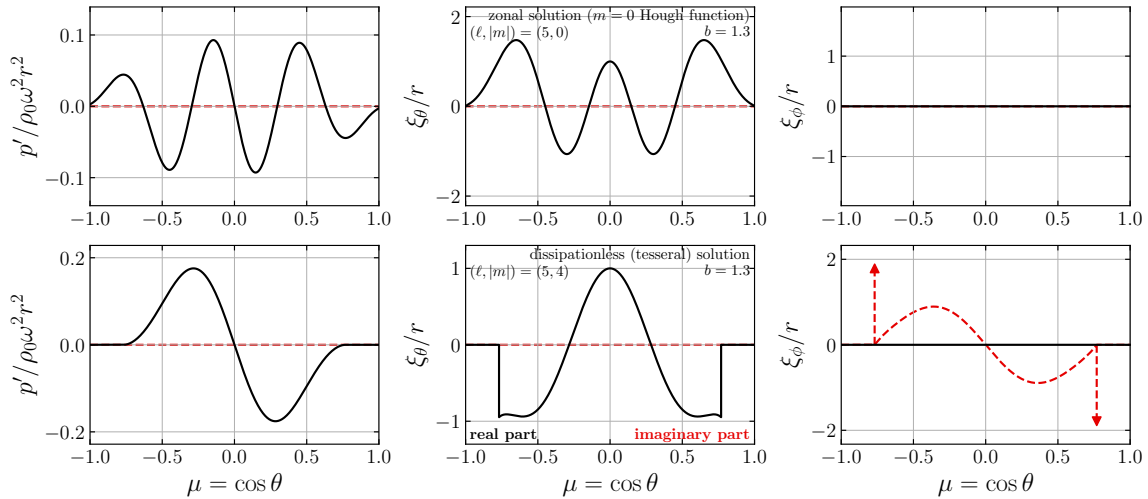


Figure 4.4: Fluid perturbations for the same mode branches as in Figure 4.3, but for $b = k_r v_A / \omega = 1.3$. The vertical arrows on the bottom right panel indicate the locations and phases of delta functions. For $b > 1$ (when parts of the mode are resonant with Alfvén waves), both the $m = 0$ and $m \neq 0$ modes become localized to the equator, but only the $m \neq 0$ modes gain sharp latitudinal features in ξ_θ and ξ_ϕ (owing to their vanishing outside of the critical latitudes).

Additionally, it is known that the Hough function eigenvalue $\lambda_{\ell 0}^b \approx (2\ell - 1)^2 b^2$ when $|b|$ is large, where the degree ℓ is equal to the number of latitudinal nodes for the $m = 0$ case. A heuristic argument for this behavior was given by Bildsten, Ushomirsky, et al. (1996), who argue that the quadratic scaling with b arises from requiring that the eigenfunctions' zero crossings be localized to the aforementioned equatorial band. The asymptotic behavior of the eigenvalues of the Hough functions was later derived more rigorously by Townsend (2003) (and more recently, to higher orders, by Townsend, 2020).

By setting $\lambda_{\ell 0}^b$ equal to b^2/a^2 (as required by the dispersion relation, Equation 4.15), one obtains for the zonal modes that b diverges to infinity at some finite cutoff height $a = a_\infty^{\ell 0}$ defined by

$$a_\infty^{\ell 0} = \frac{1}{2\ell - 1}. \quad (4.26)$$

In other words, the “cutoff height” for these modes occurs at a radial magnetic field strength

$$B_0^\infty = \frac{\sqrt{4\pi\rho_0\omega^2}r}{(2\ell - 1)N}. \quad (4.27)$$

This is approximately equal to the critical magnetic field strength derived in Fuller, Cantiello, et al., 2015, although conceptually different. For $\ell = 1$, we find numerically that the incoming wave approaches the cutoff height from above, and approaches infinite wavenumber before reaching a turning point (as can be seen in Figure 4.2). However, for all other values of ℓ , we find that the incoming wave first refracts outwards before approaching the cutoff height from below.

In addition, for each mode, there is some critical field B_c such that, for $B_0 > B_c$ (or $a > a_c$), there is no solution for a real value of b . Only complex values of b allow for solutions, implying (for real ω) complex wavenumbers k_r and evanescent waves similar to those discussed in Fuller, Cantiello, et al., 2015 and Lecoanet, Vasil, et al., 2017. Physically, this means that $m = 0$ modes will refract off of strong magnetic fields as discussed in the works above. This is different from the rotation problem where gravito-inertial waves can propagate at all radii where $N > \omega$, regardless of the rotation rate.

Using a relaxation method (see Appendix 4.B.1), we solve for the $m = 0$ eigenvalues and shown in Figure 4.2, and the eigenfunctions shown in the top panels of Figures 4.3 and 4.4. Because $\lambda_{\ell 0}^b$ approaches a constant $\ell(\ell+1)$ when b approaches zero, $a^{-1} = \sqrt{\lambda_{\ell 0}^b}/b$ diverges as b vanishes. In most cases, an internal gravity wave branch increases in $|b|$ ($\propto |k_r|$) as it is followed to higher a ($\propto Nv_A/r$), until it connects to a slow magnetic branch. The wave then reaches a turning point at a maximum value of $a = a_c$ (the “critical depth”), and it is then forced to propagate back out to smaller values of a (i.e., larger radii within a star)

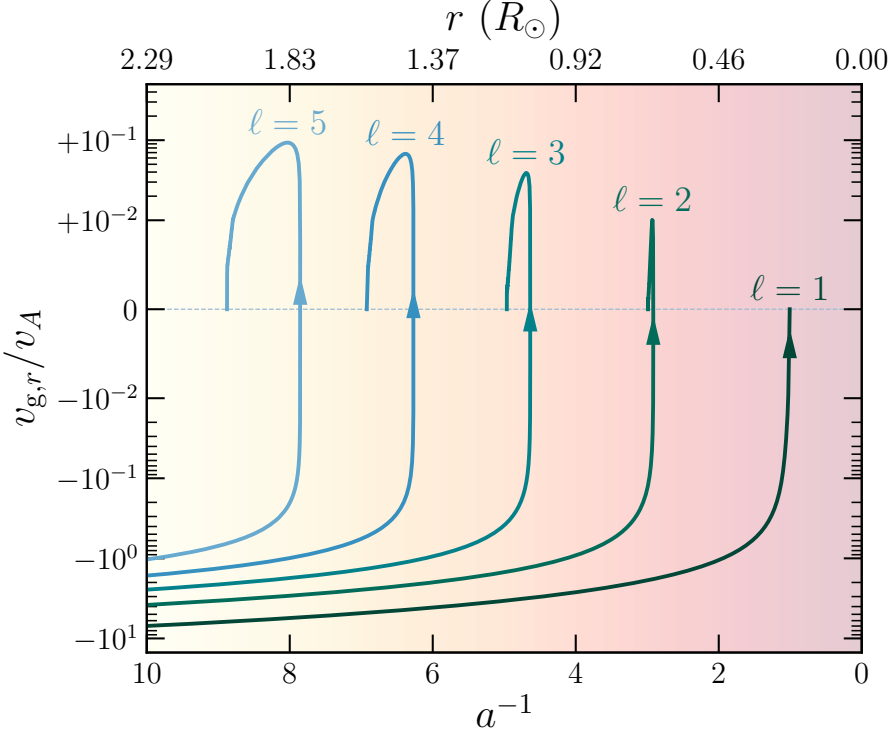


Figure 4.5: The group velocities $v_{g,r}$ for $1 \leq \ell \leq 5$ zonal ($m = 0$) magnetogravity wave branches. For most branches, ingoing magnetogravity waves refract back to larger radii at a critical depth a_c before approaching infinite radial wavenumber (as slow magnetic waves) at some cutoff depth a_∞ . For the $\ell = 1$ branch, the ingoing magnetogravity wave approaches the cutoff depth from above, without refracting outwards. The inverse depth parameter a^{-1} has been roughly translated to a physical radius r in the same manner as in Figure 4.2.

although $|b|$ continues to increase. The value of $|b|$ and the radial wavenumber then diverge at the cutoff height defined in Equation 4.26. This behavior is consistent with Lecoanet, Vasil, et al. (2017) (see Appendix 4.A.2) who discovered the same behavior in Cartesian geometry.

The one exception is the $\ell = 1$ case, where the wavenumber of the internal gravity wave branch directly diverges when approaching a from below—there is no turning point, and no distinct slow magnetic branch. In both cases there is a maximum a (minimum radius) to which the wave can propagate, and the wavenumber k_r diverges at a cutoff height within the star. We thus find that the conclusions of Fuller, Cantiello, et al. (2015) and Lecoanet, Vasil, et al. (2017) that zonal modes cannot propagate arbitrarily deep in a sufficiently magnetized star to be robust for a dipole field geometry. In Table 4.1, we report values of the critical depth a_c^{-1} and cutoff depths a_∞^{-1} for these mode branches.

Section	(ℓ, m)	b_c	$ a_c ^{-1}$	$ a_\infty ^{-1}$
dissipationless $m = 0$ (Section 4.4.1)	(1, 0)	∞	a_∞^{-1}	$a_\infty^{-1} = 2\ell - 1$ (Equation 4.26)
	(2, 0)	1.46	2.92	
	(3, 0)	1.15	4.64	
	(4, 0)	1.04	6.27	
	(5, 0)	0.99	7.85	
	(1, 1)	0.94	1.99	
dissipationless $m \neq 0$ (Section 4.4.2)	(2, 1)	0.93	3.45	$a_\infty^{-1} \approx \begin{cases} 2.26 & \ell - m = 0 \\ 4.29 & \ell - m = 1 \\ 6.30 & \ell - m = 2 \\ 8.30 & \ell - m = 3 \\ 10.31 & \ell - m = 4 \\ \vdots & \end{cases}$ (eigenvalues of Equation 4.33)
	(3, 1)	0.92	4.93	
	(4, 1)	0.92	6.42	
	(5, 1)	0.92	7.91	
	(2, 2)	∞	a_∞^{-1}	
	(3, 2)	1.66	4.28	
	(4, 2)	1.02	5.90	
	(5, 2)	0.99	7.44	
	(3, 3)	∞	a_∞^{-1}	
	(4, 3)	∞	a_∞^{-1}	
	(5, 3)	∞	a_∞^{-1}	
	(4, 4)	∞	a_∞^{-1}	
	(5, 4)	∞	a_∞^{-1}	
	(5, 5)	∞	a_∞^{-1}	
dissipative real- $v_{p,r}$ (Section 4.5.2)	(1, 1)	0.94	1.99	$ a_\infty ^{-1} \approx 2(\ell - m) + 3$ (Equation 4.44)
	(2, 1)	0.93	3.45	
	(3, 1)	0.92	4.93	
	(4, 1)	0.92	6.42	
	(5, 1)	0.92	7.91	
	(2, 2)	1.31	2.66	
	(3, 2)	1.09	4.33	
	(4, 2)	1.02	5.90	
	(5, 2)	0.99	7.44	
	(3, 3)	1.73	2.95	
	(4, 3)	1.38	4.81	
	(5, 3)	1.21	6.53	

Table 4.1: For the mode branches computed in Sections 4.4.1, 4.4.2, and 4.5.2, values of $b = b_c$ and $|a_c|^{-1}$ at the critical depth (the wave turning point), as well as values of the cutoff height $|a_\infty|^{-1}$. Rows with $b_c = \infty$ and $|a_c|^{-1} = |a_\infty|^{-1}$ denote cases where the mode branch approaches $|a_\infty|^{-1}$ from above. Because our calculations only extend to $b = 2.5$, it is possible that some branches reported as having $b_c = \infty$ have turning points at $b_c > 2.5$.

Assuming that $|\vec{k}| \approx k_r$, the radial components of the phase and group velocities $v_{p,r}$ and $v_{g,r}$ can be specified in terms of a and b as

$$\frac{v_{p,r}}{v_A} = \frac{1}{v_A} \frac{\omega}{k_r} = \frac{1}{b} \quad (4.28a)$$

$$\frac{v_{g,r}}{v_A} = \frac{1}{v_A} \frac{\partial \omega}{\partial k_r} = \frac{1}{v_A} \left(\frac{d\omega}{db} \right) \left(\frac{dk_r}{db} \right)^{-1} = -\frac{da/db}{2a - b da/db} \quad (4.28b)$$

where we have used $\omega = \sqrt{Nv_A/r}a^{-1/2}$ and $k_r = \sqrt{N/v_A}rba^{-1/2}$ (from Equations 4.5 and 4.6).

While $v_{p,r}$ follows the motion of the wave pattern, $v_{g,r}$ tracks the transport of wave energy. Figure 4.5 shows $v_{g,r}$ as a function of a^{-1} . Ingoing gravity waves (whose $v_{p,r}$ and $v_{g,r}$ are in opposite directions) refract at the critical depth a_c where $v_{g,r} = 0$. They then propagate outwards as slow magnetic waves with $v_{p,r}$ and $v_{g,r}$ in the same direction, with progressively slower group velocities as they approach the cutoff height. The group velocities for $m \neq 0$ modes (Sections 4.4.2 and 4.5.2) have similar behavior.

In Section 4.3.1, we pointed out that the Laplace tidal operator $\mathcal{L}_{\text{rot}}^{m,\nu}$ (defined in Equation 4.17) has branches of mostly negative eigenvalues for $\nu > 1$, which manifest as Rossby waves on the segments of the branches which are positive. However, in the magnetic problem, these branches are irrelevant when ω and N are real, since the eigenvalues on these branches are always negative. When $\lambda_{\ell 0}^b < 0$, this implies that b ($\propto k_r$) is imaginary (i.e., that the wave is evanescent). However, if b is imaginary, then $b^2 = -|b|^2$, and $\mathcal{L}_{\text{mag}}^{m,b}$ becomes

$$\mathcal{L}_{\text{mag}}^{m,b} p'(\mu) = \frac{d}{d\mu} \left(\frac{1 - \mu^2}{1 + |b|^2 \mu^2} \frac{dp'(\mu)}{d\mu} \right) - \frac{m^2}{(1 - \mu^2)(1 + |b|^2 \mu^2)} p'(\mu). \quad (4.29)$$

Equation 4.29 clearly has a positive P, Q on the domain of the eigenproblem, with no internal singularities at all. Sturm–Liouville theory thus implies (contrary to our initial assumption) that $\lambda_{\ell 0}^b$ must be positive (see Section 4.3.2). This contradiction implies not only that these $\lambda_{\ell 0}^b < 0$ branches are irrelevant to the magnetogravity problem but also that the magnetogravity problem does not admit purely spatially evanescent solutions (for real ω).

4.4.2 Tesselal and sectoral ($m \neq 0$) solutions

When $|b| < 1$, the $m \neq 0$ horizontal eigenfunctions (representing tesselal and sectoral modes) are simply solutions of a standard Sturm–Liouville problem with no internal singularities, and can be solved numerically using standard techniques. However, in the $|b| > 1$

case, the mode and Alfvén frequencies are resonant at a critical latitude, where Equation 4.12 develops an internal singularity (Section 4.3.2). We discuss the implications of this critical latitude in the succeeding paragraphs.

In Section 4.3.3, it is argued (vis-à-vis power series expansion) that both the pressure perturbation p' and its first derivative $dp'/d\mu$ must vanish in the vicinity of the critical latitudes $\mu = \pm 1/b$. We first consider an eigenfunction with eigenvalue λ , and form a “Rayleigh quotient” (cf. Equation 4.20), but only over the portion of the domain bounded between $\mu \in (-1/b, +1/b)$ with $b > 0$:

$$\lambda = \frac{\int_{-1/b}^{+1/b} \frac{1-\mu^2}{1-b^2\mu^2} \left| \frac{dp'(\mu)}{d\mu} \right|^2 dx + \int_{-1/b}^{+1/b} \frac{m^2}{(1-\mu^2)(1-b^2\mu^2)} |p'(\mu)|^2 dx}{\int_{-1/b}^{+1/b} |p'(\mu)|^2 d\mu} \quad (4.30)$$

where the vanishing pressure perturbation and gradient justify discarding the boundary term. It is easily seen that each of the integrands above is positive-definite over the entire subdomain, and therefore $\lambda > 0$.

However, one may write a similar Rayleigh quotient over the range $\mu \in (1/b, 1)$,

$$\lambda = \frac{\int_{1/b}^1 \frac{1-\mu^2}{1-b^2\mu^2} \left| \frac{dp'(\mu)}{d\mu} \right|^2 dx + \int_{1/b}^1 \frac{m^2}{(1-\mu^2)(1-b^2\mu^2)} |p'(\mu)|^2 dx}{\int_{1/b}^1 |p'(\mu)|^2 d\mu} \quad (4.31)$$

where it can be verified that the integrands in the numerator are now *negative*-definite. In Equation 4.31, we have similarly discarded the boundary terms—this can be done at the outer boundary $\mu = 1$ so long as p' and its derivative are finite there. This, in turn, implies that $\lambda < 0$.

Of course, by definition, an eigenfunction must have just a single eigenvalue across the entire domain. There are two ways to rectify these apparently contradictory conclusions. One possibility is that the $\lambda > 0$ eigenfunctions vanish outside of the critical latitudes, i.e., they are localized to a band of width $\Delta\mu = 2/|b|$, bounded by the critical latitudes on each side (as demonstrated in Section 4.4.1, the $\lambda < 0$ eigenvalues are not physical in this problem). A second possibility is that only complex values of b (and hence evanescent waves) exist when the real part of b is greater than unity.

In the first case, because the eigenfunction is confined to the range $\mu \in (-1/b, +1/b)$, we can restate the problem as a standard Sturm–Liouville problem (with no internal singularities) over this subinterval. In particular, Equation 4.12 can be rewritten using $x = b\mu$ as

$$\frac{d}{dx} \left(\frac{b^2 - x^2}{b^2(1-x^2)} \frac{dp'(x)}{dx} \right) - \frac{m^2}{(1-x^2)(1-b^2x^2)} p'(x) + \frac{1}{a^2} p''(x) = 0 \quad (4.32)$$

over the range $x \in (-1, +1)$. We solve for both the eigenvalues and eigenfunctions by solving Equation 4.12 when $b < 1$ and Equation 4.32 when $b > 1$, again using the relaxation method (Appendix 4.B.1). The eigenvalues for $\ell, |m| \leq 5$ are shown in Figure 4.6, and example eigenfunctions are shown in the bottom panels of Figures 4.3 (for $b < 1$) and 4.4 (for $b > 1$), respectively. While the eigenfunctions are close to spherical harmonics for low b (Figure 4.3), they become formally confined between the critical latitudes when $b > 1$, corresponding to resonances with Alfvén waves. This is in contrast to the $m = 0$ solutions which, although also experiencing some degree of equatorial confinement, are not forced to vanish outside of the resonant latitudes.

When b is large (compared to $|m|$), Equation 4.32 approaches

$$\frac{d}{dx} \left(\frac{1}{1-x^2} \frac{dp'(x)}{dx} \right) + \frac{1}{a^2} p'(x) = 0. \quad (4.33)$$

Equation 4.33 is a generalized eigenvalue problem with eigenvalues $1/a^2$. Therefore, we see that a approaches a constant cutoff value $a_\infty^{\ell m}$ in the large b limit—in other words, when approaching some cutoff value $a = a_\infty^{\ell m}$ from either above or below, b diverges. Moreover, since Equation 4.33 does not depend on m , $a_\infty^{\ell m}$ only depends on the specific solution of Equation 4.33 which is approached by a given branch. Therefore, $a = a_\infty^{\ell m}$ is a function of $\ell - |m|$, which defines the number of nodes possessed by the generalized Legendre operator. The cutoff values roughly lie between the $m = 0$ cutoff values $a_\infty^{\ell 0}$ (defined in Equation 4.26), which do not follow the same pattern (see Figure 4.6). Table 4.1 reports the eigenvalues of Equation 4.33, which give the cutoff depths a_∞^{-1} for these $m \neq 0$ mode branches (as well as the critical depths a_c^{-1}).

Another very important implication of Equation 4.32 is that the $m \neq 0$ branches cannot extend to arbitrarily large a , i.e., *in a sufficiently magnetized star, propagating modes cannot extend arbitrarily deeply*. When compared to Equation 4.18, the differential operator which appears in Equation 4.32 has $P, Q > 0$ everywhere on the domain, implying that $1/a^2 > 0$, i.e., a cannot be infinity for any finite b . Furthermore, because the differential operator in Equation 4.33 (the large- b limit of Equation 4.32) has $P > 0$ and $Q = 0$ everywhere on the domain, the Rayleigh quotient (Equation 4.20) still implies that $1/a^2 > 0$ (in the large- b limit) strictly, so long as $dp'(x)/dx \neq 0$ somewhere on the domain. As this is guaranteed to be the case for any perturbation for which $p'(x) \neq 0$ (since it must vary from its boundary values $p'(\pm 1) = 0$), a may not approach infinity even in the limit that b does. If we consider the second possibility discussed above, that b becomes complex, the waves become evanescent at large values of a , meaning they no longer propagate. This extends the conclusions of Fuller, Cantiello, et al. (2015) and Lecoanet, Vasil, et al. (2017) to the

general $m \neq 0$ case that propagating magnetogravity waves cannot exist arbitrarily deeply in a magnetized-enough star.

However, the localized nature of the pressure perturbations of the $m \neq 0$ modes has important implications for the other perturbations (which also vanish outside of the critical latitudes, by Equations 4.11). For example, since the leading-order dependence of the p' eigenfunction near the singularity is quadratic (Section 4.3.3), the discontinuity of $d^2 p' / d\mu^2$ across the critical latitudes implies via Equation 4.11b that the *value* of ξ_θ is discontinuous. The fact that ξ_θ behaves as a step function near the singularity further implies (by the continuity equation) that ξ_ϕ contains a delta function at the critical latitude. This behavior is discussed in depth in Goedbloed and Poedts, 2004, and we comment further on this behavior in Section 4.4.3.

Because of the singular denominator factors in $\mathcal{L}_{\text{mag}}^{m,b}$ and implied discontinuous eigenfunctions, it is important to consider that even infinitesimally little viscosity/Ohmic diffusivity can induce finite damping as well as global changes to the eigenfunctions. We further discuss these effects in Section 4.5. Nevertheless, the dissipationless solutions provide some analytic insight to qualitative features that they share with dissipative solutions to the magnetogravity wave problem.

4.4.3 Alfvén wave solutions

In Sections 4.3.3 and 4.4.2, we performed a power series expansion to probe the behavior of the perturbations around the critical latitude $\mu = 1/b$ and solved for the $m \neq 0$ solutions. However, as a second-order differential equation, one naïvely expects there to be *two* linearly independent solutions. More formally, when performing a Frobenius expansion, one obtains an indicial equation which can be solved to yield two solutions for the power law dependence of the solution very near the singularity (as in Section 4.3.3). When these two values are not separated by an integer, one immediately obtains these two linearly independent solutions.

However, the values of the indicial root α found in Section 4.3.3 *are* separated by an integer, so a Frobenius expansion in p' is not particularly helpful in the search for the other solution. Instead, by substituting Equations 4.11a and 4.11c into the continuity equation (Equation 4.10a), solving for p' in terms of ξ_θ , and then substituting the result into the θ momentum equation (Equation 4.10c), one obtains

$$\frac{d}{d\mu} \left[\left(\frac{b^2}{a^2} - \frac{m^2}{(1-\mu^2)(1-b^2\mu^2)} \right)^{-1} \frac{d\mathcal{Z}_\theta(\mu)}{d\mu} \right] + \frac{1-b^2\mu^2}{1-\mu^2} \mathcal{Z}_\theta(\mu) = 0 \quad (4.34)$$

where

$$\mathcal{Z}_\theta(\mu) \equiv \sqrt{1-\mu^2} \frac{\xi_\theta(\mu)}{r}. \quad (4.35)$$

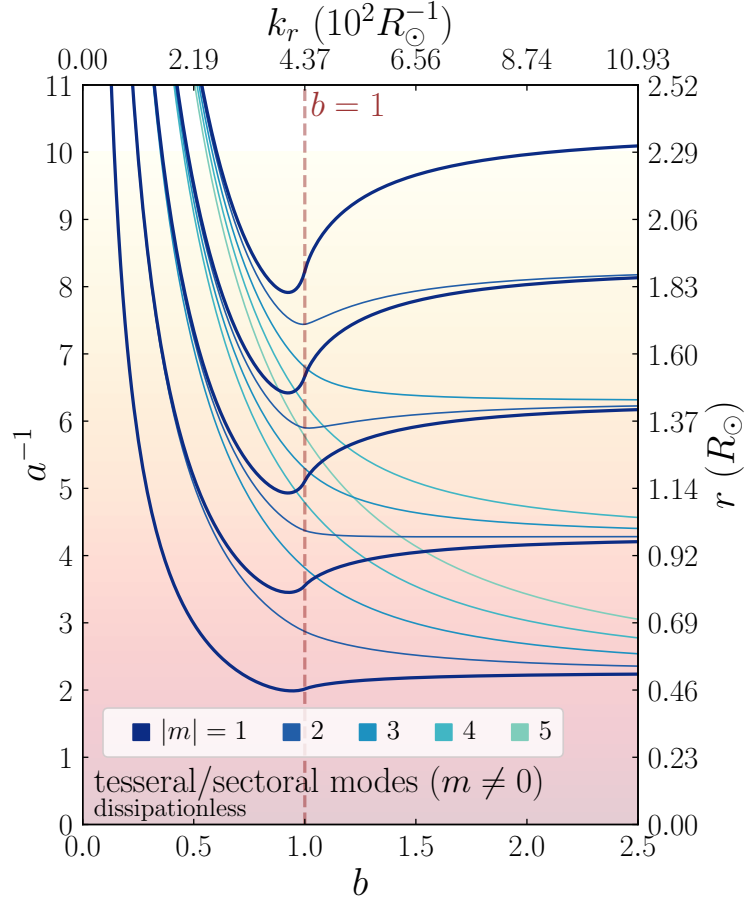


Figure 4.6: The inverse depth parameter a^{-1} plotted against b for tesseral/sectoral ($m \neq 0$) modes for the singular eigenvalue problem described in Section 4.4.2. Both a^{-1} and b have been translated to r and k_r as in Figure 4.2. As in Figure 4.2, ingoing gravity waves follow the lines to the right, and are converted to slow magnetic waves that do not propagate back to the surface.

A power series expansion of the form

$$\mathcal{Z}_\theta(\mu) = (\mu - 1/b)^\alpha \sum_{n=0}^{\infty} c_n (\mu - 1/b)^n \quad (4.36)$$

gives an indicial equation which has a double root at $\alpha = 0$, consistent with the results of Goedbloed and Poedts 2004 on a similar magnetohydrodynamic problem (see their Section 7.4).

Hereafter, for illustrative purposes, we focus on the restricted problem over the interval $\mu \in (0, 1)$ in order to focus on the critical latitude at $\mu = 1/b$ (this is justified in Section 4.B.1). The choice of $\alpha = 0$ gives a single everywhere-finite solution which can be called

$\mathcal{Z}_\theta(\mu) = \mathcal{Z}_1(\mu) = u(\mu)$. In this case, a second linearly independent solution is given by

$$\mathcal{Z}_2(\mu) = u(\mu) \ln |\mu - 1/b| + v(\mu) \quad (4.37)$$

which contains a logarithmic divergence at the critical latitude. Goedbloed and Poedts 2004 show that, while the coefficient \mathcal{Z}_1 may differ on either side of the singularity, the coefficient in front of \mathcal{Z}_2 may not. The general solution for \mathcal{Z}_θ is thus given by

$$\mathcal{Z}_\theta(\mu) = [A_1 \Theta(\mu - 1/b) + A_2 \Theta(1/b - \mu)] \mathcal{Z}_1(\mu) + A_3 \mathcal{Z}_2(\mu) \quad (4.38)$$

where Θ is the Heaviside step function. Note that the presence of *three* undetermined coefficients A_1 , A_2 , and A_3 constrained by only two boundary conditions implies a continuous spectrum of modes. This is a well-established consequence of singularities in differential equations, especially those corresponding to Alfvén resonances in plasma physics (Appert et al., 1974; Poedts et al., 1985; Rauf and Tataronis, 1995; Appert et al., 1998; Widdowson et al., 1998; Rincon and Rieutord, 2003; Goedbloed and Poedts, 2004; Reese et al., 2004; Pintér et al., 2007; Loi and Papaloizou, 2017). Physically, the continuous Alfvén spectrum arises out of a lack of discretization in the θ direction, associated with mode localization in geometries with field/plasma inhomogeneity.

In the treatment in this work, we do not explicitly impose boundary conditions in the radial direction. However, doing so would discretize the allowed values of k_r , both for the global modes and the Alfvén waves (see, e.g., Loi and Papaloizou, 2017). Alfvén resonances can exist whenever $\omega = k_r v_A |\mu|$, i.e., $b = 1/|\mu|$. The continuum Alfvén spectrum therefore occupies all frequencies ω with $|b| \geq 1$ (i.e., every point to the right of $b = 1$ in Figure 4.6). In practice, because each field line has a discrete spectrum of Alfvén waves (which are analogous to oscillations on a closed loop), a real global mode resonates with the Alfvén spectrum at only a finite (but large) number of locations (Loi and Papaloizou, 2017).

In problems possessing even vanishingly small amounts of dissipation, the Alfvén continuum has important implications both for the global forms of the eigenfunctions and wave damping. Hoven and Levin (2011) note that any dissipation couples fluid displacements across flux surfaces, destroying the continuum nature of the Alfvén spectrum (see Section 4.6.1). In Section 4.5, we find that including dissipation produces discrete spectra for which only a specific linear combination of $u(\mu)$ and $v(\mu)$ are truly eigenfunctions.

Because Alfvén waves are not associated with a pressure perturbation, the Lagrangian temperature perturbation vanishes and therefore does not produce bulk brightness fluctuations which would be asteroseismically detectable in the light curve (Houdek and Dupret, 2015). It may be possible to observe their signature in surface velocity fluctuations, if the waves do not damp before reaching the surface.

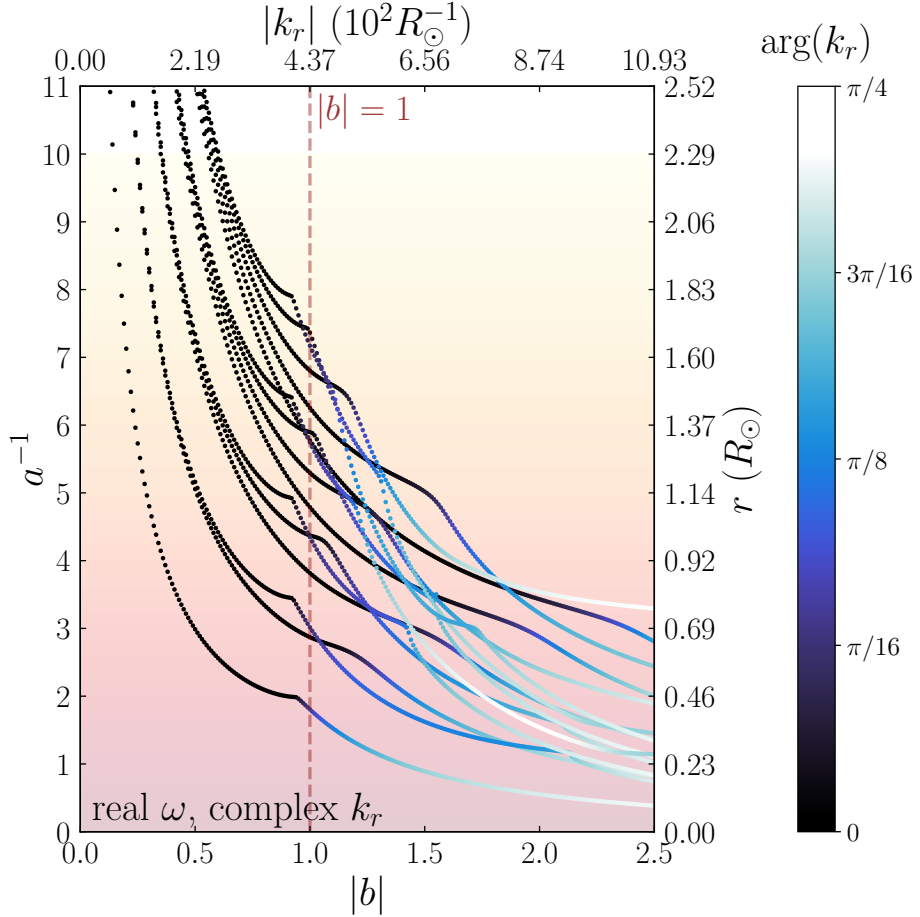


Figure 4.7: The inverse depth parameter a^{-1} plotted against b for non-axisymmetric $m \neq 0$ modes, with finite dissipation and real ω (Section 4.5.1). The color represents the complex argument of k_r , with the lower branches representing spatially evanescent solutions. Both a^{-1} and b have been translated to r and k_r as in Figure 4.2. Unlike previous figures, gravity waves do not propagate into the colored portions of the lines, where they become strongly evanescent. Instead, they are refracted upwards onto a slow magnetic wave branch not shown here (see Figure 4.10).

4.5 Oscillation modes with dissipation

So far, we have considered the mathematical problem where we have formally set all dissipation to zero. In this Section, we consider the important role played by even small amounts of dissipation in shaping the horizontal structure of magnetogravity modes.

As discussed in Section 4.4.3, the magnetogravity problem possesses a continuum of Alfvén modes, each localized to a magnetic field line. Adjacent Alfvén modes will oscillate at slightly different frequencies, corresponding to the slightly different Alfvén frequencies of their field lines. This quickly leads to a dephasing process called “phase mixing,” a kind of

quasi-damping which, while formally reversible in ideal magnetohydrodynamics, leads to finite energy damping under any (arbitrarily small) amount of dissipation. Interestingly, this energy damping approaches a finite value in the limit of even a vanishingly small dissipation, meaning that its role cannot be ignored even in stars where dissipative processes are usually considered to be negligible. For further discussion of phase mixing and its associated energy dissipation, see Goedbloed and Poedts (2004).

If dissipation, in the form of fluid viscosity and Ohmic diffusion, are included, the linearized horizontal momentum and induction equations are modified to

$$-\rho_0\omega^2\vec{\xi}_h = -\nabla p' + \frac{1}{4\pi} \left(\vec{B}_0 \cdot \nabla \right) \vec{B}' + i\omega\rho_0\nu\nabla^2\vec{\xi}_h \quad (4.39a)$$

$$\vec{B}' = \left(\vec{B}_0 \cdot \nabla \right) \vec{\xi} - i(\eta/\omega)\nabla^2\vec{B}' \quad (4.39b)$$

where we continue to assume the hierarchy of variables described in Section 4.2.1 (including taking $\nabla^2 \approx -k_r^2$). In Equations 4.39, ν and η denote the kinematic viscosity and magnetic diffusivity, respectively. We note in passing that the latter is expected to dominate the overall dissipation, but that both terms have a similar impact on the solutions.

Equations 4.39a and 4.39b can be combined to obtain

$$\nabla_h p' = \rho_0\omega^2 \left(1 - b^2\mu^2 - ic \right) \vec{\xi}_h \quad (4.40)$$

where c is given by

$$c = c_\nu b^2 + c_\eta b^4 \mu^2 \quad (4.41)$$

where

$$c_\nu = \frac{\nu\omega}{v_A^2} \quad (4.42a)$$

$$c_\eta = \frac{\eta\omega}{v_A^2}. \quad (4.42b)$$

In deriving Equations 4.40 and 4.41, we have assumed that $k_r^2\eta/\omega \ll 1$. Note that, because the effect of $c \ll 1$ is to shift the poles slightly off of the real line into the complex plane, the exact form of c does not matter, and it suffices to take it to be a small, real constant. Moreover, since dissipation is most important near the critical latitudes $\mu = \pm 1/b$, both terms scale roughly as $\propto b^2$ in the most affected regions.

Overall, the operator $\mathcal{L}_{\text{mag}}^{m,b}$ then takes the new form

$$\begin{aligned} \mathcal{L}_{\text{mag}}^{m,b} p'(\mu) &= \frac{d}{d\mu} \left(\frac{1 - \mu^2}{1 - b^2\mu^2 - ic} \frac{dp'(\mu)}{d\mu} \right) \\ &\quad - \frac{m^2}{(1 - \mu^2)(1 - b^2\mu^2 - ic)} p'(\mu) \end{aligned} \quad (4.43)$$

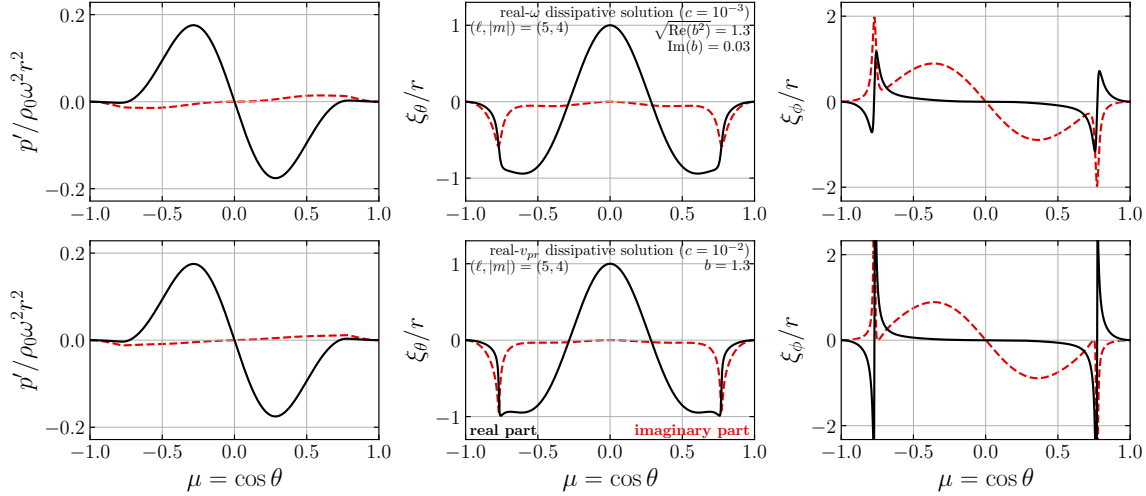


Figure 4.8: Fluid perturbations for the tesseral $(\ell, |m|) = (5, 4)$ modes for $\sqrt{\text{Re}(b^2)} = 1.3$ calculated numerically in the dissipative case where either ω is real (top; Section 4.5.1), or $v_{p,r} = \omega/k_r$ is real (bottom; Section 4.5.2). These eigenfunctions should be compared to those shown in the bottom panels of Figure 4.3 for the discontinuous case.

where c encodes the dissipative processes in the problem, and ‘softens’ the singularity.

We note in passing that terms dependent on the horizontal field B_h may be significant at the critical latitudes where dissipation is expected to be most important. The inclusion of such terms introduces higher-order horizontal derivatives to the linearized equations and greatly increases their complexity. Nevertheless, we expect that the parameterization above in terms of c will still physically select the right branch of solutions, in the limit of small dissipation. In Section 4.6.1, we comment further on the importance of such terms near the critical latitudes.

In the following subsections, we present numerical solutions for the dissipative magnetogravity eigenproblem (details in Appendix 4.B.2). Section 4.5.1 considers modes with real ω but complex k_r , i.e., possibly spatially evanescent modes, and Section 4.5.2 considers modes with real radial phase velocity $v_{p,r} = \omega/k_r$ (approximating the case of propagating waves). We will show that, while the analysis of Section 4.4.2 provides insights into realistic modes, the presence of dissipation introduces notable deviations from the idealized behavior.

4.5.1 Numerical solutions of the evanescent branch

We first consider the case where ω is real but k_r is allowed to be complex (i.e., allowing solutions to be spatially evanescent). This corresponds to fixing $a \propto \omega^{-2}$ to be real but allowing $b \propto k_r/\omega$ to be complex. As described in Appendix 4.B.2, we solve for the

eigenfunctions of the operator in Equation 4.43 up to $\ell, |m| = 5$ (using $c = 10^{-3}$) while allowing the complex argument of b to vary. For consistency, we search for only solutions with $\text{Im}(b) \geq 0$, although each such evanescent branch is accompanied by a conjugate branch of solutions.

The eigenvalues are shown in Figure 4.7 as a function of $|b|$. When $|b| \lesssim 1$ (i.e., weak magnetic fields), the singularity does not lie on the domain and dissipation does not play a major role. For decreasing values of c , b approaches a real number, as expected, and the solutions are nearly identical to those discussed in Section 4.4.2.

However, for $|b| > 1$, there are significant qualitative differences between the discontinuous solutions of Section 4.4.2 and the dissipative solutions. Even in the limit of $c \rightarrow 0$, the imaginary part of b does not correspondingly vanish, although (as we discuss below) its limiting value is sometimes quite small. This implies that the corresponding eigenfunctions are still “smoothed” with respect to the discontinuous solutions even in the $c \rightarrow 0$ limit.

For some branches of modes, there is a range extending from $|b| = 1$ to some intermediate value of $|b|$ where $\text{Im}(b)$ is small when $c \approx 0$. In these intermediate ranges, the real parts of p' , ξ_θ , and ξ_ϕ strongly resemble smoothed versions of the discontinuous solutions described in Section 4.4.2 (e.g., the top panel of Figure 4.8). In particular, ξ_θ has a smoothed step-like jump across the singularity, and ξ_ϕ retains a smoothed, but narrow, peak there. Interestingly, the imaginary part of ξ_θ approaches the logarithmic Alfvén “spike” solutions described in Section 4.4.3—the numerical solution is thus a close approximation of a superposition of these two solutions predicted in Section 4.4.3. These solutions can be visualized as equatorially focused magnetogravity modes which oscillate $\pi/2$ out of phase with an Alfvén mode. This closely resembles the example shown in Figure 11.2 by Goedbloed and Poedts (2004) (in a similar magnetohydrodynamic problem), as well as the numerical results of Lecoanet, Bowman, et al. (2022). We emphasize that, because the imaginary part of b does not approach zero in the $c \rightarrow 0$ limit, the “smoothing” *does not* go away even in this limit. It appears that the size of the intermediate range of $|b|$ for which $\text{Im}(b)$ is small appears to increase with $|m|$ for fixed ℓ . However, the origin of this trend is so far unclear.

In all branches, for large enough $|b| \gtrsim$ few, the imaginary part of b found by the solver becomes large, and a^{-1} dips as the solver follows an evanescent branch deeper into the star. At large b , all of the evanescent mode branches we solve for approach $\text{Im}(k_r)/\text{Re}(k_r) = 1$ (i.e., $\arg(k_r) \rightarrow +\pi/4$) such that waves radially decay in the same direction as they travel. In this regime, the eigenfunctions approach horizontally traveling waves which propagate away from the equator (e.g., top panel of Figure 4.9), as shown by the relative phases of

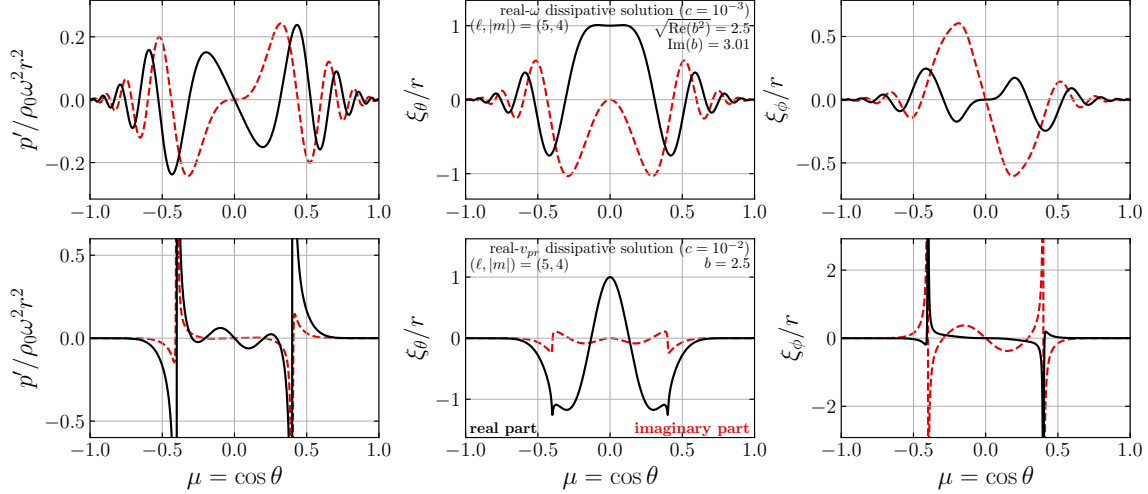


Figure 4.9: Fluid perturbations for the same mode branches as in Figure 4.8, but for $\sqrt{\text{Re}(b^2)} = 2.5$.

the real and imaginary eigenfunctions. The conjugate branches are expected to have the opposite behavior, with the eigenfunctions approaching horizontally traveling waves which propagate toward the equator. Note that, because the values of b (and therefore k_r) for these equator-ward and pole-ward traveling solutions are complex conjugates of each other, they exponentially decay in radius in opposite directions, and it is generally not possible to superpose them to form a wavefunction which is a horizontal standing wave at all radii.

Overall, the behavior at $|b| > 1$ is very complex and difficult to characterize from first principles. Branches often have multiple “kinks” in addition to the initial one at $|b| = 1$ characterizing the transition from propagation to evanescence. We suspect these kinks are related to avoided crossings between different evanescent branches of magnetogravity waves.

However, these branches represent modes that are evanescent on short length scales, implying very little wave energy propagates to larger depths. Hence, it seems clear that in the dissipative case, there are no propagating mode branches which extend arbitrarily deep into the star. This extends the two-dimensional results of Lecoanet, Vasil, et al. (2017) to non-axisymmetric modes. Physically, evanescent waves indicate the presence of either total internal reflection or (in this case) refraction. Unless the radial extent of the core is $\lesssim 1/\text{Im}(k_r)$, the wave power transmitted by these evanescent waves through the core is vanishingly small, and conservation of energy thereby enforces that the rest of the energy (which is the vast majority) be converted into some kind of outgoing propagating wave (Section 4.5.2).

4.5.2 Numerical solutions of the propagating branch

It is natural to search for solutions where waves are purely propagating (real k_r) but ω is complex (corresponding to decay). However, we find that our relaxation approach is unable to solve this particular problem formulation. Instead, we consider the case where the radial phase velocity $v_{p,r} = \omega/k_r$ is real, which is equivalent to taking $b = v_A/v_{p,r}$ to be real (placing the singularity as close to the real line as possible), but allowing $a \propto \omega^{-1}$ to be complex (i.e., so that $\arg(k_r) = \arg(\omega) \neq 0$). The eigenvalues for these calculations are shown in Figure 4.10.

Interestingly, in this formulation, the eigenvalues have similar qualitative behavior to discontinuous case in Figure 4.6. They reach some maximum $|a|$ at $b \sim 1$, at which point the waves turn and propagate outwards onto a slow magnetic branch which asymptotes to a finite cutoff height at infinite wavenumber. This corroborates the basic picture that propagating modes with real (or nearly real) k_r and ω cannot exist in a strongly magnetized star, and that gravity waves are converted to slow magnetic waves by strong magnetic fields. Table 4.1 reports the critical and cutoff depths $|a_c|^{-1}$ and $|a_\infty|^{-1}$ for these solutions.

However, there are some interesting features unique to this problem, which were unanticipated by the discontinuous solutions. First, the ‘‘cutoff’’ values of $|a|$ where the wavenumbers diverge are approximately

$$|a_\infty| \approx \frac{1}{2(\ell - |m|) + 3}. \quad (4.44)$$

This deviates from the expected cutoff heights for $m \neq 0$ modes, which are the solutions to Equation 4.33 and lie close to even numbers rather than odd numbers. The $m = 0$ modes have $a_\infty^{-1} = 2\ell - 1$ (Figure 4.2), offset by 4 (in inverse depth) for the same values of $\ell - |m|$. This should not be too surprising because, at $b \gtrsim 1$, the mode eigenfunctions are very different in each case. The modes described here gain substantial complex parts (unlike the $m = 0$ modes), and logarithmic ‘‘spike’’ features appear in the real part of p' , as shown in the bottom panel of Figure 4.9.

Figure 4.10 also shows that the imaginary components of k_r and ω are largest for b slightly larger than unity, reaching up to $\approx \text{Re}(\omega)/12$ in the $(1, 1)$ case. For larger values of b , the complex arguments of k_r and ω appear to decrease to roughly constant values of $\arg(\omega) = \arg(k_r) \sim 10^{-2}$. However, due to numerical difficulty, we are unable to confirm this behavior for $b \gtrsim 2.5$ or much lower values of c .

At values of b just above unity, the eigenfunctions behave similarly to the discontinuous solutions, with a sharp peak in ξ_ϕ and a discontinuity in ξ_θ at the critical latitude (Figure 4.8). In the dissipationless solutions (Section 4.4.2), we assumed that a given mode oscillates

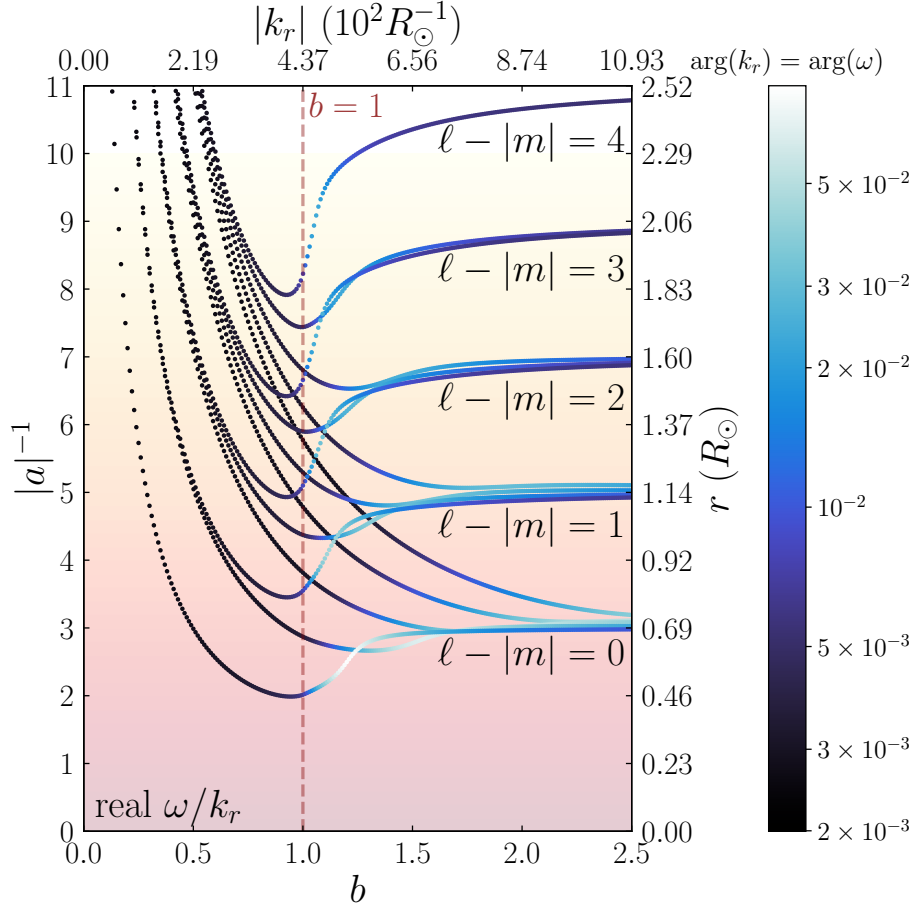


Figure 4.10: The inverse depth parameter a^{-1} plotted against b for tesseral/sectoral ($m \neq 0$) modes, with finite dissipation and real $v_{p,r} = \omega/k_r$ (Section 4.5.2). The color represents the complex argument of ω , which is enforced to be equal to the complex argument of k_r . Both a^{-1} and b have been translated to r and k_r as in Figure 4.2. As in previous figures, waves follow these tracks to the right as they are converted from gravity waves to slow magnetic waves.

entirely in phase (i.e., each perturbation was either totally real or totally imaginary). For dissipative modes with b only slightly larger than 1, this is still true—for example, for the (5, 4) mode at $b = 1.3$ (lower panels of Figure 4.8), the delta function feature in ξ_ϕ oscillates in phase with the bulk oscillation between the critical latitudes (both are imaginary). However, at higher values of b (lower panels of Figure 4.9), the sharp/discontinuous features oscillate $\pi/2$ out of phase with the bulk oscillation (e.g., the delta function in ξ_ϕ becomes real). The spike in $\text{Im}(\omega)$ (which occurs on the slow magnetic branch) coincides with a transition between these two regimes. This latter behavior is not captured by the non-dissipative solution, which assumes that ξ_ϕ and ξ_θ are purely real. It is thus unsurprising that the cutoff depths a_∞^{-1} predicted by the non-dissipative solution (Section 4.4.2) do not coincide with

those predicted by Equation 4.44. For increasingly small values of c , the spike features of the eigenfunctions at the critical latitudes become increasingly sharp and narrow. This makes calculating the eigenfunctions increasingly numerically challenging for smaller viscosities (we have chosen $c = 10^{-2}$ here). Decreasing c from this value appears to steadily decrease $\text{Im}(\omega)$ for small values of b , but only marginally for large values of b . We suspect this is due to the finite damping rates that persist at vanishing viscosities/diffusivities for waves with these sorts of internal singularities, as discussed earlier. If true, the upward-propagating branch would also be radially evanescent: this complicates the energetic argument that all initially ingoing wave power must be carried by out by the upward-propagating branch rather than the ingoing evanescent one described in Section 4.5.1. However, since in this case the damping rate $\text{Im}(\omega)$ remains finite, we believe it is most likely that the wave energy be dissipated on the upward-propagating branch, rather than transmitting through the core. Moreover, as $k_r \rightarrow 0$ on this branch, upward-propagating waves will eventually attain high enough wavenumbers that they should be efficiently damped by even arbitrarily small dissipation c : the argument that the wave energy is dissipated in the upward-propagating branch would then be the same as previous.

4.6 Further remarks

4.6.1 Behavior of the wavefunctions near the equator and critical latitudes

A primary assumption of our analysis is that perturbations vary much faster in the radial direction than the horizontal direction. This allowed us to effectively decouple the radial dependence of the mode from the horizontal dependence, and solve the latter independently as a two-dimensional problem over the sphere. The problem then reduces to a more tractable one-dimensional eigenproblem by making an assumption that the equilibrium field is axisymmetric (although some analytical insight is still available if this assumption is relaxed; see Section 4.6.3). For gravity modes at zero field, the ratio of $k_r/k_h = N/\omega$ is large, and this assumption is very reasonable. This assumption has also been instrumental in defining a hierarchy of variables whereby buoyancy and magnetism contribute at similar strengths to mode restoration (via Equation 4.3), and that k_r dominates the magnetic interaction. However, this hierarchy can be subverted in a few ways.

First, in regions where the magnetic field is nearly horizontal, $v_{Ar} \approx 0$, and the magnetic interaction $(\vec{k} \cdot \vec{v}_A)^2 = k_r^2 v_{Ar}^2 + 2k_r k_h v_{Ar} v_{Ah} + k_h^2 v_{Ah}^2$ is no longer dominated by the radial part. The other magnetic terms become comparable when $k_r v_{Ar} \lesssim k_h v_{Ah}$, which is when $v_{Ar}/v_{Ah} \lesssim k_h/k_r \sim \omega/N$. For a dipole field, this occurs in a very narrow band around the equator with angular extent $\delta\theta \sim \omega/N \ll 1$. It is possible that mode confinement between the critical latitudes found in our work may “funnel” refracted magnetogravity

waves into radially propagating solutions which may produce detectable surface power in outgoing magnetogravity waves. We further investigate such equatorially confined magnetogravity waves in Appendix 4.C. While such waves may exist, they have large horizontal wavenumbers and very large radial wavenumbers, so they may be difficult to observe.

The usual hierarchy can also be subverted very near the critical latitudes, where the solutions described in this work attain very sharp horizontal features. More specifically, our solutions predict that ξ_θ has a discontinuity and ξ_ϕ is a delta function according to the solutions in Section 4.4.2. While the presence of dissipation (Section 4.5) may smooth these sharp features somewhat, the sharpness of the features is still cause for concern in realistic stars where these effects are small. As in the example above, the $k_h v_{Ah}$ terms will become important near the critical latitude and can regulate the singularity in our equations.

Now assuming a WKB approximation in both the radial and horizontal directions and a purely poloidal field ($B_\phi = 0$), the horizontal momentum equations become

$$\begin{aligned}\omega^2 \vec{\xi}_h &= \left(\vec{k} \cdot \vec{v}_A \right)^2 \vec{\xi}_h \\ &= \left(k_r^2 v_{Ar}^2 + 2k_r k_\theta v_{Ar} v_{A\theta} + k_\theta^2 v_{A\theta}^2 \right) \vec{\xi}_h\end{aligned}\quad (4.45)$$

where we have ignored the pressure term (note that the Alfvén waves which cause the sharp features at the critical latitudes cannot be restored by pressure).

Keeping the dominant terms (and still assuming $k_r \gg k_h, B_r \sim B_h$),

$$\omega^2 - k_r^2 v_{Ar}^2 = 2k_r k_\theta v_{Ar} v_{A\theta}. \quad (4.46)$$

Because the left-hand side of Equation 4.46 is close to zero near the critical latitude, we can perform a Taylor expansion in the horizontal direction:

$$-k_r^2 \frac{\partial v_{Ar}^2}{\partial \theta} \delta\theta \approx 2k_r k_\theta v_{Ar} v_{A\theta} \approx \frac{2k_r v_{Ar} v_{A\theta}}{r \delta\theta} \quad (4.47)$$

where $\delta\theta$ is the horizontal angular distance from the resonance point where $|\omega| = |k_r v_{Ar}|$. Here we have assumed that the displacements vary on an angular length scale $\delta\theta$ such that $k_\theta \sim 1/(r \delta\theta)$. Appendix 4.D solves for the “wavefunction” $\vec{\xi}_h$ more precisely.

From Equation 4.47, we then see that the horizontal field terms become important when

$$|\delta\theta| \lesssim \sqrt{\frac{v_{A\theta}}{k_r r} \left| \frac{\partial v_{Ar}}{\partial \theta} \right|^{-1}}. \quad (4.48)$$

However, since $v_{Ar} \sim v_{A\theta}$ typically,

$$\frac{1}{v_{A\theta}} \frac{\partial v_{Ar}}{\partial \theta} \sim \frac{\partial \ln v_A}{\partial \theta} \sim 1 \quad (4.49)$$

for a large-scale (e.g., dipole) magnetic field. Therefore, near the critical latitudes, we expect that the wavefunction $\vec{\xi}_h$ will vary over an angular scale

$$|\delta\theta| \sim \frac{1}{\sqrt{k_r r}}. \quad (4.50)$$

This angular scale also naturally appears in Appendix 4.D, where it describes the angular wavenumber of Alfvén waves near the critical latitude. Note that, because magnetogravity waves with $m = 0$ have $\xi_\phi = 0$, they cannot couple to $m = 0$ Alfvén waves, which are purely toroidal (i.e., $\xi_\theta = 0$; Loi and Papaloizou, 2017). This physically explains why sharp fluid features near critical latitudes do not appear in our $m = 0$ solutions (Section 4.4.1), or earlier two-dimensional solutions (Lecoanet, Vasil, et al., 2017).

Physically, the Alfvén and magnetogravity waves, which are decoupled in the dispersion relation of Equation 4.3, may become strongly coupled in a narrow band due to additional small terms left out of Equation 4.3. Because the Alfvén waves are expected to have angular scales $\delta\theta \sim 1/\sqrt{k_r r}$ due to the effect of the horizontal field, coupling between Alfvén and magnetogravity waves should also occur within $\sim \delta\theta$ of a critical latitude (due to geometric overlap). This coupling may allow a small amount of gravity wave power to be converted into outgoing Alfvén waves. These Alfvén waves would then propagate along a closed field line, eventually curving back inwards to the critical latitude on the opposite hemisphere of the star. Here, they could be converted back into outgoing gravity waves, potentially allowing for some wave power to escape the core. This possibility could be investigated with numerical simulations.

Additionally, the presence of shear stress would also cause quantifiable departures from the horizontal mode structure derived in this work. While plasmas do not generally have shear restorative forces, Hoven and Levin (2011) argue that tangling in the equilibrium magnetic field at small scales can produce a small effective shear modulus. We investigate this possibility further in Appendix 4.E, finding that it causes the wave function to have an Airy function horizontal dependence near the critical latitude.

Out of these effects, it is most likely that the horizontal field terms have the largest impact on the mode structure (i.e., $\delta\theta$ as given by Equation 4.50 most accurately characterizes when our solutions break down). Both dissipation and shear stress (due to, e.g., tangling) are likely to be small in real stars, but any physical equilibrium fields must have horizontal

magnetic fields $B_h \sim B_r$. In general, the importance of horizontal-field terms near the equator and critical latitudes strongly suggests that a search for global solutions with those terms included is the natural next step for accurately characterizing strong-field g modes. However, the solutions become non-separable in the radial and horizontal directions, and a solution of the full, coupled partial differential equations would be necessary. A global treatment of magnetogravity modes dramatically increases the complexity of any numerical mode calculations, but is likely to reveal important (and hard to predict) departures from a separable treatment (as it has in eigenmode problems in differentially rotating planets, e.g., Takata and Saio, 2013; Dewberry et al., 2021). While we believe our solutions to capture the basic behavior of the waves, the effects of horizontal magnetic fields discussed here are likely to be the more important effect in real stars, and should be examined more thoroughly in future work.

4.6.2 The continuum spectrum and nonharmonic solutions

In this work, we have focused on harmonic solutions with time dependence $\propto e^{i\omega t}$, for some global oscillation frequency ω . However, the unusual nuances introduced by the internal singularity suggest more general approaches may be appropriate. For example, standard Sturm–Liouville theory only ensures that the eigenfunctions of $\mathcal{L}_{\text{mag}}^{m,b}$ form a basis for a real $b \propto k_r$ in the absence of internal singularities. Thus, while we have mostly discussed the discrete spectrum of eigenfunctions of $\mathcal{L}_{\text{mag}}^{m,b}$, it is not guaranteed that an arbitrary perturbation can be decomposed into them, both because b is not necessarily real and because different modes at the same radius are eigenfunctions of different differential operators (i.e., $\mathcal{L}_{\text{mag}}^{m,b}$ for different b). In general, the continuous spectrum of Alfvén waves (i.e., Section 4.4.3) plays a major role.

Similar frequency-dependent internal singularities often appear in problems related to differentially-rotating fluids. In such problems, authors such as Burger (1966) and Balbinski (1984) apply more general Laplace transform techniques involving contour integrals to solve for the time dependence of possible solutions. Specifically, Balbinski (1984) find that the continuum spectrum in a differentially-rotating cylinder corresponds to perturbations which oscillate periodically and also decay as a power law in time. In those “quasi-modal” solutions, the oscillation frequency depends on position, and hence the solutions are not separable in space and time.

Levin (2007) and Hoven and Levin (2011) intuitively explain the origin of such non-exponential time dependence in the context of the coupling of a magnetar crust mode to an Alfvén continuum in the magnetar bulk. In a toy model analogous to this problem, a

“large” oscillator (the crust mode) couples to a dense collection of “small” oscillators (the Alfvén modes). In our case, the “large” oscillator would be an ingoing gravity wave. At early times, the large oscillator’s amplitude exponentially decays as energy is distributed among the small oscillators. However, the time dependence transitions to algebraic decay to a finite, nonzero amplitude driven by coherent driving from small oscillators at the edges of the continuum. In the presence of dissipation, such edge modes retain energy for much longer than modes in the interior of the continuum. It is unclear how these edge modes manifest in the simplified model of magnetogravity waves presented in this work.

Interestingly, Boyd (1981) note in their Appendix B that the decomposition of perturbations into either real-eigenvalue continuum modes or complex-eigenvalue discrete modes are equivalent and complementary approaches. The eigenfunctions of the modes may diverge at some points, similar to an Alfvén wave confined to a single field line. However, a superposition of a continuous spectrum of modes can produce a finite-valued function. Hence, examining single continuum modes can be misleading, but they can be superposed to produce unusual decay behavior as in Balbinski (1984). In future work, application of these insights to the magnetogravity wave problem may shed more light on what to expect in real stars, including the possibility of quasi-modes with non-harmonic time dependence.

4.6.3 Magnetogravity waves in general geometries

In this work, we have focused on dipolar magnetic field configurations whose radial components have angular dependence $\propto \cos \theta$ (Equation 4.9). However, many real stars have more complex field morphologies (Maxted, Ferrario, et al., 2000; Tout, Wickramasinghe, and Ferrario, 2004; Donati and Landstreet, 2009; Kochukhov, Lundin, et al., 2010; Szary, 2013; Kochukhov and Wade, 2016). In this Section, we generalize some of the arguments made in Section 4.4 to more general magnetic fields of the form

$$B_r = B_0(r)\psi(\theta, \phi) \quad (4.51)$$

where ψ is a dimensionless function describing the horizontal dependence of the field. As in Section 4.2.3, we use a WKB approximation such that terms dependent on the horizontal component of the field are small and can be dropped. Without loss of generality, we can rescale ψ and B_0 so that the maximum of $|\psi|$ on the sphere is 1.

The general problem can be non-dimensionalized in the same way as described in Section 4.2.2. In particular, we still define b and a as in Equations 4.5 and 4.6, but interpreting v_A as the maximum Alfvén speed at a given radius (which no longer necessarily occurs at the

poles). Via Equations 4.2, the perturbations are given by

$$\xi_r = \frac{ik_r}{\rho_0 N^2} p' \quad (4.52a)$$

$$\vec{\xi}_h = \frac{1}{\rho_0 \omega^2 r (1 - b^2 \psi(\theta, \phi)^2)} \nabla_h p' \quad (4.52b)$$

$$\rho' = \frac{ik_r}{g} p' \quad (4.52c)$$

where we have defined the horizontal gradient,

$$\nabla_h = \hat{\theta} \frac{\partial}{\partial \theta} + \hat{\phi} \frac{1}{\sin \theta} \frac{\partial}{\partial \phi} \quad (4.53)$$

with the factor of $1/r$ excluded.

Substituting Equations 4.52 into the continuity equation (Equation 4.2a), we obtain

$$0 = \frac{b^2}{a^2} p' + \nabla_h \cdot \left(\frac{1}{1 - b^2 \psi^2} \nabla_h p' \right) \quad (4.54)$$

We see that Equation 4.54 can be viewed as a partial differential equation to be solved over a sphere of radius a^{-1} (i.e., Equation 4.54 can be rewritten without a after defining some $\nabla_a = a \nabla$). In other words, the depth parameter a parameterizes the effective “curvature” of the spherical domain over which the horizontal equations are to be solved. Since we have not assumed a specific magnetic field geometry here, the form of the differential eigenproblem in Equation 4.4 is generic. In the case of an axisymmetric field, the two-dimensional angular differential operator in Equation 4.54 can be reduced to a differential operator in θ only (recovering, e.g., Equation 4.12, for a dipole field).

Equation 4.52b can be rearranged to

$$\nabla_h p' = \rho_0 \omega^2 r \left(1 - b^2 \psi^2 \right) \vec{\xi}_h. \quad (4.55)$$

We therefore see that, so long as $\vec{\xi}_h$ is finite, $\nabla_h p' = 0$ along any critical surface ($|\psi| = \pm 1/|b|$) as long as b is real.

The vanishing directional derivative of p' across the critical surface generalizes an analogous result in Section 4.3.3 for the dipole geometry. Physically, this result simply reflects that, at the site of an Alfvén resonance, magnetic tension completely accounts for the (horizontal) restoring force of the mode, and the pressure perturbation makes no contribution. This fact was also used in Section 4.4.2 to show that dissipationless $m \neq 0$ solutions must vanish outside of the critical latitudes.

We can perform a similar analysis as in Section 4.4.2 by multiplying Equation 4.54 by p'^* and integrating over the region of the sphere where $|b\psi| < 1$ (i.e., where $\omega < \omega_A$), denoted by $S_<$:

$$0 = \frac{b^2}{a^2} \int_{S_<} |p'|^2 d\Omega + \int_{S_<} p'^* \nabla_h \cdot \left(\frac{1}{1 - b^2\psi^2} \nabla_h p' \right) d\Omega. \quad (4.56)$$

The second term becomes

$$\begin{aligned} & \int_{S_<} p'^* \nabla_h \cdot \left(\frac{1}{1 - b^2\psi^2} \nabla_h p' \right) d\Omega \\ &= \int_{S_<} \nabla_h \cdot \left(\frac{1}{1 - b^2\psi^2} p'^* \nabla_h p' \right) d\Omega - \int_{S_<} \frac{1}{1 - b^2\psi^2} |\nabla_h p'|^2 d\Omega \\ &= \int_{\partial S_<} \frac{1}{1 - b^2\psi^2} p'^* \nabla_h p' \cdot \hat{n} d\chi - \int_{S_<} \frac{1}{1 - b^2\psi^2} |\nabla_h p'|^2 d\Omega \end{aligned} \quad (4.57)$$

where we have first integrated by parts, and then applied the divergence theorem to the first term ($\partial S_<$ denotes the boundary of $S_<$, $d\chi$ is an angular line element, and \hat{n} points out of $S_<$). If the first (boundary) term in Equation 4.57 vanishes, then

$$\frac{b^2}{a^2} = \frac{\int_{S_<} \frac{1}{1 - b^2\psi^2} |\nabla_h p'|^2 d\Omega}{\int_{S_<} |p'|^2 d\Omega} > 0 \quad (4.58)$$

generalizes Equation 4.30. However, this process can be repeated for $S_>$, the region where $|b\psi| > 1$, to obtain

$$\frac{b^2}{a^2} = \frac{\int_{S_>} \frac{1}{1 - b^2\psi^2} |\nabla_h p'|^2 d\Omega}{\int_{S_>} |p'|^2 d\Omega} < 0. \quad (4.59)$$

Since b^2/a^2 may only have one sign or another for a given global mode, we see that modes for which k_r and ω are both real (i.e., propagating and non-decaying) will be localized to the region where $\omega < \omega_A$ in the case when the boundary term in Equation 4.57 vanishes. This condition will be satisfied when the complex winding number enclosed by $\partial S_<$ is nonzero, since $p' = \text{const.}$ on $\partial S_<$. This argument generalizes the result described in Section 4.4.2 that propagating, non-decaying $m \neq 0$ modes in the dipole geometry must be localized between the critical latitudes.

4.6.4 Stable g modes in convective regions

Standard mixing-length theory assumes a slight superadiabatic temperature gradient such that $N^2 < 0$ in convective zones. While g modes in non-rotating, non-magnetized stars are only present in stably stratified (radiative) regions, Lee and Saio (1997) show that buoyancy-restored oscillatory modes (real ω) can be stabilized even in convective regions ($N^2 < 0$) by

sufficiently high rotation. In particular, when $|\Omega| > |\omega|/2$, the coefficient functions which appear in the Laplace tidal operator $\mathcal{L}_{\text{rot}}^{m,v}$ (Equation 4.17) are no longer strictly positive, and it will possess negative eigenvalues $\lambda < 0$. In this case, $k_h = \sqrt{\lambda}/r$ becomes imaginary, and there exist solutions to $k_h/k_r = \omega/N$ when N is also imaginary. While standard g modes under strong rotation tend to be localized to the equator, these rotationally stabilized convective modes are instead localized near the poles (Lee and Saio, 1997).

However, the same argument can be applied to the magnetogravity problem, and gives meaning to the negative branches of eigenvalues λ implied by Equation 4.12. In particular, like $\mathcal{L}_{\text{rot}}^{m,v}$, the operator $\mathcal{L}_{\text{mag}}^{m,b}$ (Equation 4.13) also contains coefficients which switch signs over the domain. In this formalism, for oscillatory solutions with real ω , a becomes imaginary, and one instead must solve

$$\mathcal{L}_{\text{mag}}^{m,b} p' - \frac{b^2}{|a|^2} p' = 0 \quad (4.60)$$

where now the (negative) eigenvalues λ of $\mathcal{L}_{\text{mag}}^{m,b}$ must satisfy

$$\lambda = -b^2/|a|^2. \quad (4.61)$$

In the case of no buoyancy ($N^2 = 0$) and relaxing the Boussinesq assumption, convective regions are expected to sustain standard magnetohydrodynamic waves (Shu, 1991). On top of these modes, the aforementioned negative eigenvalue branches hint at the existence of buoyancy-restored oscillations in convective regions which are stabilized by magnetic forces. By a similar argument as made in Section 4.4.2, Equation 4.60 implies that such $\lambda < 0$ modes would be exactly localized *outside* (rather than inside) the critical latitudes. Moreover, while they require $|b| > 1$, there is no formal upper limit on the magnetic fields at which they can exist, meaning they may exist in the convective cores of strongly magnetized stars.

While the analogy to rotationally stabilized convective modes seems obvious, we note the magnitude of the Brunt–Väisälä frequency $|N|$ is typically extremely close to 0 in convective zones, owing to the extremely efficient mixing caused by the convective instability. Note that this feature is not unique to the magnetogravity problem, and would also be true for the rotational problem considered by Lee and Saio (1997). This appears to violate a fundamental assumption of our analysis that $k_r/k_h \sim N/\omega$ is large, or at least implies that stable convective oscillations which can accurately be described by our formalism must be of very low frequency. Therefore, we strongly caution against using the formalism in this work to make quantitative (or even strong qualitative) predictions about the properties of

these modes. More detailed analyses relaxing this assumption are necessary to characterize these modes accurately (if indeed they exist).

4.7 Summary

In this work, we have characterized the pulsation modes of a spherically symmetric, stratified stellar structure with a strong dipole magnetic field. We focus on radiative zones with large Brunt–Väisälä frequencies such that magnetogravity waves have short radial wavelengths. We have assumed that

- the radial wavelength is everywhere much smaller than both the stellar structure length (the radial WKB approximation) and the horizontal wavelength (i.e., the wavevector is primarily radial),
- oscillations are incompressible and adiabatic,
- perturbations to the gravitational potential can be ignored (Cowling), and
- dissipative processes are either formally absent (Section 4.4) or small (Section 4.5).

Our chief conclusions are as follows:

1. Propagating zonal ($m = 0$) magnetogravity modes merge at a finite field with a branch of slow magnetic waves whose wavenumbers diverge at a finite cutoff radius. Their horizontal eigenfunctions are Hough functions for a dipolar magnetic field. Hence, ingoing gravity waves are converted into slow magnetic waves at a critical magnetic field strength similar to that derived in Fuller, Cantiello, et al., 2015. Above this field strength, the modes become evanescent and cannot propagate. This is in agreement with the results of Lecoanet, Vasil, et al. 2017 in a similar geometry.
2. Propagating sectoral and tesseral ($m \neq 0$) modes also merge with branches of slow magnetic waves whose wavenumbers diverge at a cutoff radius within the star. Like $m = 0$ modes, ingoing gravity waves cannot propagate above a critical magnetic field strength, and are instead converted to outgoing slow magnetic waves. For strong fields and large wavenumbers, the modes are closely confined to the equator, and are bounded by sharp features in the fluid displacement profile at critical latitudes where the wave frequency is resonant with Alfvén waves.
3. Even vanishingly small dissipation can cause qualitative deviations from the problem where dissipation is formally set to zero. This can be heuristically understood because

viscosity allows for interaction between magnetogravity waves and the continuous Alfvén wave spectrum. However, even for finite dissipation, the conclusion that sufficiently high magnetic fields will destroy all propagating magnetogravity modes is robust.

4. Near the critical latitudes and equator, magnetic tension terms associated with the horizontal field are likely to affect the mode structure significantly. Thus, a global solution which includes such terms is necessary to confidently characterize the mode structure very near these regions. We speculate that such an analysis might reveal that an observable amount of wave power may be able to escape a strongly magnetized stellar core through coupling with Alfvén waves (at critical latitudes) or extremely localized magnetogravity waves (near the equator).

Our analysis reinforces conclusions from earlier studies that strong magnetic fields should convert gravity waves into slow magnetic waves that damp within stellar interiors, causing magnetic fields to suppress the amplitudes of gravity modes in red giant stars (Fuller, Cantiello, et al., 2015; Stello, Cantiello, Fuller, Huber, et al., 2016). However, it may remain possible that higher-order WKB terms (neglected in our analysis) or modes with non-harmonic time dependence (Section 4.6.2) could allow for some signatures of mixed modes in observed power spectra as claimed by Mosser, Belkacem, et al. (2017). More effort accounting for these effects will be required to robustly predict the magnetogravity pulsation spectra of stars with strong magnetic fields.

4.A Magnetogravity eigenproblems in other geometries

In this Appendix, we non-dimensionalize the fluid equations for the geometries considered by Fuller, Cantiello, et al. (2015) and Lecoanet, Vasil, et al. (2017), and show that they can be interpreted as similar eigenvalue problems as considered in our work.

4.A.1 Fuller, Cantiello, et al. (2015): Uniform radial field model

The model presented by Fuller, Cantiello, et al. (2015) can be precisely reproduced by adopting a purely uniform radial magnetic field,

$$\vec{B}_0 = B_0(r) \hat{r}. \quad (4.62)$$

Adopting a WKB approximation in the radial direction, we can define

$$b_F = \frac{k_r v_A}{\omega} \quad (4.63a)$$

$$a_F = \left(\frac{N}{\omega} \right) \left(\frac{v_A/r}{\omega} \right) \quad (4.63b)$$

where $v_A = B_0(r)/\sqrt{4\pi\rho_0}$.

While such a monopolar field is clearly unphysical, it is also a useful toy model because it retains the spherical symmetry of the zero-field problem. Therefore, its horizontal eigenfunctions are simply spherical harmonics, and its dispersion relation is

$$\frac{\ell(\ell+1)}{1-b_F^2} = b_F^2/a_F^2. \quad (4.64)$$

Equation 4.64 can be analytically solved for b_F to yield

$$b_F^2 = \frac{1}{2} \pm \frac{1}{2} \sqrt{1 - 4a_F^2\ell(\ell+1)} \quad (4.65)$$

where it can be seen that there are no real solutions for b_F for some critical $a_F > a_c^\ell$ given by

$$a_c^\ell = \frac{1}{2\sqrt{\ell(\ell+1)}}. \quad (4.66)$$

This is equivalent to the result originally presented by Fuller, Cantiello, et al. (2015) that there are no propagating solutions when the magnetogravity frequency (defined in Equation 4.1) rises above the mode frequency. At small buoyancy or Alfvén frequencies, the two solutions for b_F^2 in Equation 4.65 approach the usual internal gravity wave and Alfvén wave dispersion relations, and remain finite. Equations 4.62, 4.63, and 4.64 are analogous to Equations 4.9, 4.5 and 4.6, and 4.15 in the main text.

4.A.2 Lecoanet, Vasil, et al. (2017): Multipole Cartesian geometry

Lecoanet, Vasil, et al. (2017) consider a Cartesian geometry with the equilibrium magnetic field configuration

$$\vec{B}_0 = B_0 e^{-k_B z} [\sin(k_B x) \hat{x} + \cos(k_B x) \hat{z}] \quad (4.67)$$

where the oscillatory dependence in x is chosen to closely mimic the θ dependence of a multipole magnetic field.

Define k_P to the wavenumber which defines the periodicity of the domain, i.e., the solution is periodic in x with a period $2\pi/k_P$ (k_P is analogous to $1/r$ in the spherical problem). We can first define

$$b_L = \frac{k_z v_A}{\omega} \quad (4.68a)$$

$$a_L = \left(\frac{N}{\omega}\right) \left(\frac{k_P v_A}{\omega}\right) \quad (4.68b)$$

where $v_A = B_0 e^{-k_B z} / \sqrt{4\pi\rho_0}$.

Then, following a very similar procedure to the spherical dipole problem described in the main text, the three-dimensional Cartesian problem corresponding to the field in Equation 4.67 can be reduced to

$$\mathcal{L}^{m,b_L} p'(\mu) + \frac{b_L^2}{a_L^2} p'(\mu) = 0 \quad (4.69)$$

where $\mu = \cos(k_P x)$.

In the special case that $k_B = k_P$ (i.e., a dipole field), the differential operator \mathcal{L}_L^{m,b_L} is given by

$$\mathcal{L}_L^{m,b_L} p'(\mu) = \sqrt{1 - \mu^2} \frac{d}{d\mu} \left(\frac{\sqrt{1 - \mu^2}}{1 - b_L^2 \mu^2} \frac{dp'(\mu)}{d\mu} \right) - \frac{m^2}{1 - b_L^2 \mu^2} p'(\mu) \quad (4.70)$$

where $m = k_y/k_P$. Letting λ_L be a given (negative) eigenvalue of \mathcal{L}_L^{m,b_L} , the dispersion relation takes the form

$$\lambda_L = b_L^2/a_L^2. \quad (4.71)$$

Lecoanet, Vasil, et al. (2017) solve the problem described above in the two-dimensional zonal case (i.e., $m = 0$), taking advantage of the fact that two-dimensional incompressibility defines a “vector potential” whose direction is everywhere orthogonal to the fluid motions. They find the eigenfunctions to be Mathieu functions (Mathieu, 1868), with a branch of inward-traveling internal gravity waves refracting up into a branch of slow magnetic waves which diverge to infinite wavenumber at a finite “cutoff” radius. We reproduce this behavior in the dipole geometry for the $m = 0$ modes (see Section 4.4.1).

Equations 4.67, 4.68, 4.69, 4.70, and 4.71 are analogous to Equations 4.9, 4.5 and 4.6, 4.12, 4.13, and 4.15, in the main text. We see that, aside from geometrical factors $\propto \sqrt{1 - \mu^2}$ (which become irrelevant in the large b_L limit), $\mathcal{L}_{\text{mag}}^{m,b}$ and \mathcal{L}_L^{m,b_L} are identical.

4.B Numerically solving $\mathcal{L}_{\text{mag}}^{m,b}$

We use a relaxation scheme to numerically solve Equations 4.72 and 4.73, following closely the procedure used by Lee and Saio (1997) and Fuller and Lai (2014) to diagonalize the Laplace tidal equation, using the C++ implementation given by *Numerical Recipes* (Press et al., 2007).

However, the procedures which we adopt vary somewhat for the dissipative and dissipationless cases. The numerical solution procedure for Sections 4.4.1 and 4.4.2 is summarized in Section 4.B.1, and the procedure for Section 4.5 is summarized in Section 4.B.2.

4.B.1 Numerical solution without dissipation

In the $m = 0$ (Section 4.4.1) and $m \neq 0, |b| \leq 1$ (Section 4.4.2) cases without dissipation, little special care is required to solve the requisite two first-order differential equations. In the former case, the solutions (Hough functions) are known to be second-differentiable across the singularity. In the latter case, the problem is a standard Sturm–Liouville problem with no internal singularities. Moreover, because $\mathcal{L}_{\text{mag}}^{m,b}$ (Equation 4.13) is even with respect to μ , its eigenfunctions can be partitioned into even and odd parity, which is given by $(-1)^{\ell+m}$ for p' and $(-1)^{\ell+m+1}$ for ξ_θ . This known parity greatly simplifies the problem, allowing us to solve for the eigenfunctions for only $\mu \in [0, +1)$ rather than over the full domain.

Then, defining $\mathcal{P} = p'/\rho_0\omega^2r^2$ and $\mathcal{Z}_\theta = \sqrt{1-\mu^2}\xi_\theta/r$ as (assumed real) non-dimensionalized versions of p' and ξ_θ , our equations become

$$\frac{d\mathcal{P}}{d\mu} = -\frac{1-b^2\mu^2}{1-\mu^2}\mathcal{Z}_\theta \quad (4.72\text{a})$$

$$\frac{d\mathcal{Z}_\theta}{d\mu} = \left(\frac{b^2}{a^2} - \frac{m^2}{(1-\mu^2)(1-b^2\mu^2)} \right) \mathcal{P} \quad (4.72\text{b})$$

where the first equation follows from the θ component of the momentum equation (Equation 4.10c) and the second equation follows from the continuity equation (Equation 4.10a).

Starting from Legendre polynomials as initial guess, we gradually increase b (> 0) from 0, retaining lower b solutions as initial guesses for higher b relaxations. Note that, in the numerical implementation, we promote $a = a(\mu)$ to a function of μ , and additionally enforce $da/d\mu = 0$ (this is the standard technique for solving such eigenproblems in, e.g., Press et al., 2007). We impose boundary conditions on \mathcal{P} and \mathcal{Z}_θ at $\mu = 0$ depending on parity, setting one of these variables to 0 and the other to 1 for normalization. Additionally, at the right boundary $\mu = 1 - \epsilon$, we enforce that \mathcal{Z}_θ must vanish (which can be seen in its definition).

In the $m \neq 0, |b| < 1$ case, we demonstrate in Section 4.4.2 that eigenfunctions in the formal zero-dissipation limit are exactly localized to the band between the internal singularities at $\mu = \pm 1/b$ (where we have taken $b > 0$ without loss of generality). Then we can rescale Equations 4.72 via $x = b\mu$ to

$$\frac{d\mathcal{P}}{dx} = -\frac{1-x^2}{b^2-x^2}b^3\mathcal{Z}_\theta \quad (4.73\text{a})$$

$$\frac{d\mathcal{Z}_\theta}{dx} = \left(\frac{1}{a^2} - \frac{m^2}{(b^2-x^2)(1-x^2)} \right) b^3\mathcal{P} \quad (4.73\text{b})$$

over the range $x \in [0, +1)$ (i.e., $\mu \in [0, +1/b)$), enforcing $\mathcal{P} = 0$ at $x = 1 - \epsilon$ (see Section 4.4.2).

4.B.2 Numerical solution with dissipation

When dissipation is considered, the internal singularities are “softened” in the sense that they are shifted off of the real line. Therefore, a case-wise treatment of the singularity (as in Section 4.B.1) is not necessary. However, in general, both the perturbations and at least one of the quantities k_r and ω are complex, doubling the number of equations to be solved.

Moreover, in the dissipative case (even for arbitrarily small viscosities/diffusivities), the delta function which appears in ξ_ϕ becomes softened to a sharp peak with a finite width. Therefore, instead of solving for $\mathcal{P} \sim (1 - b^2\mu^2)\xi_\phi$ as a perturbation, we probe this peak by solving the complex versions of the following equations,

$$\frac{d\mathcal{Z}_\phi}{d\mu} = \frac{2b^2\mu}{1 - b^2\mu^2 - ic}\mathcal{Z}_\phi - \frac{1}{1 - \mu^2}\mathcal{Z}_\theta \quad (4.74a)$$

$$\frac{d\mathcal{Z}_\theta}{d\mu} = \left(\lambda \left(1 - b^2\mu^2 - ic \right) - \frac{m^2}{1 - \mu^2} \right) \mathcal{Z}_\phi \quad (4.74b)$$

where $\mathcal{Z}_\phi = \sqrt{1 - \mu^2}\xi_\phi/imr$. In Section 4.5.1, we pick $c = 10^{-3}$ and take $\lambda = |\lambda|e^{i\zeta_1}$ and $b = |b|e^{i\zeta_1/2}$ and solve for $|\lambda|$ and ζ_1 , while varying $|b|$. In Section 4.5.2, we pick $c = 10^{-2}$ and take $\lambda = |\lambda|e^{i\zeta_2}$ and $b = |b|$ (real) and solve for $|\lambda|$ and ζ_2 , while again varying $|b|$. As in Section 4.B.1, the first equation follows from the θ component of the momentum equation, and the second equation follows from the continuity equation (but in terms of different perturbations). The evenness and oddness conditions can be applied as in Section 4.B.1 to $\text{Re}(\mathcal{Z}_\phi)$ (which has the same parity as \mathcal{P}) and $\text{Re}(\mathcal{Z}_\theta)$ at the left boundary $\mu = 0$. At this same boundary, we enforce (due to overall phase invariance) $\text{Im}(\mathcal{Z}_\phi) = \text{Im}(\mathcal{Z}_\theta) = 0$. Finally, at $\mu = 1 - \epsilon$, we enforce $\text{Re}(\mathcal{Z}_\theta) = \text{Im}(\mathcal{Z}_\theta) = 0$. Equations 4.74 are then solved for increasingly large values of $|b|$, using associated Legendre polynomials as the initial $|b| = 0$ guesses.

4.C Tightly confined equatorial magnetogravity waves

In this Appendix, we investigate the behavior of magnetogravity waves very close to the equator (for a dipole field), where $v_{Ar} \approx 0$. In the following, we demonstrate in this narrow equatorial band the existence of self-consistent, propagating solutions with wavenumbers enhanced in magnitude by a factor N/ω . These solutions are not captured by the analysis in the main text, which assumed that the vertical component of the Alfvén velocity dominates the mode structure. However, the dynamics of these modes may play an important role in understanding the observable, asteroseismic consequences of strong core magnetic fields.

In this region, the assumption (used throughout this work) that the Alfvén frequency $\omega_A = \vec{k} \cdot \vec{v}_A$ is dominated by the radial component is violated. We expect this violation to be important when

$$v_{Ar}/v_{Ah} \lesssim k_h/k_r \sim \omega/N \quad (4.75)$$

or in a narrow band around the equator with angular extent $\delta\theta \sim \omega/N$.

Assuming a WKB approximation in all directions, the dispersion relation for magnetogravity waves near the equator becomes

$$\omega^2 - \frac{k_h^2}{k_r^2} N^2 - k_h^2 v_{Ah}^2 = 0, \quad (4.76)$$

where now $\omega_A \approx k_h v_{Ah}$ is dominated by the horizontal component. Then, solving for k_r , we have

$$k_r^2 = \frac{k_h^2 N^2}{\omega^2 - k_h^2 v_{Ah}^2}, \quad (4.77)$$

where the criterion for radial propagation is

$$\omega^2 > k_h^2 v_{Ah}^2. \quad (4.78)$$

Because these solutions are only accurate in an equatorial band $\delta\theta \lesssim \omega/N$, it follows that

$$k_h \gtrsim \frac{N}{\omega r}, \quad (4.79)$$

i.e., at least one horizontal wavelength fits within this band. The criteria in Equation 4.78 and 4.79 can be combined to obtain

$$\omega \gtrsim \sqrt{N v_{Ah} / r} \sim \omega_B \quad (4.80)$$

where ω_B is the critical magnetic field strength from Equation 4.7, but now applied to the horizontal field rather than the radial field. Therefore, such confined magnetogravity waves would remain radially propagating in roughly the same regions that magnetogravity waves throughout the rest of the star would (within a small, order-unity factor in radius).

Interestingly, when Equation 4.78 (for the minimum k_h) is combined with Equation 4.77 for propagating waves, we obtain

$$|k_r| \gtrsim \frac{N}{\sqrt{\omega^2/k_{h,\min}^2 - v_{Ah}^2}} \sim \left(\frac{N}{\omega}\right)^2 \frac{1}{r} \quad (4.81)$$

where we have examined the limit where $v_{Ah} \ll r\omega^2/N$ (i.e., at fields much lower than the critical field, or where $\omega \gg \omega_B$). This radial wavenumber is larger than the radial wavenumber of normal, low- ℓ gravity waves by a large factor $\sim N/\omega$, implying that magnetogravity

4.D. Structure of Alfvén resonances including horizontal-field contributions to the magnetic tension waves near the equator will develop very small radial wavelengths. This increased radial wavenumber appears to be qualitatively consistent with numerical simulations conducted by Lecoanet, Vasil, et al. (2017), which seem to exhibit such waves at locations where the radial magnetic field vanishes (see their Figure 6). However, their simulation also seems to show outgoing equatorially confined evanescent waves, whose driving we cannot explain. Moreover, due to their small spatial scale, it is unclear to us whether these modes are numerically resolved. Future work will be required to further elucidate the nature of these highly confined modes.

Note that the dispersion relation in Equation 4.77 implies that the group and phase velocities of these confined magnetogravity waves are in opposite directions (similar to normal, zero-field gravity waves). Because the refracted, outgoing magnetogravity wave solutions at $b > 1$ (described in the rest of this work) have aligned group and phase velocities, this implies that such outgoing magnetogravity waves couple most efficiently to *ingoing*, equatorially confined magnetogravity waves (described above). This poses a challenge for equatorially confined magnetogravity waves as a vehicle for bringing wave power out of the core. Moreover, the very short wavelengths of the equatorially confined waves make them much more susceptible to damping processes. Further work may elucidate the nature of these waves, and their role in wave power transport and dissipation.

4.D Structure of Alfvén resonances including horizontal-field contributions to the magnetic tension

In the solutions throughout the main text, it has been assumed that the magnetic tension terms which appear in the momentum equations are dominated by the radial component (in, e.g., Equations 4.10). However, very near to $\omega^2 = k_r^2 v_{Ar}^2$ (i.e., very near to a critical latitude), the horizontal components of the magnetic tension may become relevant. As described throughout the text (e.g., Section 4.6.1), sharp horizontal fluid features may appear in the vicinity of Alfvén resonances. To estimate the impact of such terms, we will make a WKB approximation in both the radial *and* horizontal directions (i.e., $k_r, k_h \gg 1/r$). We further hypothesize that it still remains true that $k_h \ll k_r$ (this will set a condition for validity). For Alfvén waves, we examine the horizontal momentum equation:

$$\left(k_r^2 v_{Ar}^2 + \frac{2ik_r v_{Ar} v_{A\theta}}{r} \frac{d}{d\theta} - \frac{v_{A\theta}^2}{r^2} \frac{d^2}{d\theta^2} \right) \vec{\xi}_h = \omega^2 \vec{\xi}_h, \quad (4.82)$$

where we have assumed a poloidal field ($B_\phi = 0$) for simplicity. Because we are interested in the solution in the vicinity of $\omega^2 - k_r^2 v_{Ar}^2 \approx 0$, we can perform a Taylor expansion:

$$\omega^2 - k_r^2 v_{Ar}^2 \approx -k_r^2 \frac{dv_{Ar}^2}{d\theta} \delta\theta \quad (4.83)$$

where $\delta\theta = \theta - \theta_c$, and θ_c is the critical latitude. Then Equation 4.82 becomes

$$\frac{2ik_r v_{Ar} v_{A\theta}}{r} \frac{d\vec{\xi}_h}{d\theta} = -k_r^2 \frac{dv_{Ar}^2}{d\theta} \delta\theta \vec{\xi}_h = -2k_r^2 v_{Ar}^2 \frac{d \ln v_{Ar}}{d\theta} \delta\theta \vec{\xi}_h \quad (4.84)$$

where $k_h \gg k_r$ allowed us to drop the term $\propto d^2\vec{\xi}_h/d\theta^2$. This becomes

$$\frac{d\vec{\xi}_h}{d\theta} = ik_r r \frac{v_{Ar}}{v_{A\theta}} \frac{d \ln v_{Ar}}{d\theta} \delta\theta \vec{\xi}_h. \quad (4.85)$$

Then, since $v_{Ar} \sim v_{A\theta}$ and $d \ln v_{Ar}/d\theta \simeq 1$ (since v_{Ar} varies horizontally roughly on the order of a radian), the prefactors involving v_{Ar} and v_{Ah} are order-unity. Doing this more carefully for a dipole field (where $v_{Ar} \propto 2 \cos \theta$ and $v_{Ah} \propto \sin \theta$) yields

$$\frac{d\vec{\xi}_h}{d\theta} = -2ik_r r \delta\theta \vec{\xi}_h. \quad (4.86)$$

Equation 4.86 is straightforwardly solved by

$$\vec{\xi}_h \simeq \vec{\xi}_{h,0} e^{-ik_r r \delta\theta^2}. \quad (4.87)$$

This complex Gaussian describes a wave whose wavelength decreases away from the critical latitude θ_c . The first wavelength occurs where $rk_r \delta\theta^2 = 2\pi$, yielding a characteristic angular scale of $\delta\theta \sim 1/\sqrt{k_r r}$, or characteristic angular wavenumber of $rk_\theta \sim \sqrt{k_r r}$ (compare Equation 4.50). Note that this horizontal wavenumber satisfies our assumption that $1/r \ll k_\theta \ll k_r$.

4.E Magnetic tangling-induced shear stress

While realistic stars do not have shear-restorative forces, Hoven and Levin (2011) argue that small-scale disordered magnetic fields (“tangling”) may introduce an effective shear stress, with characteristic wave speed $c_s^2 = B_{\text{rms}}^2/4\pi\rho_0$. To characterize the effect that this shear modulus term has on the Alfvén waves, we can focus on the magnetic tension term in the horizontal momentum equation, which is the only other term capable of restoring torsional mode components (Loi and Papaloizou, 2017):

$$\omega^2 \vec{\xi}_h = -c_s^2 r^{-2} \nabla_h^2 \vec{\xi}_h + \omega_{Ar}^2 \vec{\xi}_h. \quad (4.88)$$

We see that Equation 4.88 is mathematically identical to a two-dimensional Schrödinger equation, where $E = \omega^2$ plays the role of the total energy, $V = \omega_{Ar}^2$ plays the role of the potential, and the small shear speed c_s plays the role of \hbar . As noted by Hoven and Levin (2011), the effect of a small shear modulus is to transform the continuous spectrum of Alfvén

waves into a discrete one (as in standard bound-state spectra of the Schrödinger equation), whose mode spacings decrease to zero in the limit where $c_s \rightarrow 0$. If a WKB approximation is adopted for Equation 4.88 in the horizontal direction, the coupling of these discrete waves to a mode is similar to that of the continuum waves in the $c_s = 0$ case. In the region where $\omega^2 \gg \omega_{Ar}^2$, the discrete Alfvén wave oscillates spatially very rapidly, and its overlap with a global-scale g mode averages to zero. Similarly, in the region where $\omega^2 \ll \omega_{Ar}^2$, the wave decays very rapidly, and therefore is very close to zero. However, the solution very close to $\omega^2 = \omega_{Ar}^2$ (the “classical turning point”) is known to be an Airy function of angular width

$$\delta\theta = \sqrt[3]{\frac{c_s^2}{r^2} \left| \frac{\partial \omega_A^2}{\partial \theta} \right|^{-1}} \quad (4.89)$$

which sets the scale at which an interaction with a mode and Alfvén wave will be “smeared” in the angular direction, due to shear stress. Physically, the shear modulus-induced discretization of the Alfvén waves occurs because shear adds an isotropic contribution to the wave speed (so that it is not exactly zero perpendicular to the field lines), and thus couples fluid motions across field lines. This effect is likely to be small relative to similar effects associated with the horizontal component of the mean magnetic field (Section 4.6.1).

Chapter 5

ASTEROSEISMIC G-MODE PERIOD SPACINGS IN STRONGLY MAGNETIC ROTATING STARS

Rui, N. Z., J. M. J. Ong, and S. Mathis (2024). “Astroseismic g-mode period spacings in strongly magnetic rotating stars.” In: *Monthly Notices of the Royal Astronomical Society* 527.3, pp. 6346–6362. doi: [10.1093/mnras/stad3461](https://doi.org/10.1093/mnras/stad3461). arXiv: [2310.19873](https://arxiv.org/abs/2310.19873).

Strong magnetic fields are expected to significantly modify the pulsation frequencies of waves propagating in the cores of red giants or in the radiative envelopes of intermediate- and high-mass main-sequence stars. We calculate the g-mode frequencies of stars with magnetic dipole fields which are aligned with their rotational axes, treating both the Lorentz and Coriolis forces non-perturbatively. We provide a compact asymptotic formula for the g-mode period spacing, and universally find that strong magnetism decreases this period spacing substantially more than is predicted by perturbation theory. These results are validated with explicit numerical mode calculations for realistic stellar models. The approach we present is highly versatile: once the eigenvalues λ of a certain differential operator are precomputed as a function of the magnetogravity and rotational frequencies (in units of the mode frequency), the non-perturbative impact of the Coriolis and Lorentz forces is understood under a broad domain of validity, and is readily incorporated into asteroseismic modeling.

We graciously thank Conny Aerts and Jim Fuller for their very helpful and thorough comments. N.Z.R. acknowledges support from the National Science Foundation Graduate Research Fellowship under Grant No. DGE-1745301. J.M.J.O. acknowledges support from NASA through the NASA Hubble Fellowship grant HST-HF2-51517.001-A, awarded by STScI. STScI is operated by the Association of Universities for Research in Astronomy, Incorporated, under NASA contract NAS5-26555. S.M. acknowledges support from the European Research Council through HORIZON ERC SyG Grant 4D-STAR 101071505, from the CNES SOHO-GOLF and PLATO grants at CEA-DAp, and from PNPS (CNRS/INSU). We thank the referee for their positive and constructive comments which improved the quality of the final manuscript.

5.1 Introduction

Because stellar oscillations extend throughout the stars in which they propagate, they contain a wealth of information about stellar interiors. Asteroseismology is thus a sensitive probe of interior structure (Gough and Kosovichev, 1993; Christensen-Dalsgaard, 2012; Bellinger, Basu, Hekker, and Ball, 2017; Mombarg, Dotter, Van Reeth, et al., 2020; Bellinger, Basu, Hekker, Christensen-Dalsgaard, et al., 2021; Mombarg, Dotter, Rieutord, et al., 2022; Buldgen et al., 2022), rotation (Beck et al., 2012; Mosser, Goupil, Belkacem, Marques, Beck, Bloemen, De Ridder, Barban, Deheuvels, Elsworth, et al., 2012a; Deheuvels, Garcia, et al., 2012; Deheuvels, Doğan, et al., 2014; Kurtz et al., 2014; Van Reeth, Tkachenko, and Aerts, 2016; Aerts, Van Reeth, et al., 2017; Pápics et al., 2017; Deheuvels, Ballot, Eggenberger, et al., 2020; Burssens et al., 2023; Mombarg, Rieutord, et al., 2023), mixing (Constantino et al., 2015; Li, Bedding, Huber, et al., 2018; Pedersen et al., 2018; Michielsen, Pedersen, et al., 2019; Lindsay et al., 2023), evolution (Miglio, Montalbán, Noels, et al., 2008; Mosser, Benomar, et al., 2014), and binary interaction history (Rui and Fuller, 2021a; Deheuvels, Ballot, Gehan, et al., 2022; Li, Bedding, Murphy, et al., 2022; Tayar, Moyano, et al., 2022; Hekker et al., 2023).

In recent years, there has been a large amount of progress in developing asteroseismology as a probe of strong *internal* magnetic fields, particularly through their effects on the gravity (g) modes which propagate in radiative regions. Such fields likely have important consequences for the transport of angular momentum within evolved stars (Mathis and Brye, 2012; Fuller, Piro, et al., 2019; Aerts, Mathis, et al., 2019). On the red giant branch, g modes propagate in the radiative core, which may possess strong magnetic fields left over from efficient core convective dynamos on the main sequence (Fuller, Cantiello, et al., 2015; Stello, Cantiello, Fuller, Huber, et al., 2016). In these cases, magnetism may have a significant effect on the frequency spectrum: by measuring these frequency patterns, Li, Deheuvels, Ballot, and Lignières (2022) strongly constrain both the rotational periods and field strengths ($\gtrsim 30$ kG) as well as their geometries for a modest sample of red giants. Even stronger magnetic fields $\gtrsim 100$ kG are commonly invoked to explain the observed suppression of dipole ($\ell = 1$) and quadrupole ($\ell = 2$) oscillation modes in red giants (e.g., García, Hernández, et al., 2014; Stello, Cantiello, Fuller, Garcia, et al., 2016; Stello, Cantiello, Fuller, Huber, et al., 2016). Specifically, mode suppression is expected to occur in the non-perturbative “strong magnetogravity” regime (Fuller, Cantiello, et al., 2015; Lecoanet, Vasil, et al., 2017; Rui and Fuller, 2023), when a mode’s frequency ω is sufficiently close to the critical frequency

$$\omega \lesssim \omega_{\text{crit}} \sim \omega_B \equiv \sqrt{N v_{Ar} / r}. \quad (5.1)$$

In Equation 5.1, $v_{Ar} = B_r/\sqrt{4\pi\rho}$ is the radial component of the Alfvén velocity, r is the radial coordinate, and N is the Brunt–Väisälä (buoyancy) frequency, given by

$$N^2 = g \left(\gamma^{-1} \frac{d \ln p_0}{dr} - \frac{d \ln \rho_0}{dr} \right), \quad (5.2)$$

where γ is the adiabatic index.

Equivalently, mode suppression occurs at some frequency ω_{crit} when the magnetic field is at least comparable to some critical field (Fuller, Cantiello, et al., 2015):

$$B \gtrsim B_{\text{crit}} \propto \sqrt{\rho} \omega_{\text{crit}}^2 r / N. \quad (5.3)$$

Complementarily, main-sequence pulsators of intermediate mass ($\gtrsim 1.3 M_{\odot}$) have radiative, rather than convective, envelopes, and their g modes extend to their surfaces where they can be observed directly (Aerts, 2021). Examining the slowly pulsating B-type (SPB) star HD 43317, Lecoanet, Bowman, et al. (2022) demonstrate that observations of mode suppression in main sequence (MS) pulsators may place meaningful constraints on their internal magnetism. The detection of g modes in the vicinity of magnetic suppression suggests MS pulsators as a separate platform for testing the effect of strong magnetic fields on propagating gravity waves.

In the absence of effects such as magnetic fields or rotation, successive g modes are evenly spaced in period by a constant g-mode period spacing δP_g , which can be estimated as

$$\delta P_g = \frac{2\pi^2}{\sqrt{\ell(\ell+1)}} \left(\int \frac{N}{r} dr \right)^{-1}, \quad (5.4)$$

where the integral is over the part of the radial cavity within which g modes propagate ($\omega < N$).

However, both rotation and magnetism leave distinctive signatures on the period spacing, both by lifting the degeneracy between modes of different m (by breaking the spherical symmetry of the system) and by introducing period dependence (Bouabid et al., 2013; Van Reeth, Tkachenko, and Aerts, 2016; Dhouib, Mathis, et al., 2022). The period spacing as a function of period $\delta P_g = \delta P_g(P)$ is therefore a valuable measure for rotational and magnetic effects (Van Beeck et al., 2020; Henneco, Van Reeth, et al., 2021). Characterizing this observable non-perturbatively is the primary focus of this work.

Our paper proceeds as follows. Section 5.2 presents the problem statement and motivates the asymptotic treatment of magnetism and rotation. Section 5.3 derives the differential operator which governs the horizontal structure of magnetic gravito-inertial modes. In

Section 5.4, we numerically calculate this operator’s eigenvalues, which enter directly into an asymptotic formula for the period spacing. In Section 5.5, we solve the radial oscillation problem directly, including both magnetism and rotation while partially relaxing the asymptotic assumption. Section 5.6 presents the results of such calculations for models of red giants, γ Doradus (γ Dor), and SPB pulsators. Finally, Section 5.7 concludes. The reader seeking our observational predictions is guided to Equations 5.33 and 5.40 (for the asymptotic period spacing) and the discussion in Section 5.6.

5.2 Problem statement

The effect of magnetism on the asteroseismic period spacing has been previously explored by various authors. So far, this work has typically either restricted its attention to toroidal fields ($B_r = B_\theta = 0$; Rogers and MacGregor, 2010; Mathis and De Brye, 2011; MacGregor and Rogers, 2011; Dhouib, Mathis, et al., 2022), treated magnetism perturbatively ($B \ll B_{\text{crit}}$; Cantiello et al., 2016; Prat, Mathis, Buysschaert, et al., 2019; Prat, Mathis, Neiner, et al., 2020a; Prat, Mathis, Neiner, et al., 2020b; Mathis, Bugnet, et al., 2021; Bugnet et al., 2021; Bugnet, 2022; Li, Deheuvels, Ballot, and Lignières, 2022), or worked in the ray-tracing limit ($k_r, k_h \gg 1/r$; Loi and Papaloizou, 2018; Loi, 2020c; Loi, 2020b). However, in realistic situations, gravity waves couple most strongly to the radial component of the field B_r (see Section 5.2.1), which may be very strong ($B \sim B_{\text{crit}}$; Fuller, Cantiello, et al., 2015). Moreover, due to geometric cancellation, observable modes are typically of low degree ($k_h \sim 1/r$).

The central goal of this work is to calculate the period spacing pattern in the simultaneous presence of rotation and an axisymmetric *radial* magnetic field in a non-perturbative way. The work proceeds under the “traditional approximation of rotation and magnetism” defined in Section 5.2.1 (which restricts attention purely to the radial field).

5.2.1 The traditional approximation of rotation and magnetism (TARM)

Pure, low-frequency gravity waves follow the dispersion relation

$$\omega = \pm \frac{k_h}{k} N \quad (5.5)$$

when $N \gg \omega$. Therefore, their wavenumbers are primarily radial, with their radial wavenumbers exceeding their horizontal wavenumbers by ratios

$$\frac{k_r}{k_h} \simeq \frac{N}{\omega}. \quad (5.6)$$

In the presence of restoring forces other than buoyancy or pressure (e.g., Coriolis forces, magnetic tension), the dispersion relation will be modified from Equation 5.5. However,

for modes which still have g mode character (i.e., buoyancy is still a significant restorative force), k_r/k_h will still be comparable to $N/\omega \gg 1$. Throughout, we restrict our attention to modes whose wavenumbers are primarily radial: this is a crucial assumption of our work.

This approximation underlies the standard analytic treatment of gravity waves in rotating stars. The qualitative behavior of low-frequency gravito-inertial waves can be seen in the dispersion relation in the fully Jeffreys–Wentzel–Kramers–Brillouin (JWKB) limit:

$$\omega^2 - \frac{k_h^2}{k^2} N^2 - (\hat{k} \cdot \vec{\Omega})^2 = 0, \quad (5.7)$$

see, e.g., Bildsten, Ushomirsky, et al. (1996) and Lee and Saio (1997). Because low-frequency g modes have primarily radial wavenumbers, $k \approx k_r \sim (N/\omega)k_h \gg k_h$, the radial part of the rotation vector $\vec{\Omega}$ dominates in Equation 5.7. It is thus both convenient and accurate for many purposes to assume $\vec{\Omega} \approx \Omega \cos \theta \hat{r}$, i.e., to neglect the horizontal part of $\vec{\Omega}$. Given its usefulness, this assumption is appropriately known as the “traditional approximation of rotation” (TAR).

We emphasize that the TAR is only valid when $k_r \gg k_h$. It is therefore applicable when $\omega \ll N$ and $2\Omega \ll N$, with the interpretation that stratification is the dominant restorative force in the radial direction (such that the Coriolis force is only important in the horizontal directions). The utility of this approximation is that it allows the (buoyancy-driven) vertical dynamics to be decoupled from the (Coriolis-driven) horizontal dynamics. Because of this useful feature, the TAR has also found extensive use in geophysics (e.g., Eckart, 1960; Longuet-Higgins, 1968). However, if either of the hypotheses of the TAR above are not satisfied, the traditional approximation should be abandoned (Dintrans, Rieutord, and Valdettaro, 1999; Dintrans and Rieutord, 2000; Gerkema and Shrira, 2005; Ballot et al., 2010; Mathis, Neiner, et al., 2014).

When assumed, the TAR implies that the pressure perturbation varies in the horizontal directions according to the Laplace tidal equation:

$$0 = \lambda p'(\mu) + \frac{d}{d\mu} \left(\frac{1 - \mu^2}{1 - q^2 \mu^2} \frac{dp'(\mu)}{d\mu} \right) - \frac{m^2}{(1 - \mu^2)(1 - q^2 \mu^2)} p'(\mu) - \frac{mq(1 + q^2 \mu^2)}{(1 - q^2 \mu^2)^2} p'(\mu). \quad (5.8)$$

In the non-rotating limit ($q \rightarrow 0$), the Laplace tidal equation approaches the usual generalized Legendre equation, for which $\lambda = \ell(\ell + 1)$ and the eigenfunctions are associated Legendre polynomials. Here, $\mu = \cos \theta$ is the colatitude and $q = 2\Omega/\omega$ is the spin parameter. When

computing mode frequencies the TAR, the effect of rotation is thus simply to replace $\ell(\ell+1)$ with λ .

To handle the effect of a strong dipole magnetic field, Rui and Fuller (2023) borrow intuition from the TAR. The full JWKB dispersion relation for magnetogravity waves is

$$\omega^2 - \frac{k_h^2}{k^2} N^2 - (\vec{k} \cdot \vec{v}_A)^2 = 0, \quad (5.9)$$

where $\vec{v}_A = \vec{B}_0 / \sqrt{4\pi\rho_0}$ is the Alfvén velocity, e.g., Unno, Osaki, Ando, Saio, et al. (1989) and Fuller, Cantiello, et al. (2015). Analogously with the rotational argument, we see that the radial part of \vec{B} dominates, and it suffices for a dipole magnetic field to assume $\vec{B} \approx B_0 \cos \theta \hat{r}$. The pressure perturbation then follows

$$0 = \lambda p'(\mu) + \frac{d}{d\mu} \left(\frac{1 - \mu^2}{1 - b^2\mu^2} \frac{dp'(\mu)}{d\mu} \right) - \frac{m^2}{(1 - \mu^2)(1 - b^2\mu^2)} p'(\mu), \quad (5.10)$$

where $b = k_r v_{Ar} / \omega$. The interpretation of this approximation is that the fluid is sufficiently stratified that buoyancy is the only important restorative force in the radial direction (i.e., the Lorentz force need only be included in the horizontal directions). As in the TAR, including magnetism in a calculation of mode frequencies under this approximation simply involves replacing $\ell(\ell+1)$ with a suitably computed λ when solving the radial problem.

We note the similar forms of Equation 5.8 (for rotation) and Equation 5.10 (for magnetism). However, unlike the singularities in Equation 5.8 (around which the eigenfunctions are smooth), the singularities in Equation 5.10 are of significantly different character, and imply sharp fluid features corresponding to resonances with Alfvén waves (Rui and Fuller, 2023). For the frequency-shift analysis conducted in this work, this property of the singularities in Equation 5.10 motivates restriction to solutions for which $b < 1$ (so that the Alfvén resonances are not on the domain).

In this work, we generalize both the traditional approximation of rotation and its magnetic analogue to incorporate both effects: in other words, we consider only the effects of the *radial* components of both the rotation vector and magnetic field. Equivalently, we include only the horizontal components of the Coriolis and Lorentz forces. Hereafter, we refer to this joint approximation as the traditional approximation of rotation and magnetism (TARM).

5.2.2 Assumptions, conventions, and scope

In addition to assuming that $k_r \gg k_h$, we adopt the JWKB approximation in the radial direction *only*, i.e., we assume that the equilibrium structure and field of the star vary on length scales much larger than the radial wavelength (the “asymptotic” regime). Because

such length scales are typically $\sim r$, this assumption is usually justified, although it may be violated in the presence of sharp compositional gradients which are known to produce mode-trapping phenomena (e.g., Miglio, Montalbán, Noels, et al., 2008; Pedersen et al., 2018; Michelsen, Pedersen, et al., 2019). In Section 5.5, we solve for the full radial dependence of the wavefunction without directly assuming that the radial wavenumber is large. However, under the TARM, we perform this calculation using a precomputed grid of horizontal eigenvalues λ (see Section 5.4) which *does* make this assumption. Therefore, the calculation described in Section 5.5 is expected to partially, but not fully, capture non-JWKB effects in the radial direction.

We index branches by the angular degree ℓ and order m . In particular, a mode is said to have some value of ℓ and m when the horizontal dependence becomes the spherical harmonic $Y_{\ell m}$ when both the field and rotation are smoothly taken to zero. We caution that, while we may refer to some mode as having some degree ℓ in a rotating and/or magnetized star, $Y_{\ell m}$ is not the correct horizontal dependence, and the eigenvalues are no longer $\ell(\ell + 1)$. For the angular order m , we adopt the sign convention used by Lee and Saio (1997) and Rui and Fuller (2023) that $mq > 0$ ($mq < 0$) corresponds to retrograde (prograde) modes. Additionally, without loss of generality, we consider throughout the case where $q > 0$ and $b > 0$ (which appear in, e.g., Equations 5.8 and 5.10, respectively), i.e., positive (negative) azimuthal order m corresponds to retrograde (prograde) modes. In this problem, the sign of b is irrelevant, and the effect of a sign change in q can be fully compensated by changing the sign convention of m .

In the presence of (solid-body) rotation, it is important to distinguish the mode frequency in the inertial frame (which is observable) from the mode frequency in the frame co-rotating with the star (in which the effect of rotation appears as a Coriolis force). Hereafter, we use ω ($\bar{\omega}$) to denote the mode frequency in the inertial (co-rotating) frame. Hence, we calculate the oscillation modes directly with respect to $\bar{\omega}$, but convert to ω for observational purposes.

We restrict our attention to a magnetic field whose radial part has a dipolar horizontal dependence. However, our results are not sensitive to the radial dependence of the field (as long as it is not very steep), or the geometry of the horizontal field components (as long as they are not much larger than the radial component). While Section 5.3.2 makes no additional assumptions about the field than those listed above, Section 5.5 requires a radial magnetic field profile $B_{0r} = B_{0r}(r)$. For this work, we adopt the Prendergast magnetic field geometry (Prendergast, 1956). For our purposes, it suffices to specify the radial component

of the magnetic field:

$$B_{0r} = B_c \frac{2R^2}{r^2} \frac{\beta}{\Lambda^2} \left(\frac{r^2}{R^2} - \frac{r}{R} \frac{j_1(\Lambda r/R)}{j_1(\Lambda)} \right) \cos \theta, \quad (5.11)$$

where $j_1(x) = \sin x/x^2 - \cos x/x$ is the first spherical Bessel function and R is the radius of the star. Although Kaufman et al. (2022) have recently shown that the Prendergast geometry is likely unstable over timescales relevant to stellar evolution, we adopt it simply as a closed-form model for a large-scale, dipole-like field, and we expect our findings to be insensitive to the exact radial dependence of the field. Following, e.g., Kaufman et al. (2022), we take $\Lambda \approx 5.76346$ and $\beta \approx 1.31765$, corresponding to the normalized, lowest-energy field solution with a vanishing surface field. Hereafter, B_c should be understood to refer to the *radial* component of the core magnetic field amplitude, although it is typically expected that the radial and horizontal components of the field are comparable. We expect all of the chief results of this work to be robust to magnetic field geometry, as long as $B_{0h}/B_{0r} \lesssim N/\omega$ and $k_r \gg d \ln B_{0r}/dr$.

We specialize to the case where magnetism is not strong enough to suppress the modes (although we explore the mode frequencies right up to this limit). While the suppression mechanism of magnetogravity waves is not fully understood, suppression may occur when magnetogravity waves refract upwards at some critical $\omega = \omega_B$ to infinite wavenumber (Lecoanet, Vasil, et al., 2017; Lecoanet, Bowman, et al., 2022; Rui and Fuller, 2023) or are damped out by phase-mixing processes once resonant with Alfvén waves ($b > 1$) in a manner similar to that described by Loi and Papaloizou (2017). Therefore, we restrict the scope of our calculations to the case where $b = k_r v_{Ar}/\omega < 1$ and $\omega < \omega_B$. Under these circumstances, the effects of magnetism on g modes should be well-modeled by our method.

For demonstrative purposes, we restrict most of our attention in this work to the dipole ($\ell=1$) and quadrupole ($\ell=2$) modes, although our calculations do not assume this, and it is not more complicated to extend this analysis to higher ℓ . Low-degree g modes suffer the least from geometric cancellation and are thus the easiest g modes to observe (there are no radial g modes). For simplicity, we assume modes are adiabatic, and neglect perturbations to the gravitational potential (i.e., we adopt the Cowling approximation). The general result that the perturbative theory underestimates the impact of magnetism on the period spacings for the dipole modes (Section 5.6) is also expected to hold for the quadrupole modes, although the asymmetry in the frequency shifts of different multiplets is known to behave differently (cf. Section 5.6.1 of Bugnet et al., 2021).

5.3 Analytic formulation

In this Section, we derive an expression for the horizontal equation obeyed by low-frequency g modes under the simultaneous influence of uniform (or weak differential) rotation and a dipolar magnetic field (Section 5.3.1). Under the TARM, the eigenvalues associated with these normal modes can be easily translated to an asymptotic expression for the period spacing (Section 5.3.2).

5.3.1 Fluid equations for gravity modes

In the presence of gravity, magnetic tension and pressure, and Coriolis forces, the linearized momentum equation is

$$\begin{aligned} \rho_0 \partial_t^2 \vec{\xi} + 2\rho_0 \vec{\Omega} \times \partial_t \vec{\xi} \\ = -\nabla \left(p' + \frac{1}{4\pi} \vec{B}_0 \cdot \vec{B}' \right) - \rho' g \hat{r} + \frac{1}{4\pi} (\vec{B}_0 \cdot \nabla) \vec{B}' \end{aligned} \quad (5.12)$$

where $\vec{\xi}$ is the fluid displacement, subscript 0 and primes denote equilibrium and perturbed quantities respectively, g is the gravitational acceleration, and

$$\vec{B}' = (\vec{B}_0 \cdot \nabla) \vec{\xi} \quad (5.13)$$

is the magnetic field perturbation. Equations 5.12 ignore the centrifugal force, and apply a Cowling approximation to neglect perturbations in g . Under the TARM, $\partial_r \rightarrow -ik_r$ when acting on a perturbation, and the magnetic tension term in Equation 5.12 thus becomes

$$\frac{1}{4\pi} (\vec{B}_0 \cdot \nabla) \vec{B}' = -\frac{k_r^2 B_0^2}{4\pi} \vec{\xi} \equiv \rho_0 k_r^2 v_{Ar}^2 \cos^2 \theta \vec{\xi} \quad (5.14)$$

where $|v_{Ar} \cos \theta|$ is the radial component of the Alfvén velocity, with the angular dependence explicitly factored out.

In spherical coordinates and applying the traditional approximation, the momentum equation becomes

$$-\rho_0 \bar{\omega}^2 \xi_r = ik_r p' - \rho' g - \rho_0 k_r^2 v_{Ar}^2 \cos^2 \theta \xi_r \quad (5.15a)$$

$$-\rho_0 \bar{\omega}^2 \xi_\theta - 2i\rho_0 \bar{\omega} \Omega \cos \theta \xi_\phi = -\frac{1}{r} \frac{dp'}{d\theta} - \rho_0 k_r^2 v_{Ar}^2 \cos^2 \theta \xi_\theta \quad (5.15b)$$

$$-\rho_0 \bar{\omega}^2 \xi_\phi + 2i\rho_0 \bar{\omega} \Omega \cos \theta \xi_\theta = -\frac{im}{r \sin \theta} p' - \rho_0 k_r^2 v_{Ar}^2 \cos^2 \theta \xi_\phi \quad (5.15c)$$

where we have assumed harmonic time dependence, $\partial_t \rightarrow i\bar{\omega}$, and used axisymmetry to take $\partial_\phi \rightarrow im$. Magnetic tension dominates over magnetic pressure in the asymptotic regime, and so the latter is ignored in Equations 5.15.

For adiabatic oscillations, the pressure and density p and ρ are related by

$$\frac{D \ln p}{Dt} = \gamma \frac{D \ln \rho}{Dt}, \quad (5.16)$$

where $D/Dt = \partial/\partial t + \vec{u} \cdot \nabla$ denotes the advective derivative. Equation 5.16 can be linearized to

$$\rho' = \rho_0 N^2 \xi_r / g + p' / c_s^2 \quad (5.17)$$

where $c_s = \sqrt{\gamma p_0 / \rho_0}$ is the sound speed. For gravity waves, the first term dominates, so that

$$\rho' \approx \rho_0 N^2 \xi_r / g. \quad (5.18)$$

Finally, the fluid perturbation must satisfy the equation of continuity, so that

$$\nabla \cdot \vec{\xi} = 0, \quad (5.19)$$

where we have applied the Boussinesq approximation (Proctor and Weiss, 1982).

Now, the horizontal momentum equations give a linear system of equations for ξ_θ and ξ_ϕ in terms of p' :

$$(1 - b^2 \cos^2 \theta) \xi_\theta + iq \cos \theta \xi_\phi = \frac{1}{\rho_0 \bar{\omega}^2 r} \frac{dp'}{d\theta} \quad (5.20a)$$

$$-iq \cos \theta \xi_\theta + (1 - b^2 \cos^2 \theta) \xi_\phi = \frac{im}{\rho_0 \bar{\omega}^2 r \sin \theta} p' \quad (5.20b)$$

where $b = k_r v_{Ar} / \bar{\omega}$ (Rui and Fuller, 2023) and again $q = 2\Omega / \bar{\omega}$ (Lee and Saio, 1997) are the dimensionless parameters governing the effects of magnetism and rotation on the horizontal eigenfunctions. Equations 5.20 can be solved to obtain

$$\xi_\theta = \frac{\sqrt{1 - \mu^2}}{\rho_0 \bar{\omega}^2 r [(1 - b^2 \mu^2)^2 - q^2 \mu^2]} \left(\frac{mq\mu}{1 - \mu^2} p' - (1 - b^2 \mu^2) \frac{dp'}{d\mu} \right) \quad (5.21a)$$

$$\xi_\phi = \frac{i\sqrt{1 - \mu^2}}{\rho_0 \bar{\omega}^2 r [(1 - b^2 \mu^2)^2 - q^2 \mu^2]} \left((1 - b^2 \mu^2) \frac{m}{1 - \mu^2} p' - q\mu \frac{dp'}{d\mu} \right) \quad (5.21b)$$

where $\mu = \cos \theta$. Likewise, the radial component of the momentum equation (Equation 5.15a) can be solved to yield

$$\xi_r = \frac{ik_r}{\rho_0 N^2} p'. \quad (5.22)$$

Substituting Equations 5.17, 5.21, and 5.22 into the continuity equation (Equation 5.19), we obtain

$$\mathcal{L}^{m,b,q}[p'] + \frac{\bar{\omega}^2 r^2 k_r^2}{N^2} p' = 0, \quad (5.23)$$

where the differential operator $\mathcal{L}^{m,b,q}$ is given by

$$\begin{aligned}\mathcal{L}^{m,b,q}[f(\mu)] &= \frac{d}{d\mu} \left(\frac{(1-\mu^2)(1-b^2\mu^2)}{(1-b^2\mu^2)^2 - q^2\mu^2} \frac{df(\mu)}{d\mu} \right) \\ &\quad - \frac{m^2}{1-\mu^2} \frac{1-b^2\mu^2}{(1-b^2\mu^2)^2 - q^2\mu^2} f(\mu) \\ &\quad - mq \left(\frac{4b^2\mu^2(1-b^2\mu^2) + 2q^2\mu^2}{[(1-b^2\mu^2)^2 - q^2\mu^2]^2} + \frac{1}{(1-b^2\mu^2)^2 - q^2\mu^2} \right) f(\mu).\end{aligned}\quad (5.24)$$

The operator $\mathcal{L}^{m,b,q}$ further reduces to the standard Laplace tidal operator (e.g., Lee and Saio, 1997) when $b = 0$ (no magnetism), and to the magnetic operator discussed by Rui and Fuller (2023) when $q = 0$ (no rotation). Hereafter, we define the “eigenvalues” λ of $\mathcal{L}^{m,b,q}$ as constants admitting solutions $f(\mu)$ to

$$\mathcal{L}^{m,b,q}[f(\mu)] + \lambda f(\mu) = 0, \quad (5.25)$$

i.e., the eigenvalues of $\mathcal{L}^{m,b,q}$ in the “standard” sign convention are $-\lambda$.

When $b = q = 0$ (i.e., no magnetism or rotation), $\mathcal{L}^{m,b,q}[f(\mu)]$ reduces further still to the standard Laplacian operator on a sphere, where solutions to the associated boundary value problem are the spherical harmonics, indexed by integers ℓ, m with eigenvalues $\ell(\ell + 1)$. Equation 5.23 becomes

$$\bar{\omega}^2 = \frac{\lambda/r^2}{k_r^2} N^2 = \frac{\tilde{k}_h^2}{k_r^2} N^2, \quad (5.26)$$

where $\tilde{k}_h \equiv \sqrt{\lambda}/r$ is an effective horizontal wavenumber, which incorporates the effects of rotation and magnetism. By analogy with the spherically symmetric case, we may define an effective degree

$$\ell_e = \sqrt{\lambda + 1/4} - 1/2, \quad (5.27)$$

such that $\lambda = \ell_e(\ell_e + 1)$. In the TARM, oscillation modes are calculated by replacing ℓ with ℓ_e throughout the entire star, in the same manner as is done in the standard TAR.

5.3.2 Asymptotic period spacing

In the absence of rotation and magnetism, gravity modes obey the dispersion relation $\bar{\omega} = \pm k_h N / k_r \propto k_r^{-1}$. In the asymptotic regime (where $k_r r \rightarrow \infty$), this implies that adjacent g modes (with relative radial orders $\delta n_g = 1$, and $k_r \sim n_g/r$) are spaced uniformly in the mode period P . In this Section, we derive an expression for the asymptotic period spacing δP_g for g modes. We note that further departures from the asymptotic formula are expected when the stellar structure varies over a comparable radial scale to the wavefunction, or when there is mode mixing.

Before proceeding, we review a fundamental difference between the inclusion of uniform rotation and magnetism. For rotation, the fluid equations are solved by eigenfunctions whose shapes are solely parameterized by the spin parameter $q = 2\Omega/\bar{\omega}$, which can be calculated using stellar model parameters and the mode frequency, i.e., without knowledge of k_r . Observed spin parameters for intermediate-mass g-mode pulsations range from $q \simeq 0.1$ to $q \simeq 30$ (Aerts, Van Reeth, et al., 2017). However, for magnetism, the parameter which controls the shapes of the eigenfunctions, $b = k_r v_{Ar}/\bar{\omega}$, *does* depend on k_r (which varies mode-to-mode and with r in a complicated way). Fortunately, Equation 5.26 can also be rewritten

$$\lambda = b^2/a^2, \quad (5.28)$$

where the parameter a (described by Rui and Fuller, 2023) is given by

$$a = \frac{Nv_{Ar}}{r\bar{\omega}^2}. \quad (5.29)$$

This parameter is the squared ratio of the magnetogravity frequency ω_B (Equation 5.1) to the mode frequency ($a \sim \omega_B^2/\bar{\omega}^2$) and, conveniently, *can* be computed in terms of the stellar model and $\bar{\omega}$ alone. By computing the horizontal eigenfunctions λ as a function of b and then inverting Equation 5.28, λ can be found as a function of a .

To compute the period spacing in the co-rotating frame, we first observe that the radial phase φ_g across the gravity mode cavity is

$$\varphi_g = \pi(n_g + \epsilon_g) = \int k_r dr = \frac{\bar{P}}{2\pi} \int \sqrt{\lambda} \frac{N}{r} dr, \quad (5.30)$$

where we have used Equation 5.26, and the integral is over the region of the star where $\omega < N$ and $\omega < k_h c_s$. In Equation 5.30, n_g is the radial order, and ϵ_g is a (here unimportant) phase offset. Adjacent modes (with $\delta n_g = 1$) will thus have

$$\pi\delta n_g = \pi = \frac{\delta\bar{P}_g}{2\pi} \int \sqrt{\lambda} \frac{N}{r} dr + \frac{\pi\bar{P}}{4\pi} \int \frac{\delta\lambda}{\sqrt{\lambda}} \frac{N}{r} dr, \quad (5.31)$$

where we have neglected the frequency dependence of the bounds of the buoyancy integral.

Because $q \propto \bar{\omega}^{-1} \propto \bar{P}$ and $a \propto \bar{\omega}^{-2} \propto \bar{P}^2$,

$$\delta\lambda = \frac{d\lambda}{d\bar{P}} \delta\bar{P}_g = \frac{\lambda}{\bar{P}} \frac{d\ln\lambda}{d\ln\bar{P}} \delta\bar{P}_g = \frac{\lambda}{\bar{P}} \left(\frac{1}{2} \frac{\partial \ln\lambda}{\partial \ln q} + \frac{\partial \ln\lambda}{\partial \ln a} \right) \delta\bar{P}_g. \quad (5.32)$$

Combining Equations 5.31 and 5.32 and solving for $\delta\bar{P}_g$ gives

$$\delta\bar{P}_g = 2\pi^2 \left(\int \sqrt{\lambda} \left(1 + \frac{1}{2} \frac{\partial \ln\lambda}{\partial \ln q} + \frac{\partial \ln\lambda}{\partial \ln a} \right) \frac{N}{r} dr \right)^{-1}. \quad (5.33)$$

This approaches the well-known, zero-field, zero-rotation asymptotic formula in the relevant limit (Equation 5.4), as well as Equation 4 of Bouabid et al. (2013) which was derived for the purely rotational case.

Equation 5.33 requires the calculation of $(\partial \ln \lambda / \partial \ln q)_a$ and $(\partial \ln \lambda / \partial \ln a)_q$, where subscripts denote fixed variables with respect to the partial derivative. In Section 5.4.1, we compute λ and its derivatives on a discrete, rectangular grid of b and q . While $(\partial \ln \lambda / \partial \ln a)_q$ is easy to calculate numerically via a finite difference formula (since fixing q is straightforward), computing $(\partial \ln \lambda / \partial \ln q)_a$ is slightly trickier because it is harder to fix a . Via Equation 5.28, we see that

$$\left(\frac{\partial \lambda}{\partial q} \right)_a = \frac{2b}{a^2} \left(\frac{\partial b}{\partial q} \right)_a. \quad (5.34)$$

Using the identity that

$$-1 = \left(\frac{\partial b}{\partial q} \right)_a \left(\frac{\partial a}{\partial b} \right)_q \left(\frac{\partial q}{\partial a} \right)_b, \quad (5.35)$$

we obtain

$$\left(\frac{\partial \lambda}{\partial q} \right)_a = -\frac{2b}{a^2} \left(\frac{\partial a}{\partial q} \right)_b \left(\frac{\partial a}{\partial b} \right)_q^{-1} \quad (5.36)$$

so that

$$\left(\frac{\partial \ln \lambda}{\partial \ln q} \right)_a = -\frac{2q}{b} \left(\frac{\partial a}{\partial q} \right)_b \left(\frac{\partial a}{\partial b} \right)_q^{-1}. \quad (5.37)$$

We use Equation 5.37 in our numerical calculation of δP_g .

In the *inertial* frame, the observed frequencies ω are related to $\bar{\omega}$ under our sign convention by

$$\omega = \bar{\omega} - m\Omega, \quad (5.38)$$

so that the periods P and \bar{P} in the inertial and co-rotating frames are related by

$$P = \frac{\bar{P}}{1 - m\bar{P}/P_{\text{rot}}}, \quad (5.39)$$

where P_{rot} is the rotation period. The (asymptotic) period spacing measured by an observer is thus given by

$$\delta P_g = \frac{\delta \bar{P}_g}{(1 - m\bar{P}/P_{\text{rot}})^2}. \quad (5.40)$$

Thus, the inclusion of either rotation or magnetism will also leave distinct imprints on δP_g as a function of mode period: understanding these signatures is crucial for extracting these properties from δP_g .

5.4 Numerical solutions of the horizontal problem

In preceding sections, we have introduced an analytic formulation of the magnetorotational pulsation problem. However, applying the TARM to concrete predictions of oscillation spectra requires robust numerical solutions for the horizontal eigenvalues λ . We describe our numerical procedure for this calculation in this Section.

5.4.1 Numerical collocation scheme

Rui and Fuller (2023) calculate numerical solutions to the horizontal problem (Equation 5.25) in the nonrotating case ($q=0$) by introducing a small artificial dissipation and using a relaxation scheme. While this method satisfactorily treats numerical pathologies associated with a singularity at critical latitudes $\mu_{\pm} = \pm 1/b$ for large fields, it is computationally inefficient. Relatedly, because the coefficients of Equation 5.24 vary quickly across μ_{\pm} , unreasonably large dissipation coefficients must be assumed to avoid needing prohibitively high resolution near those latitudes.

The more general form of Equation 5.25 that we consider here is still of the Boyd type (e.g., Boyd, 1981), but now has solutions, and singular points, indexed by two parameters, b and q . In particular, Equation 5.25 produces four additional singular points, obeying

$$\mu^2 = \frac{2b^2 + q^2 \pm \sqrt{4b^2q^2 + q^4}}{2b^4}, \quad (5.41)$$

two of which may lie within the solution domain even for fields too weak to resonate with a given oscillation mode (i.e., $b < 1$).

We therefore seek an alternative solution strategy that is robust to the presence of such regular singular points. For $q < 1 - b^2$, no singularities lie on the domain, and it suffices to perform standard Chebyshev collocation on the real line (e.g., Wang, Boyd, et al., 2016). However, the collocation procedure must be modified somewhat to work for $q > 1 - b^2$. We note that since the Sturm–Liouville linear operator in Equation 5.24 is analytic, it may be treated as defining an ordinary differential equation on the complex plane. Solutions to the standard Sturm–Liouville problem on the real line coincide with those of this analytically continued problem, restricted to the real line. Thus, we may construct numerical solutions to the analytically continued problem on a contour on the complex plane, chosen to match the boundary conditions of the real problem on the interval $\mu \in [-1, +1]$. Eigenvalues of the analytically continued problem will not depend on this choice of contour. Thus, the contour may be chosen to avoid the singular points that we have described above, and therefore to improve the numerical conditioning (e.g. stiffness) of the problem. We refer the reader to, e.g., Boyd (1985) for a more detailed examination of this procedure, and nature of the

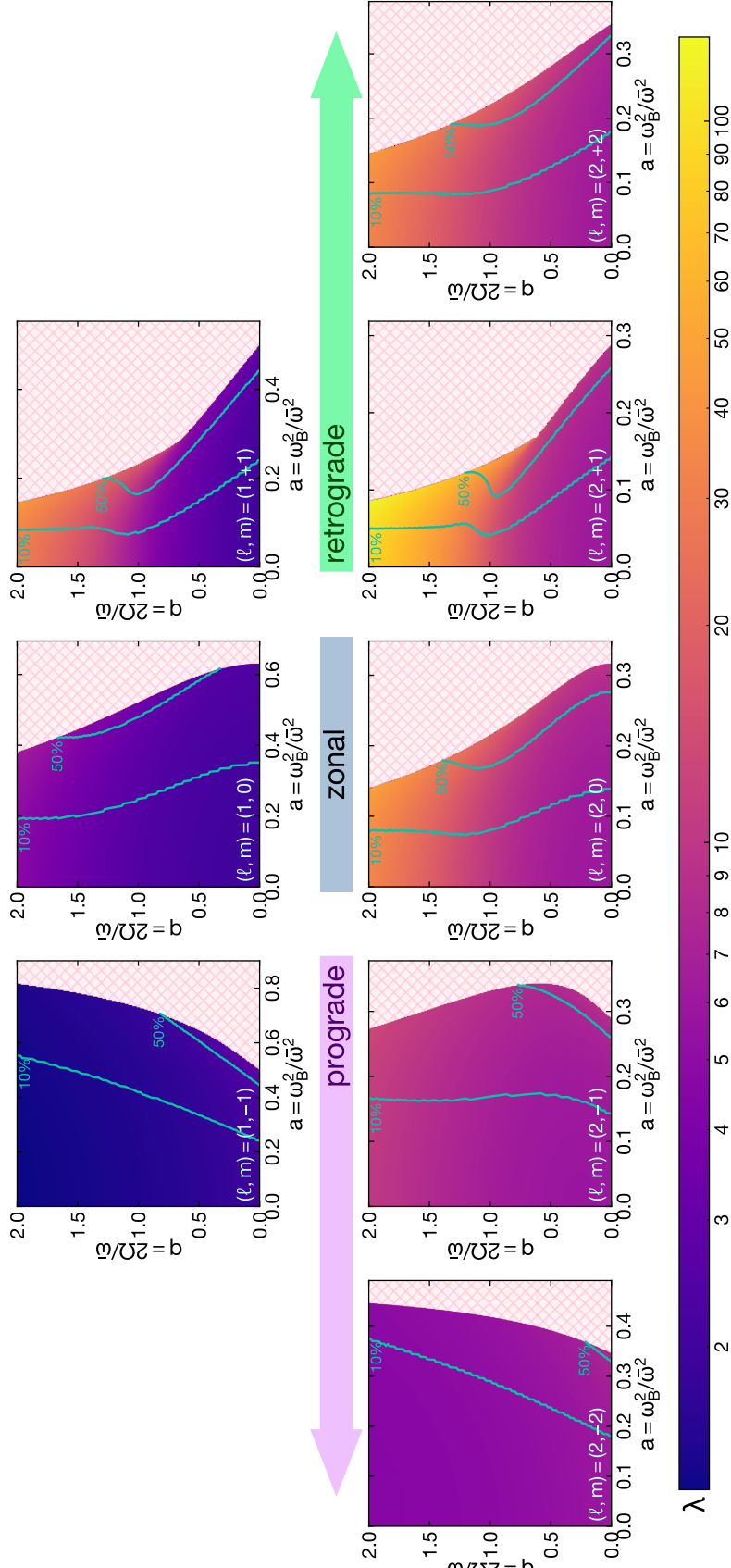


Figure 5.1: The eigenvalues λ of the differential operator $\mathcal{L}^{m,b,q}$ (Equation 5.24) for the dipole (top) and quadrupole (bottom) modes. We plot λ against the dimensionless parameters $a = \omega_B^2/\bar{\omega}^2 = N v_{Ar}/r \bar{\omega}^2$ and $q = 2\Omega/\bar{\omega}$, which govern the effects of magnetism and rotation, respectively. The eigenvalue λ enters the asymptotic period spacing as in Equation 5.33. The turquoise lines show contours to the right of which the integrand in Equation 5.33 deviates from a perturbative treatment by 10% and 50%. The pink hatched zones indicate $b = k_r v_{Ar}/\omega > 1$, i.e., modes which occupy these values of a and q at some layer within the star are likely to be suppressed.

resulting solutions. We find the standard collocation procedure to be sufficient for $m = 0$ and $m = \pm 2$ for any values of $q \in [0, 2]$ and $b \in [0, 1)$. However, solutions for the $m = \pm 1$ modes under this procedure are numerically badly behaved for $q > 1 - b^2$. In these cases, we perform a complex coordinate transformation from μ to ζ given by

$$\mu = \zeta \left(2 - \zeta^2 \right) + \zeta \left(1 - \zeta^2 \right)^2 i, \quad (5.42)$$

and then solve the resulting problem using Chebyshev collocation on the interval $\zeta \in [-1, 1]$. This contour is chosen to share endpoints with the original real interval, while being tangent with the real line from the $|\mu| > 1$ (rather than $|\mu| < 1$) direction.

The eigenvalue λ depends on the relationship between the mode frequency $\bar{\omega}$, rotational frequency Ω (via $q = 2\Omega/\bar{\omega}$), and magnetogravity frequency ω_B (via $a = \omega_B^2/\bar{\omega}^2$). Therefore, once λ is computed for a given pair of b and q , we retroactively compute $a = b/\sqrt{\lambda}$, and regard λ as being a function of a and q . Because this procedure only produces values of a below some critical $a_{\text{crit}} = a_{\text{crit}}(q)$ (corresponding to the maximum field which permits propagating magnetogravity waves), we excise two families of solutions: the Alfvén resonant ones for which $b > 1$ (which are expected to experience phase mixing, e.g., Loi and Papaloizou, 2017), and those which lie on the “slow” branch described by Rui and Fuller (2023) (which are expected to approach infinite wavenumber). Within this work, we consider both such solutions to be “suppressed”: we do not otherwise make claims about the degree of suppression or the mode frequencies of suppressed modes.

Figure 5.1 shows values of λ computed for all dipole ($\ell = 1$) and quadrupole ($\ell = 2$) modes. In particular, for the zonal ($m = 0$) and retrograde ($m > 0$) modes calculated here, the critical magnetic field needed to cause mode suppression *decreases* with increasing rotation rate. This is because, for these branches, λ increases relatively strongly with q (for $b = 0$, $\lambda \propto q^2$; Bildsten, Ushomirsky, et al., 1996; Townsend, 2003; Townsend, 2020). Therefore, $a_{\text{crit}} = b_{\text{crit}}/\sqrt{\lambda}$ decreases with q . However, since larger rotation rates cause the prograde Kelvin modes (which have $m = -\ell$) to attain larger horizontal scales (λ decreases to a smaller constant value with q , when $b = 0$), the critical field *increases* with increasing rotation rate. For the $(\ell, m) = (2, -1)$ case, the dependence of λ on q and b is slightly more complicated, hence the non-monotonic behavior of the corresponding critical field with rotation rate. In any case, a straightforward prediction of this formalism is thus that different branches of modes should undergo suppression at different mode frequencies. Observational measurements of these critical periods may therefore impose strong constraints on the magnetic and rotational properties of the star.

5.5 Numerical solutions of the radial problem

5.5.1 Non-asymptotic numerical scheme

In the asymptotic regime, the perturbations vary with radius as $\sim e^{i\varphi_g}$, where φ_g is given by Equation 5.30 (using the appropriate bounds). In other words, in this regime, the wavefunctions in the g-mode cavity are expected to be sinusoidal with respect to a modified buoyancy radius Π given by

$$\Pi(r) = \frac{\int_{r_1}^r \frac{N}{r} dr}{\int_{r_1}^{r_2} \frac{N}{r} dr} \quad (5.43)$$

which we define over the entire main radiative cavity (with respective inner and outer boundaries r_1 and r_2). This quantity is normalized such that Π ranges from 0 to 1.

However, the asymptotic assumption is violated in the proximity of sharp features in N (i.e., buoyancy glitches) when their characteristic widths are $\lesssim k_r^{-1}$. In such cases, the period spacing is expected to be modified from the asymptotic estimate in Equation 5.33. Sharp peaks in N are known to develop at the lower boundaries of the radiative envelopes of evolved MS stars (in which they cause periodic “dips” in the δP_g pattern with P ; Miglio, Montalbán, Noels, et al., 2008; Pedersen et al., 2018), and similar buoyancy glitches have recently been observed asteroseismically in red giants (Cunha, Stello, et al., 2015; Vrard, Cunha, et al., 2022b), although their structure is very sensitive to the details of convective boundary mixing (e.g., Michielsen, Aerts, et al., 2021; Lindsay et al., 2023). The asymptotic assumption is also strongly violated for g modes with low radial order, which may be observable in subgiants or some pulsators on the MS.

To model some of the non-asymptotic effects, we use a shooting method to solve the stellar pulsation equations under the assumption of adiabaticity, cast in the dimensionless form of Dziembowski (1971). This form of the pulsation equations is also employed by commonly used mode-solving codes such as GYRE (Townsend and Teitler, 2013). Rotation and magnetism are implemented only by replacing the angular degree ℓ in the equations with an effective degree ℓ_e , defined in Equation 5.27. Thus, we account only for the dynamical effects of rotation and magnetism, and neglect their indirect effects on stellar structure itself. Additionally, we emphasize that this “1.5D” approach still includes both rotation and magnetism asymptotically (similarly to the treatment of rotation in GYRE), and thus relies on the rotation and magnetic field profiles varying slowly in r compared to the wavefunctions themselves. In other words, while this procedure captures phenomena like wave-trapping due to peaks in N , it does *not* accurately model the effects of sharp radial gradients in the magnetic field or rotation profiles, or coupling to, e.g., inertial modes.

In what follows, M and R denote the total mass and radius of the star, and m denotes the mass interior to radius r . We solve the radial problem for

$$y_1 = x^{2-\ell_i} \frac{\xi_r}{r} \quad (5.44a)$$

$$y_2 = x^{2-\ell_i} \frac{p'}{\rho_0 g r} \quad (5.44b)$$

where $x = r/R$, and $\ell_i = \ell_e(r_1)$ is evaluated at the inner boundary. In buoyancy coordinates, the perturbed time-independent oscillation equations then become

$$S(\Pi) \frac{d\vec{y}}{d\Pi} = \mathbf{A} \vec{y} \quad (5.45)$$

where

$$S(\Pi) = \frac{N}{x \int_{r_1}^{r_2} \frac{N}{r} dr}, \quad (5.46)$$

$$\vec{y} = (y_1, y_2), \sigma = \bar{\omega} \sqrt{R^3/GM},$$

$$\mathbf{A} = \begin{pmatrix} V/\gamma - 1 - \ell_e & \lambda/c_1 \sigma^2 \\ c_1 \sigma^2 - A^* & 3 - U + A^* - \ell_e \end{pmatrix}, \quad (5.47)$$

and

$$V = \rho_0 r g / p_0 \quad (5.48a)$$

$$c_1 = x^3 M / m \quad (5.48b)$$

$$A^* = N^2 r / g \quad (5.48c)$$

$$U = 4\pi r^3 \rho / m. \quad (5.48d)$$

Equations 5.45 reflect the γ -mode localization scheme of Ong and Basu (2020) as well as the Cowling approximation (neglecting perturbations to the gravitational potential). These approximations are made to restrict our attention to the effect of magnetism and rotation on pure g modes, and to avoid boundary condition-related numerical artifacts (see Section 2.2 of Ong and Basu, 2020). Because the Cowling approximation is well-justified at high radial orders (where the TARM is valid), this approach should capture all of the robust predictions of our formalism. For the red giant model (Section 5.5.2), the resulting modes should be compared to the output of the stretching procedure typically used to extract δP_g from solar-like oscillators (Mosser, Vrard, et al., 2015).

For our numerical shooting, we first integrate Equation 5.45 outwards from the stellar centre as an initial value problem to produce inner basis solutions which are consistent with the

boundary conditions imposed there. In this work, we impose the boundary condition $y_1 = 0$ ($x_r = 0$) on both boundaries. The solution vector evaluated at any intermediate point (here taken to be $\Pi = 1/2$) should thus be equivalent (up to linear dependence) when obtained by integrating from either boundary (starting from $\vec{y} = (0, 1)$). These two solution vectors (obtained using a Radau integration scheme; Wanner and Hairer, 1996) can then be formed into a 2×2 matrix whose determinant $\mathcal{D}(\bar{\omega})$ must vanish at a normal mode $\bar{\omega} = \bar{\omega}^*$.

The adiabatic prescription of Equation 5.45 produces strictly real eigenvalues. To search for modes, we evaluate $\mathcal{D}(\bar{\omega})$ over some frequency grid. Between frequency grid points where \mathcal{D} changes sign, we use a bisection algorithm to locate the roots of \mathcal{D} . These oscillation modes $\bar{\omega}$ are then converted to their values ω in the inertial frame via Equation 5.39 (when there is rotation).

5.5.2 Stellar models

We find the oscillation modes of stellar models produced using version r22.11.1 of the Modules for Stellar Experiments (MESA) code (Paxton, Bildsten, et al., 2010; Paxton, Cantiello, et al., 2013; Paxton, Marchant, et al., 2015; Paxton, Schwab, et al., 2018; Paxton, Smolec, et al., 2019). We incorporate realistic convective overshoot using exponential overmixing with scale height $f_{\text{ov}}H_p = 0.015H_p$ (where H_p is the local pressure scale height), with the overshooting region starting a distance $0.005H_p$ inside the convective zone.

The stellar profiles as well as the rotation periods and magnetic fields we assume for them are summarized in Table 5.1. In particular, we choose three snapshots from a $1.5M_\odot$ model to assess the behavior of the period spacing on the early-MS (MS-1.5-young), late-MS (MS-1.5-evolved), and lower RG (RG-1.5), and two snapshots from a $6.0M_\odot$ star on the early-MS (MS-6.0-young) and late-MS (MS-6.0-evolved). These models are chosen to be representative of γ Dor (MS-1.5-young, MS-1.5-evolved), slowly pulsating B-type (SPB; MS-6.0-young, MS-6.0-evolved), and red giant solar-like (RG-1.5) oscillators. We solve for the dipole ($\ell = 1$) oscillation modes over a realistic range of frequencies. For RG-1.5, we compute these frequencies with both rotation and magnetism, as well as in the absence of either, in order to benchmark the prediction of perturbation theory (Equation 5.6.1). For the main-sequence models, the mode frequencies are computed three times, including the effects of magnetism and rotation both separately and simultaneously (Equation 5.6.2). The magnetic field is chosen to be strong enough to exhibit the effects of strong magnetic modification and suppression of some branch of oscillation modes. The mode period/frequency ranges shown in Table 5.1 are given in the inertial frame. When

Model	MS-1.5-young	MS-1.5-evolved	RG-1.5	MS-6.0-young	MS-6.0-evolved
$M (M_\odot)$	1.5	1.5	1.5	6.0	6.0
age	92 Myr	2.49 Gyr	2.67 Gyr	5 Myr	64 Gyr
$P_{\min} (\text{d})$	0.1	0.1	0.026 (450 μHz)	1.0	1.0
$P_{\max} (\text{d})$	1.0	1.0	0.077 (150 μHz)	3.0	3.0
$P_{\text{rot}} (\text{d})$	1.5	1.5	30	3.0	3.0
$B_c (\text{kG})$	475	98	824	172	62
evolutionary stage	young MS	evolved MS	red giant	young MS	evolved MS
analogue	young γ Dor	evolved γ Dor	red giant	young SPB	evolved SPB
results	Figure 5.4	Figure 5.5	Figure 5.2	Figure 5.6	Figure 5.7

Table 5.1: Summary of stellar models for which we calculate oscillation modes using the non-asymptotic scheme described in Section 5.5.1.

relevant, we solve only for co-rotating frequencies $\bar{\omega} \gtrsim 0$ to avoid the pile-up of g modes close to $\bar{\omega} = 0$.

Our models do not take into account distortions of the stellar structure due to centrifugal forces and magnetic pressure. While these effects are unlikely to matter in most observed γ Dor and SPB stars (Henneco, Van Reeth, et al., 2021), they are likely to be important in rapidly rotating p-mode pulsators (such as δ Sct stars, e.g., Lignières et al., 2006).

5.6 Results and discussion

5.6.1 Strong fields in red giant cores

Strong magnetic fields in red giant cores have two main asteroseismic manifestations. First, they may produce frequency shifts on the nonradial modes which tend to shift modes of all m in the same direction (as opposed to rotation, which creates a frequency multiplet). Measurements of such frequency shifts have recently been used to make inferences about the field strength and, in one case, even geometry (Li, Deheuvels, Ballot, and Lignières, 2022; Li, Deheuvels, Li, et al., 2023). Second, if the magnetic field is extraordinarily strong, the magnetic field is expected to suppress the amplitudes of dipole modes whose frequencies lie below some $\omega_{\text{crit}} \sim \omega_B$ (Fuller, Cantiello, et al., 2015; Lecoanet, Vasil, et al., 2017; Rui and Fuller, 2023).

Our red giant model (RG-1.5; described in Section 5.5.2) is chosen to mimic a star on the lower red giant branch (for which mixed modes are easiest to observe) with a typical rotation rate ($P_{\text{rot}} = 30$ d). For a frequency of maximum power $\nu_{\text{max}} \approx 300 \mu\text{Hz}$, we calculate all dipole modes within the frequency range $\nu_{\text{max}}/2$ and $3\nu_{\text{max}}/2$ in the simultaneous presence of magnetism and rotation, using the scheme described in Section 5.5.1. The width of the adopted frequency range is comparable to the full width at half maximum value $\delta\nu_{\text{env}} \approx 100 \mu\text{Hz} \approx \nu_{\text{max}}/3$ calculated using the scaling relation of Mosser, Elsworth, et al. (2012). The large central magnetic field $B_c \approx 820 \text{ kG}$ is chosen such that the $m = \pm 1$ sectoral modes are suppressed at the lower frequency range, to show the effect of a strong field. Note that B_c refers to the maximum value of the radial component of the field at the center of the star, rather than some horizontally averaged version of this quantity. Therefore, this value of B_c corresponds to a horizontally averaged field $\overline{B_r^2}^{1/2} \approx B_c/\sqrt{3} \approx 470 \text{ kG}$ when normalized in the same way as the values reported by Li, Deheuvels, Ballot, and Lignières (2022) (30–100 kG), Deheuvels, Li, et al. (2023) (40–610 kG), and Li, Deheuvels, Li, et al. (2023) (20–150 kG). The middle panels of Figure 5.2 show mock period echelle diagrams corresponding to these calculations.

We additionally calculate the mode frequencies for the same stellar model in the absence of either rotation and magnetism, in order to test the perturbative formalism. At high frequencies (where both rotation and magnetism are perturbative), the mode frequencies are closely consistent with the perturbative frequency shifts derived by Li, Deheuvels, Ballot, and Lignières (2022) (the unfilled symbols in the middle panels of Figure 5.2). However, at low frequencies close to suppression ($\nu \lesssim 220 \mu\text{Hz}$), the TARM and perturbative results deviate substantially, with the TARM results tending to predict much larger frequency shifts than the perturbative formulae. This effect becomes increasingly dramatic until, at $\nu \approx 170 \mu\text{Hz}$, the sectoral modes are totally suppressed (although the zonal $m = 0$ mode remains propagating, and is suppressed at a frequency below the chosen observed frequency range). Disagreement between the perturbative and TARM frequency shifts is fully expected: at or near suppression, the effects of magnetism are, by definition, highly non-perturbative.

To formally demonstrate consistency with the perturbative formulae at high mode frequencies, we can expand the operator in Equation 5.24 in b and q and perform a perturbation analysis. Corrections to the subsequent analysis enter at $\mathcal{O}(q^3, qa^2, a^4) \sim \mathcal{O}(\Omega^3, \Omega\omega_B^4, \omega_B^8)$. We obtain the following eigenvalue equation:

$$0 = \lambda p'(\mu) + \mathcal{L}_0^m[p'(\mu)] + \mathcal{L}_{\text{pert}}^{m,b,q}[p'(\mu)] \quad (5.49)$$

where

$$\begin{aligned} \mathcal{L}_{\text{pert}}^{m,b,q}[p'(\mu)] &= -mqp'(\mu) \\ &+ (b^2 + q^2) \left[\frac{d}{d\mu} \left(\mu^2(1 - \mu^2) \frac{dp'}{d\mu} \right) - \frac{m^2\mu^2}{1 - \mu^2} p'(\mu) \right]. \end{aligned} \quad (5.50)$$

To find the effect of $\mathcal{L}_{\text{pert}}^{m,b,q}$ on the eigenvalues, we perform first-order perturbation theory. If the dipole eigenvalues are given by

$$\lambda = \ell(\ell + 1) + \tilde{\lambda}^{m,b,q} = 2 + \tilde{\lambda}^{m,b,q}, \quad (5.51)$$

where

$$0 = \tilde{\lambda}^{m,b,q} + \int_{-1}^{+1} p_m'^0(\mu)^* \mathcal{L}_{\text{pert}}^{m,b,q}[p_m'^0(\mu)] d\mu \quad (5.52)$$

and $p_m'^0(\mu)$ are the unperturbed eigenfunctions (of \mathcal{L}_0^m). We emphasize that this is a perturbative expansion on the space of latitudinal functions all of the same m (for the generalized Legendre operators), and *not* on the full space of spherical harmonics (as done by Li, Deheuvels, Ballot, and Lignières, 2022). Degenerate perturbation theory is thus not

necessary here, since the eigenvalues of the generalized Legendre operator for a given m do not repeat. Furthermore, while in principle corrections may enter in an expression at second-order in perturbation theory, the only relevant term $\propto -mq$ in $\mathcal{L}_{\text{pert}}^{m,b,q}$ shifts all of the eigenvalues of a given m equally, and thus does not induce a second-order perturbation in λ .

The unperturbed pressure perturbations are the associated Legendre polynomials,

$$p_m'^0(\mu) = \begin{cases} \sqrt{\frac{3}{2}}\mu & m=0 \\ \sqrt{\frac{3}{4}}\sqrt{1-\mu^2} & m=\pm 1 \end{cases} \quad (5.53)$$

where we have normalized the functions to square-integrate to unity and ignored the overall (Condon–Shortley) phase. The integral in Equation 5.52 can therefore be evaluated to give

$$\lambda = \begin{cases} 2 + \frac{2}{5}(b^2 + q^2) & m=0 \\ 2 \pm q + \frac{4}{5}(b^2 + q^2) & m=\pm 1 \end{cases} \quad (5.54)$$

so that

$$\sqrt{\lambda} = \begin{cases} \sqrt{2} + \frac{1}{5\sqrt{2}}(b^2 + q^2) & m=0 \\ \sqrt{2} \pm \frac{1}{2\sqrt{2}}q + \frac{1}{80\sqrt{2}}(32b^2 + 27q^2) & m=\pm 1 \end{cases} \quad (5.55)$$

To transform the independent variable b to a (which can directly be specified given a field and stellar profile), we note that

$$b = a\sqrt{\lambda} \approx a\sqrt{2} \quad (5.56)$$

up to the relevant order. Then

$$\sqrt{\lambda} = \begin{cases} \sqrt{2} + \frac{1}{5\sqrt{2}}(2a^2 + q^2) & m=0 \\ \sqrt{2} \pm \frac{1}{2\sqrt{2}}q + \frac{1}{80\sqrt{2}}(64a^2 + 27q^2) & m=\pm 1 \end{cases} \quad (5.57)$$

The mode frequencies in the co-rotating frame are given by

$$\bar{\omega} = \frac{1}{\varphi_g} \int_{r_1}^{r_2} \sqrt{\lambda} \frac{N}{r} dr \quad (5.58)$$

in the asymptotic regime, where $\varphi_g = \pi(n_g + \varepsilon_g)$ (Tassoul, 1980) is the total radial phase (note that λ depends implicitly on $\bar{\omega}$ in a complicated way). We again proceed in ignoring the frequency dependence of the bounds of the integral in Equation 5.58 (which should formally only enclose the part of the main radiative cavity where $\omega < N$).

We define the “buoyant average”:

$$\langle \dots \rangle_g = \frac{\int_{r_1}^{r_2} (\dots) \frac{N}{r} dr}{\int_{r_1}^{r_2} \frac{N}{r} dr}. \quad (5.59)$$

Assuming that $\delta\bar{\omega} \ll \bar{\omega}_0$ (sufficient for the desired order of the expansion), we may expand Equation 5.58 as

$$\delta\bar{\omega} = \left(\frac{\langle \omega_B^4 \rangle_g}{5\bar{\omega}_0^3} + \frac{2\langle \Omega^2 \rangle_g}{5\bar{\omega}_0} \right) - \sqrt{2} \left(\frac{2\langle \omega_B^4 \rangle_g}{5\bar{\omega}_0^3} + \frac{2\langle \Omega^2 \rangle_g}{5\bar{\omega}_0} \right) \frac{\delta\bar{\omega}}{\bar{\omega}_0} \quad (5.60)$$

for $m=0$, and

$$\begin{aligned} \delta\bar{\omega} = & \left(\pm \frac{\langle \Omega \rangle_g}{2} + \frac{2\langle \omega_B^4 \rangle_g}{5\bar{\omega}_0^3} + \frac{27\langle \Omega^2 \rangle_g}{40\bar{\omega}_0} \right) \\ & - \sqrt{2} \left(\pm \frac{\langle \Omega \rangle_g}{4} - \frac{8\langle \omega_B^4 \rangle_g}{5\bar{\omega}_0^3} - \frac{27\langle \Omega^2 \rangle_g}{40\bar{\omega}_0} \right) \frac{\delta\bar{\omega}}{\bar{\omega}_0} \end{aligned} \quad (5.61)$$

for $m=\pm 1$. Equations 5.60 and 5.61 can be solved to yield the following frequency shifts:

$$\delta\bar{\omega}_{m=0} = \frac{1}{5} \frac{\langle \omega_B^4 \rangle_g}{\bar{\omega}_0^3} + \frac{2}{5} \frac{\langle \Omega^2 \rangle_g}{\bar{\omega}_0} \quad (5.62a)$$

$$\delta\bar{\omega}_{m=\pm 1} = \pm \frac{\langle \Omega \rangle_g}{2} + \frac{2}{5} \frac{\langle \omega_B^4 \rangle_g}{\bar{\omega}_0^3} + \frac{27\langle \Omega^2 \rangle_g - 10\langle \Omega \rangle_g^2}{40\bar{\omega}_0}. \quad (5.62b)$$

We keep one higher order of the rotation rate than do Li, Deheuvels, Ballot, and Lignières (2022). We distinguish between $\langle \Omega^2 \rangle_g$ and $\langle \Omega \rangle_g^2$ in the above to allow for the possibility of weak differential rotation (e.g., Beck et al., 2012), which may distinguish between the two. However, in the case of uniform rotation (assumed throughout this work), $\langle \Omega^2 \rangle_g = \langle \Omega \rangle_g^2 = \Omega^2$. In the inertial frame, these frequency shifts become

$$\delta\omega_{m=0} = \frac{1}{5} \frac{\langle \omega_B^4 \rangle_g}{\omega_0^3} + \frac{2}{5} \frac{\langle \Omega^2 \rangle_g}{\omega_0} \quad (5.63a)$$

$$\delta\bar{\omega}_{m=\pm 1} = \mp \frac{\langle \Omega \rangle_g}{2} + \frac{2}{5} \frac{\langle \omega_B^4 \rangle_g}{\omega_0^3} + \frac{27\langle \Omega^2 \rangle_g - 10\langle \Omega \rangle_g^2}{40\omega_0} \quad (5.63b)$$

where $\bar{\omega}_0 = \omega_0$ for the unperturbed modes. We have full consistency with the perturbation formulae of Li, Deheuvels, Ballot, and Lignières (2022) (their Equations 61 and 62, with $\zeta = 1$). Note that the star-averaged quantity which they define to be ω_B ($\equiv \omega_{B,L22}$) is equal to $\omega_{B,L22} = \langle \omega_B^4 \rangle_g / 3\bar{\omega}_0^3$.

We caution that both the direct role of the centrifugal force as a restorative force and its indirect impact on the stellar structure (e.g., Ballot et al., 2010) also enter at $\propto \Omega^2$. Inclusion of these effects is likely necessary to accurately capture the second-order effects of rotation.

Our non-perturbative mode calculations imply a few straightforward predictions. First, as mentioned previously, the magnetic frequency shifts become substantially stronger than implied by a perturbative estimate. While the relative change in the period spacing is still small (δP_g decreases by $\approx 10\%$ before suppression), the frequency shifts still substantially modify the period echelle diagram. Conversely, if the period spacing pattern of a strongly magnetic red giant is fit using the perturbative formulae, the inferred magnetic field is likely to be a significant overestimate. For example, Deheuvels, Li, et al. (2023) claim the detection of a red giant (KIC 6975038) whose magnetic field (≈ 286 kG) significantly exceeds the critical field B_{crit} by a factor ~ 1.7 . Under our formalism, a field near or exceeding B_{crit} should efficiently damp magnetogravity waves, either through phase mixing or refraction to infinite wavenumbers. Indeed, Deheuvels, Li, et al. (2023) observe nearly total dipole suppression in the same star for only low-frequency modes $\lesssim \nu_{\text{max}}$, consistent with ω_{crit} lying on their observed frequency range. Their results could potentially be brought into accord with ours if non-perturbative effects have caused an observational overestimate of the field by a factor of a few.

To characterize the severity of such systematic overestimates, we compute the dipole frequency shifts in the red giant model for a range of internal magnetic fields (by numerically solving Equation 5.58). For each order m , we then calculate the internal magnetic field which would be needed to produce the same frequency shift in perturbation theory. Figure 5.3 shows that the magnetic field $\langle B_r^2 \rangle^{1/2}$ implied by perturbation theory can exceed the “true” value for fields which are almost strong enough to cause suppression. Specifically, we use $\langle B_r^2 \rangle^{1/2}$ to denote the field averaged over all angles and over the radial kernel (following Li, Deheuvels, Ballot, and Lignières, 2022):

$$\langle B_r^2 \rangle = \frac{1}{3} \int_{r_1}^{r_2} K(r) B_r^2 \, dr. \quad (5.64)$$

where $K(r)$ is given by Equation 5.67 in the asymptotic limit.

While the errors accrued by the perturbative formulae in Figure 5.3 are relatively small and do not rise to a factor ~ 1.7 , the degree to which perturbation theory overestimates the field likely depends on the field geometry adopted and the exact structure of the star (via, e.g., how far up the red giant branch the star is). Moreover, it likely depends on the exact procedure used to extract the field. For example, Figure 5.3 shows magnetic field values inferred using only one azimuthal order at one frequency, but an inference using

the whole oscillation spectrum may yield a different answer. In the future, the manner in which perturbation theory misestimates the field should be characterized in more detail as a function of these factors. Large relative errors in the inferred magnetic field may also appear at low fields and if second-order rotational effects are mistaken for magnetic shifts (top panel of Figure 5.3).

Second, Li, Deheuvels, Ballot, and Lignières (2022) and Li, Deheuvels, Li, et al. (2023) measure the dipole asymmetry parameter, defined by

$$a_{\text{asym}} = \frac{\delta\omega_{m=+1} + \delta\omega_{m=-1} - 2\delta\omega_{m=0}}{\delta\omega_{m=+1} + \delta\omega_{m=-1} + \delta\omega_{m=0}}. \quad (5.65)$$

This should not be confused with the parameter $a = \omega_B^2/\omega^2$ defined in this work and by Rui and Fuller (2023). In the perturbative regime, they show that

$$a_{\text{asym}} = \frac{\int_{r_1}^{r_2} dr K(r) \iint \sin \theta d\theta d\phi B_{0r}^2 P_2(\cos \theta)}{\int_{r_1}^{r_2} dr K(r) \iint \sin \theta d\theta d\phi B_{0r}^2}, \quad (5.66)$$

where $P_2(\mu) = (3\mu^2 - 1)/2$ is the second-order Legendre polynomial and $K(r)$ is a radial kernel function given by

$$K(r) = \frac{\rho^{-1}(N/r)^3}{\int_{r_1}^{r_2} \rho^{-1}(N/r)^3 dr}. \quad (5.67)$$

In particular, when the horizontal dependence of B_{0r} is given by $\psi(\theta, \phi)$ (i.e., the horizontal geometry is radius-independent), the radial integral in Equation 5.66 can be eliminated, yielding

$$a_{\text{asym}} = \frac{\iint \sin \theta d\theta d\phi \psi(\theta, \phi)^2 P_2(\cos \theta)}{\iint \sin \theta d\theta d\phi \psi(\theta, \phi)^2}. \quad (5.68)$$

In the special case of a dipole magnetic field whose axis is aligned with the rotational axis ($\psi(\theta, \phi) = \cos \theta$), it can be seen that $a_{\text{asym}} = 2/5 = 0.4$ in this expression.

In the bottom panel of Figure 5.2, we see that this expectation holds at high frequencies, but increases slightly to ≈ 0.5 at lower frequencies (near ω_{crit}). While likely difficult to measure, a value of a_{asym} that varies towards lower frequencies (coinciding with the inference of a large magnetic field from the frequency shifts) may be an independent signature of a near-critical field. This non-perturbative asymmetry effect is related to the different magnetic fields implied by perturbation theory's predictions for the frequency shifts of different azimuthal orders (Figure 5.3).

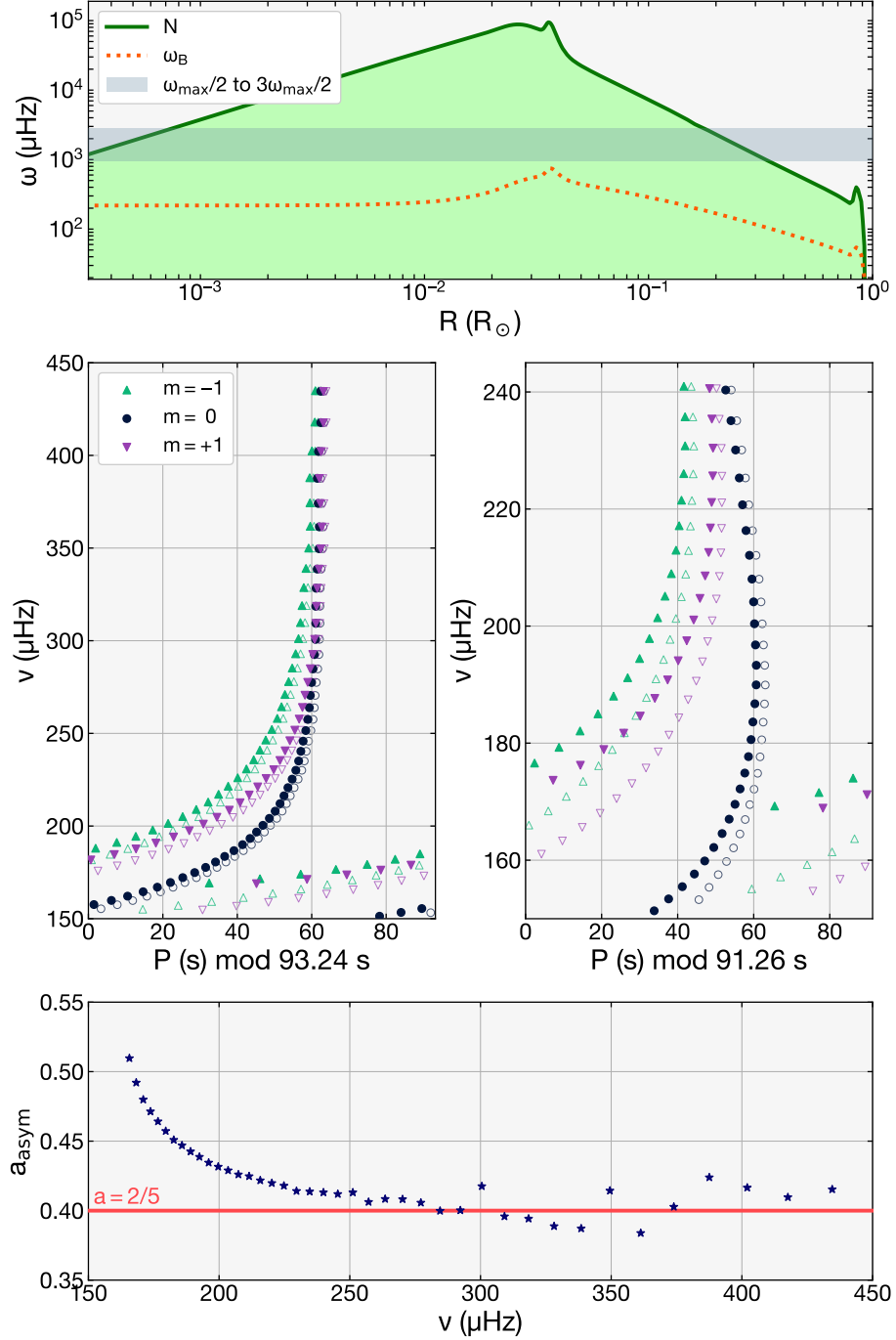


Figure 5.2: *Top:* The Brunt–Väisälä (N) and magnetogravity (ω_B) frequencies for the red giant model (RG-1.5), plotted in relation to the range over which we solve for mode frequencies. The rotational frequency $\Omega \approx 2.4 \mu\text{Hz}$ ($P_{\text{rot}} = 30$ d) is below the bottom bound of this plot. *Center:* Period echelle diagram for the red giant’s core g modes. The right panel zooms into the low frequency modes of the left panel, and folds on a different period for clarity. Solid symbols denote mode frequencies calculated using the TARM, whereas hollow symbols denote the lowest-order prediction of perturbation theory. *Bottom:* The dipole asymmetry parameter (Equation 5.65) plotted against unperturbed mode frequency.

In stars with especially weak magnetic fields, it is in principle possible for the dipole asymmetry to be dominated by rotation, *even if* it is slow enough for perturbation theory to be applicable. From Equation 5.63 and Equations 5.65, we have

$$a_{\text{asym}} = \frac{8\langle\omega_B^4\rangle_g/\bar{\omega}_0^2 + 11\langle\Omega^2\rangle_g - 10\langle\Omega\rangle_g^2}{20\langle\omega_B^4\rangle_g/\bar{\omega}_0^2 + 35\langle\Omega^2\rangle_g - 10\langle\Omega\rangle_g^2} \quad (5.69)$$

such that, for a uniform rotation rate Ω , $\langle\Omega^2\rangle_g = \langle\Omega\rangle_g^2 = \Omega^2$, Equation 5.69 possesses the limiting behavior

$$a_{\text{asym}} = \begin{cases} \frac{2}{5} - \frac{9}{20} \frac{\bar{\omega}_0^2 \Omega^2}{\langle\omega_B^4\rangle_g} & \langle\omega_B^4\rangle_g \gg \bar{\omega}_0^2 \Omega^2 \\ \frac{1}{25} + \frac{36}{125} \frac{\langle\omega_B^4\rangle_g}{\bar{\omega}_0^2 \Omega^2} & \langle\omega_B^4\rangle_g \ll \bar{\omega}_0^2 \Omega^2 \end{cases}. \quad (5.70)$$

When the magnetic asymmetry dominates ($\langle\omega_B^4\rangle_g/\bar{\omega}_0^2 \gg \langle\Omega\rangle_g^2 \simeq \Omega^2$), $a_{\text{asym}} \approx 2/5 = 0.40$. However, when the Coriolis-induced rotational asymmetry dominates ($\Omega^2 \gg \langle\omega_B^4\rangle_g/\bar{\omega}_0^2$), we instead have $a_{\text{asym}} \approx 1/25 = 0.04$. We stress that this is a fully perturbative effect: it only deviates from the result of Li, Deheuvels, Ballot, and Lignières (2022) because it includes a single higher-order effect of rotation. The upshot is that, even when both rotation and magnetism are individually small, $a_{\text{asym}} \neq 2/5$ for aligned rotational/magnetic axes if the effect of rotation is *relatively* at least comparable to that of magnetism. We again caution that the centrifugal force (which is also relevant at this order in Ω) has been neglected—this likely implies that the rotation-dominated asymmetry does not exactly approach 1/25 but some other value. Inclusion of such effects (as done by, e.g., Mathis and Prat, 2019; Dhouib, Prat, et al., 2021b; Dhouib, Prat, et al., 2021a) is needed to properly predict the true rotation-dominated asymmetry value. Nevertheless, we expect the qualitative ability for rotation to dominate over magnetism in determining the dipole asymmetry to be robust.

Li, Deheuvels, Ballot, and Lignières (2022) and Li, Deheuvels, Li, et al. (2023) neglect the rotational asymmetry effect on the basis that the core rotation rates in the stars in their sample are typical (i.e., low): we hereafter check this explicitly. As a crude estimate, the magnetic asymmetry dominates the rotational asymmetry in a red giant core when $\langle\omega_B^4\rangle_g/\omega_{\text{max}}^2 \Omega^2 \gg 1$. In the three stars investigated by Li, Deheuvels, Ballot, and Lignières (2022), $\langle\omega_B^4\rangle_g/\omega_{\text{max}}^2 \Omega^2 \gtrsim 10^2$ and their asymmetries are thus indeed very magnetically dominated. Most of the stars reported by Li, Deheuvels, Li, et al. (2023) have values of $\langle\omega_B^4\rangle_g/\omega_{\text{max}}^2$ in the tens or hundreds. However, this parameter reaches a minimum for KIC 8540034, for which $\langle\omega_B^4\rangle_g/\omega_{\text{max}}^2 \Omega^2 \approx 9$. In this star, rotation may affect the asymmetry parameter for low-frequency modes (note the frequency dependence of $\langle\omega_B^4\rangle_g/\omega^2 \Omega^2$) In general, magnetic domination of the dipole asymmetry may not be the case for giants with

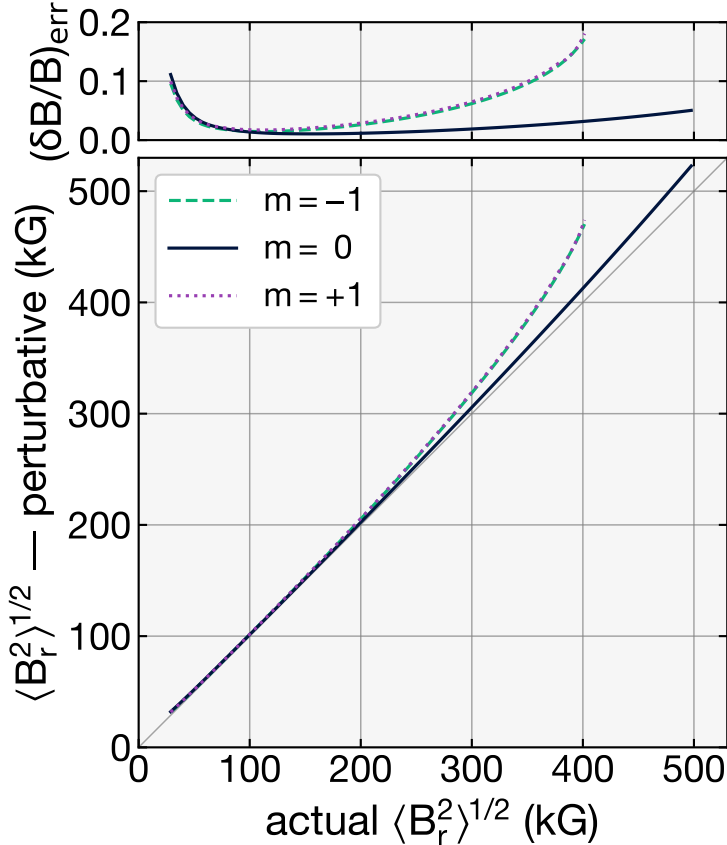


Figure 5.3: For the red giant model (RG-1.5): *Top*: The relative error on the inferred magnetic field $\langle B_r^2 \rangle^{1/2}$ associated with perturbation theory. $\langle B_r^2 \rangle^{1/2}$ refers to an angle- and radial kernel-averaged field, following the notation of Li, Deheuvels, Ballot, and Lignières (2022) (see Equation 5.64). *Bottom*: The internal magnetic field $\langle B_r^2 \rangle^{1/2}$ implied by perturbation theory using the frequency shift for some angular degree m , plotted against the “real” value (given by our non-perturbative TARM formalism). The frequency shift is evaluated using $\varphi_g \simeq \pi n_g$ for a physically realistic radial order $n_g = 70$ ($\nu_{\text{max}} \approx 150 \mu\text{Hz}$), roughly the bottom of the frequency range shown in the period echelle diagram in Figure 5.2.

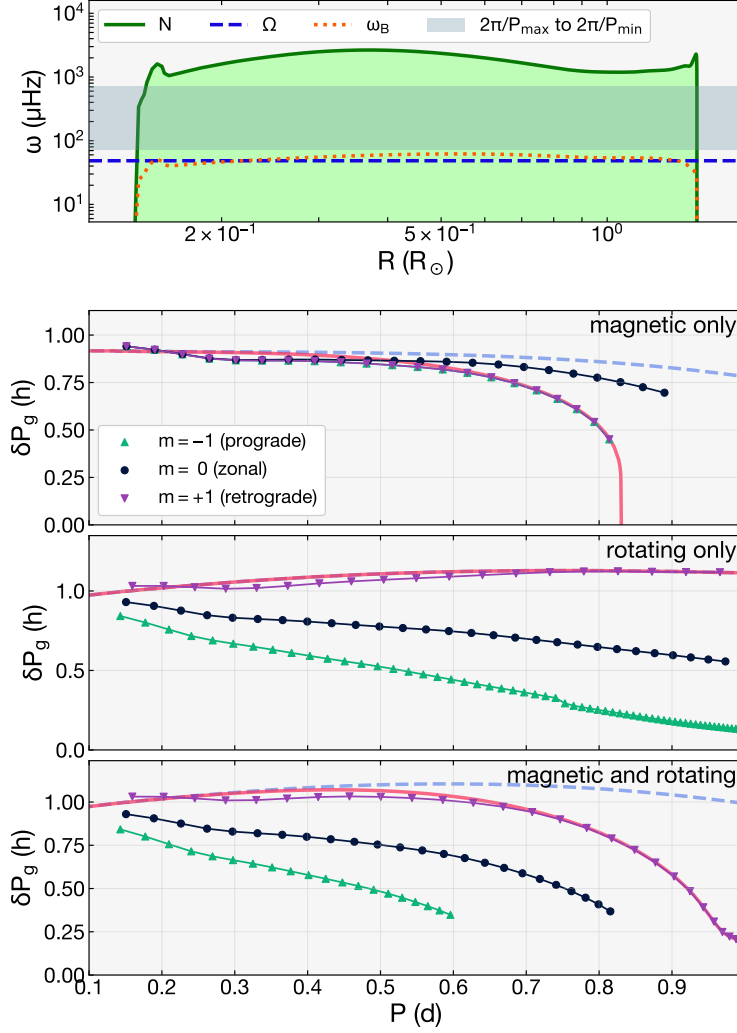


Figure 5.4: Characteristic frequency profiles and mode frequencies for a young γ Dor analogue (MS-1.5-young). *Top*: The Brunt–Väisälä (N), rotational (Ω), and magnetogravity (ω_B) frequencies, plotted in relation to the range over which we solve for mode frequencies. *Bottom*: The period spacing δP_g versus period P in the inertial frame for the dipole modes, in the magnetic, rotating, and magnetic and rotating cases. Predictions for the asymptotic period spacing for the $m=1$ branch (using Equation 5.33) are shown in *solid red*. We also show predictions for the asymptotic period spacing handling rotation non-perturbatively but magnetism only perturbatively (using Equation 5.71; *dashed blue* curves).

either fast core rotation rates *or* weak fields, and we caution against using a_{asym} alone to make an inference of the field geometry without checking this criterion explicitly.

5.6.2 Strong fields threading the envelopes of main-sequence pulsators

Stars with masses $\gtrsim 1.3M_\odot$ have radiative envelopes and convective cores on the main sequence. Therefore, such stars may pulsate in g modes which are directly detectable,

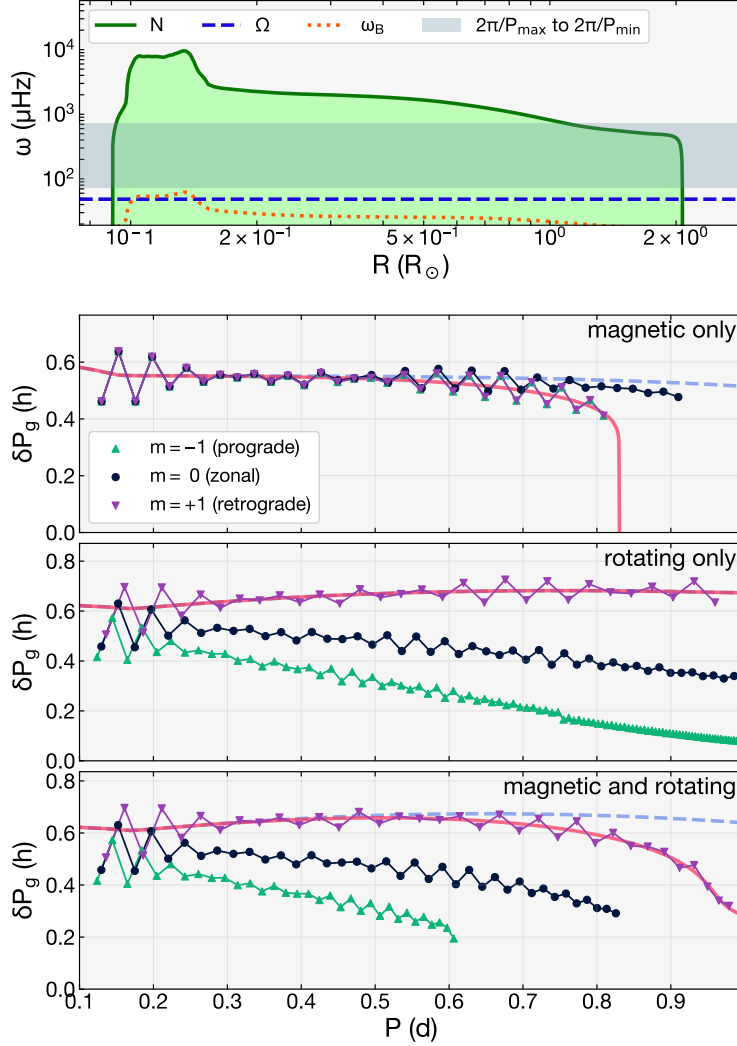


Figure 5.5: Same as Figure 5.4, but for an evolved γ Dor analogue (MS-1.5-evolved).

without needing to be disentangled from p modes as in solar-like oscillators. Such oscillators are ubiquitous: as discussed previously, they include γ Dor (AF-type) and SPB (B-type) variables. The pulsations are driven by coherent mechanisms such as convective flux blocking (in γ Dors; Guzik, Kaye, Bradley, Cox, Neuforge-Verheecke, et al., 2002; Dupret, Grigahcine, et al., 2004) and the κ mechanism (in B-type pulsators; Gautschy and Saio, 1993; Dziembowski, Moskalik, et al., 1993). This is in contrast to the broadband, stochastic driving present in solar-like oscillators (Samadi et al., 2015). Crucially, in these pulsators, there is no guarantee that the measurable modes are complete over some observed frequency range. The selection mechanism for mode excitation is poorly understood, and the asteroseismic power spectra are often sparse. Observational studies of such pulsators thus typically apply a forward-modeling approach based on the identified modes (e.g., Aerts,

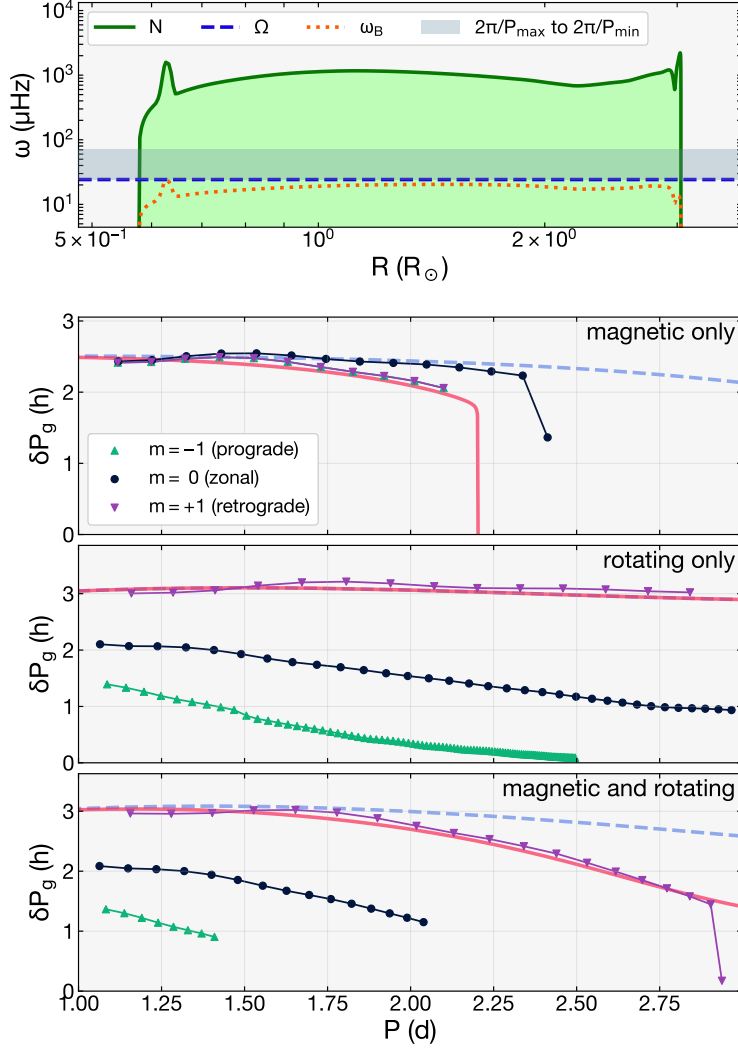


Figure 5.6: Same as Figure 5.4, but for a young SPB analogue (MS-6.0-young).

Molenberghs, et al., 2018), which rely on good models for predicting observed oscillation spectra.

In this Section, we primarily focus on the period spacing pattern $\delta P_g = \delta P_g(P)$ for modes of a given m . This is a standard observable in the study of main-sequence pulsators. The period spacing pattern is known to encode the rotation rate of the star (through an overall slope; Bouabid et al., 2013; Ouazzani, Salmon, et al., 2017), as well as the presence of buoyancy glitches (e.g., Miglio, Montalbán, Noels, et al., 2008).

We first calculate the dipole oscillation modes for two γ Dor-like models, one near the zero-age main sequence (MS-1.5-young) and one near the terminal-age main sequence (MS-1.5-evolved), shown respectively in Figures 5.4 and 5.5. The chief difference between

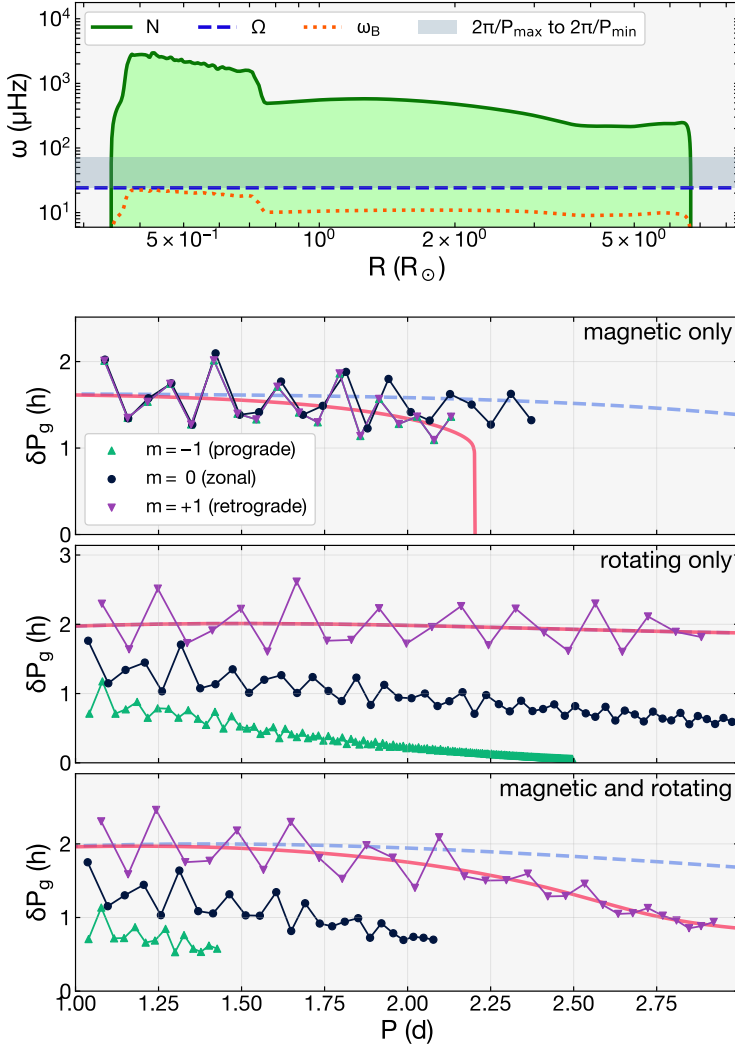


Figure 5.7: Same as Figure 5.4, but for a evolved SPB analogue (MS-6.0-evolved).

these models is that the convective core in the latter model has had time to develop a large compositional gradient at the base of its radiative envelope: this produces a jump in N (see the top panel of Figure 5.5). Qualitatively, this sharp feature in N results in a trapping phenomenon which results in a period spacing δP_g which oscillates as a function of mode period P (Miglio, Montalbán, Noels, et al., 2008; Pedersen et al., 2018; Vanlaer et al., 2023). We adopt a fairly typical core rotation rate of 1.5 d to accentuate the effects of rotation (Van Reeth, Tkachenko, and Aerts, 2016; Li, Van Reeth, et al., 2020). Unlike in the red giant model described in Section 5.6.1 (where realistic rotation rates are small, such that $q \ll 1$), rotation in the MS models is fast enough to cause frequency splittings/shifts which are nonlinear with respect to Ω .

The lower panels of Figures 5.4 and 5.5 show δP_g versus P_g for the young and evolved $1.5M_\odot$ models, under the effects of magnetism and rotation individually as well as simultaneously. First, since rotation distinguishes between prograde and retrograde modes, the slope it imparts onto the period spacing pattern is different for the $m = +1$ and $m = -1$ modes. In contrast, the oscillation modes are not sensitive to the overall sign of the magnetic field, and thus magnetism affects the $m = \pm 1$ modes identically (but still differently than the $m = 0$ mode).

Moreover, while rotation produces values of P_g which vary fairly linearly with P , magnetism produces a curvature in the pattern, especially near suppression. This effect is similar to what was demonstrated by Dhouib, Mathis, et al. (2022) in the case of a purely toroidal field. In particular, when the maximum allowed value of $a = a_{\text{crit}}$ is determined by connection to the evanescent region (rather than the presence of a critical Alfvén latitude), the asymptotic expression (in Equation 5.33) predicts that δP_g sharply approaches zero at $\omega \approx \omega_B$. This is because the term $\propto d \ln \lambda / d \ln a$ in Equation 5.33 diverges at radii where the main magnetogravity wave branch connects to the slow branch described by Lecoanet, Vasil, et al. (2017) and Rui and Fuller (2023). In reality, there is not likely to be an infinitely dense forest of modes, since the asymptotic formula is based on a linear approximation which is likely to break down close to suppression. Nevertheless, the curvature is conspicuous, especially for the young model, where the period spacing drops from its high-frequency value by $\simeq 50\%$ near the critical frequency. Moreover, this curvature is apparent even when rotation is included alongside magnetism, with the added feature that fast rotation can cause the $m = +1$ and $m = -1$ modes to become magnetically suppressed at very different frequencies. This curvature effect on the period spacing pattern is very different than those caused by inertial-mode coupling in main-sequence convective cores (which manifest as isolated “dips”; Tokuno and Takata, 2022) and mode-trapping near strong compositional gradients outside of those cores (which manifests as “oscillations”; Miglio, Montalbán, Noels, et al., 2008).

This sharp curvature feature is not adequately captured by any low-order perturbative treatment of magnetism. To make comparison to the perturbative prediction generous, we expand Equation 5.33 around $a = 0$, while treating rotation non-perturbatively (through the traditional approximation of rotation, cf. Van Beeck et al., 2020). The effect of magnetism then enters the period spacing earliest through $a^2 \propto \omega_B^4 / \omega^4 \propto B^2 / B_{\text{crit}}^2$ (as predicted by Cantiello et al., 2016). Specifically, defining λ_H to be the eigenvalue calculated including

rotation only, we have

$$\begin{aligned} \delta\bar{P}_g \approx & \frac{2\pi^2}{\sqrt{\lambda_H}} \left(\int \left(1 + \frac{1}{2} \frac{d \ln \lambda_H}{d \ln q} \right) \frac{N}{r} dr \right)^{-1} \\ & - \frac{16\pi^6 \lambda'}{\lambda_H^{3/2}} \bar{P}^{-4} \left(\int \omega_B^4 \left(1 + \frac{1}{2} \frac{d \ln \lambda_H}{d \ln q} \right) \frac{N}{r} dr \right)^{-1}, \end{aligned} \quad (5.71)$$

where we have used

$$\left(\frac{d \ln \lambda}{d \ln a} \right)_{a=0} = 0. \quad (5.72)$$

In addition to lacking the suppression phenomenon entirely, the perturbative prediction (shown for the $m = +1$ mode as the blue-dashed lines in Figures 5.4 and 5.5) dramatically underestimates the magnetic curvature predicted by the full TARM-based formalism. To further demonstrate this point, in Figure 5.1, we show contours where the perturbative estimate misestimates the integrand of the integral in the asymptotic formula (Equation 5.33) by 10% and 50%, respectively. As expected, departure from the full TARM calculation becomes increasingly severe close to suppression. Non-perturbative effects must therefore be taken into account predicting the frequency spectrum close to ω_{crit} . For example, the magnetic ‘‘sawtooth’’ pattern in the period spacing pattern predicted by some authors (Prat, Mathis, Buysschaert, et al., 2019; Prat, Mathis, Neiner, et al., 2020a; Van Beeck et al., 2020) was derived using perturbation theory at low frequencies, and preliminary results suggest that this feature does not appear once magnetism is incorporated non-perturbatively (Dhouib et al., in prep.).

An important observation is that the magnetically induced curvature in the period spacing pattern is more conspicuous in the young model than in the evolved one. This is because the relative magnetic frequency shifts are primarily determined by the quantity $\langle \omega_B^4 \rangle_g^{1/4} / \bar{\omega}_0$ (as shown in Section 5.6.1), which is maximized when as many layers of the star have $\omega_B \sim \bar{\omega}_0$ as possible. However, within our physical picture, the entire oscillation mode becomes suppressed when even a small layer of the star has $\bar{\omega}_0 \lesssim \omega_{\text{crit}} \sim \omega_B$. Because N accounts for most of the variation of $\omega_B \propto \sqrt{N}$ (the Prendergast field we adopt varies comparatively more slowly with radius), ω_B is a much broader function of r in the young model versus in the evolved one, where it is peaked at the composition gradient at the lower boundary of the radiative envelope. Therefore, the young model reaches a larger maximum value of $\langle \omega_B^4 \rangle_g^{1/4} / \bar{\omega}_0$ than the evolved one, and furthermore in general attains large values of $\langle \omega_B^4 \rangle_g^{1/4} / \bar{\omega}_0$ over a wider frequency range. This heuristic explanation is even stronger for higher-order terms in the perturbative expansion, which involve buoyant integrals of higher powers of $\omega_B^4 / \bar{\omega}_0^4$.

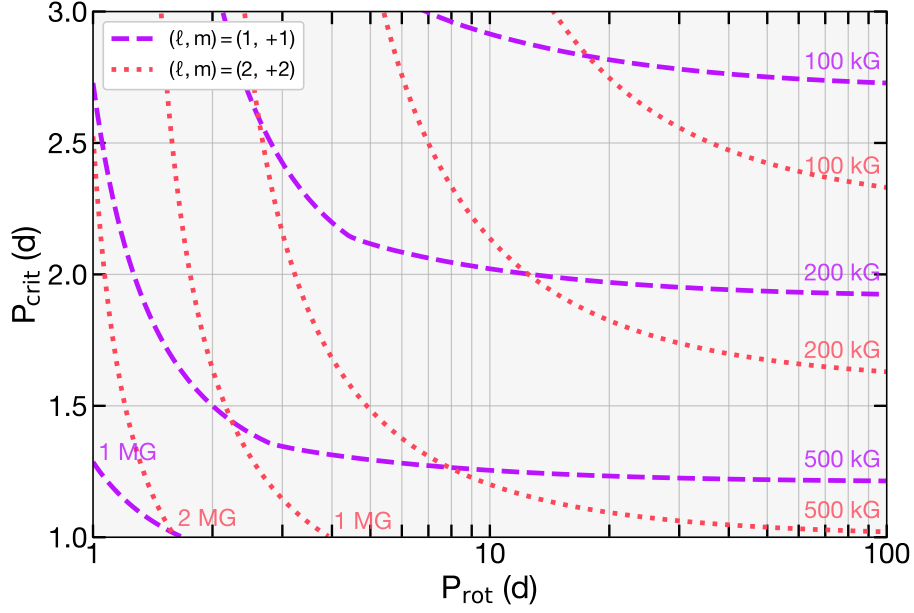


Figure 5.8: The critical period P_{crit} against the rotation period P_{rot} for a young SPB-like model (MS-6.0-young), for fixed values of the field near the compositional gradient at the base of the radiative envelope (which most easily experiences magnetic suppression). P_{crit} is given in the inertial frame.

The magnetic curvature is in principle detectable even in evolved main-sequence pulsators, as long as it can be deconvolved from other effects. It should be noted that the typical uncertainties in γ Dor period spacings in *Kepler* are small, comparable to the marker sizes of Figures 5.4 and 5.5 (Van Reeth, Tkachenko, Aerts, et al., 2015; Li, Van Reeth, et al., 2020). Moreover, because of the sensitivity of the magnetic curvature in the period spacing pattern to the compositional profile, strongly magnetized main-sequence pulsators may be a promising avenue for constraining mixing processes. However, in nonasymptotic cases where sharp features in the buoyancy profile are expected, the limitations of the TARM must carefully be considered.

For completeness, we also examine young (MS-6.0-young) and evolved (MS-6.0-evolved) SPB analogues, with masses $6M_{\odot}$ (Figures 5.6 and 5.7, respectively). The qualitative features of the period spacing pattern are similar, except that the peak in ω_B at the base of the radiative region in the young model (due to the peak in N) exceeds the value of ω_B throughout the rest of the cavity. Therefore, for similar reasons as in the evolved γ Dor model, the curvature in the period spacing pattern due to magnetism is not as prominent as in the young γ Dor model.

For illustrative purposes, we calculate the critical mode frequencies for a variety of internal magnetic fields and rotation rates, using the MS-6.0-young model. Figure 5.8 shows the critical mode period $P_{\text{crit}} = 2\pi/\omega_{\text{crit}}$ for the dipole and quadrupole prograde sectoral modes. Interestingly, although rotation is expected to make prograde modes suppress at higher frequencies in the co-rotating frame (see Figure 5.1), higher rotation rates actually cause modes to suppress at *lower* frequencies in the inertial frame. Simultaneous knowledge of the suppression frequency for one identified mode branch together with the rotation rate should be sufficient to make a model-dependent estimate of the magnetic field at the interior of the star. Alternatively, while potentially challenging, simultaneous measurement of the suppression frequencies for two identified mode branches may be able to put a constraint on both the internal magnetic field as well as rotation rate. Because the shapes of the contours in Figure 5.8 are largely determined by change-of-frame effects (vis-à-vis Equation 5.39), the latter method is most viable when the two mode branches have different azimuthal order m .

Roughly $\sim 10\%$ of massive dwarf stars possess significant (inclined dipolar) fossil fields up to tens of kilogauss at their surfaces (Grunhut et al., 2016; Shultz et al., 2019). Such fields may be strong enough in the interiors of such stars to suppress low-frequency g-mode oscillations. Recently, Lecoanet, Bowman, et al. (2022) attributed missing low-frequency modes in the magnetic SPB star HD 43317 (observed with CoRoT; Buyschaert, Neiner, et al., 2017; Buyschaert, Aerts, et al., 2018) to magnetic suppression caused by a near-core radial field $B_r \simeq 500$ kG. As in our MS-6.0-early model, suppression in their model occurs when $\omega_{\text{crit}} > \omega$ in the compositional peak in N at the base of the radiative cavity (see their Figure 2). Moreover, Aerts, Van Reeth, et al. (2017) predict that core dynamos in B-type (AF-type) pulsators may produce strong magnetic fields 20–400 kG (0.1–3 kG) where non-perturbative magnetic effects may be realized. Magnetic g-mode main-sequence stars thus appear to be natural environments to observe g modes which are non-perturbatively modified by magnetism.

Pulsators in the γ Dor mass range may also possess influential magnetic fields (Aerts, Augustson, et al., 2021). Surface fields of hundreds to thousands of gauss are typical of the enigmatic family of rapidly oscillating Ap-type (roAp) stars (Hubrig et al., 2004), and the magnetic field is believed to play an important role in the (still not fully understood) driving mechanism of their high-overtone p-mode oscillations (Gautschy, Saio, and Harzenmoser, 1998; Balmforth et al., 2001). It has been speculated (e.g., by Handler, 2012) and claimed (Balona et al., 2011) that some roAp stars may also pulsate in g modes (on the basis of overlap between roAp and γ Dor stars on the Hertzsprung–Russell diagram). However, this is far

from certain. On the basis of non-adiabatic mode calculations, Murphy, Saio, et al. (2020) argue that high-order g modes are likely to be very efficiently damped, possibly explaining the current lack of observed hybrid γ Dor/roAp pulsators. However, if roAp stars containing high-order g modes do turn out to exist, they would serve as ideal laboratories for strong magnetogravity waves. Moreover, the understanding of high-order magnetogravity waves presented in this work may extend some insight into the behavior of low-order magnetic g modes (for which the asymptotic limit is not appropriate).

5.6.3 Future prospects

This work presents a non-perturbative formalism for calculating the g -mode oscillation frequencies of a magnetized and rotating star, including both effects asymptotically (i.e., applying the TARM). We have considered only with the case where the magnetic field is dipolar and aligned with the rotational axis. As test examples we have only applied it to red giant cores and g -mode pulsators on the main sequence. Here, we describe future possible directions of study in relation to the TARM formalism, and potential extensions.

This work represents a joint generalization of the traditional approximation of rotation (Lee and Saio, 1997) and an analogous approximation for a purely dipolar magnetic field (Rui and Fuller, 2023), in order to non-perturbatively incorporate the effects of both. Generalizations of the traditional approximation have, in the past, also incorporated centrifugal distortion (Mathis and Prat, 2019; Dhouib, Prat, et al., 2021b; Dhouib, Prat, et al., 2021a), differential rotation (Ogilvie and Lin, 2004; Mathis, 2009; Van Reeth, Mombarg, et al., 2018; Dhouib, Prat, et al., 2021a), and axisymmetric toroidal fields, both with constant Alfvén and rotation frequencies (Mathis and De Brye, 2011) as well as with more general field geometries together with differential rotation (Dhouib, Mathis, et al., 2022). Based on observational demands (or theoretical intrigue), it is likely possible to add any combination of these effects to the operator $\mathcal{L}^{m,b,q}$ defined in Equation 5.24. Although λ would then be a function of more than two dimensionless parameters, such an approach would retain much of the advantage of non-perturbatively capturing complex rotational/magnetic effects while only interpolating over a precomputed eigenvalue grid.

Unlike Rui and Fuller (2023), this work has focused on the regime where suppression is not likely to occur, i.e., when there are no Alfvén resonances on the domain and where the slow magnetic branch has been ignored. We have ignored modes with these effects because their observational implications are unclear, but the behavior of the operator $\mathcal{L}^{m,b,q}$ in this regime is an extremely rich mathematical problem with so far unexplored structure. Rui and Fuller (2023) find that solutions with $b > 1$ develop sharp fluid features at the Alfvén-resonant

critical latitudes, where processes such as phase-mixing are likely to efficiently damp the waves. In this regime, the magnetic operator in Equation 5.10 is of Boyd-type (Boyd, 1981), and the interior singularities give dissipation an important role in determining the physically appropriate branch cut. The eigenvalues λ for the $b > 1$ are thus not guaranteed to be real even in the formal limit where dissipation is taken to zero (and the numerical results of Rui and Fuller (2023) suggest that they are not). For reasons of scope, we have also ignored magneto-Rossby waves and magnetically stabilized gravity waves (Rui and Fuller, 2023), which do not connect to any spherical harmonic in the limits $a, q \rightarrow 0$. These, too, may conceal detectable predictions which are implied by the breakdown of positive-(semi)definiteness of $\mathcal{L}^{m,b,q}$.

As such, our calculations also do not capture the coupling between magnetic g modes and magneto-inertial modes which propagate in the convective core of intermediate-mass main-sequence stars (within which dynamo-generated magnetic fields are expected; Brun, Browning, and Toomre, 2005; Featherstone et al., 2009). Coupling with inertial modes is known to result in isolated dips in the $\delta P_g - P$ diagram at frequencies corresponding to those of inertial modes. This effect provides a seismic probe of the core rotation rates of such stars (Ouazzani, Lignières, et al., 2020; Saio, Takata, et al., 2021; Tokuno and Takata, 2022). In the future, it may be interesting to explore how this picture is modified by magnetism, and whether similar inference of the magnetic field in these convective cores is possible. We emphasize that coupling to (magneto-)inertial waves produces *localized* dip features in the period spacing pattern, and is very different than the *global* curvature in the pattern predicted by this work.

While we have only explicitly modeled analogues of γ Dor and SPB stars, our analysis applies to any magnetized pulsator with pulsations of high radial order. This includes compact pulsators such as white dwarfs and hot subdwarfs. Since both of these species result from red giants whose envelopes have been lost (either in isolation or through binary evolution), it is natural to expect that they will retain the strong fields believed to cause dipole suppression in red giants. While a small handful of magnetized hot subdwarfs (100s of kG) are known (Pelisoli, Dorsch, et al., 2022), white dwarfs with kilogauss surface fields are believed to make up a fourth of all white dwarfs (Cuadrado et al., 2004; Valyavin et al., 2006), and a number of magnetized white dwarfs with fields up to hundreds of megagauss have been discovered (Kepler et al., 2013; Bagnulo and Landstreet, 2021). The latter fields are likely to be so strong that they outright suppress g mode oscillations altogether (Lecoanet, Vasil, et al., 2017). However, it may be possible for a white dwarf to have a

field strong enough to significantly shift the frequencies of the g modes, without being not strong enough to suppress them outright.

While a dipolar field is expected at the surfaces of stars with fossil fields (Braithwaite and Nordlund, 2006; Duez and Mathis, 2010), that field need not be aligned with the rotation axis (Duez, 2011; Keszthelyi, 2023), and is unlikely to be dipolar at all if the field is generated by a dynamo. In the perturbative regime, Mathis and Bugnet (2023) recently characterized the frequency shifts associated to an inclined dipole field. Extending the TARM formalism to describe a non-axisymmetric horizontal field dependence requires solving for the eigenvalues of families of two-dimensional differential operators over the sphere, rather than a one-dimensional one (as in $\mathcal{L}^{m,b,q}$), and this analysis would need to be repeated for every different horizontal field dependence desired. Nevertheless, near suppression, departures in the frequency shifts from the perturbative theory are likely, and may be required for accurate magnetic field inference in this regime.

Finally, low-frequency propagating gravity waves are one of the best candidates for the strong angular momentum transport needed in stellar radiative zones to reproduce the observed internal rotation revealed in all types of stars by helio- and asteroseismology (e.g., Schatzman, 1993; Zahn, 1997; Charbonnel and Talon, 2005; Aerts, 2015; Rogers, 2015; Pinçon, Belkacem, et al., 2017; Neiner et al., 2020). The manner in which this wave-mediated angular momentum transport occurs can be significantly modified by the presence of a magnetic field. In general, the net angular momentum flux implied by this mechanism is given by the sum of the wave-induced Reynolds and Maxwell contributions to the stress tensor. The relevant gravity waves are precisely those which are most strongly affected by the combined action of rotation and magnetism (see, e.g., Mathis and Brye, 2012, in the case of weak, shellular differential rotation and a purely toroidal field with constant Alfvén frequency). Because our TARM-based formalism is relevant to exactly this kind of wave, its application to this problem is likely to yield insights into the rotational state and internal chemical mixing of rotating, magnetic stars.

5.7 Conclusion

Rapidly evolving progress in observational magnetoasteroseismology demands refinements in our theoretical understanding of magnetic effects on stellar pulsations. In this work, we develop a formalism for incorporating the effects of an aligned dipole magnetic field into g mode calculations, valid for rapidly rotating stars. This method relies on an asymptotic treatment of magnetism and rotation (under a “traditional approximation of rotation and magnetism”), and can be partitioned into two main steps:

1. Calculate the eigenvalues λ of the horizontal differential operator $\mathcal{L}^{m,b,q}$ (Equation 5.24) as a function of the dimensionless magnetic and rotational parameters $a = \omega_B^2/\bar{\omega}^2$ and $q = 2\Omega/\bar{\omega}$.
2. In either an asymptotic mode formula (Equation 5.58) or a non-asymptotic numerical scheme (e.g., shooting; Section 5.5.1), include the effects of magnetism and rotation by replacing $\ell(\ell + 1)$ throughout the star with a suitably interpolated λ , calculated using the magnetic and rotational profiles.

These steps are done relatively independently of each other: once the eigenvalues λ are computed once over a sufficiently large grid of a and q (for the desired ℓ and m), they do not need to be calculated again for any individual stellar model. Moreover, modifications to existing mode solving procedures are “minimal” in the sense of being localized to the interpolation of λ and its substitution into the relevant equations.

As proofs of concept, we have computed the g modes in the cores of red giants as well as in the radiative envelopes of high-mass main-sequence stars. In both cases, strong magnetic fields tend to decrease the period spacing significantly more than is suggested by the perturbative theory, especially for low frequencies close to the critical frequency $\omega_{\text{crit}} \sim \sqrt{Nv_{Ar}/r}$. This results in a curvature in the period spacing pattern which can in some cases be very conspicuous (e.g., Figure 5.4). Non-perturbative effects may also introduce asymmetry in the dipole frequency shifts which is not predicted by perturbation theory.

This regime is expected to be directly realized in the SPB star described by Lecoanet, Bowman, et al. (2022) and some of the red giants described by Deheuvels, Li, et al. (2023). Refined understanding of these effects is therefore prerequisite to perform accurate magnetic field inference using asteroseismology.

Chapter 6

IT'S NOT JUST A PHASE: OBLIQUE PULSATIONS IN MAGNETIC RED GIANTS AND OTHER STOCHASTIC OSCILLATORS

Rui, N. Z., J. Fuller, and J. M. J. Ong (2025). “It’s not just a phase: oblique pulsations in magnetic red giants and other stochastic oscillators.” In: *The Astrophysical Journal Letters* 985.2, L39. doi: 10.3847/2041-8213/add5e2. arXiv: 2505.03169.

Magnetic fields play a significant role in stellar evolution. In the last few years, asteroseismology has enabled the measurement of strong magnetic fields 10^4 – 10^6 G in the cores of dozens of red giants, and is the only known way to directly measure internal stellar magnetic fields. However, current data are still interpreted assuming that these fields are too weak or too axisymmetric to affect the orientation of the pulsations (i.e., make the pulsations “oblique”), rendering stronger field strengths beyond the reach of existing asteroseismic searches. We show that, even when an oblique pulsator is also stochastic (such as in a red giant with a strong non-axisymmetric magnetic field), geometric effects will cause the signal to contain frequency components which remain in perfect relative phase with each other. This perfect phase relationship persists even over timescales in which stochasticity erases absolute phase information. This perfect relative coherence is a distinctive observational signature of oblique pulsation that does not require a model for mode frequencies to search for. However, due to its dependence on phase, this effect will not be evident in the power spectral density alone, and phase information should be retained in order to detect it. Coherence-based searches for oblique pulsations may pave the way to measurements of magnetic fields of currently inaccessible strengths in red giants, as well as some main-sequence and compact pulsators.

We thank Emily Hatt for sharing a catalog of asteroseismic magnetic field measurements in a recent sample of red giants. We also thank Janosz Dewberry, Masao Takata, and the anonymous referee for their helpful comments. We are grateful for support from the United States–Israel Binational Science Foundation through grant BSF-2022175. N.Z.R. acknowledges support from the National Science Foundation Graduate Research Fellowship under Grant No. DGE-1745301. J.M.J.O. acknowledges support from NASA through the NASA Hubble Fellowship grant HST-HF2-51517.001, awarded by STScI. STScI is operated by the Association of Universities for Research in Astronomy, Incorporated, under NASA contract NAS5-26555.

6.1 Introduction

Although stellar magnetic fields are common, their formation, evolution, diversity, and role in angular momentum transport in stars and compact objects form a tangled web of open problems across astrophysics (Donati and Landstreet, 2009; Ferrario, Melatos, et al., 2015; Aerts, Mathis, et al., 2019). Our understanding of stellar magnetism is tethered to the uncertain strengths and structures of *subsurface* magnetic fields, which are invisible to standard observational techniques.

Asteroseismology—the measurement and interpretation of stellar oscillations—exploits the translucency of stars to hydrodynamical waves to constrain internal stellar properties, such as stellar mixing processes, internal rotation profiles, and evolutionary states (Aerts, 2021). Magnetic fields with strengths $\simeq 20\text{--}600\text{ kG}$ have recently been asteroseismically measured in the cores of several dozen lower red giant branch stars (Li, Deheuvels, Ballot, and Lignières, 2022; Deheuvels, Li, et al., 2023; Li, Deheuvels, Li, et al., 2023; Hatt et al., 2024). These measurements make use of the sensitivity of gravity-mode (g-mode) frequencies to the magnetic tension. “Seismic magnetometry,” which is still in its infancy, remains the only direct way to probe *internal* stellar magnetic fields.

When incorporating magnetic fields, present data analyses assume the pulsations to be aligned with the rotation axis. This occurs either when the magnetic field is axisymmetric about the rotation axis, or otherwise is weak enough that its effects are subdominant to those of the Coriolis and centrifugal forces. In the opposite case, the magnetic field is strong enough to *misalign* the pulsations from the rotation axis, i.e., make the pulsations oblique. In this regime, individual oscillation modes appear as multiple, Doppler-shifted periodicities to the observer. This breaks the one-to-one mapping between oscillation modes and frequency components in the light curve (hereafter “periodicities”), and produces complicated pulsation spectra which can be difficult to interpret (Kurtz, 1982; Shibahashi and Takata, 1993; Dziembowski and Goode, 1996; Bigot and Dziembowski, 2002; Saio and Gautschy, 2004; Loi, 2021). In some pulsators such as red giants, the oscillations are additionally *stochastic*: each mode decoheres on a characteristic mode lifetime τ (between tens of days to several years in red giants; Dupret, Belkacem, et al., 2009; Grosjean et al., 2014).

In this Letter, we show that oblique, stochastically driven pulsators (such as red giants with strong non-axisymmetric magnetic fields) display some coherent properties which can be used to identify them in a general, model-independent way. Because ordinary stochastic pulsations lack a mechanism for “remembering” phase information for times $\gg \tau$, this long-lived coherence is a smoking-gun signature of oblique pulsations. Since this signature

involves phase information, usual analyses based on the power spectral density (PSD) will be insensitive to it.

6.2 Pulsation model

We construct a simple toy model which exhibits the essential behavior of stochastic, oblique pulsations. The key observable is the intensity perturbation $\delta I(t)$, which has contributions from each oscillation mode:

$$\delta I(t) = \Re \sum_j \delta I_j(t), \quad (6.1)$$

where we have indexed the modes by j and allowed the intensity $\delta I_j(t)$ of each individual mode to be complex.

The individual mode intensities are given by integrals of the surface flux perturbation $\delta F_j(t; \theta', \phi')$ over the visible disk of the star:

$$\delta I_j(t) \propto \int_0^{2\pi} \int_0^1 \delta F_j(t; \theta', \phi') W(\theta') \cos \theta' d(\cos \theta') d\phi', \quad (6.2)$$

where $W(\theta')$ is an arbitrary limb-darkening function on which the details of this analysis do not depend. The primed variables (θ', ϕ') denote spherical coordinates in the *inertial* (observer) frame, with the north pole $(\theta' = 0)$ fixed to the line of sight (direction pointing to the observer). This is the frame in which integrals over the disk are most natural to compute.

Assuming surface flux perturbations trace scalar fluid perturbations (e.g., Gizon and Solanki, 2003), the flux perturbation due to a single mode can be decomposed into time- and angle-dependent factors:

$$\delta F_j(t; \theta, \phi) \propto A_j(t) \psi_j(\theta, \phi), \quad (6.3)$$

where the unprimed spherical coordinates (θ, ϕ) are in the frame *corotating* with the star, with the north pole $(\theta = 0)$ fixed to the rotation axis. This is the frame in which the oscillation modes of the star are most natural to compute.

The angular dependence of a mode pattern can, in turn, be decomposed into spherical harmonics:

$$\psi_j(\theta, \phi) = \sum_{\ell m} c_{j;\ell m} Y_{\ell m}(\theta, \phi), \quad (6.4)$$

where $c_{j;\ell m}$ is the contribution of each spherical harmonic to the flux perturbation of mode j . We show in Appendix 6.A that, upon changing coordinates from the corotating frame to the observer's frame, these spherical harmonics transform as

$$Y_{\ell m}(\theta, \phi) = \sum_{m'} e^{-im\Omega t} d_{m'm}^{\ell}(i) Y_{\ell m'}(\theta', \phi'), \quad (6.5)$$

where the Wigner matrix d^ℓ captures the effect of inclination on visibilities.

Combining Equations 6.2, 6.3, 6.4, and 6.5 gives

$$\delta I_j(t) \propto A_j(t) \sum_{\ell m} V_\ell c_{j;\ell m} d_{0m}^\ell(i) e^{-im\Omega t}, \quad (6.6)$$

where we have used the fact that spherical harmonics with $m \neq 0$ have vanishing disk integrals, and defined

$$V_\ell = \int_0^{2\pi} \int_{-1}^{+1} Y_{\ell 0}(\theta', \phi') W(\theta') \cos \theta' d(\cos \theta') d\phi' \quad (6.7)$$

to be the mode visibilities, which only depend on ℓ .

The time dependence of a stochastically excited mode is well described by a damped harmonic oscillator driven by noise (e.g., Stello, Kjeldsen, et al., 2004). As we show in Appendix 6.B, A_j is well modeled as

$$A_j(t) = \bar{A}_j(t) e^{i\sigma_j t}, \quad (6.8)$$

where σ_j is the corotating mode frequency and the complex prefactor $\bar{A}_j(t)$ stays roughly constant for short times $t \ll \tau$ while varying randomly for long times $t \gtrsim \tau$. We illustratively define $\bar{A}_j = H_j e^{i\varphi_j}$, so that

$$A_j(t) = H_j(t) e^{i(\sigma_j t + \varphi_j(t))}, \quad (6.9)$$

where the mode amplitude $H_j = H_j(t)$ and phase $\varphi_j = \varphi_j(t)$ are real-valued functions which, like \bar{A}_j , vary substantially only on timescales $\gg \tau$.

Our final expression for the total intensity perturbation follows from Equations 6.1 and 6.6:

$$\delta I(t) \propto \Re \sum_j A_j(t) \sum_{\ell m} V_\ell c_{j;\ell m} d_{0m}^\ell(i) e^{-im\Omega t}. \quad (6.10)$$

A mode is “rotationally aligned” when its horizontal structure is well described by a single spherical harmonic (i.e., $c_{j;\ell',m'} \approx \delta_{\ell\ell'} \delta_{mm'}$ for some ℓ and m). In this special case, the sum over ℓ and m in Equation 6.10 reduces to a single term, and the mode appears to an observer as a single sinusoidal signal. Conversely, if more than one expansion coefficient $c_{j;\ell',m'}$ is nonzero, the mode is “oblique,” and the observed signal will be non-sinusoidal.

6.2.1 Rotationally aligned pulsations

It is common to assume that pulsations are rotationally aligned which, for g modes, occurs when the Coriolis effect supplies the strongest non-spherically symmetric restoring force. Via Equations 6.6 and 6.8, the intensity perturbation due to such a mode is

$$\delta I_{\ell m}(t) \propto V_\ell \bar{A}_{\ell m}(t) d_{0m}^\ell(i) e^{i(\sigma_{\ell m} - m\Omega)t}. \quad (6.11)$$

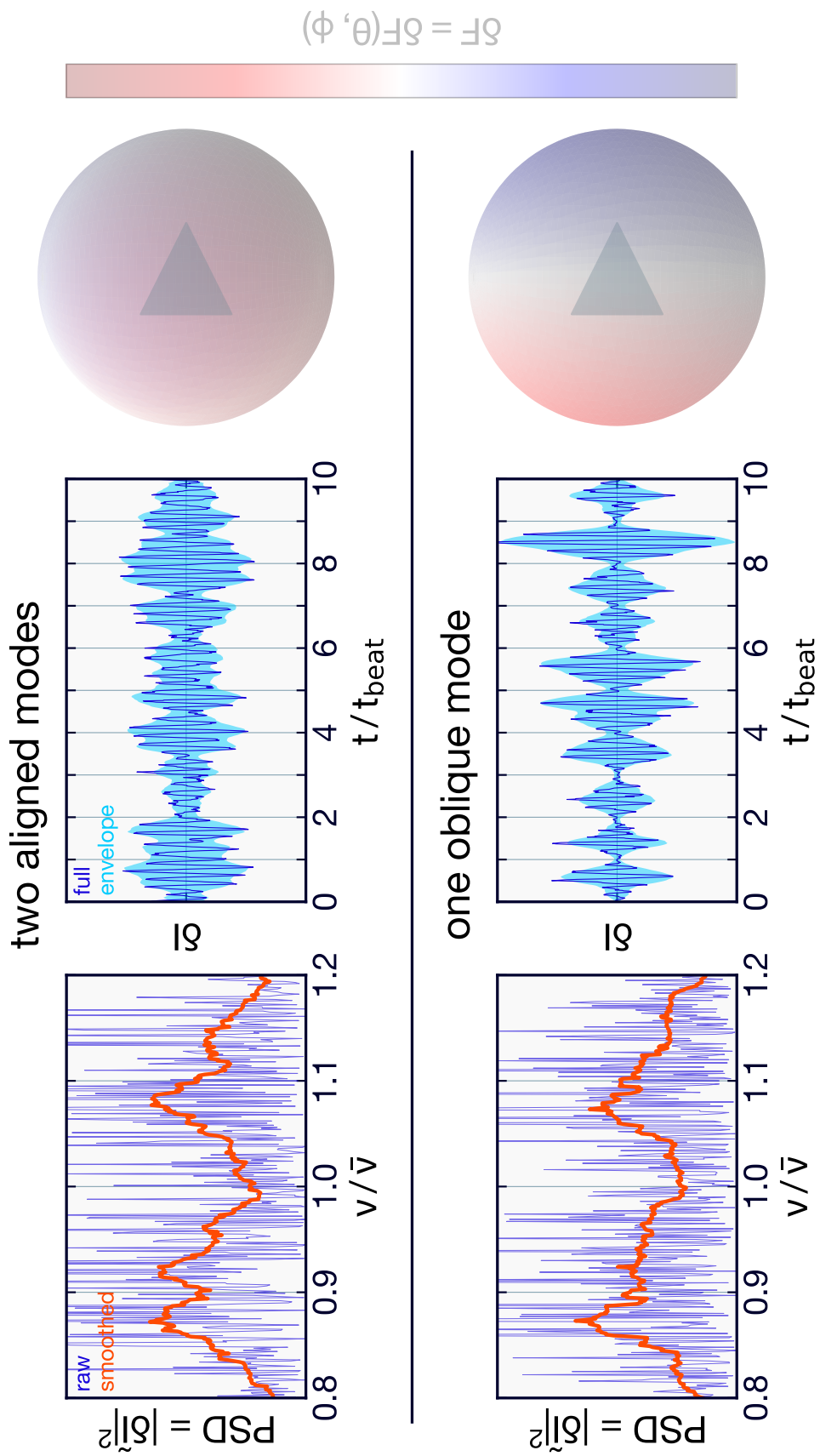


Figure 6.1: Comparison between two double-periodicity stochastic pulsations: two rotationally aligned modes (*top*) and one oblique mode (*bottom*). *Left column*: Power spectral density (PSD). A boxcar-smoothed PSD is shown as a *thick orange line*. *Middle column*: Time series disk-integrated intensity, where the time is normalized to the beat period $t_{\text{beat}} = 2\pi/\delta\omega$. A Hilbert transform-based estimator for the beating envelope (Kress, 1989) is shown as a *blue region* to guide the eye. *Right column*: Animated map of the surface flux perturbation. These panels can be viewed in the animated version of this figure in the HTML version of the online article, or in a corresponding Zenodo upload at <https://zenodo.org/records/15338766>.

Equation 6.11 shows that the observer measures a Doppler-shifted mode frequency

$$\omega_{\ell m} = \sigma_{\ell m} - m\Omega, \quad (6.12)$$

under the convention that positive-frequency modes with $m\Omega > 0$ are retrograde.

Rotation also produces a Coriolis force which contributes to the restoration of fluid motions, causing an additional frequency shift

$$\sigma_{\ell m} = \sigma_{\ell}^{(0)} + mC_{\ell}\Omega, \quad (6.13)$$

where $\sigma_{\ell}^{(0)}$ is the mode frequency in the absence of rotation, and the Ledoux coefficient $C_{\ell} \approx 1/\ell(\ell + 1)$ for high-radial order g modes (Ledoux, 1951).

These effects taken together, the observer measures an apparent rotational frequency shift

$$\delta\omega = \omega_{\ell m} - \sigma_{\ell}^{(0)} = -m(1 - C_{\ell})\Omega. \quad (6.14)$$

While $\delta\omega$ resembles a single shift proportional to m , it is actually caused by a combination of effects due to the Doppler shift (which is purely geometric) and the Coriolis force (which is physical). These two very different effects become unnatural to group together when analyzing stochastic, oblique pulsators.

6.2.2 Do two periodicities mean one mode or two?

When a pulsation is oblique (i.e., not rotationally aligned), a single oscillation mode is no longer a traveling wave of fixed m around the rotation axis. Instead, the morphology $\psi_j(\theta, \phi)$ of the mode has multiple components with different values of m which Doppler shift into multiple periodicities via Equation 6.12. Because of this, a single oblique oscillation mode can therefore be misinterpreted as multiple (rotationally aligned) oscillation modes. The so-called “oblique pulsator model” successfully describes the magnetically tilted pressure-mode (p-mode) pulsations of rapidly oscillating Ap stars (Dziembowski and Goode, 1996).

Fortunately, if the modes are observed for long enough to resolve their stochasticity (i.e., for baselines $T \gtrsim \tau$), it is possible to tell whether two periodicities are caused by two distinct modes or a single mode which is oblique *without* any model for their amplitudes and frequencies. To illustrate this, we consider two toy scenarios which produce almost indistinguishable empirical PSDs peaked at two close frequencies ($\omega_1 = \bar{\omega} - \delta\omega/2$ and $\omega_2 = \bar{\omega} + \delta\omega/2$) despite their corresponding time series’ obviously different properties (Figure 6.1, in which $\omega_1 = 0.9\bar{\omega}$ and $\omega_2 = 1.1\bar{\omega}$). The two periodicities can be resolved as long as $\delta\omega \gtrsim 1/\tau$.

In the first scenario, we consider two rotationally aligned modes with frequencies $\sigma_1 = \omega_1$ and $\sigma_2 = \omega_2$ with quantum numbers $(\ell, m) = (1, +1)$ and $(1, -1)$, respectively. The star is assumed to be non-rotating (or, for self-consistency, rotating at a negligible rate $\Omega \approx 0$). By Equation 6.10, the intensity perturbation due to these two modes is

$$\begin{aligned}\delta I &\propto \Re [A_1 + A_2] \\ &= \Re \left[e^{i\bar{\omega}t} \left(H_1 e^{i(-\delta\omega t/2 + \varphi_1)} - H_2 e^{i(+\delta\omega t/2 + \varphi_2)} \right) \right],\end{aligned}\quad (6.15)$$

where we have used the fact that $d_{0,-1}^1(i) = -d_{0,+1}^1(i)$ (Rose, 1995) and omitted overall constant prefactors. Defining $\bar{H} = (H_1 + H_2)/2$, $\bar{\varphi} = (\varphi_1 + \varphi_2)/2$, $\delta H = H_2 - H_1$, and $\delta\varphi = \varphi_2 - \varphi_1$, Equation 6.15 simplifies to

$$\begin{aligned}\delta I &\propto 2\bar{H} \underbrace{\sin(\delta\omega t/2 + \delta\varphi/2)}_{\text{beat}} \underbrace{\sin(\bar{\omega}t + \bar{\varphi})}_{\text{carrier}} \\ &\quad - \delta H \underbrace{\cos(\delta\omega t/2 + \delta\varphi/2)}_{\text{beat}} \underbrace{\cos(\bar{\omega}t + \bar{\varphi})}_{\text{carrier}}.\end{aligned}\quad (6.16)$$

The intensity pattern consists of a high-frequency oscillation with a carrier frequency $\bar{\omega}$ modulated by a beating envelope with a lower frequency $\delta\omega$ (a factor of two arises because the envelope refers to the absolute value of the beat sinusoid). On short timescales ($t \ll \tau$), the quantities \bar{H} , $\bar{\varphi}$, δH , and $\delta\varphi$ are all approximately constant, and the oscillation is roughly coherent. However, for longer observation baselines $T \gtrsim \tau$, both the carrier and beat oscillations dephase, i.e., $\bar{\varphi}$ and $\delta\varphi$ vary randomly (*top middle panel* of Figure 6.1).

In the second scenario, we consider a single oblique mode with corotating frequency $\sigma = \bar{\omega}$ with two equal spherical harmonic components with $m = \pm 1$ (i.e., $c_{1,+1} = c_{1,-1}$). Additionally, the star itself rotates with a rate $\Omega = \delta\omega/2$. By Equation 6.10, the resulting intensity perturbation due to this single mode is

$$\begin{aligned}\delta I &\propto \Re \left[A \left(e^{-i\delta\omega t/2} - e^{i\delta\omega t/2} \right) \right] \\ &= \Re \left[-2iH e^{i(\bar{\omega}t + \varphi)} \sin(\delta\omega t/2) \right].\end{aligned}\quad (6.17)$$

Upon taking the real part, Equation 6.17 becomes

$$\delta I \propto 2H \underbrace{\sin(\delta\omega t/2)}_{\text{beat}} \underbrace{\sin(\bar{\omega}t + \varphi)}_{\text{carrier}}.\quad (6.18)$$

Similarly to the first scenario, the two periodicities generated by the oblique mode oscillate with a carrier frequency $\bar{\omega}$ modulated by an envelope with a beat frequency $\delta\omega$. On

short timescales ($t \ll \tau$), the intensity perturbation is indistinguishable from that of the first scenario, or, indeed, a purely coherent beat pattern. However, while the overall amplitude H and carrier phase offset φ vary randomly as before, the beating envelope is perfectly coherent and *never dephases*. In the corresponding time series (*bottom middle panel* of Figure 6.1), the beating envelope vanishes on exact multiples of the beat period $t_{\text{beat}} = 2\pi/\delta\omega$. Intuitively, the non-axisymmetric magnetic field misaligning the oblique pulsation serves as a “clock hand” which perfectly tracks the rotational phase. In contrast, stars with no magnetic fields (or other non-axisymmetric features) have no mechanism by which to keep track of their absolute rotational phases over timescales $\gg \tau$.

Attempting to interpret the intensity perturbation generated by the single oblique mode as two separate rotationally aligned modes would imply the bizarre conclusion that the amplitude ratio H_2/H_1 and phase offset difference $\delta\varphi$ between the two stochastic modes are exactly constant in time. Despite this, both the *average* amplitude $H \rightarrow \bar{H}$ and phase offset $\varphi \rightarrow \bar{\varphi}$ would be observed to vary stochastically in the expected way.

By construction, the periodicities in both scenarios have identical frequencies and linewidths. The two scenarios thus produce very similar-looking PSDs, each consisting of an envelope of two broad Lorentzians multiplied by noise (the *left panels* of Figure 6.1, cf. Cunha, Avelino, et al. 2020). Nevertheless, since the time-domain intensities δI in the two scenarios are fundamentally different, the Fourier transforms $\delta \tilde{I}$ (which encode identical information) must also be different in some distinctive way.

The frequency-domain manifestation of oblique stochastic pulsation becomes apparent when comparing the Fourier transforms of Equations 6.16 and 6.18, which are

$$\delta \tilde{I} \propto \frac{1}{2} \left[\tilde{\tilde{A}}_1(\omega - \omega_1) - \tilde{\tilde{A}}_2(\omega - \omega_2) \right] + \text{sym.} \quad (6.19)$$

for two aligned modes, and

$$\delta \tilde{I} \propto \frac{1}{2} \left[\tilde{\tilde{A}}(\omega - \omega_1) - \tilde{\tilde{A}}(\omega - \omega_2) \right] + \text{sym.} \quad (6.20)$$

for one oblique mode, where “sym.” denotes the frequency-flipped, complex conjugate of the first term (which arises from taking the real part). In the case of two aligned modes, the Fourier profiles of the two periodicities ($\tilde{\tilde{A}}_1$ and $\tilde{\tilde{A}}_2$) are different, i.e., the noise multiplying the square-root Lorentzians in the Fourier transform are different from each other. In contrast, in the case of one oblique mode, the Fourier profiles of the two periodicities are identical, i.e., the noise multiplying the square-root Lorentzians are the same across the two Fourier peaks.

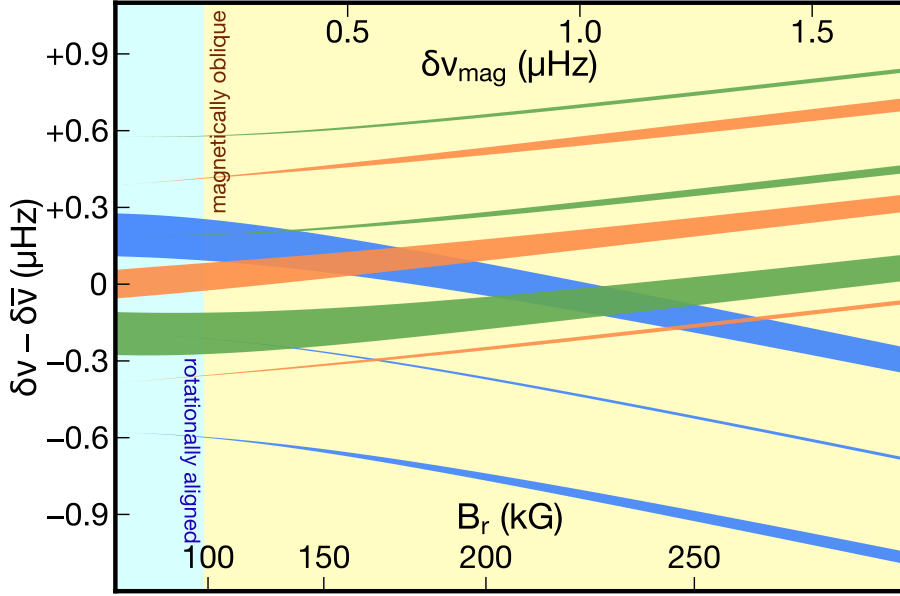


Figure 6.2: Linear g-mode frequency shifts $\delta\nu = \delta\omega/2\pi$ relative to the power-weighted average shift of the triplet $\delta\bar{\nu}$ (defined in the main text), plotted against the strength of the magnetic perturbation $\delta\nu_{\text{mag}} = \delta\omega_{\text{mag}}/2\pi$. The magnetic field strengths corresponding to $\delta\nu_{\text{mag}}$ are also shown for the $M = 1.5M_{\odot}$, $R = 5.2R_{\odot}$ red giant model described in Section 6.2.3. For illustrative purposes here we have fixed $2\pi\sigma_0 = 180 \mu\text{Hz}$, $\delta\omega_{\text{rot}} \approx 1.2 \mu\text{Hz}$, $i = 60^\circ$, and $\beta = 70^\circ$. Line colors indicate the underlying mode, and line thicknesses are proportional to the spectral power. Low field strengths leave the rotational triplet symmetrically split, moderate field strengths introduce asymmetry in the triplet, and higher field strengths induce oblique pulsations in which each mode individually appears as a triplet.

Although frequency resolution, noise floor, and nonuniform sampling effects will cause non-ideal behavior, oblique pulsation will still generally produce spectral correlation which cannot be caused by separate, rotationally aligned, stochastic modes. We note that spectral correlation describes correlation between frequency components, and is conceptually distinct from temporal correlation, which describes the time-domain correlations which are characteristic of colored (but stationary) noise. *Fourier peaks with identical noise profiles are smoking-gun signals of oblique pulsation* and, thus, the likely presence of a strong non-axisymmetric magnetic field. Since the PSD ($|\tilde{I}^2|$) discards all of the phase information in $\delta\tilde{I}$, data analyses which start from the PSD are likely to overlook oblique pulsations. *It's not just a phase.*

6.2.3 Magnetic red giants: a theoretical case study

Seismically, red giants are especially rich: near-surface convection drives information-dense pulsations containing up to dozens of independent oscillation modes (Chaplin and Miglio, 2013). In lower red giant branch ($R \lesssim 10R_\odot$) and red clump stars, dipole ($\ell = 1$) p modes are also well-coupled to g modes, which propagate exclusively in the stars' radiative cores. Strong *core* magnetic fields appreciably modify internal restorative forces, shifting mode frequencies in distinctive ways. Measurement of these frequency shifts has recently enabled the precise extraction of core magnetic field strengths in dozens of red giants (Li, Deheuvels, Ballot, and Lignières, 2022; Deheuvels, Li, et al., 2023; Li, Deheuvels, Li, et al., 2023; Hatt et al., 2024).

We briefly summarize known theoretical predictions of magnetic effects on red giant mixed modes (Li, Deheuvels, Ballot, and Lignières, 2022; Mathis and Bugnet, 2023; Das et al., 2024), deferring many details to Appendix 6.C. Although red giant g modes can only be observed when coupled to p modes, the non-axisymmetric nature of the problem suggests that mixed-mode coupling may affect the spectrum in a complicated way. Thus, for simplicity, we hereafter consider only pure g modes.

The seismic effects of rotation and magnetism are calculated by solving the eigenvalue problem

$$\delta\sigma \mathbf{c}_\ell = (\mathbf{R}_\ell + \mathbf{M}_\ell) \mathbf{c}_\ell \quad (6.21)$$

for the corotating frequency shifts $\delta\sigma$ and the spherical harmonic expansion coefficient vectors \mathbf{c}_ℓ (see Equation 6.4). The matrices \mathbf{R}_ℓ and \mathbf{M}_ℓ describe the effects of the Coriolis and Lorentz forces.

The $\ell = 1$ Coriolis matrix $\mathbf{R}_{\ell=1}$ is given by

$$\mathbf{R}_{\ell=1} = \delta\omega_{\text{rot}} \text{diag}(-1, 0, +1) \quad (6.22)$$

where $\delta\omega_{\text{rot}} \propto \Omega$. Because \mathbf{R}_ℓ is purely diagonal (for any ℓ), the off-diagonal elements of $\mathbf{R}_\ell + \mathbf{M}_\ell$ are totally set by magnetic effects. The elements of the Lorentz matrix \mathbf{M}_ℓ are, in turn, highly dependent on the geometry of the magnetic field. For illustrative purposes, we subsequently adopt a dipolar magnetic field misaligned with the rotation axis by an angle β , for which the $\ell = 1$ Lorentz matrix is

$$\mathbf{M}_{\ell=1} = \frac{3}{20} \delta\omega_{\text{mag}} \begin{pmatrix} 7 + C_\beta & -\sqrt{2}S_\beta & 1 - C_\beta \\ -\sqrt{2}S_\beta & 6 - 2C_\beta & \sqrt{2}S_\beta \\ 1 - C_\beta & \sqrt{2}S_\beta & 7 + C_\beta \end{pmatrix}, \quad (6.23)$$

where $C_\beta = \cos 2\beta$, $S_\beta = \sin 2\beta$, and $\delta\omega_{\text{mag}}$ depends on some stellar interior-averaged magnetic field ($\delta\omega_{\text{mag}} \propto \langle B_r^2 \rangle$). While this form of $\mathbf{M}_{\ell=1}$ only describes a specific magnetic

field configuration, the qualitative results of this analysis generalize to other large-scale non-axisymmetric magnetic fields.

Dipole mode frequency shifts can be decomposed into a mean component $\delta\bar{v}$ which shifts the entire triplet and an asymmetric component which changes the triplet's structure. Figure 6.2 shows the observed frequency structure of the rotational triplet as a function of $\delta\omega_{\text{mag}}$, for oblique g-modes with $\beta = 70^\circ$. Specifically, Figure 6.2 shows the rotational and magnetic frequency shifts with $\delta\bar{v}$ subtracted off, where $\delta\bar{v}$ is the mean frequency shift of the nine periodicities weighted by the observed spectral power $\propto |c_{j,\ell m} d_{0m}^\ell(i)|^2$. When the Coriolis force dominates ($\delta\omega_{\text{mag}} \lesssim \delta\omega_{\text{rot}}$; the *blue region* in Figure 6.2), the off-diagonal elements of $\mathbf{R}_\ell + \mathbf{M}_\ell$ are negligible, and magnetism shifts the mode frequencies without creating extra observed periodicities. This is the familiar limit assumed by most observational (Li, Deheuvels, Ballot, and Lignières, 2022; Deheuvels, Li, et al., 2023; Li, Deheuvels, Li, et al., 2023; Hatt et al., 2024) and many theoretical (Bugnet et al., 2021; Bugnet, 2022; Mathis and Bugnet, 2023; Das et al., 2024) studies (although see Loi, 2021; Li, Deheuvels, Ballot, and Lignières, 2022). In this regime, magnetism causes rotational multiplets to be asymmetric, but does not introduce extra periodicities to the signal.

In contrast, when the Lorentz force dominates ($\delta\omega_{\text{mag}} \gtrsim \delta\omega_{\text{rot}}$; the *yellow region* in Figure 6.2), the off-diagonal elements of $\mathbf{R}_\ell + \mathbf{M}_\ell$ cause the eigenvectors \mathbf{c}_ℓ to mix across m : the pulsations are oblique. The rotationally aligned and magnetically oblique regimes are respectively indicated by the *blue* and *yellow regions* in Figure 6.3 for a standard $M = 1.5M_\odot$, $R = 5.2R_\odot$ red giant stellar model generated using version r24.08.1 of Modules for Experiments in Stellar Astrophysics (MESA; Paxton, Bildsten, et al., 2010; Paxton, Cantiello, et al., 2013; Paxton, Marchant, et al., 2015; Paxton, Schwab, et al., 2018; Paxton, Smolec, et al., 2019; Jermyn et al., 2023). Magnetic fields detected thus far lie primarily in the rotationally aligned regime, consistent with the modeling assumptions used to identify and interpret them. However, magnetically oblique pulsators should exist at slightly larger field strengths, especially for low core rotation rates (as also speculated by Li, Deheuvels, Li, et al., 2023).

There is a different (but overlapping) condition under which the magnetic field significantly alters the propagation of gravity waves, such that the weak-field theory breaks down. This occurs for magnetic fields near a critical field strength which Fuller, Cantiello, et al. (2015) gives as

$$B_{r,\text{crit}} \simeq \sqrt{\frac{\pi}{\ell(\ell+1)}} \frac{\sqrt{\rho}\omega^2 r}{N}. \quad (6.24)$$

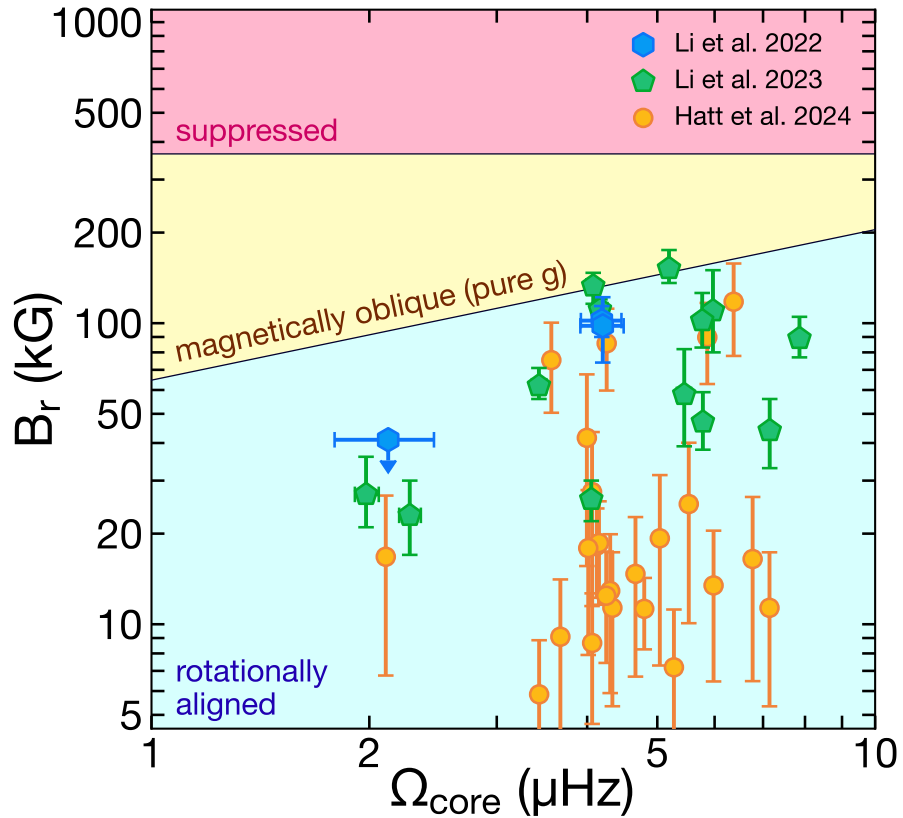


Figure 6.3: “Phase diagram” of pulsation regimes in the space of magnetic field versus rotation rate, where data points indicate known magnetic red giants with observed rotational triplets. Regions of rotational alignment ($\delta\omega_{\text{mag}} < \delta\omega_{\text{rot}}$) and magnetic obliquity ($\delta\omega_{\text{mag}} > \delta\omega_{\text{rot}}$) are shown for the case of pure g modes, assuming the stellar model described in Section 6.2.3 and the stellar parameters described in Section 6.2.4. The condition for magnetic g-mode suppression ($B > B_{\text{crit}}$; Equation 6.24) is also shown for the same model. These shaded regions show approximate, model-dependent estimates for these regimes, and the precise boundaries between the regimes depend on stellar parameters and therefore vary from star to star.

Magnetic fields stronger than $B_{r,\text{crit}}$ (the *red region* in Figure 6.3) are expected to suppress g-mode propagation (Fuller, Cantiello, et al., 2015; Rui and Fuller, 2023; Stello, Cantiello, Fuller, Huber, et al., 2016). Notably, Deheuvels, Li, et al. (2023) discovered and characterized 11 red giants with distorted period spacing patterns consistent with relatively strong internal magnetic fields. In particular, one of their stars (KIC 6975038) appears to experience magnetic suppression which exclusively affects its lowest-frequency mixed modes, consistent with theoretical expectations. The magnetically oblique and suppressed regions would shift to smaller field strengths for stars farther up the red giant branch.

6.2.4 Simulated observations of oblique pulsations

We simulate observations of a single g-mode triplet under the effects of a strong inclined magnetic dipole by numerically solving Equation 6.21 for the frequencies in the observer's inertial frame. We choose parameters which produce the rotational triplet structure at the maximum value of $\delta\nu_{\text{mag}} = 1.7 \mu\text{Hz}$ shown in Figure 6.2. In addition to the parameters described in Section 6.2.3, this corresponds for our red giant model to the realistic (though optimistic) rotation period $P_{\text{rot}} = 2\pi/\Omega = 30 \text{ d}$ and a field strength $B_r \approx 292 \text{ kG}$ (for a flat magnetic field radial profile). We also assume a typical mode lifetime $\tau = 2 \text{ months}$.

Our mock observations are evenly sampled in time with a cadence $\Delta t = 30 \text{ min}$ and a baseline $T_{\text{obs}} = 8 \text{ yr}$ (twice that of the main *Kepler* mission; Borucki, 2016). We also inject a white noise background to mimic a realistic height-to-background ratio (cf. Li, Deheuvels, Ballot, and Lignières, 2022). Details of our procedure for generating synthetic data can be found in Appendix 6.B. The empirical PSD derived from these mock observations is shown in the *top panel* of Figure 6.4. Figure 6.4 also shows the theoretically expected value of the PSD (*orange curve*). However, since the statistics of the process now explicitly modulate with time, the process is not stationary and is therefore not fully described by the PSD like in the usual case of a stationary process (see, e.g., Gardner, 2003).

We perform a mock analysis of our simulated observations by calculating a windowed, complex-valued version of a normalized cross correlation (NCC; Kirch, 2008) of $\delta\tilde{I}(\omega)$. The NCC measures the overlap between two arrays, and is extensively applied to image comparison. Specifically, we compute

$$\text{NCC}_{\delta\omega_{\text{win}}}(\omega_1, \omega_2) = \frac{\mathcal{I}_{\delta\omega_{\text{win}}}(\omega_1, \omega_2)}{\sqrt{\mathcal{I}_{\delta\omega_{\text{win}}}(\omega_1, \omega_1)\mathcal{I}_{\delta\omega_{\text{win}}}(\omega_2, \omega_2)}}, \quad (6.25)$$

where we have defined the windowed inner product

$$\mathcal{I}_{\delta\omega_{\text{win}}}(\omega_1, \omega_2) \equiv \frac{1}{2\delta\omega_{\text{win}}} \int_{-\delta\omega_{\text{win}}}^{+\delta\omega_{\text{win}}} \delta\tilde{I}^*(\omega_1 + \xi)\delta\tilde{I}(\omega_2 + \xi) \text{d}\xi, \quad (6.26)$$

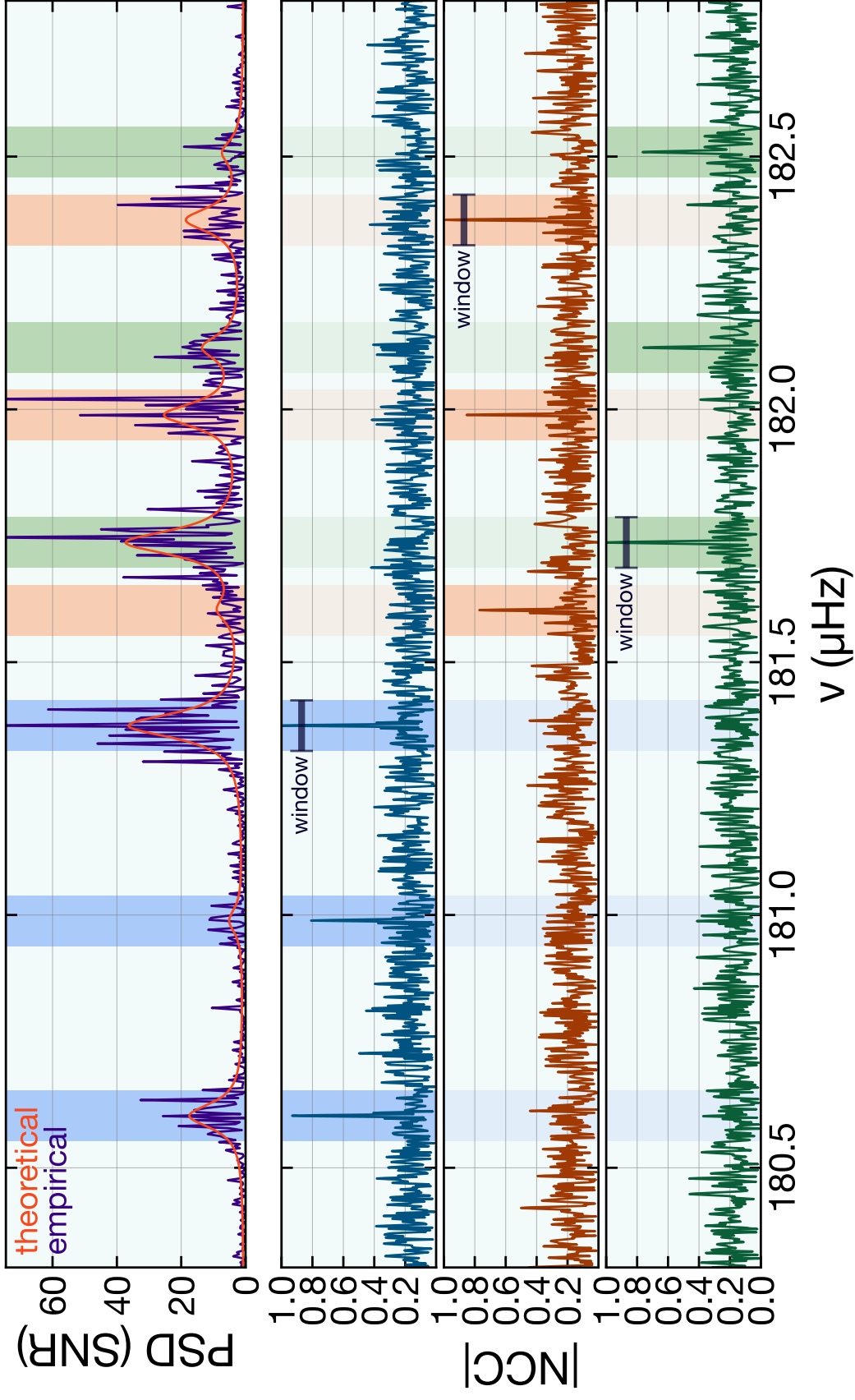


Figure 6.4: Synthetic data of a magnetically oblique g-mode triplet in a red giant, described further in Section 6.2.3). Background shading indicates the location of a periodicity, where the color represents the physical mode from which a periodicity originates. *Top:* The observed PSD $|\delta \tilde{f}|^2$, normalized to the expectation value of the simulated white noise floor. *Bottom:* The absolute value of the windowed normalized cross-correlation ($|\text{NCC}|$) with respect to the three windows indicated by the black bars. $|\text{NCC}|$ measures whether segments of the Fourier transform are spectrally correlated to the chosen window. As discussed in Section 6.2.3, $|\text{NCC}|$ peaks at secondary periodicities whose corresponding mode matches the periodicity in the window, while mostly ignoring periodicities corresponding to different modes.

for some choice of window width $\delta\omega_{\text{win}}$. Intuitively, $\text{NCC}_{\delta\omega_{\text{win}}}(\omega_1, \omega_2)$ quantifies the degree of spectral correlation between two segments of the Fourier transform centered at ω_1 and ω_2 with widths $\delta\omega_{\text{win}}$. The absolute value of NCC is 1 when the segments are exactly identical, up to a constant scaling factor, and tends to 0 when the segments are totally spectrally uncorrelated.

In practice, owing to the finite baseline, we compute a discrete version of the windowed NCC by taking

$$\mathcal{I}(\omega_1, \omega_2) \approx \sum_{k=-\delta n_{\text{win}}}^{+\delta n_{\text{win}}} \delta \tilde{I}_{n_{\omega_1}+k}^* \delta \tilde{I}_{n_{\omega_2}+k}, \quad (6.27)$$

where $\delta \tilde{I}_n$ denotes elements of the discrete Fourier transform, $\delta n_{\text{win}} \approx \delta\omega_{\text{win}}/\Delta\omega$ (where $\Delta\omega$ is the frequency resolution), and n_{ω_1} (n_{ω_2}) refers to the index whose corresponding frequency is closest to ω_1 (ω_2). To mitigate non-ideal frequency-resolution effects, we also sinc-interpolate the discrete Fourier transform by zero-padding the time series by a factor of ten (Schanze, 1995).

Each of the *bottom panels* of Figure 6.4 shows the windowed NCC of our mock triplet, with ω_1 fixed to the frequency of a different power spectral peak and the window width to $\delta\omega_{\text{win}}/2\pi = 0.05 \mu\text{Hz}$. When ω_1 is chosen this way, the NCC measures how spectrally correlated segments of the Fourier transform are with the windowed peak. It is thus expected to spike when ω_2 coincides with the frequency of another periodicity arising from the same mode (i.e., another peak with the same shading in Figure 6.4). Indeed, Figure 6.4 shows that the NCC peaks substantially in absolute value at these other periodicities, which are often lower in amplitude (but still significant). In contrast, the magnitude of the windowed NCC does not peak significantly at periodicities corresponding to other modes, since their different noise profiles destructively interfere with the window within the inner product in Equation 6.27. This proof-of-concept mock analysis demonstrates the ability to perform model-independent searches for oblique, stochastic pulsations in the frequency domain.

6.3 Summary and prospects

Sufficiently strong non-axisymmetric magnetic fields can misalign stellar pulsations from the rotation axis, i.e., cause the pulsations to be oblique. The oblique pulsator model is the standard framework for interpreting the pulsations of rapidly oscillating Ap stars, which are known to harbor strong surface oblique dipolar-like magnetic fields (Kurtz, 1982; Dziembowski and Goode, 1996). Additionally, oblique pulsations appear to have been detected in the prototype DBV white dwarf pulsator (GD 358; Montgomery, Provencal, et al., 2010) and have been suggested to produce the quintuplet of periodicities observed

in the main-sequence pulsator β Cephei (Telting, Aerts, et al., 1997; Shibahashi and Aerts, 2000). More recently, two blue large-amplitude pulsators (BLAPs) were also suggested to exhibit oblique pulsations (Pigulski et al., 2024).

In this work, we show that time series observations of oblique pulsators with stochasticity share generic signatures which can be used to identify them. These signatures take the form of a permanent periodic mode amplitude modulation (in the time domain) or, equivalently, spectrally correlated line profiles in the Fourier transform (in the frequency domain). Due to their dependence on stochasticity, these signatures are easiest to detect for modes with shorter lifetimes (i.e., larger linewidths). Promisingly, searches for these signatures can be agnostic to the precise pattern of mode frequencies predicted by models. Data analyses looking for spectrally correlated signals may identify magnetic red giants in the *yellow region* in Figure 6.3, within which current analyses are inapplicable.

While magnetic red giants are the motivating use case for this work, our results apply to oblique pulsations in any pulsator with detectable stochasticity. Outside of red giants, stochasticity is a prominent characteristic of main-sequence solar-like oscillators (such as the Sun itself; Chaplin and Miglio, 2013), and has also been observed in some modes in classical pulsators (such as δ Scuti stars; Breger and Pamyatnykh, 1998) and compact pulsators (such as white dwarfs and hot subdwarfs; Winget, Nather, et al., 1994; Reed et al., 2007; Østensen et al., 2014; Hermes, Gänsicke, Kawaler, et al., 2017).

A similar analysis is likely also applicable to tidally tilted pulsations (TTPs), which are misaligned from the rotation axis by tidal forces from a companion rather than a strong magnetic field (Handler et al., 2020; Fuller, Kurtz, et al., 2020; Fuller, Rappaport, et al., 2025). As such, TTPs are also oblique pulsations, and are similarly characterized by multiple periodicities with fixed relative phase and amplitude relationships (e.g., Fuller, Rappaport, et al., 2025). While TTPs have been discovered in coherent pulsators such as δ Scuti (Handler et al., 2020) and subdwarf B (Jayaraman et al., 2022) stars, searches for anomalous long-term coherence may enable the discovery of TTPs in stochastic pulsators.

Magnetic fields produce oblique pulsations when they are strong enough to overwhelm rotational effects such as the Coriolis force (i.e., for parameters within the *yellow region* in Figure 6.3). Magnetic fields which are close in strength to $B_{r,\text{crit}}$ mix modes across values of ℓ (Lecocanet, Vasil, et al., 2017; Loi, 2020b; Dhouib, Mathis, et al., 2022; Rui and Fuller, 2023; Rui, Ong, et al., 2024; Lecocanet, Bowman, et al., 2022), not just m as in this work. This will produce additional peaks (e.g., more than three for $\ell = 1$) spaced by the stellar spin frequency in the PSD, which can likely be detected by the same method outlined here.

In future work, we plan to extend our analysis of magnetic obliquity to stronger magnetic field strengths $B_r \sim B_{r,\text{crit}}$.

6.A Transforming between the observer and corotating frames

Performing the disk integral in Equation 6.2 requires a change of coordinates from the corotating frame (unprimed; θ, ϕ) to the observer's frame (primed; θ', ϕ'). In this Appendix, we describe how spherical harmonics transform under this change of coordinates.

These two coordinate systems differ in relative rotation (by the stellar rotation rate Ω) and choice of polar axis (by the inclination angle i). The transformation between the two frames is characterized by the Euler angles $(\alpha_e, \beta_e, \gamma_e) = (0, i, \Omega t)$ (in an intrinsic z-y-z convention, following Rose, 1995). Under rotation, spherical harmonics transform as

$$Y_{\ell m}(\theta, \phi) = \sum_{m'} D_{m'm}^{\ell}(\alpha_e, \beta_e, \gamma_e) Y_{\ell m'}(\theta', \phi'), \quad (6.28)$$

where D^{ℓ} is the Wigner D -matrix, whose elements are

$$D_{m'm}^{\ell}(\alpha_e, \beta_e, \gamma_e) = e^{-im'\alpha_e - im\gamma_e} d_{m'm}^{\ell}(\beta_e), \quad (6.29)$$

where d^{ℓ} is a matrix which only depends on ℓ . For our particular transformation,

$$Y_{\ell m}(\theta, \phi) = \sum_{m'} e^{-im\Omega t} d_{m'm}^{\ell}(i) Y_{\ell m'}(\theta', \phi'), \quad (6.30)$$

reproducing Equation 6.5 in the main text.

6.B Amplitude evolution under stochastic driving

A stochastic mode is oscillatory (with a corotating frequency σ_0) on short timescales ($t \ll \tau$) but decoheres on longer timescales ($t \gg \tau$). To mimic this behavior, we model the complex amplitude $A(t)$ as an underdamped harmonic oscillator with frequency σ_0 and damping rate $\eta = 1/\tau > 0$ driven by noise $f(t)$. The time dependence of the amplitudes follow

$$\partial_t A(t) = (i\sigma_0 - \eta)A(t) + \eta f(t), \quad (6.31)$$

which is the stochastically driven amplitude equation (Buchler et al., 1993) evaluated in the linear regime. We have included an extra prefactor η multiplying f to normalize the height of the power spectral peak to be independent of η . Solutions to Equation 6.31 behave similarly to those of the usual damped driven harmonic oscillator equation, $\ddot{A} + 2\eta\dot{A} + (\sigma_0^2 + \eta^2)A = f$. The difference is that the former excites only a single complex oscillation $\propto e^{i\sigma_0 t}$ whereas the latter (as a second-order differential equation) excites linear combinations of two complex

oscillations $\propto e^{i\sigma_0 t}$ and $\propto e^{-i\sigma_0 t}$. Aiming to construct a simple excitation model for a single complex oscillation, we therefore solve Equation 6.31 rather than the usual damped driven harmonic oscillator equation.

In the frequency domain, the Fourier transform of $A(t)$ is given by

$$\tilde{A}(\sigma) = \frac{1}{1 + i(\sigma - \sigma_0)/\eta} \tilde{f}(\sigma), \quad (6.32)$$

i.e., the product of a peaked complex function whose squared norm is a Lorentzian and the spectrum \tilde{f} of the stochastic driving. Although the square-root-Lorentzian factor has a complex phase profile (reflecting the phase lag of a damped driven harmonic oscillator), this phase is irrelevant as long as the stochastic driving is spectrally uncorrelated.

In the time domain, $A(t)$ is given by the inverse Fourier transform

$$A(t) = \int_{-\infty}^{+\infty} \frac{\tilde{f}(\sigma)}{1 + i(\sigma - \sigma_0)/\eta} e^{i\sigma t} d\sigma. \quad (6.33)$$

Applying the change of variables $\sigma' = \sigma - \sigma_0$ allows us to rewrite Equation 6.33 as

$$A(t) = e^{i\sigma_0 t} \int_{-\infty}^{+\infty} \frac{\tilde{f}(\sigma_0 + \sigma')}{1 + i\sigma'/\eta} e^{i\sigma' t} d\sigma'. \quad (6.34)$$

Defining

$$\bar{A}(t) \equiv \int_{-\infty}^{+\infty} \frac{\tilde{f}(\sigma_0 + \sigma')}{1 + i\sigma'/\eta} e^{i\sigma' t} d\sigma' \equiv \int_{-\infty}^{+\infty} \tilde{\bar{A}}(\sigma') e^{i\sigma' t} d\sigma' \quad (6.35)$$

recovers Equation 6.8 in the main text. As a complex function, $\bar{A}(t)$ stores the departure in amplitude and phase of $A(t)$ from a perfect sinusoid. Equation 6.35 represents $\bar{A}(t)$ as the Fourier transform of a square-root Lorentzian multiplied by noise. Since $\tilde{\bar{A}}$ is very roughly localized to frequencies $|\sigma'| \lesssim \eta$, $\bar{A}(t)$ remains roughly constant on short timescales $\lesssim \tau$ while varying randomly on longer timescales $\gg \tau$.

For simplicity, we assume the driving to be white noise, although our results are not sensitive to this choice and extend to colored (but spectrally uncorrelated) noise. To simulate a single statistical realization of $\tilde{A}(\sigma)$ on a discrete frequency grid (Section 6.2.4), we independently draw values from a χ^2 distribution with two degrees of freedom, take their square roots, and multiply them by random complex phases drawn uniformly from the unit circle. This ensures that the values of the PSD of the driving $|\tilde{f}(\sigma)|^2$ obey a χ^2 distribution with two degrees of freedom, a standard assumption in the study of solar-like oscillations (Woodard, 1985; Duvall and Harvey, 1986; Anderson et al., 1990) which results from the values of the real and imaginary parts of $\tilde{f}(\sigma)$ each individually following Gaussian distributions with identical statistics. We then compute $\tilde{A}(\sigma)$ using Equation 6.32. The simulated time series

$\delta I(t)$ is then obtained by applying an inverse fast Fourier transform to $\tilde{A}_j(\sigma)$ to obtain $A_j(t)$ for each mode j and evaluating Equation 6.10. A simulated observational noise background is generated in the same way as $\tilde{f}(\sigma)$, and its inverse fast Fourier transform added to $\delta I(t)$.

6.C Rotating and magnetic g-mode frequencies and eigenfunctions

At lowest order, the simultaneous effects of rotation and magnetism can be calculated using degenerate perturbation theory. In this Appendix, we quote the main results of this type of analysis for pure dipole ($\ell = 1$) g modes (in particular, those of Gomes and Lopes, 2020; Bugnet, 2022; Li, Deheuvels, Ballot, and Lignières, 2022; Mathis and Bugnet, 2023; Das et al., 2024) in the asymptotic limit. These conditions reasonably describe observable g modes in red giants.

The scale $\delta\omega_{\text{rot}}$ of the Coriolis frequency shift is given by

$$\delta\omega_{\text{rot}} = \frac{1}{2}\langle\Omega\rangle_g \equiv \frac{1}{2}\Omega, \quad (6.36)$$

where $\langle\Omega\rangle_g$ is the average rotation rate of the g-mode cavity (core). Similarly, the scale of magnetic frequency shifts $\delta\omega_{\text{mag}}$ is given by

$$\delta\omega_{\text{mag}} = \frac{\mathcal{J}}{4\pi\omega_0^3}\langle B_r^2 \rangle. \quad (6.37)$$

The value of $\delta\omega_{\text{mag}}$ depends on a particular average of the squared radial component of the magnetic field over the g-mode cavity:

$$\langle B_r^2 \rangle = \int_{r_1}^{r_2} dr K(r) \int_{S^2} d\Omega_2 B_r^2, \quad (6.38)$$

where r_1 and r_2 are the boundaries of the g-mode cavity (demarcated by $\omega^2 < \min(S_1^2, N^2)$ where S_1 and N are the $\ell = 1$ Lamb and Brunt–Väisälä frequencies) and $d\Omega_2 = d(\cos\theta) d\phi$ is an infinitesimal solid angle element. This average is weighted in radius by a function

$$K(r) \simeq \begin{cases} \frac{N^3/\rho r^3}{\int_{\mathcal{R}\ell_v}^{r_2} (N^3/\rho r^3) dr} & r_1 \leq r \leq r_2 \\ 0 & \text{otherwise,} \end{cases} \quad (6.39)$$

which peaks near the hydrogen-burning shell in red giants. Finally, the sensitivity factor

$$\mathcal{J} = \frac{\int_{r_1}^{r_2} (N^3/\rho r^3) dr}{\int_{r_1}^{r_2} (N/r) dr} \quad (6.40)$$

depends on the stellar structure.

For general magnetic configurations, the $\ell = 1$ Lorentz force matrix $\mathbf{M}_{\ell=1}$ is

$$\mathbf{M}_{\ell=1} = \delta\omega_{\text{mag}} \frac{\int_{r_1}^{r_2} dr K(r) \int_{S^2} d\Omega_2 \mathcal{M}_{\ell=1}(\theta, \phi) B_r^2}{\int_{r_1}^{r_2} dr K(r) \int_{S^2} d\Omega_2 B_r^2} \quad (6.41)$$

where

$$\mathcal{M}_{\ell=1}(\theta, \phi) = \frac{3}{8} \begin{pmatrix} 3 + C_\theta & -\sqrt{2}e^{i\phi}S_\theta & e^{2i\phi}(1 - C_\theta) \\ -\sqrt{2}e^{-i\phi}S_\theta & 2 - 2C_\theta & \sqrt{2}e^{i\phi}S_\theta \\ e^{-2i\phi}(1 - C_\theta) & \sqrt{2}e^{-i\phi}S_\theta & 3 + C_\theta \end{pmatrix} \quad (6.42)$$

is a matrix-valued horizontal weighting function, with $S_\theta \equiv \sin 2\theta$ and $C_\theta \equiv \cos 2\theta$. Magnetic obliquity is generated by the off-diagonal elements of $\mathbf{M}_{\ell=1}$, which are related to the $m = 1$ and $m = 2$ coefficients of the azimuthal Fourier transform of B_r^2 (see the Supplementary Information of Li, Deheuvels, Ballot, and Lignières, 2022). Azimuthal Fourier coefficients of higher m correspond to smaller-scale azimuthal non-axisymmetry in the magnetic field which do not couple to the dipole modes in perturbation theory.

In this work, we illustratively assume an inclined dipolar magnetic field such that $B_r \propto \cos \beta \cos \theta + \sin \beta \sin \theta \cos \phi$, where β is the misalignment angle between the rotation and magnetic axes. Combining Equations 6.37, 6.41, and 6.42 yields

$$\mathbf{M}_{\ell=1} = \frac{3}{20} \delta\omega_{\text{mag}} \begin{pmatrix} 7 + \cos 2\beta & -\sqrt{2} \sin 2\beta & 1 - \cos 2\beta \\ -\sqrt{2} \sin 2\beta & 6 - 2 \cos 2\beta & \sqrt{2} \sin 2\beta \\ 1 - \cos 2\beta & \sqrt{2} \sin 2\beta & 7 + \cos 2\beta \end{pmatrix}, \quad (6.43)$$

reproducing Equation 6.23 in the text.

While this particular field geometry keeps the off-diagonal elements of $\mathbf{M}_{\ell=1}$ real, the off-diagonal elements can be complex in general. Complex off-diagonal elements can cause phase shifts between periodicities associated with the same mode, but do not otherwise modify our general conclusions

Chapter 7

SUPERSENSITIVE SEISMIC MAGNETOMETRY OF WHITE DWARFS

Rui, N. Z., J. Fuller, and J. J. Hermes (2025). “Supersensitive Seismic Magnetometry of White Dwarfs.” In: *The Astrophysical Journal* 981.1, 72. doi: 10.3847/1538-4357/adaf9e. arXiv: 2410.20557.

The origin of magnetic fields in white dwarfs (WDs) remains mysterious. Magnetic WDs are traditionally associated with field strengths $\gtrsim 1$ MG, set by the sensitivity of typical spectroscopic magnetic field measurements. Informed by recent developments in red giant magnetoasteroseismology, we revisit the use of WD pulsations as a seismic magnetometer. WD pulsations primarily probe near-surface magnetic fields, whose effect on oscillation mode frequencies is to asymmetrize rotational multiplets and, if strong enough, suppress gravity-mode propagation altogether. The sensitivity of seismology to magnetic fields increases strongly with mode period and decreases quickly with the depth of the partial ionization-driven surface convective zone. We place upper limits for magnetic fields in 24 pulsating WDs: 20 hydrogen-atmosphere (DAV) and three helium-atmosphere (DBV) carbon–oxygen WDs, and one extremely low-mass (helium-core) pulsator. These bounds are typically ~ 1 –10 kG, although they can reach down to ~ 10 –100 G for DAVs and helium-core WDs in which lower-frequency modes are excited. Seismic magnetometry may enable new insights into the formation and evolution of WD magnetism.

We thank Sivan Ginzburg for helpful discussions and comments on the manuscript, as well as the anonymous referee for their useful suggestions. We are grateful for support from the United States–Israel Binational Science Foundation through grant BSF-2022175. N.Z.R. acknowledges support from the National Science Foundation Graduate Research Fellowship under Grant No. DGE-1745301.

7.1 Introduction

White dwarfs (WDs) are the compact remnants of low- and intermediate-mass ($\lesssim 8M_{\odot}$) stars. Although a large fraction of WDs are now known to be magnetic ($\approx 20\%$; Bagnulo and Landstreet, 2021), the origins of their magnetic fields are still largely mysterious.

Magnetic fields in WDs are typically measured using Zeeman splitting of spectral absorption or emission lines (Landstreet, 2014; Ferrario, Martino, et al., 2015). Recent volume-limited surveys have revealed that magnetism in typical WDs (with masses $M \leq 0.75M_{\odot}$) experience a delayed onset, with both the incidence and strength of magnetism increasing at cooling ages of 2–3 Gyr (Bagnulo and Landstreet, 2021; Bagnulo and Landstreet, 2022). The late appearance of magnetic fields in these WDs may be due to some combination of an outward-diffusing fossil field from earlier evolutionary stages and a magnetic dynamo activated during core crystallization (Isern et al., 2017; Schreiber, Belloni, et al., 2021; Ginzburg et al., 2022; Blatman and Ginzburg, 2024a; Fuentes et al., 2024; Blatman and Ginzburg, 2024b). In contrast, strong magnetic fields occur in a large fraction ($\sim 40\%$) of ultramassive ($M \gtrsim 1.1M_{\odot}$) WDs (Bagnulo and Landstreet, 2022; Kilic, Moss, et al., 2023), suggesting a merger-related origin may be responsible for some of them (Tout, Wickramasinghe, Liebert, et al., 2008; García-Berro et al., 2012; Briggs et al., 2018; Schneider, Ohlmann, Podsiadlowski, Röpke, Balbus, and Pakmor, 2020). The puzzle of WD magnetism is a timely one.

In parallel with these developments, leaps and bounds have been made in the asteroseismic inference of magnetic fields in the interiors of red giants in the last few years. The propagation of buoyancy-restored gravity waves through stably stratified regions (such as in the radiative cores of red giants) is sensitive to the magnetic field. The degree to which a standing gravity wave (g mode) of period P is locally influenced by magnetism is determined by the comparison between the radial component of the magnetic field, B_r , to the critical field

$$B_{r,\text{crit}} \sim \frac{2\pi^2}{\sqrt{\ell(\ell+1)}} \frac{\sqrt{4\pi\rho} r}{NP^2}, \quad (7.1)$$

where ρ is the density, r is the radial coordinate, and N is the Brunt–Väisälä (buoyancy) frequency, given in Gaussian units (Fuller, Cantiello, et al., 2015).

Magnetism (due to fields $\gtrsim 100$ kG) is thought to dampen or outright suppress dipolar oscillations in approximately one-fifth of observed red giants (García, Hernández, et al. 2014; Stello, Cantiello, Fuller, Huber, et al. 2016; Cantiello et al. 2016, although see Mosser, Belkacem, et al. 2017). This magnetic suppression can occur when $B_r > B_{r,\text{crit}}$ somewhere in the g-mode cavity (Fuller, Cantiello, et al., 2015; Lecoanet, Vasil, et al., 2017;

Lecoanet, Bowman, et al., 2022; Rui and Fuller, 2023). However, in the last few years, asteroseismic frequency *shifts* due to weaker magnetic fields of tens to a hundred kilogauss have been detected for the very first time (Li, Deheuvels, Ballot, and Lignières, 2022; Deheuvels, Li, et al., 2023; Li, Deheuvels, Li, et al., 2023; Hatt et al., 2024). Magnetic frequency shifts depend not only the magnetic field’s strength but also its geometry.

The majority of existing red giant magnetic field measurements based on seismic frequency shifts have relied on asymmetries in observed dipole ($\ell = 1$) triplets (Li, Deheuvels, Ballot, and Lignières, 2022; Li, Deheuvels, Li, et al., 2023). While rotation (to first order) splits a single peak in the asteroseismic power spectrum into a symmetric multiplet of $2\ell + 1$ distinct modes, the Lorentz force typically causes asymmetric splitting within the multiplet (Bugnet et al., 2021; Li, Deheuvels, Ballot, and Lignières, 2022; Das et al., 2024). Even when other sources of asymmetry cannot be excluded (e.g., near-degeneracy effects; Deheuvels, Ouazzani, et al., 2017; Ong, Bugnet, et al., 2022), the degree (or lack) of asymmetry imposes an upper bound on the magnetic field.

The concept of performing similar, asymmetry-based magnetic field measurements in pulsating WDs dates back to Jones et al. (1989), who predicted that seismology would be sensitive to weak fields far below the “traditional” megagauss WD magnetic field. Soon after, Winget, Nather, et al. (1994) reported the seismic detection of a kilogauss-level magnetic field in Whole Earth Telescope observations of the brightest DBV, GD 358 (i.e., the prototype DBV, V777 Herculis). Similar seismic field constraints have been placed on various other WDs over the years (Kawaler et al., 1995; Schmidt and Grauer, 1997; Vauclair et al., 2002; Dolez et al., 2006; Fu et al., 2007; Hermes, Kawaler, et al., 2017), but a uniform analysis for a large sample of WDs has not been performed. Although DQVs have previously been thought to be pulsating, magnetic WDs (Dufour, Fontaine, et al., 2008), their variability is now generally believed to be due to surface spots (Williams et al., 2016). We are not aware of any definitive detections of pulsations in known magnetic WDs.

In this work, we use asteroseismic data to place approximate upper limits on the magnetic fields in the near-surface layers of 24 WDs. In doing so, we aim to add seismology to the toolkit of WD magnetometry. Seismic magnetometry has the potential to complement traditional Zeeman effect-based techniques in constraining the formation and evolution of WD magnetic fields (Figure 7.1). Section 7.2 summarizes our present understanding of gravity waves under magnetic fields. Section 7.3 describes our stellar models and the procedure by which we place seismic upper bounds on WD fields. Section 7.4 presents and discusses our findings. Section 7.5 summarizes and presents optimistic prospects.

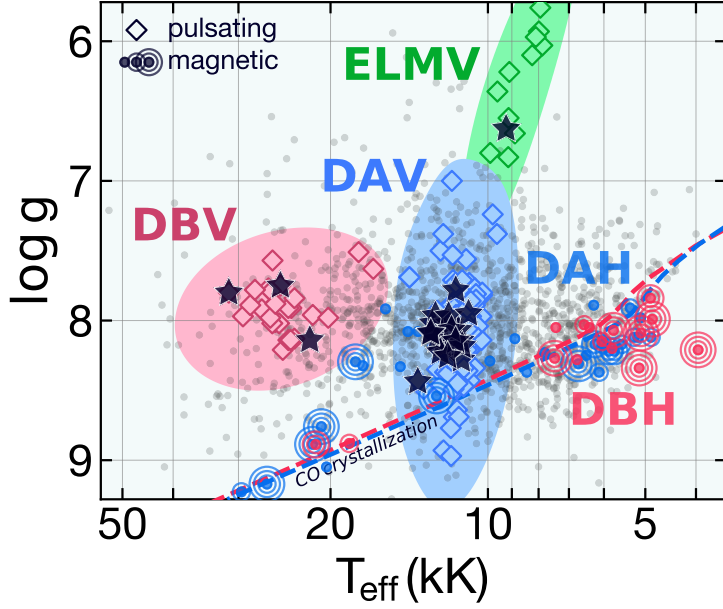


Figure 7.1: Kiel diagram showing various classes of pulsating (*diamonds*; C  rsico et al., 2019) and magnetic (*colored circles*; Bagnulo and Landstreet 2021; Bagnulo and Landstreet 2022, with some values of $\log g$ taken from the Gaia EDR3 catalog of Gentile Fusillo et al. 2021) WDs. *Black stars* indicate WDs whose magnetic fields we constrain in this study, while blue points are DA WDs and red points are DB WDs from the literature. Following the plotting convention of Bagnulo and Landstreet (2022), magnetic WD points surrounded by zero, one, two, and three *concentric circles* have measured fields $B < 1$ MG, 1 MG $\leq B < 10$ MG, and 10 MG $\leq B < 100$ MG, and $B \geq 100$ MG, respectively. The background *translucent gray points* indicate a subsample of other WDs in the catalog of Gentile Fusillo et al. (2021). The innermost 5% by mass of carbon–oxygen WDs with thin (thick) hydrogen envelopes will crystallize once they reach the *red* (*blue*) *dashed lines* (B  dard et al., 2020).

7.2 Theoretical background

Here, we outline the existing formalism on gravity waves under the influence of the Lorentz force. Sections 7.2.1 and 7.2.2 summarize theoretical predictions for frequency shifts and conditions for mode suppression, respectively.

The following formulae for the frequency shifts are valid in the perturbative regime where both magnetism and rotation are treated at lowest order, with the additional assumption that rotation is strong enough to set the preferred direction of the problem (see Li, Deheuvels, Ballot, and Lign  res, 2022; Das et al., 2024). Mode suppression conditions arise from a non-perturbative treatment of the magnetogravity problem (e.g., Fuller, Cantiello, et al., 2015; Lecoanet, Vasil, et al., 2017; Lecoanet, Bowman, et al., 2022; Rui and Fuller, 2023; Rui, Ong, et al., 2024). Both calculations rely heavily on the incompressible approximation

(which filters out pressure waves), the asymptotic approximation (which relies on high radial orders), and the Cowling approximation. Departures from these assumptions are treated in this work as an ad hoc correction factor (Appendix 7.B). Under these assumptions, g modes are primarily sensitive to the radial component of the magnetic field B_r and insensitive to the horizontal components B_θ and B_ϕ , which are hereafter neglected.

The aim of this work is to provide a constraint on WD field using both magnetic asymmetries and mode suppression. While both effects are primarily sensitive to the outer layers of the WD (as we subsequently explain), the exact layers probed by each effect are different, and additionally they depend on the mode period, P . Since all seismic methods we discuss probe the field in geometrically thin, near-surface layers, we speak of bounding “the” surface field B_r , which assumes that the magnetic field is roughly constant near the surface of the WD.

7.2.1 Seismic frequency shifts

A non-rotating, non-magnetic star such as a WD possesses spherical symmetry, so that each radial order k and angular degree ℓ are assigned to a multiplet of $2\ell + 1$ modes of varying azimuthal order $-\ell \leq m \leq \ell$ with degenerate frequencies $\nu_{n\ell}^{(0)}$. Due to geometric cancellation effects, observable g modes are typically low- ℓ , either $\ell = 1$ dipole modes or $\ell = 2$ quadrupole modes, forming mode triplets and quintuplets, respectively. The first-order effect of rotation is to split these modes into a symmetric multiplet (Ledoux, 1951; Unno, Osaki, Ando, and Shibahashi, 1979; Aerts, Christensen-Dalsgaard, et al., 2010; Aerts, 2021):

$$\nu_{k\ell m} \approx \nu_{k\ell}^{(0)} + m \left(1 - \frac{1}{\ell(\ell + 1)} \right) \frac{\langle \Omega \rangle_g}{2\pi}, \quad (7.2)$$

where

$$\langle \Omega \rangle_g \approx \frac{\int_{\mathcal{R}_v^\ell} \Omega (N/r) dr}{\int_{\mathcal{R}_v^\ell} (N/r) dr} \quad (7.3)$$

is a wave-cavity-averaged rotation rate. The symbol \mathcal{R}_v^ℓ denotes the g-mode cavity, the contiguous range of radii where the linear mode frequency ν satisfies $2\pi\nu < N, S_\ell$, where $S_\ell = \sqrt{\ell(\ell + 1)}c_s/r$ is the degree- ℓ Lamb frequency (Unno, Osaki, Ando, and Shibahashi, 1979; Aerts, Christensen-Dalsgaard, et al., 2010). The rotational frequency shift is due to a combination of the Coriolis force (which is a physical effect) and a Doppler effect acting on the mode frequencies (which is a geometric one).

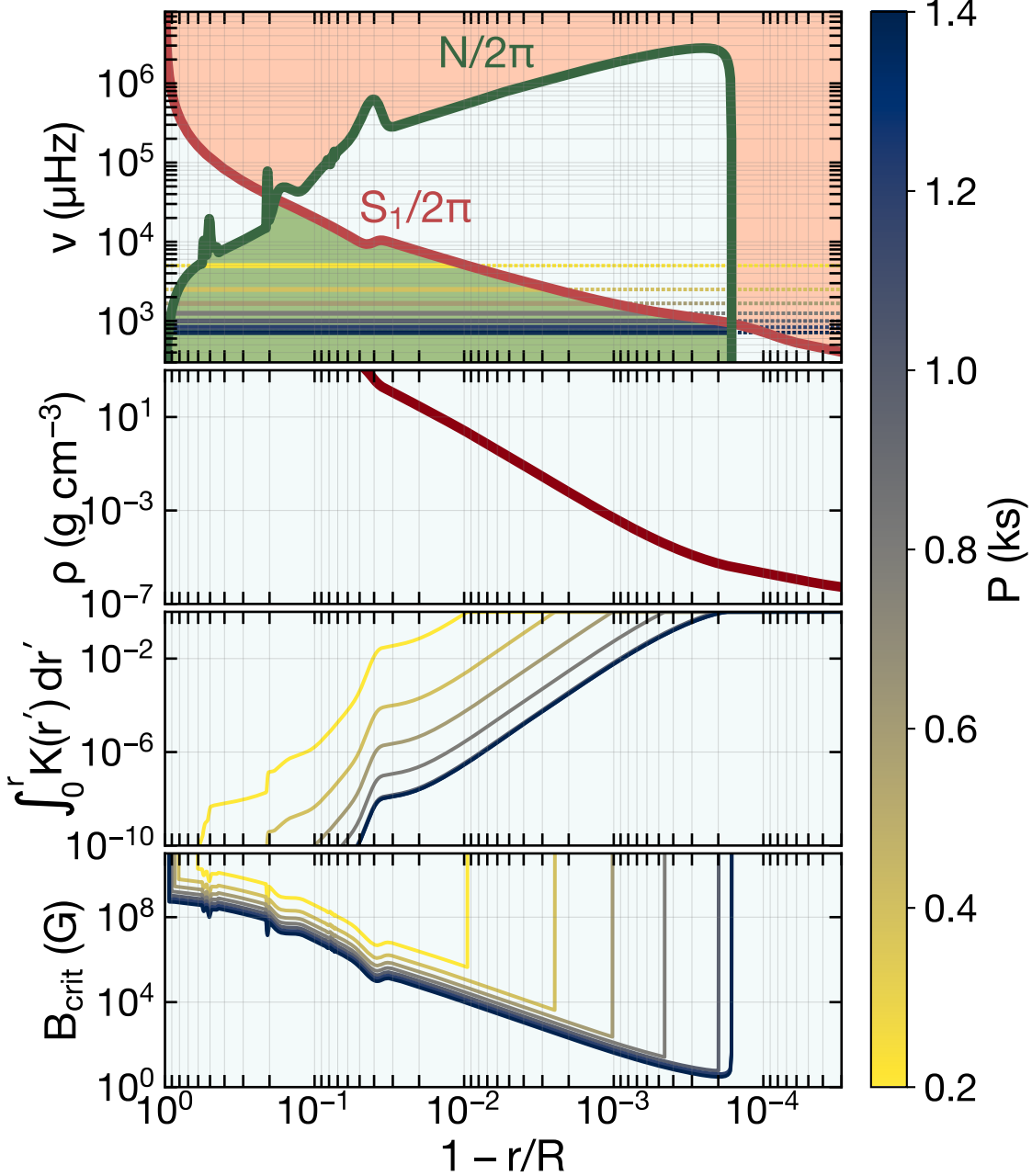


Figure 7.2: *Top:* Astroseismic propagation diagram for the dipole ($\ell = 1$) modes of a WD model with $M = 0.64M_\odot$ and $T_{\text{eff}} = 12 \text{ kK}$, with $1 - r/R$ on the x axis (fractional radius from the outermost shell of the model). The green and brown curves show the Brunt–Väisala (N) and dipole Lamb (S_1) frequencies, respectively. The green shaded region denotes the g-mode cavity. *Second from top:* Density as a function of radius. *Third from top:* Cumulative magnetic weight function (defined in Equation 7.7) for the same model, for a variety of mode periods. The function $\int_0^r K(r') dr'$ represents the cumulative contribution of the magnetic field in shells within radii r to the average $\langle B_r^2 \rangle$ (Equation 7.6). *Bottom:* Critical field $B_{r,\text{crit}}$ required to suppress gravity waves, for a variety of mode periods.

When the star is also magnetic, the magnetic tension serves as an additional, “stiffening” restorative force which shifts gravity mode frequencies by roughly

$$\begin{aligned} \nu_B^\ell &\equiv \frac{A_\ell}{64\pi^5} \frac{P^3}{\int_{\mathcal{R}_\nu^\ell} (N/r) \, dr} \int_{\mathcal{R}_\nu^\ell} dr \frac{N^3}{\rho r^3} \int \frac{B_r^2}{4\pi} \, d\Omega \\ &= A_\ell \frac{\mathcal{J}}{64\pi^5} \langle B_r^2 \rangle P^3, \end{aligned} \quad (7.4)$$

where $d\Omega$ is an integral over a spherical surface and

$$\mathcal{J} \simeq \frac{\int_{\mathcal{R}_\nu^\ell} (N^3/\rho r^3) \, dr}{\int_{\mathcal{R}_\nu^\ell} (N/r) \, dr}, \quad (7.5)$$

and $P = 1/\nu$ is the period of the mode and $A_\ell = \ell(\ell+1)/2$. The characteristic scale ν_B^ℓ of the frequency shift can be computed from a field strength and stellar model (which enters Equation 7.4 purely through \mathcal{J}).

The weighted average $\langle B_r^2 \rangle$ which appears in Equation 7.4 is given by Li, Deheuvels, Ballot, and Lignières (2022):

$$\langle B_r^2 \rangle = \int_{\mathcal{R}_\nu^\ell} dr K(r) \int \frac{d\Omega}{4\pi} B_r^2, \quad (7.6)$$

where the weight function is

$$K(r) \simeq \begin{cases} \frac{N^3/\rho r^3}{\int_{\mathcal{R}_\nu^\ell} (N^3/\rho r^3) \, dr} & \text{in } \mathcal{R}_\nu^\ell \\ 0 & \text{otherwise} \end{cases}. \quad (7.7)$$

The quantity ν_B^ℓ is the mean frequency shift averaged over a multiplet. However, individual modes within the multiplet will experience different frequency shifts from each other. The precise order-unity prefactor relating a mode’s magnetic frequency shift to ν_B^ℓ depends both on the quantum numbers of the mode and the geometry of the field (Li, Deheuvels, Ballot, and Lignières, 2022). As a consequence, unlike rotation, magnetism does not generically preserve the symmetry of the multiplet, and the asymmetry of the multiplet can distinguish frequency shifts due to magnetism from those due to first-order rotation. We assume throughout this work that the pulsations are aligned with the rotation axis, so that each mode is observed as a single sinusoidal periodicity. This is appropriate when the magnetic force is weaker than the Coriolis force (although see Section 7.4.2).

The asymmetry of a multiplet can be parameterized by dimensionless asymmetry parameters $a_{m_1 m_2 m_3}^\ell$, the most commonly used of which (“ a ”) is defined as

$$a_{-10+1}^{\ell=1} = \frac{\Delta_{-10+1}^{\ell=1}}{3 \nu_B^{\ell=1}}, \quad (7.8)$$

where

$$\Delta_{-1 0 +1}^{\ell=1} = \nu_{m=-1}^{\ell=1} - 2 \nu_{m=0}^{\ell=1} + \nu_{m=+1}^{\ell=1} \quad (7.9)$$

is a linear combination of the three dipole modes in a triplet (Li, Deheuvels, Ballot, and Lignières, 2022; Mathis and Bugnet, 2023; Das et al., 2024). This is the only possible asymmetry parameter for $\ell = 1$.

We similarly construct quadrupole asymmetry parameters by taking linear combinations $\Delta_{m_1 m_2 m_3}^{\ell} \propto \nu_B^{\ell}$ of three modes within the same multiplet such that the first-order rotational splitting terms cancel out (our adopted definitions for $\Delta_{m_1 m_2 m_3}^{\ell=2}$ are given by Equations 7.22). We define the ten quadrupole asymmetry parameters $a_{m_1 m_2 m_3}^{\ell}$ as

$$a_{m_1 m_2 m_3}^{\ell} = \frac{\Delta_{m_1 m_2 m_3}^{\ell=2}}{5 \nu_B^{\ell=2}}. \quad (7.10)$$

In Appendix 7.A, we relate them to the magnetic field geometry and compute them for an inclined dipolar magnetic field (see also Das et al., 2024).

In WDs, ρ sharply decreases towards surface, and N often also reaches its peak value there, just below the surface convective zone. The weight function $K(r)$ is thus very sharply peaked just below the surface, at depths $1 - r/R \sim 10^{-3} - 10^{-2}$, and asteroseismology is most sensitive to the near-surface field (*center panel* of Figure 7.2). This is in contrast to the cases of red giant or intermediate-mass main-sequence stars, within which $K(r)$ peaks at some highly stratified layer in the deep interior of the star (the hydrogen-burning shell and near-core composition gradient, respectively; Fuller, Cantiello, et al., 2015; Lecoanet, Bowman, et al., 2022). While the pulsations of WDs are in principle modified by deep internal magnetic fields, the influence of these fields is highly diluted. In the $0.64M_{\odot}$ WD model in Figure 7.2, a uniform magnetic field of $\simeq 1$ MG restricted to the inner $r/R \lesssim 0.993$ of the WD affects a $P = 1200$ s gravity mode identically to a uniform $\simeq 1$ G field restricted to the outer layers with $r/R \gtrsim 0.993$. Long-period modes probe the magnetic field at very low-density layers ($\rho \simeq 4 \times 10^{-6}$ g cm $^{-3}$ for the $P = 1200$ s mode in Figure 7.2), although still far within the photosphere of the WD.

In principle, magnetic shifts also modify the spacing between adjacent multiplets, causing a period-dependent period spacing $\Delta\Pi_{\ell} = \Delta\Pi_{\ell}(P)$ (e.g., Cantiello et al., 2016; Rui, Ong, et al., 2024). Deheuvels, Li, et al. (2023) used this effect to measure strong magnetic fields in red giants in which dipole triplets were not detected. However, this is likely difficult in WDs, whose g modes already depart from period-uniformity due to non-asymptotic mode trapping effects due to, e.g., near-surface composition gradients (Brassard, Fontaine, Wesemael, and Hansen, 1992). We instead focus on intra-multiplet asymmetries, since

non-asymptotic effects are expected to affect each component of a multiplet in the same way.

7.2.2 Mode suppression

About $\simeq 20\%$ of observed red giants have unusually low-amplitude non-radial (dipole) oscillations (García, Hernández, et al., 2014; Stello, Cantiello, Fuller, Huber, et al., 2016). Fuller, Cantiello, et al. (2015) show that the amplitudes of these suppressed oscillations are consistent with nearly total damping of g-mode oscillations in the core. They argue that such near-total suppression of g modes can occur if the damping mechanism is magnetic in nature. Simple scaling arguments (Fuller, Cantiello, et al., 2015; Cantiello et al., 2016; Rui and Fuller, 2023) show that g modes will be significantly affected by a magnetic field when the radial component of the field approaches $B_{r,\text{crit}}$ as defined in Equation 7.1, and detailed calculations validate several magnetic dissipation mechanisms (Lecoanet, Vasil, et al., 2017; Loi and Papaloizou, 2017; Loi and Papaloizou, 2018; Loi, 2020b; Lecoanet, Bowman, et al., 2022; Rui and Fuller, 2023). Throughout this work, we assume that magnetic g-mode suppression damps out all g-mode energy (although see Mosser, Belkacem, et al., 2017), and use the presence of non-suppressed g modes in WDs to set upper bounds on the magnetic field.

As can be seen in Equation 7.1, longer-period modes require weaker magnetic fields to suppress. At fixed ℓ , the longest-period modes observed in a WD therefore set the strongest upper limits on the WD field. Also, since $B_{r,\text{crit}} \propto \sqrt{\rho}/N$, the value of $B_{r,\text{crit}}$ reaches a minimum near the outer edge of the WD g-mode cavity. Therefore, like magnetic asymmetries, magnetic mode suppression probes the near-surface layers. The bottom panel of Figure 7.2 shows $B_{r,\text{crit}}$ for various g modes in a $0.64M_{\odot}$ WD. While fields of $\simeq 3$ G at a depth of $r/R = 0.998$ are sufficient to suppress $P = 1200$ s oscillations, a $\simeq 10$ MG field is needed to achieve the same effect at a depth of $r/R = 0.9$.

For simplicity, when calculating $B_{r,\text{crit}}$, we adopt the dimensionless prefactors shown in Equation 7.1 originally derived by Fuller, Cantiello, et al. (2015). In reality, this prefactor actually depends on ℓ , m , and the field geometry in complicated ways (Lecoanet, Vasil, et al., 2017; Loi and Papaloizou, 2018; Rui and Fuller, 2023). Because this prefactor is order-unity (Lecoanet, Vasil, et al., 2017; Rui and Fuller, 2023), its uncertain value translates to order-unity errors in the inferred field strength, but changes in its value are unlikely to greatly affect the field constraint.

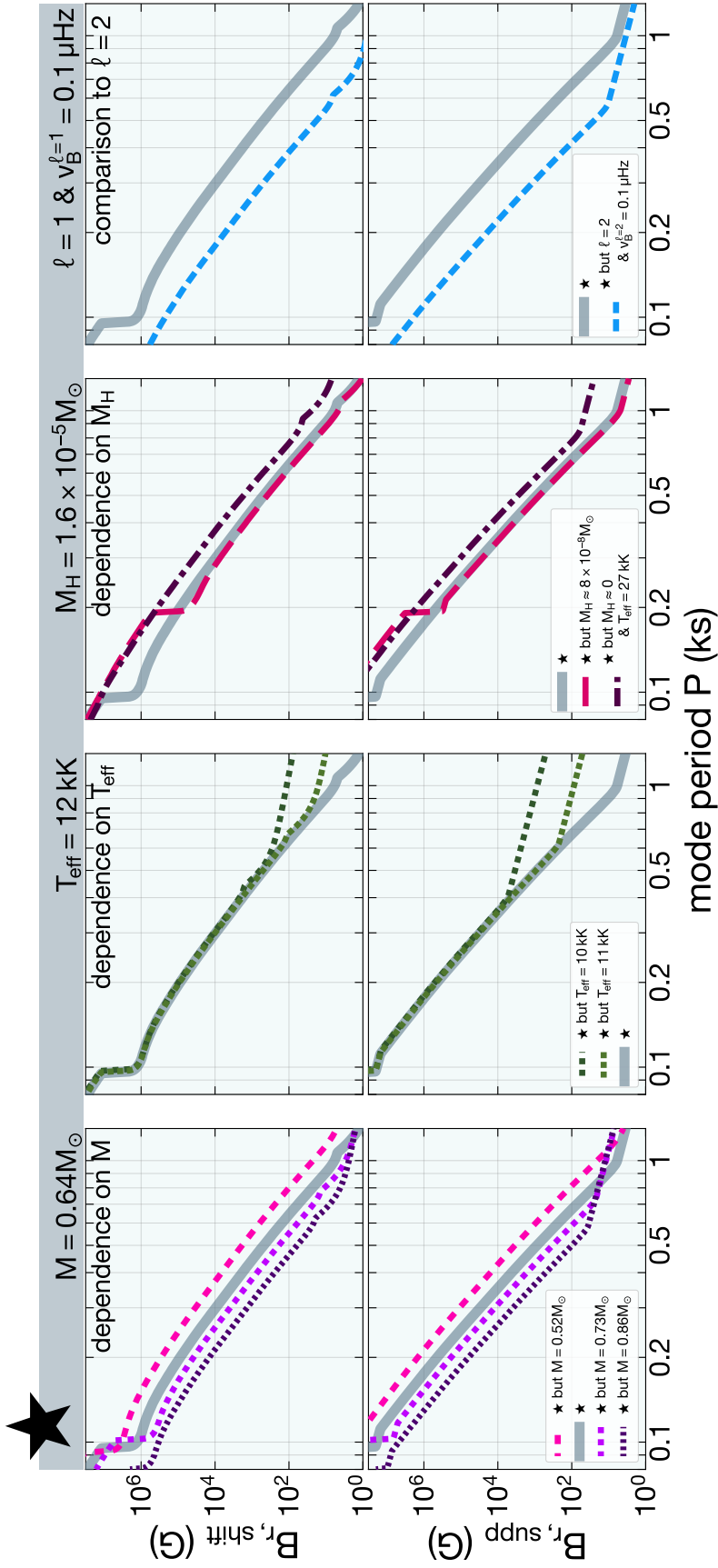


Figure 7.3: Model seismic magnetic field sensitivities $B_{r,\text{shift}}$ and $B_{r,\text{supp}}$. From *left* to *right*, columns show the effect of varying total mass M , effective temperature T_{eff} , hydrogen atmosphere mass M_H , and angular degree ℓ . These comparisons are made relative to fiducial parameters (listed in the top gray box), which we plot in gray and denote with \star . In particular, we show the value of $B_{r,\text{shift}}$ implied by a dipole multiplet with an asymmetry of $v_B^{\ell=1} = 0.1 \mu\text{Hz}$. Note that $B_{r,\text{shift}} \propto \sqrt{v_B^\ell}$ whereas $B_{r,\text{supp}}$ does not depend on v_B^ℓ at all.

7.3 Methods

7.3.1 White dwarf models

Seismic magnetic field estimates rely on detailed stellar models. To this end, we use several helium-core and carbon–oxygen WD models prepackaged with version r10398 of the Modules for Experiments in Stellar Astrophysics code (MESA; Paxton, Bildsten, et al., 2010; Paxton, Cantiello, et al., 2013; Paxton, Marchant, et al., 2015; Paxton, Schwab, et al., 2018). We evolve models down a cooling track in the presence of gravitational settling using as diffusion representatives ^1H , ^4He , ^{12}C , ^{16}O , ^{20}Ne , and ^{22}Ne . In order to avoid helium shell flashes and/or help with numerical convergence issues, we sometimes artificially reduce the size of the hydrogen atmosphere by replacing its inner layers with helium. In one case ($M = 0.73M_\odot$), we replace the outer layers of the originally helium-atmosphere model with hydrogen to create a DA WD model. We also evolve several helium-atmosphere (DB) and DA WD models with lower total hydrogen masses M_H , initialized by replacing some of the WD’s hydrogen with helium prior to evolution.

We apply the Ledoux criterion for convective stability. This sometimes produces short-lived convective zones owing to the particular composition gradient in the initial stellar model. Although these convective zones can technically split the WD into multiple g mode cavities (requiring more sophisticated analysis Pinçon and Takata, 2022), the appearance times, locations, and lifetimes of these convective zones are hard to predict. When performing integrals over the g mode cavity (i.e., when determining \mathcal{R}_ν^ℓ), we therefore integrate over all shells satisfying the gravity wave propagation condition ($2\pi\nu < N, S_\ell$) without enforcing that the g-mode cavity is contiguous. Our WD models are summarized in Table 7.1.¹

7.3.2 Seismic field constraints

Magnetism tends to asymmetrize rotational multiplets. Symmetric multiplets therefore place upper limits on the magnetic field present in a WD. For each multiplet, we use Equations 7.8 (for $\ell = 1$) or 7.10 (for $\ell = 2$) to convert a measured asymmetry to ν_B^ℓ . To be conservative, we calculate this magnetic field bound assuming that the measured asymmetry is underestimated by 2σ , i.e., using as the asymmetry $|\Delta_{m_1 m_2 m_3}^\ell| + 2\delta\Delta_{m_1 m_2 m_3}^\ell$ where $\delta\Delta_{m_1 m_2 m_3}^\ell$ is the uncertainty on the asymmetry implied by the measurement uncertainties on the mode frequencies. Finally, we invert Equation 7.4 to solve for the upper limit

¹These MESA models can be reproduced with the inlists, `run_star_extras.f`, and other files at the following link: <https://doi.org/10.5281/zenodo.14457127>

core	type	$M (M_{\odot})$	$M_{\text{H}} (M_{\odot})$	$M_{\text{He}} (M_{\odot})$
He	DA	0.15*	9.95×10^{-4}	...
He	DA	0.20	9.54×10^{-4}	...
He	DA	0.40*	7.26×10^{-5}	...
CO	DA	0.52	8.53×10^{-5}	2.90×10^{-2}
CO	DB	0.52	0	2.91×10^{-2}
CO	DA	0.64	1.64×10^{-5}	4.23×10^{-3}
CO	DA	0.64*	8.00×10^{-8}	4.25×10^{-3}
CO	DB	0.64	0	4.25×10^{-3}
CO	DA	0.73	3.48×10^{-6}	2.53×10^{-3}
CO	DB	0.73	0	2.54×10^{-3}
CO	DA	0.86	3.99×10^{-6}	1.64×10^{-3}
CO	DB	0.86	0	1.65×10^{-2}

Table 7.1: Summary of the WD models used in this work (Section 7.3.1). Asterisks (*) indicate that we checked the magnetic sensitivity of the model, but did not use it in fitting WD observations.

$$B_{r,\text{shift}} = \sqrt{\langle B_r^2 \rangle}:$$

$$B_{r,\text{shift}} = 8\pi^{5/2} \sqrt{\min \left\{ \frac{|\Delta_{m_1 m_2 m_3}^{\ell}| + 2\delta\Delta_{m_1 m_2 m_3}^{\ell}}{(2\ell+1)|a_{m_1 m_2 m_3}^{\ell}|A_{\ell}\mathcal{J}P^3} \right\}} \quad (7.11)$$

where the minimum is over all combinations of three modes (indexed by m_1 , m_2 , and m_3) within the same multiplet. The quantity \mathcal{J} is corrected for non-asymptotic effects using an ad hoc factor described in Appendix 7.B.

In this work, we assume asymmetry parameters $a_{m_1 m_2 m_3}^{\ell}$ typical for an inclined, centered dipolar magnetic field (derived in Appendix 7.A.3). This sets $a_{-10+1}^{\ell=1} \approx 0.253$ and $a_{m_1 m_2 m_3}^{\ell=2}$ to values between -0.217 and -0.036 , depending on the values of m_1 , m_2 , and m_3 . While the field geometry is uncertain in reality, changes to the field geometry only modify the field strength estimate by order-unity factors. Mode asymmetries can also be non-magnetic in origin (e.g., from second-order rotational effects or near-degeneracy effects). However, we assume that other sources of asymmetry do not decrease the rough scale of the observed symmetry. In principle, we can underestimate the magnetic field if another source of asymmetry happens to nearly cancel out the magnetic asymmetry.

When $B_r > B_{r,\text{crit}}(P)$, a g mode of period P is expected to be suppressed. Therefore, the presence of a g mode indicates that the field does not exceed $B_{r,\text{crit}}$. We use this fact to place additional suppression-based upper bounds $B_{r,\text{supp}}$ by setting $B_{r,\text{supp}} = B_{r,\text{crit}}$ and inverting

Equation 7.1 for each mode:

$$B_{r,\text{supp}} = 4\pi^{5/2} \min \left\{ \frac{(\sqrt{\rho} r/N)_{\min g,P_0}}{\sqrt{\ell(\ell+1)}P_0^2} \right\} \quad (7.12)$$

where the minimum is over all observed radial orders. The quantity $(\sqrt{\rho} r/N)_{\min g,P}$ is the minimum value of $\sqrt{\rho} r/N$ in the g-mode cavity corresponding to period P . The period P_0 indicates the central frequency of the multiplet, which we take as an estimate for the unperturbed mode period. When the $m = 0$ component is reported, we take its period to be P_0 . Otherwise, if two or more components are reported, we calculate $P_0 = 1/\nu^{(0)}$, where $\nu^{(0)}$ is the y-intercept of a fit to the mode frequencies ν within a multiplet to a linear function of m . Finally, if there is only a single mode within the multiplet, we take its period as P_0 . As can be seen in Equation 7.1, the minimum is always set by either the longest-period dipole multiplet or longest-period quadrupole multiplet. Since this constraint relies on the *existence* of an excited radial order rather than a rotational multiplet asymmetry, we only require a single observed mode within a multiplet.

7.3.3 Dependence of magnetic sensitivity on white dwarf properties

The sensitivity of a WD's oscillation modes to magnetism depends on the WD's structure, particularly through \mathcal{J} (defined in Equation 7.5) for $B_{r,\text{shift}}$ and $(\sqrt{\rho} r/N)_{\min g,P}$ (through Equation 7.12) for $B_{r,\text{supp}}$.

The first three columns of Figure 7.3 show how $B_{r,\text{shift}}$ and $B_{r,\text{supp}}$ depend on various WD properties relative to a fiducial DAV model with $M = 0.64M_\odot$ and $T_{\text{eff}} = 12\text{ kK}$. To good approximation, both $B_{r,\text{shift}}$ (at fixed ν_B^ℓ) and $B_{r,\text{supp}}$ can be described as broken power laws, with a shallower power law index at higher mode periods. The transition period P_t between these two regimes corresponds to the mode period above (below) which the outer boundary g-mode cavity is set by $N(S_\ell)$. It is given by $P_t = 2\pi/S_\ell$ at the outer intersection between N and S_ℓ , and corresponds to a long period $P_t \approx 1100\text{ s}$ ($\nu \approx 900\text{ }\mu\text{Hz}$) for dipole modes in the model in Figure 7.2 (consistent with the value computed by Montgomery, Hermes, et al., 2020). Hereafter, we refer to modes with long periods $P > P_t$ (short periods $P < P_t$) as N -limited (S_ℓ -limited).

The Lamb frequency S_ℓ has a gradually varying profile. This means the outer boundary of the g-mode cavity varies substantially with P for S_ℓ -limited modes. Since the layers of the WD most sensitive to magnetism are those closest to the outer boundary of the radiative zone, both $B_{r,\text{shift}}$ and $B_{r,\text{supp}}$ for S_ℓ -limited modes strongly depend on P . Conversely, the Brunt–Väisälä frequency N drops sharply at the outer boundary of the radiative zone. Accordingly, the outer g-mode-cavity boundaries of N -limited modes are essentially identical to each

other. In this regime, $B_{r,\text{shift}}$ and $B_{r,\text{supp}}$ have the approximate scalings $B_{r,\text{shift}} \propto P^{-3/2}$ and $B_{r,\text{supp}} \propto P^{-2}$, reflecting only the explicit period dependences in Equations 7.11 and 7.12.

More massive WDs have higher dynamical frequencies, which in turn increases both N and S_ℓ (*first column* of Figure 7.3). In the S_ℓ -limited regime, the increased S_ℓ in more massive WDs translates to an outer g-mode cavity boundary which is closer to the surface. S_ℓ -limited modes in more massive WDs are thus more magnetically sensitive than those in less massive WDs. We find that the magnetic sensitivity of N -limited modes, however, is almost independent of mass.

The primary effect of varying the effective temperature T_{eff} (*second column* of Figure 7.3) is to change the extent of the outer, partial ionization-driven convection zone. As DA WDs cool below $T_{\text{eff}} \sim 13$ kK, they develop progressively deeper (albeit low mass; $M_{\text{conv}}/M_{\text{WD}} \sim 10^{-12}$) convective zones driven by a near-surface partial ionization zone (e.g., Tremblay, Ludwig, et al., 2015). The result is that both $B_{r,\text{shift}}$ and $B_{r,\text{supp}}$ are unaffected for S_ℓ -limited modes. However, N -limited modes are less sensitive to magnetic fields in cooler WDs because they are confined deeper in the WD where ρ is larger and N is smaller. Furthermore, cooler WDs have lower P_t : as they cool, the range of frequencies which are N -limited widens. While only very-long dipole period modes are N -limited in most cases, P_t drops dramatically near the very red edge of the DAV instability strip ($P_t \simeq 600$ s in the $T_{\text{eff}} = 10$ kK model in the *second panel* of Figure 7.3).

Because the near-surface partial ionization zone is also responsible for mode excitation (Brickhill, 1991; Goldreich and Wu, 1999), the DA instability strip contains DAVs with both deep and shallow convective zones on its red and blue sides, respectively. Deep convective zones also develop within the the DBV instability strip for similar reasons, albeit at a hotter temperature $T_{\text{eff}} \approx 30$ kK (Fontaine and Wesemael, 1987). Diminished sensitivity of long-period modes in cooler WDs (relative to hotter ones) trades off with the tendency of cooler WDs to excite more sensitive longer-period modes (e.g., Van Grootel et al., 2012; Hermes, Gänsicke, Kawaler, et al., 2017).

Although hydrogen spectral lines in DA WDs indicate the presence of surface hydrogen, the precise amount of this hydrogen is very uncertain. The *third column* of Figure 7.3 shows that the effect of changing the hydrogen mass M_{H} is minor. This is because the depth of the surface convective zone is largely insensitive to M_{H} , as long as it is enough to prevent the development of a helium partial ionization-driven convection zone around $\simeq 25$ kK. Figure 7.3 also shows the sensitivity of a DB model in the DBV instability strip which, despite being much hotter, has a similar sensitivity to the DAV model.

At fixed v_B^ℓ , quadrupole modes are more sensitive than dipole modes (*last column* in Figure 7.3), especially for S_ℓ -limited modes. Since $S_\ell \propto \sqrt{\ell(\ell+1)}$, the outer boundary of the g-mode cavity of S_ℓ -limited quadrupole modes is farther out than those of S_ℓ -limited dipole modes. For the same reason, P_t is significantly lower for quadrupole modes ($P_t \simeq 600$ s for the model in Figure 7.3).

In contrast, N -limited quadrupole modes only achieve a modest improvement in sensitivity over their dipole counterparts. In this case, both $B_{r,\text{shift}}$ and $B_{r,\text{supp}}$ are decreased by a factor of $\approx \sqrt{3}$, owing to their explicit dependences on ℓ in Equations 7.11 and 7.12.

7.4 Seismic field constraints in observed white dwarfs

We place asymmetry- and suppression-based upper bounds on the magnetic field for 24 observed pulsating WDs of varying types (Table 7.2). For each WD, we first identify the stellar model which best minimizes

$$\chi^2 = \left(\frac{T_{\text{eff,spec}} - T_{\text{eff,model}}}{100 \text{ K}} \right)^2 + \left(\frac{\log g_{\text{spec}} - \log g_{\text{model}}}{0.01} \right)^2, \quad (7.13)$$

where $T_{\text{eff,spec}}$ and $\log g_{\text{eff,spec}}$ are spectroscopically measured values of T_{eff} and $\log g$ taken from the literature. In other words, we choose the stellar model which best matches the location of the WD on the Kiel diagram. Using this model, we then compute $B_{r,\text{shift}}$ and $B_{r,\text{supp}}$ using Equations 7.11 and 7.12. These upper bounds are shown in Table 7.2 and Figure 7.4.

7.4.1 Magnetic leaf diagrams

We visualize the impact of magnetism on seismology using “leaf diagrams,” such as those shown in Figure 7.5. For each ℓ , the leaf diagram plots as *brown circles* the value of v_B^ℓ implied by a measurement of the asymmetry $\Delta_{m_1 m_2 m_3}^\ell$ (Equations 7.8 and 7.10) against the mode period P . The error bars on these points denote 2σ uncertainty intervals on the asymmetries. The magnetic field required to reproduce an observed asymmetry can be read off of the diagram by comparing to the contours in the background of the leaf diagram, which show model predictions for v_B^ℓ (from Equation 7.4). The *solid blue stripe* shows $B_{r,\text{shift}}$, corresponding to the weakest-field strength contour which entirely encloses the lowest asymmetry point (the one closest to the x axis), including its full error bar.

The *yellow dotted regions* show “magnetically forbidden” values of v_B^ℓ . Observed asymmetries in this region are so high that the field required to generate them (in the perturbative theory) would also magnetically suppress the mode. Under the present assumptions, such asymmetries must therefore be non-magnetic in origin. Accordingly, if a field contour is in

Table 7.2: Observed and model spectroscopic/seismic properties and upper limits on the magnetic field of 24 WDs

name	type	model M	P (ks)		T_{eff} (kK)		$\log g$		B_r upper bound (G)	
			P_{min}	P_{max}	data	model	data	model	$B_{r,\text{shift}}$	$B_{r,\text{supp}}$
GD 278 ^{1,2}	ELMV	0.20	2.29	6.73	9.23	9.33	6.63	6.65	100	70
KIC 4357037 ³	DAV	0.64	0.28	0.35	12.75	12.81	8.02	8.07	<u>4k</u>	10k
KIC 4552982 ³	DAV	0.73	0.36	0.36	11.24	11.15	8.28	8.24	<u>1k</u>	4k
KIC 7594781 ³	DAV	0.64	0.28	0.30	12.04	11.93	8.17	8.07	<u>10k</u>	30k
KIC 10132702 ³	DAV	0.73	0.62	0.89	12.22	12.20	8.17	8.23	8	4
KIC 11911480 ³	DAV	0.64	0.20	0.32	11.88	11.93	8.02	8.07	<u>8k</u>	20k
EPIC 60017836 ³	DAV	0.73	0.83	1.22	11.28	11.34	8.14	8.23	50	20
EPIC 201719578 ³	DAV	0.64	0.37	0.46	11.39	11.39	8.07	8.08	<u>1k</u>	2k
EPIC 201730811 ³	DAV	0.64	0.16	0.35	12.60	12.63	7.96	8.07	<u>10k</u>	10k
EPIC 201802933 ³	DAV	0.73	0.12	0.40	12.53	12.51	8.14	8.23	<u>2k</u>	2k
EPIC 201806008 ³	DAV	0.73	0.41	0.41	11.20	11.15	8.18	8.24	<u>1k</u>	1k
EPIC 210397465 ³	DAV	0.52	0.67	1.39	11.52	11.56	7.78	7.85	200	5
EPIC 211596649 ³	DAV	0.64	0.27	0.30	11.89	11.93	7.97	8.07	<u>7k</u>	30k
EPIC 211629697 ³	DAV	0.52	0.49	0.49	10.89	10.85	7.95	7.85	<u>3k</u>	4k
EPIC 211914185 ³	DAV	0.86	0.11	0.20	13.62	13.66	8.44	8.42	<u>60k</u>	80k
EPIC 211926430 ³	DAV	0.64	0.12	0.30	11.74	11.56	8.06	8.08	<u>9k</u>	30k
EPIC 228682478 ³	DAV	0.73	0.29	0.29	12.34	12.20	8.23	8.23	<u>4k</u>	10k
EPIC 229227292 ³	DAV	0.64	0.29	0.37	11.53	11.56	8.15	8.08	<u>3k</u>	7k
EPIC 220204626 ³	DAV	0.73	0.51	0.80	11.94	11.82	8.26	8.23	60	20
EPIC 220258806 ³	DAV	0.64	0.15	0.30	12.89	12.81	8.09	8.07	<u>10k</u>	30k
EPIC 220347759 ³	DAV	0.64	0.12	0.25	12.86	12.81	8.09	8.07	<u>20k</u>	90k
EPIC 228782059 ⁴	DBV	0.73	0.23	0.34	21.91	21.76	8.14	8.23	<u>6k</u>	3k
GD 358 ^{5,6}	DBV	0.52	0.42	0.77	24.94	24.86	7.75	7.83	700	500
PG 0112+104 ^{7,8}	DBV	0.52	0.15	0.50	31.30	31.30	7.80	7.80	200k	<u>10k</u>

For the 24 WDs for which we place a magnetic field upper limit, the WD type, model mass M , minimum P_{min} and maximum P_{max} retained pulsation period, spectroscopically measured and model T_{eff} and $\log g$, and asymmetry- and suppression-based magnetic field upper limits $B_{r,\text{shift}}$ and $B_{r,\text{supp}}$ (with the stronger upper limit underlined). 1: Lopez et al. (2021) 2: Calcaferro et al. (2023) 3: Hermes, Gänsicke, Kawaler, et al. (2017) 4: Duan et al. (2021) 5: Winget, Nather, et al. (1994) 6: Côrsico et al. (2019) 7: Hermes, Kawaler, et al. (2017) 8: Dufour, Desharnais, et al. (2010)

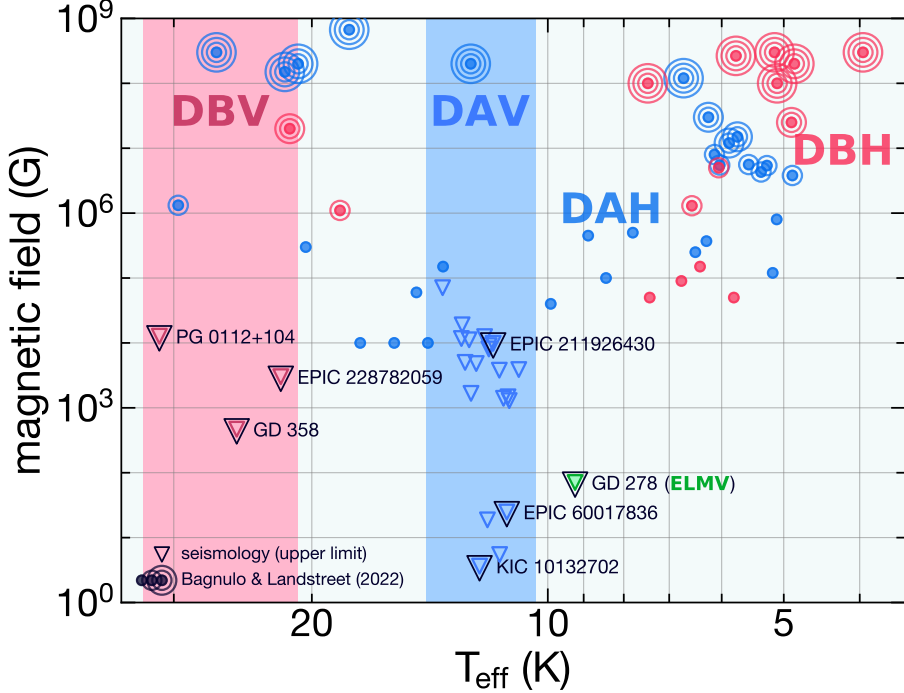


Figure 7.4: Seismic upper limits on WD magnetic fields $\min(B_{r,\text{shift}}, B_{r,\text{supp}})$ (triangles) versus T_{eff} , compared to the spectropolarimetric measurements (circles) of Bagnulo and Landstreet (2022). Concentric circles have the same meaning as in Figure 7.1. We explicitly label WDs whose leaf diagrams are shown in Figures 7.5, 7.6, and 7.8.

the forbidden region at some period P , that magnetic field strength suppresses a g mode of period P . The boundary of the forbidden region is demarcated by v_B^ℓ evaluated at $B_{r,\text{crit}}$. The *vertical gray lines* show the estimated central components of the multiplets, including those too incomplete for an asymmetry measurement. The suppression constraint $B_{r,\text{supp}}$ (the *dotted red stripe*) can be read off the diagram by finding the weakest-field v_B^ℓ contour which intersects with all *vertical gray lines* before entering the forbidden region.

As defined in Equation 7.4, v_B^ℓ is strictly non-negative. Negative values of v_B^ℓ on the leaf diagram represent those where the sign of the measured asymmetry differs from the assumed sign of $a_{m_1 m_2 m_3}^\ell$ (given for this work in Appendix 7.A.3). For example, Li, Deheuvels, Ballot, and Lignières (2022) show that $a_{-10+1}^{\ell=1}$ can take a range of values from $-1/2$ to 1, depending on the horizontal structure of the magnetic field. A negative value thus indicates an incorrect assumption about the magnetic field geometry, or a non-magnetic origin for the asymmetry altogether. However, as $a_{m_1 m_2 m_3}^\ell$ is an order-unity constant, incorrect assumptions about its value only affect $B_{r,\text{shift}}$ by order-unity factors.

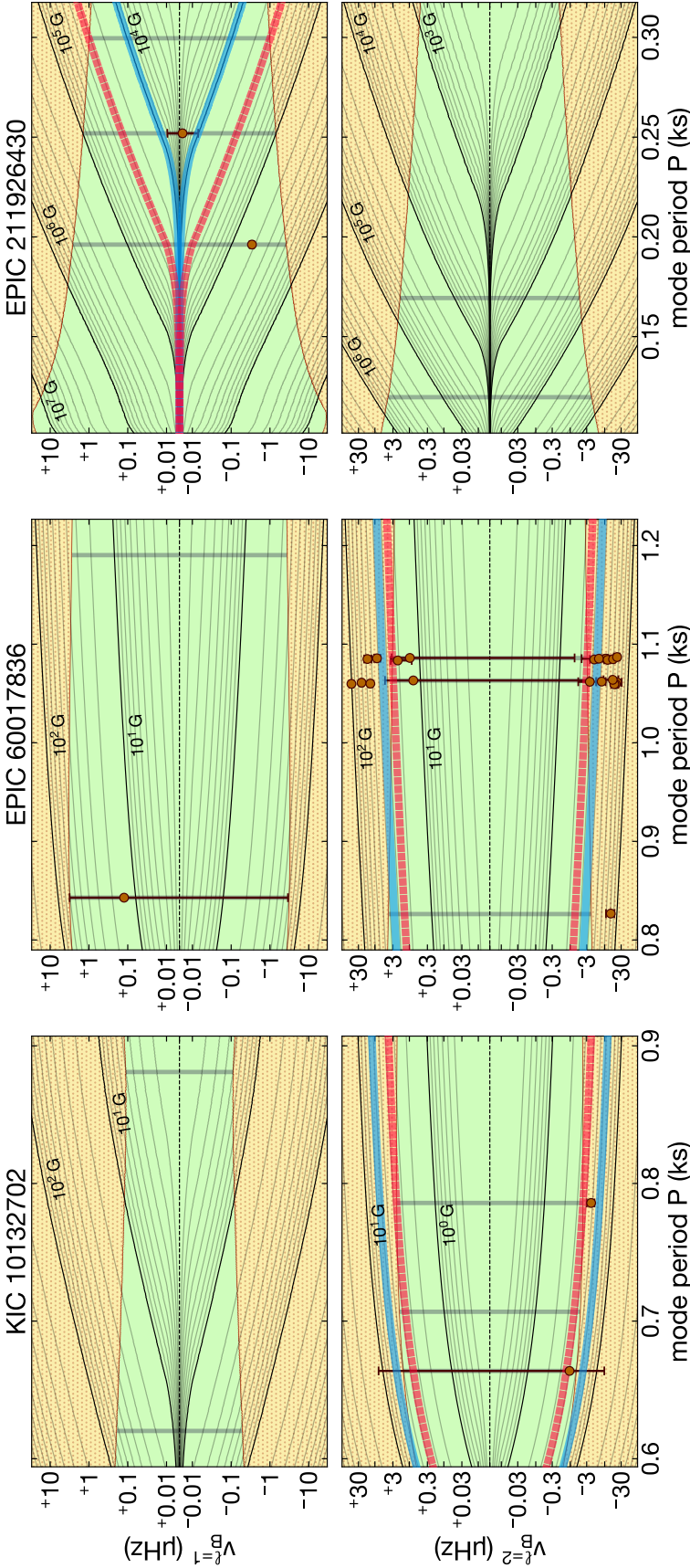


Figure 7.5: Leaf diagrams of three DAV WDs from Hermes, Kawaler, et al. (2017). Brown circles show measured asymmetry values, with error bars enclosing the 2σ confidence interval set by frequency measurement uncertainties. Gray vertical lines indicate an estimate for the central frequency of a multiplet. Contours indicate the degree of asymmetry implied by a given magnetic field. The yellow dotted region indicates the forbidden region within which magnetic mode suppression is expected. The blue solid contour indicates $B_{r,\text{shift}}$: this is the lowest-field strength contour that fully encloses a single brown circle, including its error bar. The red dashed contour indicates $B_{r,\text{supp}}$: this denotes the lowest-field strength contour that crosses all gray vertical lines outside of the yellow dotted region.

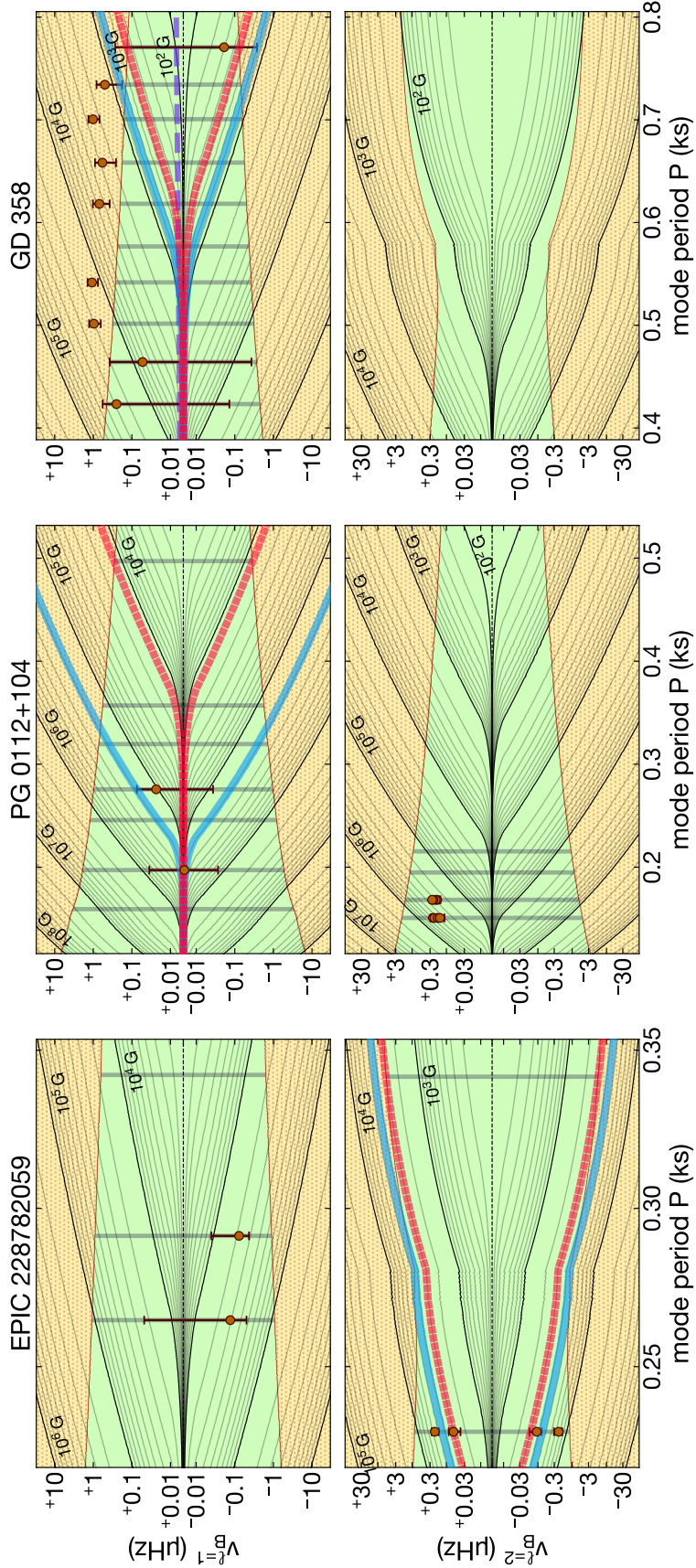


Figure 7.6: Same as Figure 7.6, but for the DBV WDs EPIC 228782059 (Duan et al., 2021), PG 0112+104 (Hermes, Kawaler, et al., 2017), and GD 358 (Winget, Nather, et al., 1994). The *dashed purple curve* shows the predicted dipole asymmetry from second-order rotational effects.

7.4.2 Carbon–oxygen white dwarfs

As Figure 7.1 shows, both the DAV and DBV WD instability strips lie blueward of both the concentration of magnetic WDs ~ 6 kK and the onset of carbon–oxygen crystallization for near-canonical masses $\simeq 0.6M_{\odot}$. Pulsating WDs may thus represent present-day magnetic WDs when they were younger and hotter. It takes > 2 Gyr for both our $0.64M_{\odot}$ DA and DB models to cool from the DAV and DBV instability strips to 6 kK.

Our sample of DAV WDs is taken from the *K2* catalog of Hermes, Gänsicke, Kawaler, et al. (2017). Whenever possible, we use mode periods and uncertainties given by their nonlinear least-squares method. However, they also find that some (usually low-period; $P \gtrsim 800$ s) modes have power spectral linewidths which are significantly broader than implied by the spectral window, consistent with a lack of phase stability (see also Winget, Nather, et al., 1994; Bischoff-Kim et al., 2019; Montgomery, Hermes, et al., 2020). In these cases, they fit a Lorentzian to the power spectral peak. When the nonlinear least-squares uncertainties are not reported, we adopt the uncertainties on the mode period derived from this Lorentzian fit.

To be conservative, we have excluded uncertain or unknown identifications of ℓ for calculating $B_{r,\text{supp}}$, as well as either ℓ or m for $B_{r,\text{shift}}$. We have also excluded all modes which are labeled as combination frequencies. This leaves 20 DAVs for which we place upper bounds on the magnetic field. These upper bounds are usually in the range 1–10 kG, but sometimes are as low as a few gauss for DAVs within which long-period modes are excited. We show leaf diagrams for three selected DAVs in Figure 7.5.

Additionally, we select 3 DBVs which span the temperature range of the DBV instability strip. Using mode frequencies reported by Duan et al. (2021), we place an upper bound $B_{r,\text{shift}} \sim 3$ kG for the “cool” ($T_{\text{eff}} \approx 22$ kK) WD EPIC 228782059. We similarly place an upper bound $B_{r,\text{shift}} \sim 10$ kG for the “hot” ($T_{\text{eff}} \approx 31$ kK; Dufour, Desharnais, et al., 2010) DBV PG 0112+104, consistent with the bound placed by Hermes, Kawaler, et al. (2017). The leaf diagrams of these WDs are shown in Figure 7.6.

As a further consistency check, we revisit GD 358, finding an asymmetry-based bound $B_{r,\text{shift}} \sim 800$ G set by the lowest-frequency triplet (similar to their inferred value ≈ 1.3 kG), as well as a formally slightly stronger suppression-based bound $B_{r,\text{supp}} \sim 500$ G. Curiously, subsequent observations of GD 358 have observed time variation in both the amplitudes and *frequencies* of the oscillation modes (e.g., Bischoff-Kim et al., 2019). The wandering of the frequencies takes place on timescales much longer than an observing season (roughly several months; Provencal et al., 2009), and the frequencies vary by much more than the measured asymmetries of ~ 1 μ Hz shown in Figure 7.6. Both time-varying dynamo magnetic fields

(Markiel et al., 1994) and convective zone thicknesses (Montgomery, Provencal, et al., 2010; Montgomery, Hermes, et al., 2020) have been proposed for this phenomenon, although a definitive explanation remains elusive.

Curiously, most of GD 358’s asymmetries in Figure 7.6 lie in the magnetically forbidden region. The degree of asymmetry is too large to be explained by second-order rotational effects (Dziembowski and Goode, 1992), which predict $\Delta_{-10+1}^{\ell=1} = P/20P_{\text{rot}}^2 \lesssim 10^{-2} \mu\text{Hz}$ (the *dashed purple curve* in Figure 7.5), much lower than the observed values $\Delta_{-10+1}^{\ell=1} \sim 0.5 \mu\text{Hz}$. If the asymmetries are magnetic in origin, ν_B^ℓ must be overestimated by a factor of $\gtrsim 6$. It is plausible that order-unity uncertainties in Equation 7.1 (for $B_{r,\text{crit}}$) and $a_{-10+1}^{\ell=1}$ may account for this. However, the measured asymmetries require very different field strengths for different radial orders. This suggests either that the magnetic field falls off quickly in the outer layers or that the asymmetries have a non-magnetic origin. In the latter case, the asymmetries may instead originate from GD 358’s drifting mode frequencies. This frequency wandering does not keep the asymmetry constant over time (cf. Figure 9 of Bischoff-Kim et al., 2019). Notably, after the *sforzando* event of August 1996 during which the $k = 8$ and $k = 9$ modes briefly dominated the light curve, the asymmetries of the $k = 8$ and $k = 9$ triplets were permanently modified (Provencal et al., 2009; Montgomery, Provencal, et al., 2010). We therefore suspect that the measured asymmetries result from wandering mode frequencies rather than magnetic shifts.

Curiously, Montgomery, Provencal, et al. (2010) show that the $k = 12$ triplet in GD 358 exhibits signatures of oblique pulsation, which occurs when the Lorentz force exceeds the Coriolis force in strength and misaligns the pulsations from the rotation axis (the $k = 12$ triplet was not observed by the Whole Earth Telescope May 1990 run data examined in this work; Winget, Nather, et al., 1994). In the case of oblique pulsation, the magnetic field still shifts mode frequencies by $\sim \nu_B^\ell$. However, contrary to the prediction in Section 7.2.1 (which assumes rotationally aligned pulsations), the magnetic field does not simply produce an asymmetric rotational multiplet from the perspective of an inertial observer. Instead, each mode manifests as multiple peaks in the power spectrum (Loi, 2021). In this case, the asymmetry-based upper bounds $B_{r,\text{shift}}$ in this work and Winget, Nather, et al. (1994) should be replaced by a more elaborate fit to an oblique pulsator model. The parameters extracted by Montgomery, Provencal, et al. (2010) in this way are consistent with a magnetic field strength $B_r \sim 40 \text{ kG} \sim 10B_{r,\text{crit}}$, placing their result at tension with our assumptions regarding the fundamental g-mode suppression physics (Section 7.2.2).

Bagnulo and Landstreet (2022) conduct a volume-limited spectropolarimetric survey of nearby WDs, finding a dearth of magnetic fields in young ($\lesssim 2 \text{ Gyr}$), canonical-mass WDs

down to their detection limit (a few kilogauss). These spectropolarimetric measurements are shown in Figure 7.4. The low ($\lesssim 10$ kG) magnetic field limits we place on most of our carbon–oxygen WDs are consistent with this finding. In many cases, our seismic limits appear to be much more constraining, entailing magnetic fields less than ~ 100 G in several WDs with long-period pulsation modes.

In addition to placing upper limits on magnetism in individual WDs, the observation of (non-suppressed) pulsations can constrain the distribution of magnetic fields in the WD population as a whole. If the DAVs included in this work are representative, the high purity of the instability strip (e.g., Gianninas, Bergeron, et al., 2005) suggests that most DA WDs at instability-strip temperatures lack magnetic fields $\gtrsim 10$ kG.

7.4.3 ELMVs: probing the stripped cores of red giants?

Unlike carbon–oxygen WDs, helium-core WDs are exclusively produced by binary stellar evolution. These low-mass ($M \lesssim 0.5M_{\odot}$) WDs are the leftover cores of red giants whose envelopes have been stripped by a companion or ejected during a common-envelope event. To date, roughly 20 helium-core WDs are known to pulsate (Hermes, Montgomery, Winget, Brown, Kilic, et al., 2012; Hermes, Montgomery, Winget, Brown, Gianninas, et al., 2013; Hermes, Montgomery, Gianninas, et al., 2013; Kilic, Hermes, Gianninas, et al., 2015; Gianninas, Curd, et al., 2016; Bell, Gianninas, et al., 2017; Bell, Pelisoli, et al., 2018; Kilic, Hermes, Corsico, et al., 2018; Pelisoli, Kepler, et al., 2018; Pelisoli, Bell, et al., 2019; Wang, Zhang, et al., 2020). These “extremely low-mass variables,” or ELMVs, are all located on a low-log g extension of the DAV instability strip (Gianninas, Kilic, et al., 2015; Tremblay, Gianninas, et al., 2015). As the direct descendants of the same red giants for which seismic magnetometry is already possible, helium-core WDs likely inherit the field strengths of the cores of their progenitors. Figure 7.7 shows the magnetic fields to which helium-core WD pulsators are sensitive.

We place an upper bound on GD 278, a low-mass ($M \approx 0.19M_{\odot}$) WD which pulsates in low-frequency gravity modes ($P \simeq 2400$ –6700 s; Lopez et al., 2021). To date, GD 278 is the only known ELMV for which rotational splittings have been measured. Assuming the mode identifications determined by Calcaferro et al. (2023), we find that the magnetic field in GD 278 is no larger than $B_{r,\text{supp}} \sim 70$ G (Figure 7.8). This field is much lower than those inferred for dipole-suppressed red giants ($\approx 20\%$ of all red giants; Stello, Cantiello, Fuller, Huber, et al., 2016), and smaller than the field expected to be generated by a core convective dynamo on the main sequence (Cantiello et al., 2016).

GD 278's asymmetries are often close to or within the forbidden region, i.e., within the *yellow dotted region* in Figure 7.8). As discussed for GD 358, a magnetic origin for these asymmetries may still be possible if some order-unity prefactors are misestimated. The relatively fast rotation period $P_{\text{rot}} \approx 10$ hr (Lopez et al., 2021) corresponds to $P/P_{\text{rot}} \sim 10\%$ for the observed modes, suggesting that second-order rotational effects may play a role (shown as the *dashed purple curves* in Figure 7.8). Second-order rotational effects are expected to produce asymmetries $\Delta_{-10+1}^{\ell=1} = P/20P_{\text{rot}}^2 \simeq 0.2 \mu\text{Hz}$ in the two complete observed triplets at $P \approx 4030$ s and $P \approx 4760$ s (Dziembowski and Goode, 1992). The observed asymmetries ($\Delta_{-10+1}^{\ell=1} = (0.44 \pm 0.06) \mu\text{Hz}$ and $\Delta_{-10+1}^{\ell=1} = (0.07 \pm 0.07) \mu\text{Hz}$, respectively) are similar in scale to (though at significant tension with) those predicted by second-order rotational effects. Further, we find that observed asymmetries do not consistently match second-order rotational asymmetries in sign. We also curiously find that observed quadrupole asymmetries are often lower than the expected second-order asymmetries by factors $\sim 3\text{--}10$ relative to predicted values (Dziembowski and Goode, 1992). The ultimate origin of asymmetries in GD 278 are puzzling.

It is possible that GD 278's progenitor was a lower-mass ($M \lesssim 1.2M_{\odot}$) main-sequence star below the Kraft break. Such stars have radiative cores, and are thus not expected to generate strong fields during the main sequence. If this is the case, it suggests that, in the absence of a convective core, the core field of a main-sequence star can be extremely low. In a $1M_{\odot}$ MESA model, mass coordinates $\leq 0.19M_{\odot}$ are enclosed by a radius $R \approx 0.1R_{\odot}$ during the main-sequence. This decreases to $\approx 0.025R_{\odot}$ during the red giant branch, once the helium core has grown to $\approx 0.19R_{\odot}$. Assuming flux conservation, this implies that the core magnetic field of GD 278's progenitor was no larger than $\simeq 4$ G on the main sequence. Alternatively, our upper bound may challenge the assumption of magnetic flux conservation between evolutionary stages.

At a time of rapid progress in red giant magnetoasteroseismology, ELMVs may help test our understanding of magnetism in stellar cores as well as the essential pulsation physics itself. Since the near-surface WD fields to which seismology is sensitive can also be probed by spectroscopy or spectropolarimetry, comparison between the field strengths inferred by these techniques and seismology may serve as a valuable consistency check. While thorough spectroscopic surveys of ELMs have been conducted (e.g., Brown, Kilic, Prieto, et al., 2010; Brown, Kilic, Prieto, et al., 2011; Brown, Kilic, Kosakowski, et al., 2020; Wang, Németh, et al., 2022; Kosakowski et al., 2023), we are not presently aware of any detections of Zeeman splitting in low-mass WDs (although Pichardo Marcano, Rivera Sandoval, et al. 2023 and Pichardo Marcano, Sandoval, et al. 2025 report photometric variability in two

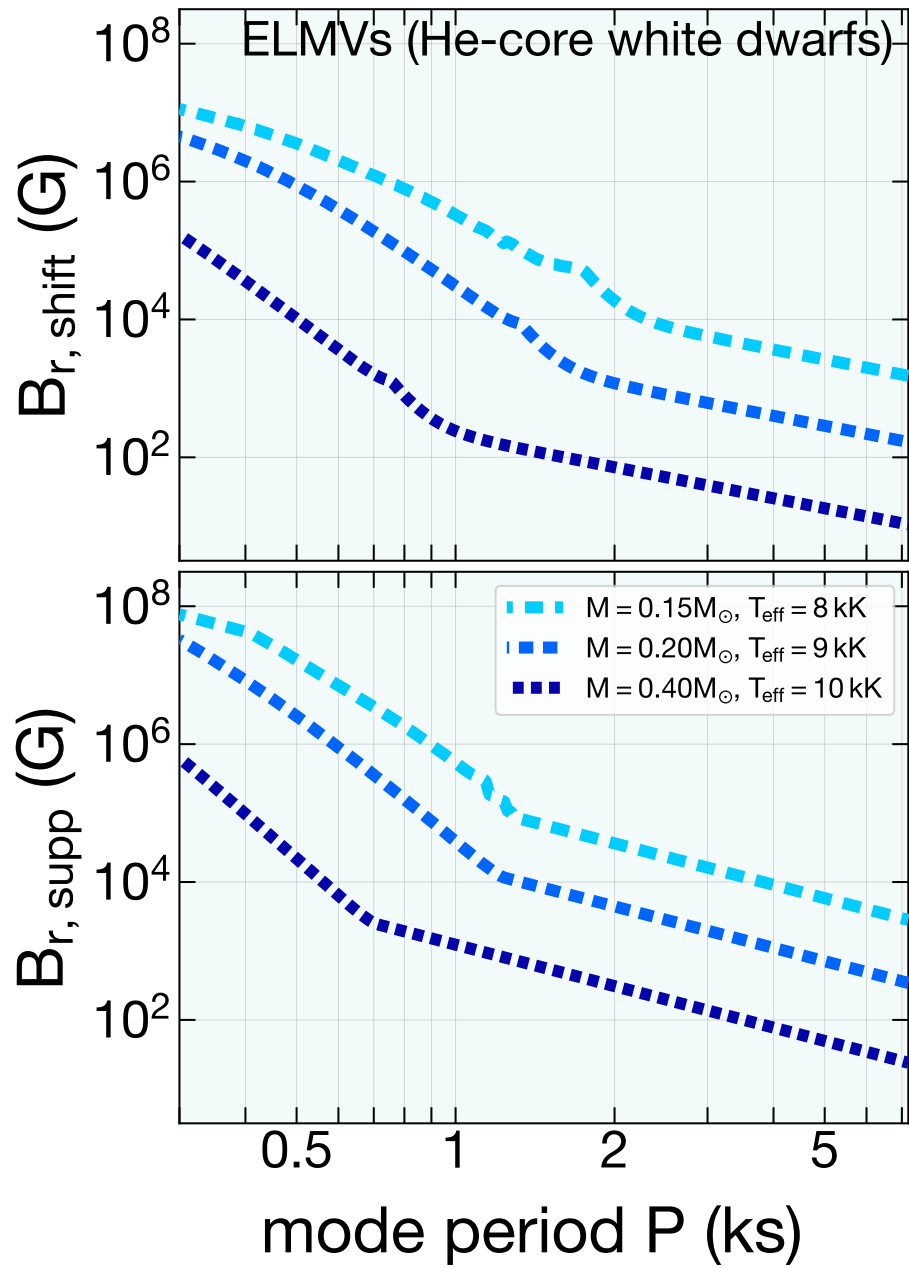


Figure 7.7: Model seismic magnetic field sensitivities $B_{r,\text{shift}}$ and $B_{r,\text{supp}}$ for $0.15M_{\odot}$, $0.20M_{\odot}$, and $0.40M_{\odot}$ helium-core WD pulsators on the DAV instability strip. These curves have been calculated for $\ell = 1$ and $v_B^{\ell=1} = 0.1 \mu\text{Hz}$.

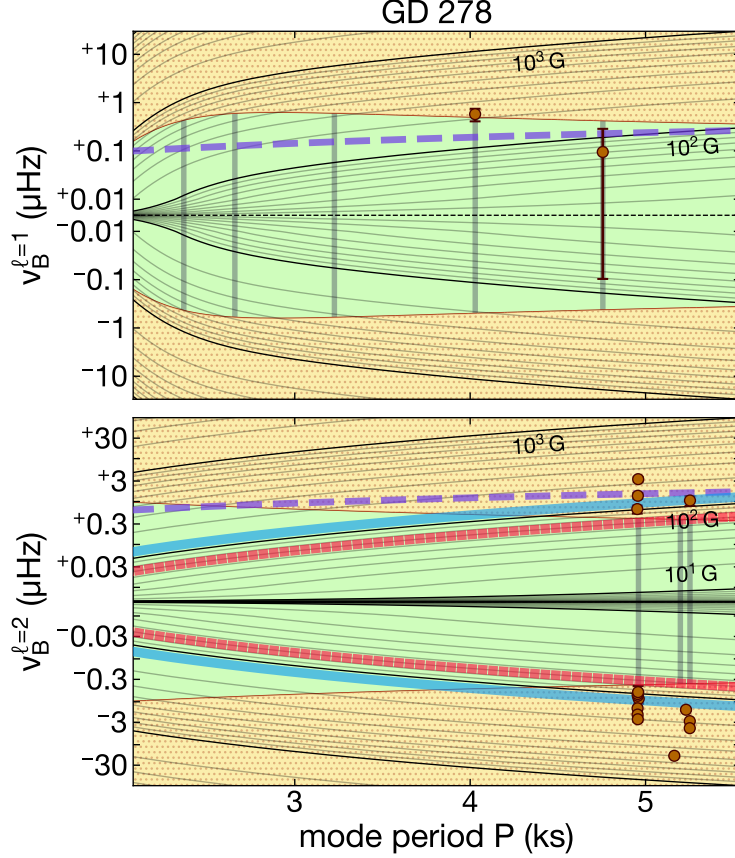


Figure 7.8: Same as Figure 7.5, but for the ELMV GD 278 (Lopez et al., 2021; Calcaferro et al., 2023). The *dashed purple curves* show the predicted asymmetries from second-order rotational effects on the dipole asymmetry $\Delta_{-10+1}^{\ell=2}$ and a typical quadrupole asymmetry $\Delta_{-10+2}^{\ell=2}$.

candidate ELM WDs in the globular cluster NGC 6397 that might arise from magnetic spots).

7.4.4 Caveats

The behavior of high-frequency pulsations under magnetic fields should be investigated in more detail. While we make a rudimentary correction for some non-asymptotic effects in this work, our correction leaves out some additional effects. Non-asymptotic modes may produce significant displacements in evanescent regions, which are ignored by our integral estimate for \mathcal{J} in Equation 7.5. Further, as described in Appendix 7.B, our results correct for non-asymptotic eigenfunctions in the calculation of \mathcal{J} . However, the derivation of Equation 7.4 (which writes v_B^ℓ in terms of \mathcal{J}) still assumes certain terms scaling as $\sim 2\pi\nu/N$ are negligible, including effects of the horizontal field components and the radial

displacement in the calculation of the mode inertia. Our estimates of magnetic effects also assume the mode wavelength is smaller than the scale height H on which quantities such as ρ and B change. For the long-period modes shown in Figure 7.2, the mode wavelengths are comparable to H just below the convective zone, making magnetic effects on modes more difficult to calculate. The effect of relaxing these assumptions should be investigated in more detail.

Our analysis also required basic assumptions about the dimensionless asymmetry parameters $a_{m_1 m_2 m_3}^\ell$, as well as the prefactor which appears in Equation 7.1 for $B_{r,\text{crit}}$. Both of these are order-unity functions of the field geometry (Lecoanet, Vasil, et al., 2017; Rui and Fuller, 2023; Lecoanet, Bowman, et al., 2022) and the rotation rate, if it is high enough (Rui, Ong, et al., 2024). This introduces an uncertain order-unity factor to our field estimates (e.g., Das et al., 2024). However, dipole/quadrupole asymmetries may fail more catastrophically when faced with, e.g., small-scale magnetic structures that cannot be resolved by $\ell = 1$ or $\ell = 2$ modes well enough to produce significant rotational multiplet asymmetries.

We also assume that the frequencies of each multiplet component have not been affected by nonlinear resonant mode coupling. However, WD pulsation modes occasionally show large, nonsecular frequency changes (e.g., Hermes, Montgomery, Mullally, et al., 2013; Dalessio et al., 2013). In fact, some multiplet components within a pulsating WD have shown correlated, periodic frequency changes, a signature of resonant mode coupling (Zong et al., 2016). Such frequency changes could produce non-magnetic multiplet asymmetries.

Finally, this work stitches together a perturbative theory in $(B_r/B_{r,\text{crit}})^2$ for $B_r < B_{r,\text{crit}}$ with the assumption of total suppression when $B_r > B_{r,\text{crit}}$. In reality, perturbation theory is no longer valid once B_r is a large fraction of $B_{r,\text{crit}}$. Rui, Ong, et al. (2024) show, for example, that the inappropriate application of perturbation theory overestimates the field strength in the case of a centered dipolar field aligned with the rotation axis. Along similar lines, strong-enough fields in slow-enough rotators are expected to align pulsations with the magnetic axis, dramatically increasing the complexity of a rotational multiplet in the power spectrum. These strong magnetic effects should be more thoroughly investigated.

7.5 Summary and future directions

We summarize our conclusions in this work as follows:

1. WD pulsations can be used as a highly sensitive probe of the radial components of their near-surface magnetic fields. Magnetic fields are expected to asymmetrize

rotational multiplets at intermediate field strengths $B_r \lesssim B_{r,\text{crit}}$ and suppress g-mode propagation when $B_r > B_{r,\text{crit}}$.

2. Seismology is most sensitive to magnetic fields in pulsating WDs with lower-frequency modes and thinner surface convection zones.
3. We place upper limits on the magnetic field in 20 DAV and 3 DBV carbon–oxygen WDs. Most upper limits in carbon–oxygen WDs lie within roughly $\sim 1\text{--}10\text{ kG}$, but they can be as low as *a few to tens of gauss* when low-frequency modes ($\gtrsim 800\text{ s}$) are not observed to be suppressed. Seismology may help uncover the as-of-yet unknown formation mechanism of strong magnetic fields in WDs at low effective temperatures.
4. We also place an upper limit on the near-surface magnetic field $\simeq 70\text{ G}$ in the ELMV GD 278 (helium-core) WD. As stripped red giants, ELMVs may present a valuable opportunity to test our understanding of red giant magnetism as well as the fundamental pulsation physics.

Following results from red giant asteroseismology, this work assumes that strong magnetic fields $B_r > B_{r,\text{crit}}$ strongly suppress gravity waves (Fuller, Cantiello, et al., 2015; Stello, Cantiello, Fuller, Huber, et al., 2016; Cantiello et al., 2016). However, despite some informative theoretical work (Lecoanet, Vasil, et al., 2017; Loi and Papaloizou, 2017; Loi and Papaloizou, 2018; Loi, 2020b; Lecoanet, Bowman, et al., 2022; Rui and Fuller, 2023), some details of the damping mechanism are not fully understood. If pulsations can instead persist in the presence of a strong magnetic field, our suppression-based upper bounds on the field strength $B_{r,\text{supp}}$ no longer apply, although our asymmetry-based upper bounds $B_{r,\text{shift}}$ (which are grounded on more certain physics and are typically of similar order) are still valid.

Although definitive evidence of magnetic g-mode suppression remains largely elusive, the massive WD SDSS J1529+2928 may be an example of magnetic g-mode suppression acting in a white dwarf. Despite lying within the DAV instability strip, SDSS J1529 has not been observed to pulsate. Furthermore, although spectroscopy excludes a magnetic field $\gtrsim 70\text{ kG}$, SDSS J1529 exhibits variability consistent with a magnetic spot (Kilic, Gianninas, et al., 2015). SDSS J1529 may therefore be an illustrative example of magnetic suppression of oscillations, either by damping the gravity waves magnetically (the mechanism invoked in this work) or by obstructing the convection involved in driving the pulsations (not considered in this work, although see, e.g., Tremblay, Fontaine, et al., 2015).

Seismic WD magnetometry affords many further possibilities. Pulsating WDs are a highly diverse class which also include pre-WDs (GW Virs/DOVs/PNNVs, e.g., Winget, Hansen, et al., 1991; Sowicka et al., 2023), pre-ELMVs (e.g., Maxted, Serenelli, et al., 2013), and pulsating accretors in cataclysmic variables (GW Lib, e.g., Van Zyl et al., 2004). Additionally, several pulsating ultramassive ($M \gtrsim 1.1M_{\odot}$) DAV WDs are known (Hermes, Kepler, et al., 2013; Curd et al., 2017; Kanaan et al., 2005; Rowan et al., 2019; Vincent et al., 2020; Kilic, Córscico, et al., 2023) which, unlike the WDs considered in this work, have already begun to crystallize on the DAV instability strip. This is expected to affect their pulsations (Kanaan et al., 2005; Nitta et al., 2015; De Gerónimo et al., 2019), possibly allowing them to help uncover the relationship between their crystallization and magnetization. Finally, some hot subdwarfs are known to pulsate in gravity modes (Pablo et al., 2012; Telting, Östensen, et al., 2014; Baran, Telting, Németh, et al., 2016; Baran, Telting, Jeffery, et al., 2019; Silvotti, Uzundag, et al., 2019; Sanjayan et al., 2022; Silvotti, Németh, et al., 2022; Ma, Zong, et al., 2023), which are likely sensitive to their near-core fields. Seismology may contribute to the solution of an open problem regarding the dearth of observed magnetic fields in hot subdwarfs (Dorsch, Reindl, et al., 2022; Pelisoli, Dorsch, et al., 2022; Pakmor et al., 2024; Dorsch, Jeffery, et al., 2024).

7.A Magnetic formalism

The asymmetry-based magnetic field bounds placed in this work require concrete assumptions about the asymmetry parameters $a_{m_1 m_2 m_3}^{\ell}$. This Appendix derives the dipole and quadrupole asymmetry parameters assumed in this study.

7.A.1 Magnetic frequency shifts of g-mode pulsations

In the most common formalism (Bugnet et al., 2021; Li, Deheuvels, Ballot, and Lignières, 2022; Das et al., 2024), the Coriolis and Lorentz forces are assumed to be weak and degenerate perturbation theory is applied. The incompressible and asymptotic approximations (appropriate for high-radial order g modes) are additionally assumed. Furthermore, it is assumed either that the magnetic field is axisymmetric about the rotation axis or that the effect of the Coriolis force on the waves is much stronger than that of the Lorentz force. In both cases, the eigenfunctions are aligned with the rotation axis, and the frequency shifts are only sensitive to azimuthal averages of B_r^2 , i.e.,

$$\langle B_r^2 \rangle_{\phi} = \int_0^{2\pi} \frac{d\phi}{2\pi} B_r^2, \quad (7.14)$$

although the field's dependence on the colatitude $\mu = \cos \theta$ still matters.

In the inertial frame, the frequency shifts $\delta\nu$ of the dipole modes are given by Equations 32 and 33 of Li, Deheuvels, Ballot, and Lignières (2022):

$$\delta\nu_{m=0}^{\ell=1} = \mathcal{B}^{\ell=1} \left[\frac{3}{2}(1 - \mu^2) \right] \quad (7.15a)$$

$$\delta\nu_{m=\pm 1}^{\ell=1} = \pm \frac{1}{2} \frac{\langle \Omega \rangle_g}{2\pi} + \mathcal{B}^{\ell=1} \left[\frac{3}{4}(1 + \mu^2) \right], \quad (7.15b)$$

and the same for the quadrupole modes are given by Appendix C.1 of Das et al. (2024):

$$\delta\nu_{m=0}^{\ell=2} = \mathcal{B}^{\ell=2} \left[\frac{15}{2}(\mu^2 - \mu^4) \right] \quad (7.16a)$$

$$\delta\nu_{m=\pm 1}^{\ell=2} = \pm \frac{5}{6} \frac{\langle \Omega \rangle_g}{2\pi} + \mathcal{B}^{\ell=2} \left[\frac{5}{4}(1 - 3\mu^2 + 4\mu^4) \right] \quad (7.16b)$$

$$\delta\nu_{m=\pm 2}^{\ell=2} = \pm \frac{5}{3} \frac{\langle \Omega \rangle_g}{2\pi} + \mathcal{B}^{\ell=2} \left[\frac{5}{4}(1 - \mu^4) \right], \quad (7.16c)$$

where the relevant integral average operation $\mathcal{B}^{\ell}[\cdot]$ is given under the present assumptions by

$$\mathcal{B}^{\ell}[f(\mu)] \approx \nu_B^{\ell} \int_{\mathcal{R}_v^{\ell}} dr K(r) \int_{S^2} \frac{d\Omega}{4\pi} B_r^2 f(\mu). \quad (7.17)$$

If the Lorentz force is instead comparable to or stronger than the Coriolis force, the frequency shifts it causes are still at the same order of magnitude as ν_B^{ℓ} (as in Equation 7.4), although the dimensionless prefactors are given by the solution of a more complicated matrix problem, and multiplets generally possess more than $2\ell + 1$ peaks in the inertial frame (see the discussion in the Supplementary Information of Li, Deheuvels, Ballot, and Lignières 2022). This does not seem to be the case in any of the WDs we analyze, since all of their (possibly incomplete) rotational multiplets are broadly recognizable and lack significant extra frequency peaks.

7.A.2 Multiplet asymmetries due to magnetism

When $K(r)$ is sharply peaked and the magnetic frequency shifts are only sensitive to a geometrically thin radial shell (which is often true, especially in the WD case), the radial integral in Equation 7.17 becomes independent of the angular one, and we can speak of a single horizontal dependence of B_r . In other words, we can approximately take

$$B_r(r, \mu, \phi) = A(r) \psi(\mu, \phi), \quad (7.18)$$

where we normalize the horizontal dependence of B_r to $\psi = \psi(\mu, \phi)$ such that $\int_{S^2} \psi^2 \sin \theta d\theta d\phi = 1$. We define the azimuthal average $\langle \psi^2 \rangle_\phi$ as

$$\langle \psi^2 \rangle_\phi \equiv \int_0^{2\pi} \frac{d\phi}{2\pi} \psi^2. \quad (7.19)$$

Under this condition, Li, Deheuvels, Ballot, and Lignières (2022) show that the dipole asymmetry parameter is given by

$$a_{-10+1}^{\ell=1} = \int_{-1}^{+1} \langle \psi^2 \rangle_\phi \frac{1}{2} (3\mu^2 - 1) d\mu, \quad (7.20)$$

and encodes some information about the geometry of the field.

We generalize the parameter $a_{-10+1}^{\ell=1}$ to describe the asymmetry between any three modes within the same multiplet, including those involving higher-degree ($\ell > 1$) modes such as quadrupole modes ($\ell = 2$). We start by noticing that the linear combination of frequencies in Equation 7.9 is useful because it depends on neither the unperturbed frequencies $\nu^{(0)}$ (which are the same for all modes within a multiplet) nor the rotational splitting (which is proportional to m). In other words, for three modes with equal k and ℓ but distinct azimuthal orders m_1 , m_2 , and m_3 , maximally “useful” linear combinations $\Delta_{m_1 m_2 m_3}^\ell$ of measured frequencies of the form

$$\Delta_{m_1 m_2 m_3}^\ell = c_1 \nu_{m_1}^\ell + c_2 \nu_{m_2}^\ell + c_3 \nu_{m_3}^\ell. \quad (7.21)$$

should satisfy $c_1 + c_2 + c_3 = 0$ and $m_1 c_1 + m_2 c_2 + m_3 c_3 = 0$ to cancel out $\nu^{(0)}$ and $\langle \Omega \rangle_g$, respectively.

For concreteness, for the quadrupole modes, we choose the coefficients c_1 , c_2 , and c_3 to be small integers. There are ${}_{2\ell+1}C_3 = 10$ distinct useful linear combinations:

$$\Delta_{-2-10}^{\ell=2} = \nu_{m=-2}^{\ell=2} - 2 \nu_{m=-1}^{\ell=2} + \nu_{m=0}^{\ell=2} \quad (7.22a)$$

$$\Delta_{-2-1+1}^{\ell=2} = 2 \nu_{m=-2}^{\ell=2} - 3 \nu_{m=-1}^{\ell=2} + \nu_{m=+1}^{\ell=2} \quad (7.22b)$$

$$\Delta_{-2-1+2}^{\ell=2} = 3 \nu_{m=-2}^{\ell=2} - 4 \nu_{m=-1}^{\ell=2} + \nu_{m=+2}^{\ell=2} \quad (7.22c)$$

$$\Delta_{-20+1}^{\ell=2} = \nu_{m=-2}^{\ell=2} - 3 \nu_{m=0}^{\ell=2} + 2 \nu_{m=+1}^{\ell=2} \quad (7.22d)$$

$$\Delta_{-20+2}^{\ell=2} = \nu_{m=-2}^{\ell=2} - 2 \nu_{m=0}^{\ell=2} + \nu_{m=+2}^{\ell=2} \quad (7.22e)$$

$$\Delta_{-2+1+2}^{\ell=2} = \nu_{m=-2}^{\ell=2} - 4 \nu_{m=+1}^{\ell=2} + 3 \nu_{m=+2}^{\ell=2} \quad (7.22f)$$

$$\Delta_{-10+1}^{\ell=2} = \nu_{m=-1}^{\ell=2} - 2 \nu_{m=0}^{\ell=2} + \nu_{m=+1}^{\ell=2} \quad (7.22g)$$

$$\Delta_{-10+2}^{\ell=2} = 2 \nu_{m=-1}^{\ell=2} - 3 \nu_{m=0}^{\ell=2} + \nu_{m=+2}^{\ell=2} \quad (7.22h)$$

$$\Delta_{-1+1+2}^{\ell=2} = \nu_{m=-1}^{\ell=2} - 3 \nu_{m=+1}^{\ell=2} + 2 \nu_{m=+2}^{\ell=2} \quad (7.22i)$$

$$\Delta_{0+1+2}^{\ell=2} = \nu_{m=0}^{\ell=2} - 2 \nu_{m=+1}^{\ell=2} + \nu_{m=+2}^{\ell=2}. \quad (7.22j)$$

Although only $2\ell - 1 = 3$ of these contain independent information, observed multiplets are often incomplete, restricting which of these 10 asymmetry parameters can be calculated. In general, whether a given mode is observable depends on the excitation mechanism as well as viewing angle (see Gizon and Solanki 2003 and Das et al. 2024 for further discussion). WD modes are also not generally in energy equipartition, and even modes within the same multiplet can be excited to very different amplitudes (Hermes, Gänsicke, Bischoff-Kim, et al., 2015).

Following the normalization convention of Li, Deheuvels, Ballot, and Lignières (2022) and Das et al. (2024), these linear combinations are related to dimensionless asymmetry parameters $a_{m_1 m_2 m_3}^\ell$ using Equations 7.8 and 7.10. Using Equation 7.19, we rewrite the operator $\mathcal{B}^\ell[\cdot]$ as

$$\mathcal{B}^\ell[f(\mu)] \approx \nu_B^\ell \int_{-1}^{+1} \langle \psi^2 \rangle_\phi f(\mu) d\mu. \quad (7.23)$$

Equations 7.16 for the quadrupole frequency shifts then imply that

$$\begin{aligned} a_{-2-10}^{\ell=2} &= a_{0+1+2}^{\ell=2} \\ &= \int_{-1}^{+1} \langle \psi^2 \rangle_\phi \frac{1}{4} (-15\mu^4 + 12\mu^2 - 1) d\mu \end{aligned} \quad (7.24a)$$

$$\begin{aligned} a_{-2-1+1}^{\ell=2} &= a_{-2-1+2}^{\ell=2} = a_{-2+1+2}^{\ell=2} = a_{-1+1+2}^{\ell=2} \\ &= \int_{-1}^{+1} \langle \psi^2 \rangle_\phi \frac{1}{2} (-5\mu^4 + 3\mu^2) d\mu \end{aligned} \quad (7.24b)$$

$$\begin{aligned} a_{-20+1}^{\ell=2} &= a_{-10+2}^{\ell=2} \\ &= \int_{-1}^{+1} \langle \psi^2 \rangle_\phi \frac{1}{4} (25\mu^4 - 24\mu^2 + 3) d\mu \end{aligned} \quad (7.24c)$$

$$a_{-20+2}^{\ell=2} = \int_{-1}^{+1} \langle \psi^2 \rangle_\phi \frac{1}{2} (5\mu^4 - 6\mu^2 + 1) d\mu \quad (7.24d)$$

$$a_{-10+1}^{\ell=2} = \int_{-1}^{+1} \langle \psi^2 \rangle_\phi \frac{1}{2} (10\mu^4 - 9\mu^2 + 1) d\mu. \quad (7.24e)$$

Curiously, five groups of dimensionless asymmetry parameters in Equations 7.24 are constrained to be equal. This is not a field geometry-dependent fact, but rather a result of the assumption that rotation fixes the preferred direction respected by the modes. It is also distinct from the linear dependence of the linear combinations of frequencies in Equations 7.22, although they are self-consistent. For example, Equations 7.22 and 7.10 easily show that $\Delta_{-10+1}^{\ell=2} + 2\Delta_{0+1+2}^{\ell=2} = \Delta_{-1+1+2}^{\ell=2}$, a relationship which is obeyed by the expressions in Equations 7.24.

On the one hand, this implies that not all of the modes in a quintuplet are required to be measured to extract all of the information the quintuplet encodes. Conversely, checking that these linear combinations of quadrupole modes in fact obey these relationships may be a useful test in determining whether observed asymmetries are in fact magnetic in origin (under the present assumptions).

7.A.3 Asymmetry parameters for an inclined dipole

For a centered dipole magnetic field with some obliquity angle β relative to the rotation axis, the normalized horizontal dependence of B_r is given by

$$\psi(\mu, \phi) = \frac{1}{2} \sqrt{\frac{3}{\pi}} (\cos \beta \cos \theta + \sin \beta \sin \theta \cos \phi), \quad (7.25)$$

cf. Mathis and Bugnet (2023) and Das et al. (2024). Averaging ψ^2 over ϕ gives

$$\langle \psi^2 \rangle_\phi = \frac{3}{2} P_2(\cos \beta) \mu^2 + \frac{3}{4} \sin^2 \beta \quad (7.26)$$

where $P_2(x) = (3x^2 - 1)/2$ is a Legendre polynomial.

The form of Equation 7.26 is highly instructive. It writes $\langle \psi^2 \rangle_\phi$ as two terms, the second of which is a constant over the star and therefore shifts all modes equally (i.e., cannot introduce asymmetries). Since all asymmetry parameters only depend on the field through latitudinal averages over $\langle \psi^2 \rangle_\phi$, *every* asymmetry parameter defined in Equations 7.20 and 7.24 must be proportional to $P_2(\cos \beta)$ (and therefore to each other, in ratios which are independent of β). Moreover, *all* asymmetry parameters of any ℓ (including $\ell > 2$) must vanish for all β at some critical obliquity $\beta = \arccos(-1/3)/2$ where $P_2(\cos \beta)$ vanishes (this has been noticed in special cases by Mathis and Bugnet 2023 and Das et al. 2024). This appears to be a special property of the dipole geometry, where the relevant component of $\langle \psi^2 \rangle_\phi$ depends on β and μ only in a “disentangled” way.

Evaluating Equations 7.20 and 7.24, we have

$$a_{-10+1}^{\ell=1} = \frac{2}{5} P_2(\cos \beta) \quad (7.27)$$

for $\ell = 1$, and

$$a_{-2-10}^{\ell=2} = a_{-10+1}^{\ell=2} = a_{0+1+2}^{\ell=2} = -\frac{2}{35} P_2(\cos \beta) \quad (7.28a)$$

$$a_{-2-1+1}^{\ell=2} = a_{-20+1}^{\ell=2} = a_{-10+2}^{\ell=2} = a_{-1+1+2}^{\ell=2} = -\frac{6}{35} P_2(\cos \beta) \quad (7.28b)$$

$$a_{-2-1+2}^{\ell=2} = a_{-2+1+2}^{\ell=2} = -\frac{12}{35} P_2(\cos \beta) \quad (7.28c)$$

$$a_{-20+2}^{\ell=2} = -\frac{8}{35} P_2(\cos \beta) \quad (7.28d)$$

for $\ell = 2$.

If all possible magnetic axes are equally probable, $P_2(\cos \beta)$ has a root-mean-square value

$$\begin{aligned} P_2(\cos \beta)_{\text{rms}} &= \sqrt{\frac{1}{2} \int_{-1}^{+1} P_2(\cos \beta)^2 d(\cos \beta)} \\ &= \sqrt{\frac{2}{5}} \approx 0.63. \end{aligned} \quad (7.29)$$

We adopt this root-mean-square value as the fiducial value of $P_2(\cos \beta)$ when modeling asymmetry parameters in this study.

7.B Correction for non-asymptotic effects

The exposition in Section 7.2 makes extensive use of the asymptotic approximation and related assumptions. For example, the expressions in Section 7.2 require incompressibility, as well as the condition that the radial wavelength is small compared both to the horizontal wavelength $\lambda_h/2\pi = r/\sqrt{\ell(\ell+1)}$ and the pressure scale height. Both assumptions are challenged for WD pulsations, which are usually localized to the outer edge of the g-mode cavity near the surface of the star, and are low-radial order at the high-frequency end. Non-asymptotic effects may be particularly important for the magnetism, whose effects are especially confined to the outer turning point of the g-mode cavity.

To investigate the effect of relaxing these assumptions, we numerically solve for the adiabatic oscillation modes using version 7.2.1 of the GYRE code (Townsend and Teitler, 2013). GYRE computes both mode frequencies and fluid perturbations in the absence of assumptions about the size of the density scale height or perturbations to the gravitational potential. Equation 7.5 gives an asymptotic estimate of \mathcal{J} . We then compute a non-asymptotic estimate \mathcal{J} using the mode periods P and horizontal fluid displacements ξ_h from GYRE (cf. Equation 40 in Li, Deheuvels, Ballot, and Lignières, 2022):

$$\mathcal{J} = \frac{4\pi^2}{\ell(\ell+1)} P^{-2} \frac{\int_{\mathcal{R}_v^\ell} [\partial_r(r\xi_h)]^2 dr}{\int_{\mathcal{R}_v^\ell} \xi_h^2 \rho r^2 dr}. \quad (7.30)$$

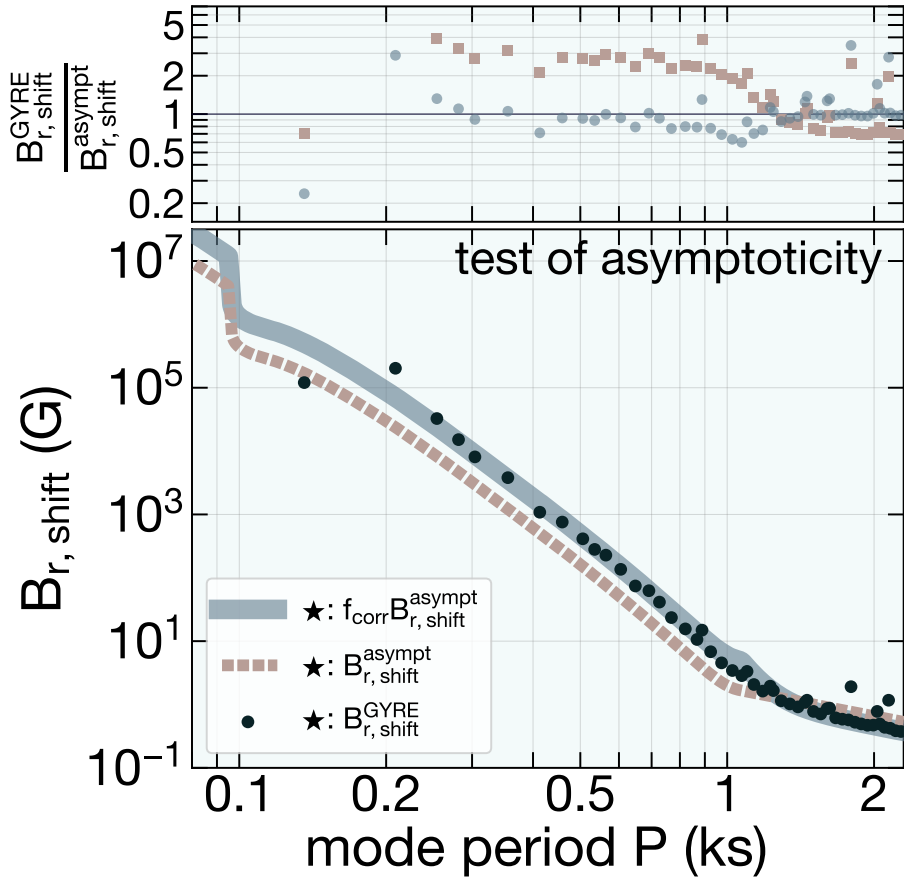


Figure 7.9: Model seismic magnetic field sensitivity $B_{r,\text{shift}}$, with or without the non-asymptotic correction in Equation 7.31 applied. *Black points* denote the non-asymptotic result using eigenfunctions calculated by GYRE (Equation 7.30). The *top panel* shows the ratio of the GYRE result to the asymptotic estimate (with or without correction) to the non-asymptotic result. This figure has been extended to longer periods to emphasize the behavior of N -limited modes. The symbol \star denotes the same choice of parameters as in Figure 7.3.

The derivation of Equation 7.30 applies assumptions such as incompressibility and approximately radial wavenumber, and it ignores a surface term contribution which has been found to make a small difference (Jones et al., 1989). Nevertheless, it stops short of substituting in the full asymptotic expression for ξ_h (see the Appendix of Li, Deheuvels, Ballot, and Lignières, 2022). GYRE does not assume that the radial wavenumber is large relative to the scale height, nor does it assume the Cowling approximation. In the asymptotic limit (taking $\xi_h \propto \rho^{-1/2} r^{-3/2} N^{1/2} \sin \Phi$ with $k_r = \partial_r \Phi = \sqrt{\ell(\ell+1)} N / \omega r$), we recover Equation 7.5. However, \mathcal{J} may differ from its value in Equation 7.5 for various reasons, including corrections to the outer turning point and domination of the integrals in Equation 7.30 by only a single wavelength.

We bundle non-asymptotic effects into a simple, ad hoc correction factor f_{corr} , defined such that the inferred field $B_{r,\text{shift}}$ from the asymmetries is related to its asymptotic estimate by

$$f_{\text{corr}} = \frac{B_{r,\text{shift}}}{B_{r,\text{shift}}^{\text{asympt}}} = \sqrt{\frac{\mathcal{J}_{\text{asympt}}}{\mathcal{J}}} \quad (7.31)$$

where superscript ‘‘asympt’’ denotes the application of Equation 7.5 for calculating \mathcal{J} .

We find that f_{corr} is approximately described by

$$f_{\text{corr}} = f_N + (f_{S_\ell} - f_N) \left(\frac{2\pi}{PS_\ell} \right)_{\text{out}}^{10} \quad (7.32)$$

where $f_N = 1/\sqrt{2}$ and $f_{S_\ell} = 3$, respectively, and $(2\pi/PS_\ell)_{\text{out}}$ is evaluated at the outer turning point of the mode. This form is chosen to set $f_{\text{corr}} = f_N$ for N -limited modes and $f_{\text{corr}} = f_{S_\ell}$ for S_ℓ -limited modes, with a fast but smooth transition in between the regimes enforced by an arbitrary but steep power index (10). Figure 7.9 shows that there is good agreement between $B_{r,\text{shift}}^{\text{GYRE}}$ (computed using GYRE eigenfunctions) and $B_{r,\text{shift}} = f_{\text{corr}} B_{r,\text{shift}}^{\text{asympt}}$. Future work should more thoroughly investigate the impact of non-asymptotic effects on seismic magnetic field measurements.

Chapter 8

CONCLUSION

This thesis investigates the seismic properties of stars whose structures have been shaped by violent mergers (**Chapters II–III**) and whose interiors harbor strong magnetic fields (**Chapters IV–VII**). It focuses on stellar exotica which either have only recently been discovered or are likely to be discoverable with the instruments and surveys we will soon have. Where do we go from here?

I am optimistic about the near-term potential of asteroseismology to enable new and interesting discoveries. Much of what we know about asteroseismology comes from data taken during the *Kepler* satellite’s four-year main mission¹ (Borucki et al., 2010). Despite having ended in 2013, *Kepler*’s main mission supplied a wealth of archival data which is still routinely mined for scientific discoveries in the present day. Moreover, the TESS² mission continues to provide high-quality light curves for bright sources across the sky (Ricker et al., 2015). In this time, it has detected solar-like oscillations in $\approx 1.6 \times 10^5$ RGs—an order of magnitude more than *Kepler*’s main mission (Hon, Huber, Kuszlewicz, et al., 2021). Now seven years old, TESS will continue to enhance seismic science for as long as its useful lifetime can be extended.

Both metaphorically and literally, the future is also bright. The *Roman Space Telescope*’s Galactic Bulge Time Domain Survey (GBTDS)³, to launch in 2026, will closely monitor a Galactic-bulge field at 15-minute cadence during six ≈ 70 d campaigns. In the process, *Roman* is projected to detect solar-like oscillations in $\simeq 6 \times 10^5$ RGs (Gould et al., 2015; Huber et al., 2023), vastly expanding the number of known pulsating RGs and seismically probing the Galactic-bulge population for the first time. Measurements of ν_{\max} for these RGs (and $\Delta\nu$ for a subset of them) combined with radii inferred using parallaxes (either from *Gaia* or *Roman* itself) will yield precise stellar masses and ages.

These measurements will be indispensable to galactic archaeology of the thin disk, thick disk, and bulge populations. The PLATO mission, also slated to launch in 2026, is designed

¹*Kepler*’s primary aim was to detect exoplanetary transits.

²TESS is short for Transiting Exoplanet Survey Satellite—its primary aim is to detect exoplanetary transits.

³A primary aim of *Roman* is to detect exoplanets using gravitational microlensing.

specifically with asteroseismology as a primary goal⁴. The combination of its wide field of view, numerous pointings, and fast cadence will allow PLATO to measure the oscillation modes in main-sequence, subgiant, giant, and compact pulsators across the Hertzsprung–Russell diagram. PLATO is projected to take exquisite light curves for $\simeq 10^6$ targets and seismically measure the masses, radii, and ages of $\approx 8.5 \times 10^4$ bright sun-like stars (Rauer et al., 2014).

Astrophysics has a tradition of frequent, near-synchronous dialogue between observations and theory—stellar merger genealogy is no different. While this thesis discusses the seismic properties of two types of merger remnants, stellar interactions are extremely diverse, and the structure and evolution of their products remain largely mysterious. For example, while mergers of main-sequence stars with carbon–oxygen white dwarfs (Zorotovic and Schreiber, 2022) and hot subdwarfs (Schaffenroth et al., 2022) both appear to be implied by censuses of close binaries, the remnants of these mergers are not well understood theoretically (other than that they probably inflate into red-giant-like stars). The last few years have also seen growing interest in characterizing the seismic properties of massive main-sequence and Hertzsprung-gap stars which have experienced mass transfer (Wagg et al., 2024) or merger (Henneco, Schneider, Hekker, et al., 2024; Henneco, Schneider, Heller, et al., 2025). It has even been recently suggested that asteroseismology may reveal the as-yet puzzling (possibly binary) origin of blue supergiants (Ma, Johnston, et al., 2024; Bellinger, Mink, et al., 2024). However, one-dimensional studies of merger remnant evolution depend on the messy hydrodynamics of the merger, particularly for merger remnants with a less clear core–envelope distinction—study of this merger physics itself promises to be fruitful (e.g., Lombardi et al., 2002; Gaburov et al., 2008). Remnants also likely possess unusual but highly uncertain rotational and magnetic properties (Ceillier et al., 2017; Schneider, Ohlmann, Podsiadlowski, Röpke, Balbus, Pakmor, and Springel, 2019; Schneider, Ohlmann, Podsiadlowski, Röpke, Balbus, and Pakmor, 2020) which merit further investigation. Translation of system-level physics to population-level statistics is the domain of binary population synthesis (e.g., Han et al., 2020), which will likely be critical for connecting remnant occurrence rates to stellar evolutionary predictions.

Within seismic magnetometry, there is also plenty left for theorists to do. This thesis includes non-perturbative calculations of g modes under strong, dipolar magnetic fields, but the basic method I have outlined can be vastly generalized to magnetic fields with arbitrary large-scale geometries. Such strong magnetic fields can mix g modes across

⁴Uniquely, PLATO places stellar oscillations at enough of a focus to warrant their representation in a full 20% of the mission’s acronym: “O” stands for “Oscillations of stars.” (Naturally, “PLAT” stands for “PLAnetary Transits.”)

different angular degrees ℓ (not just m), further increasing the complexity of stellar pulsation spectra. A qualitative understanding of the way in which strong magnetic fields affect mixed modes (as in RGs) also remains elusive and should be investigated systematically. Highly magnetically distorted g modes also violate the asymptotic approximation, suggesting that multi-dimensional simulations may be an important way to better understand their behavior (e.g., Lecoanet, Vasil, et al., 2017). On the applied side, it seems very natural to study what the pulsations of ultramassive white dwarfs (within which magnetism is common; Kilic, Córscico, et al., 2023, Blatman et al., in preparation) and hot subdwarfs (within which magnetism is exceedingly rare; Pelisoli, Dorsch, et al., 2022) can teach us about these objects' magnetic fields. Finally, the ideas explored in this thesis in the context of stellar magnetism may also aid in the calculation of oscillation modes in tidally deformed Sun-like stars (cf. Fuller, Rappaport, et al., 2025), broadening the applicability of these techniques.

Taking the long view, this era is one in which binary or magnetic processes (and often both together) are important actors in many open problems in stellar physics and beyond. It is now widely recognized that both effects are important across a wide variety of systems, though their rich phenomenology promises to remain an unexplored playground for many years to come. Perhaps uncommonly, the depth of the complexity caused by both is something about which even the theorists do not claim to feel certain. Advances in seismology will likely shed further insights into how these effects manifest within stellar interiors.

Following the scientist's conceit: I hope this work becomes *obsolete*. I hope this happens soon, and that there is more to do. I hope what I have written is wrong, but in interesting ways. I hope the stars continue to wiggle and change color and explode, so that we may learn more about them. This thesis does not aspire to be timeless—it is only the latest data point in a time series whose overall trend is not yet clear.

BIBLIOGRAPHY

Abblimit, I., K. Maeda, and X.-D. Li (2016). “Monte Carlo population synthesis of post-common-envelope white dwarf binaries and type Ia supernova rate.” In: *The Astrophysical Journal* 826.1, 53.

Aerts, C. (2015). “The age and interior rotation of stars from asteroseismology.” In: *Astronomische Nachrichten* 336.5, pp. 477–486.

Aerts, C. (2021). “Probing the interior physics of stars through asteroseismology.” In: *Reviews of Modern Physics* 93.1, 015001.

Aerts, C., K. Augustson, et al. (2021). “Rossby numbers and stiffness values inferred from gravity-mode asteroseismology of rotating F-and B-type dwarfs-Consequences for mixing, transport, magnetism, and convective penetration.” In: *Astronomy & Astrophysics* 656, A121.

Aerts, C., J. Christensen-Dalsgaard, and D. W. Kurtz (2010). “Asteroseismology.” Springer Science & Business Media.

Aerts, C., S. Mathis, and T. M. Rogers (2019). “Angular momentum transport in stellar interiors.” In: *Annual Review of Astronomy and Astrophysics* 57, pp. 35–78.

Aerts, C., G. Molenberghs, et al. (2018). “Forward asteroseismic modeling of stars with a convective core from gravity-mode oscillations: parameter estimation and stellar model selection.” In: *The Astrophysical Journal Supplement Series* 237.1, 15.

Aerts, C., T. Van Reeth, and A. Tkachenko (2017). “The interior angular momentum of core hydrogen burning stars from gravity-mode oscillations.” In: *The Astrophysical Journal Letters* 847.1, L7.

Ahlborn, F. et al. (2020). “Asteroseismic sensitivity to internal rotation along the red-giant branch.” In: *Astronomy & Astrophysics* 639, A98.

Althaus, L. G. et al. (2005). “Mass-radius relations for massive white dwarf stars.” In: *Astronomy & Astrophysics* 441.2, pp. 689–694.

Anderson, E. R., T. L. Duvall Jr., and S. M. Jefferies (1990). “Modeling of solar oscillation power spectra.” In: *The Astrophysical Journal* 364, pp. 699–705.

Angel, J. R. P. (1977). “Magnetism in white dwarfs.” In: *The Astrophysical Journal* 216, pp. 1–17.

Appert, K., R. Gruber, and J. Vaclavik (1974). “Continuous spectra of a cylindrical magnetohydrodynamic equilibrium.” In: *Physics of Fluids* 17.7, pp. 1471–1472.

Appert, K., R. Gruber, and J. Vaclavik (1998). *Continuous spectra of a cylindrical magnetohydrodynamic equilibrium: the derivation*. Tech. rep.

Arentoft, T. et al. (2017). “Convective-core overshoot and suppression of oscillations: Constraints from red giants in ngc 6811.” In: *The Astrophysical Journal* 838.2, 115.

Asplund, M. et al. (2009). “The chemical composition of the Sun.” In: *Annual Review of Astronomy and Astrophysics* 47, pp. 481–522.

Atkinson, F. V., W. N. Everitt, and A. Zettl (1988). “Regularization of a Sturm-Liouville problem with an interior singularity using quasiderivatives.” In: *Differential and Integral Equations* 1.2, pp. 213–221.

Aurière, M. et al. (2015). “The magnetic fields at the surface of active single G-K giants.” In: *Astronomy & Astrophysics* 574, A90.

Bagnulo, S. and J. D. Landstreet (2021). “New insight into the magnetism of degenerate stars from the analysis of a volume-limited sample of white dwarfs.” In: *Monthly Notices of the Royal Astronomical Society* 507.4, pp. 5902–5951.

Bagnulo, S. and J. D. Landstreet (2022). “Multiple channels for the onset of magnetism in isolated white dwarfs.” In: *The Astrophysical Journal Letters* 935.1, L12.

Bailyn, C. D. (1995). “Blue stragglers and other stellar anomalies: Implications for the dynamics of globular clusters.” In: *Annual Review of Astronomy and Astrophysics* 33.1, pp. 133–162.

Balbinski, E. (1984). “The continuous spectrum in differentially rotating perfect fluids: a model with an analytic solution.” In: *Monthly Notices of the Royal Astronomical Society* 209.2, pp. 145–157.

Baliunas, S. L. et al. (1996). “A dynamo interpretation of stellar activity cycles.” In: *The Astrophysical Journal* 460, 848.

Ballot, J. et al. (2010). “Gravity modes in rapidly rotating stars-Limits of perturbative methods.” In: *Astronomy & Astrophysics* 518, A30.

Balmforth, N. J. et al. (2001). “On the excitation mechanism in roAp stars.” In: *Monthly Notices of the Royal Astronomical Society* 323.2, pp. 362–372.

Balona, L. A. et al. (2011). “Kepler observations of rapidly oscillating Ap, δ Scuti and γ Doradus pulsations in Ap stars.” In: *Monthly Notices of the Royal Astronomical Society* 410.1, pp. 517–524.

Baran, A. S., J. H. Telting, C. S. Jeffery, et al. (2019). “K2 observations of the sdBV + dM/bd binaries PHL 457 and EQ Psc.” In: *Monthly Notices of the Royal Astronomical Society* 489.2, pp. 1556–1571.

Baran, A. S., J. H. Telting, P. Németh, et al. (2016). “A subsynchronously rotating pulsating subdwarf B star in a short-period binary with a white dwarf companion.” In: *Astronomy & Astrophysics* 585, A66.

Barceló Forteza, S., T. Roca Cortés, and R. A. García (2018). “The envelope of the power spectra of over a thousand δ Scuti stars..” In: *Astronomy & Astrophysics* 614.

Barenblatt, G. I. (1996). “Scaling, self-similarity, and intermediate asymptotics: dimensional analysis and intermediate asymptotics.” 14. Cambridge University Press.

Basu, S. et al. (2012). “Effect of uncertainties in stellar model parameters on estimated masses and radii of single stars.” In: *The Astrophysical Journal* 746.1, 76.

Bear, E. and N. Soker (2010). “Spinning-up the envelope before entering a common envelope phase.” In: *New Astronomy* 15.5, pp. 483–490.

Beck, P. G. et al. (2012). “Fast core rotation in red-giant stars as revealed by gravity-dominated mixed modes.” In: *Nature* 481.7379, pp. 55–57.

Bédard, A. et al. (2020). “On the spectral evolution of hot white dwarf stars. I. A detailed model atmosphere analysis of hot white dwarfs from SDSS DR12.” In: *The Astrophysical Journal* 901.2, 93.

Bedding, T. R. et al. (2011). “Gravity modes as a way to distinguish between hydrogen- and helium-burning red giant stars.” In: *Nature* 471.7340, pp. 608–611.

Belczynski, K., T. Bulik, and A. J. Ruiter (2005). “New constraints on type Ia supernova progenitor models.” In: *The Astrophysical Journal* 629.2, 915.

Belkacem, K. et al. (2013). “On the Seismic Scaling Relations $\Delta\nu-\rho$ and $\nu_{\max}-\nu_c$.” In: *ASP Conf. Ser.* Vol. 479, 61.

Bell, K. J., A. Gianninas, et al. (2017). “Pruning the ELM survey: characterizing candidate low-mass white dwarfs through photometric variability.” In: *The Astrophysical Journal* 835.2, 180.

Bell, K. J., I. Pelisoli, et al. (2018). “The McDonald Observatory search for pulsating sdA stars—Asteroseismic support for multiple populations.” In: *Astronomy & Astrophysics* 617, A6.

Bellazzini, M., F. R. Ferraro, and E. Pancino (2001). “A step toward the calibration of the red giant branch tip as a standard candle.” In: *The Astrophysical Journal* 556.2, 635.

Bellazzini, M., F. R. Ferraro, A. Sollima, et al. (2004). “The calibration of the RGB Tip as a Standard Candle—Extension to Near Infrared colors and higher metallicity.” In: *Astronomy & Astrophysics* 424.1, pp. 199–211.

Bellinger, E. P., S. Basu, S. Hekker, and W. H. Ball (2017). “Model-independent measurement of internal stellar structure in 16 Cygni A and B.” In: *The Astrophysical Journal* 851.2, 80.

Bellinger, E. P., S. Basu, S. Hekker, J. Christensen-Dalsgaard, et al. (2021). “Asteroseismic inference of the central structure in a subgiant star.” In: *The Astrophysical Journal* 915.2, 100.

Bellinger, E. P., S. E. de Mink, et al. (2024). “The Potential of Asteroseismology to Resolve the Blue Supergiant Problem.” In: *The Astrophysical Journal Letters* 967.2, L39.

Belloni, D. et al. (2018). “No cataclysmic variables missing: higher merger rate brings into agreement observed and predicted space densities.” In: *Monthly Notices of the Royal Astronomical Society* 478.4, pp. 5626–5637.

Bidelman, W. P. and D. J. MacConnell (1973). “The brighter stars astrophysical interest in the southern sky..” In: *Astronomical Journal* 78, pp. 687–733.

Bigot, L. and W. A. Dziembowski (2002). “The oblique pulsator model revisited.” In: *Astronomy & Astrophysics* 391.1, pp. 235–245.

Bildsten, L. and C. Cutler (1995). “Nonradial oscillations in neutron star oceans: a source of quasi-periodic x-ray oscillations?.” In: *The Astrophysical Journal* 449, 800.

Bildsten, L., B. Paxton, et al. (2011). “Acoustic signatures of the helium core flash.” In: *The Astrophysical Journal Letters* 744.1, L6.

Bildsten, L., G. Ushomirsky, and C. Cutler (1996). “Ocean g-Modes on Rotating Neutron Stars.” In: *The Astrophysical Journal* 460, 827.

Bischoff-Kim, A. et al. (2019). “GD358: three decades of observations for the in-depth asteroseismology of a DBV star.” In: *The Astrophysical Journal* 871.1, 13.

Blatman, D. and S. Ginzburg (2024a). “Magnetic field breakout from white dwarf crystallization dynamos.” In: *Monthly Notices of the Royal Astronomical Society* 528.2, pp. 3153–3162.

Blatman, D. and S. Ginzburg (2024b). “Magnetic field breakout in ultramassive crystallizing white dwarfs.” In: *Monthly Notices of the Royal Astronomical Society: Letters*, pp. L13–L18.

Bond, H. E. (2019). “Carbon-deficient Red Giants.” In: *The Astrophysical Journal* 887.1, 12.

Borucki, W. J. (2016). “KEPLER Mission: development and overview.” In: *Reports on Progress in Physics* 79.3, 036901.

Borucki, W. J. et al. (2010). “Kepler planet-detection mission: introduction and first results.” In: *Science* 327.5968, pp. 977–980.

Bouabid, M.-P. et al. (2013). “Effects of the Coriolis force on high-order g modes in γ Doradus stars.” In: *Monthly Notices of the Royal Astronomical Society* 429.3, pp. 2500–2514.

Boyd, J. P. (1976). “Planetary waves and the semiannual wind oscillation in the tropical upper stratosphere”. PhD thesis. Harvard University.

Boyd, J. P. (1981). “Sturm–Liouville eigenproblems with an interior pole.” In: *Journal of Mathematical Physics* 22.8, pp. 1575–1590.

Boyd, J. P. (1982). “The influence of meridional shear on planetary waves. Part 2: Critical latitudes.” In: *Journal of Atmospheric Sciences* 39.4, pp. 770–790.

Boyd, J. P. (1985). “Complex Coordinate Methods for Hydrodynamic Instabilities and Sturm-Liouville Eigenproblems with an Interior Singularity.” In: *Journal of Computational Physics* 57.3, pp. 454–471.

Braithwaite, J. and Å. Nordlund (2006). “Stable magnetic fields in stellar interiors.” In: *Astronomy & Astrophysics* 450.3, pp. 1077–1095.

Braithwaite, J. and H. C. Spruit (2004). “A fossil origin for the magnetic field in A stars and white dwarfs.” In: *Nature* 431.7010, pp. 819–821.

Brassard, P., G. Fontaine, F. Wesemael, and C. J. Hansen (1992). “Adiabatic properties of pulsating DA white dwarfs. II-Mode trapping in compositionally stratified models.” In: *The Astrophysical Journal Supplement Series* 80.1, pp. 369–401.

Brassard, P., G. Fontaine, F. Wesemael, S. D. Kawaler, et al. (1991). “Adiabatic properties of pulsating DA white dwarfs. I-the treatment of the Brunt-Vaisala frequency and the region of period formation.” In: *The Astrophysical Journal* 367, pp. 601–611.

Breger, M. and A. A. Pamyatnykh (1998). “Period changes of delta Scuti stars and stellar evolution.” In: *Astronomy & Astrophysics* 332, pp. 958–968.

Brickhill, A. J. (1991). “The pulsations of ZZ Ceti stars–III. The driving mechanism.” In: *Monthly Notices of the Royal Astronomical Society* 251.4, pp. 673–680.

Briggs, G. P. et al. (2018). “Genesis of magnetic fields in isolated white dwarfs.” In: *Monthly Notices of the Royal Astronomical Society* 478.1, pp. 899–905.

Brogaard, K. et al. (2021). “Astroseismology of overmassive, undermassive, and potential past members of the open cluster NGC 6791..” In: *Monthly Notices of the Royal Astronomical Society*.

Brown, T. M., R. L. Gilliland, et al. (1991). “Detection of possible p-mode oscillations on Procyon.” In: *The Astrophysical Journal* 368, pp. 599–609.

Brown, W. R., M. Kilic, A. Kosakowski, et al. (2020). “The ELM survey. VIII. Ninety-eight double white dwarf binaries.” In: *The Astrophysical Journal* 889.1, 49.

Brown, W. R., M. Kilic, C. A. Prieto, et al. (2010). “The ELM survey. I. A complete sample of extremely low-mass white dwarfs.” In: *The Astrophysical Journal* 723.2, 1072.

Brown, W. R., M. Kilic, C. A. Prieto, et al. (2011). “The ELM survey. III. A successful targeted survey for extremely low mass white dwarfs.” In: *The Astrophysical Journal* 744.2, 142.

Brun, A. S. and M. K. Browning (2017). “Magnetism, dynamo action and the solar-stellar connection.” In: *Living Reviews in Solar Physics* 14.1, pp. 1–133.

Brun, A. S., M. K. Browning, and J. Toomre (2005). “Simulations of Core Convection in Rotating A-Type Stars: Magnetic Dynamo Action.” In: *The Astrophysical Journal* 629.1, pp. 461–481.

Buchler, J. R., M.-J. Goupil, and G. Kovacs (1993). “Stellar pulsations with stochastic driving.” In: *Astronomy and Astrophysics* 280.1, pp. 157–168.

Buckingham, E. (1914). “On physically similar systems; illustrations of the use of dimensional equations.” In: *Physical Review* 4.4, 345.

Buder, S. et al. (2018). “The GALAH Survey: second data release.” In: *Monthly Notices of the Royal Astronomical Society* 478.4, pp. 4513–4552.

Bufanda, E. et al. (2023). “Investigating APOKASC Red Giant Stars with Abnormal Carbon-to-nitrogen Ratios.” In: *The Astrophysical Journal* 959.2, 123.

Bugnet, L. (2022). “Magnetic signatures on mixed-mode frequencies-II. Period spacings as a probe of the internal magnetism of red giants.” In: *Astronomy & Astrophysics* 667, A68.

Bugnet, L. et al. (2021). “Magnetic signatures on mixed-mode frequencies-I. An axisymmetric fossil field inside the core of red giants.” In: *Astronomy & Astrophysics* 650, A53.

Buldgen, G. et al. (2022). “Inversions of stellar structure from asteroseismic data.” In: *Frontiers in Astronomy and Space Sciences* 9, 942373.

Burger, A. (1966). “Instability associated with the continuous spectrum in a baroclinic flow.” In: *Journal of Atmospheric Sciences* 23.3, pp. 272–277.

Burssens, S. et al. (2023). “A calibration point for stellar evolution from massive star asteroseismology.” In: *Nature Astronomy* 7, pp. 913–930.

Buysschaert, B., C. Aerts, et al. (2018). “Forward seismic modeling of the pulsating magnetic B-type star HD 43317.” In: *Astronomy & Astrophysics* 616, A148.

Buysschaert, B., C. Neiner, et al. (2017). “Magnetic characterization of the SPB/β Cep hybrid pulsator HD 43317.” In: *Astronomy & Astrophysics* 605, A104.

Calcaferro, L. M. et al. (2023). “Exploring the internal rotation of the extremely low-mass He-core white dwarf GD 278 with TESS asteroseismology.” In: *Astronomy & Astrophysics* 673, A135.

Camacho, J. et al. (2014). “Monte Carlo simulations of post-common-envelope white dwarf + main sequence binaries: comparison with the SDSS DR7 observed sample.” In: *Astronomy & Astrophysics* 566, A86.

Cameron, A. G. W. and W. A. Fowler (1971). “Lithium and the s-PROCESS in Red-Giant Stars.” In: *The Astrophysical Journal* 164, 111.

Cantiello, M., J. Fuller, and L. Bildsten (2016). “Asteroseismic signatures of evolving internal stellar magnetic fields.” In: *The Astrophysical Journal* 824.1, 14.

Carlberg, J. K., K. Cunha, et al. (2012). “Observable signatures of planet accretion in red giant stars. I. Rapid rotation and light element replenishment.” In: *The Astrophysical Journal* 757.2, 109.

Carlberg, J. K., S. R. Majewski, et al. (2011). “The frequency of rapid rotation among K giant stars.” In: *The Astrophysical Journal* 732.1, 39.

Casey, A. R., A. Y. Q. Ho, M. Ness, D. W. Hogg, H.-W. Rix, G. C. Angelou, S. Hekker, C. A. Tout, J. C. Lattanzio, A. I. Karakas, et al. (2019a). “Tidal interactions between binary stars can drive lithium production in low-mass red giants.” In: *The Astrophysical Journal* 880.2, 125.

Casey, A. R., A. Y. Q. Ho, M. Ness, D. W. Hogg, H.-W. Rix, G. C. Angelou, S. Hekker, C. A. Tout, J. C. Lattanzio, A. I. Karakas, et al. (2019b). “Tidal Interactions between Binary Stars Can Drive Lithium Production in Low-mass Red Giants.” In: *The Astrophysical Journal* 880.2, 125.

Cassisi, S., I. Iben Jr., and A. Tornambè (1998). “Hydrogen-accreting carbon-oxygen white dwarfs.” In: *The Astrophysical Journal* 496.1, 376.

Cassisi, S., H. Schlattl, et al. (2002). “First full evolutionary computation of the helium flash-induced mixing in population II stars.” In: *The Astrophysical Journal* 582.1, L43.

Catelan, M. (2009). “Horizontal branch stars: the interplay between observations and theory, and insights into the formation of the Galaxy.” In: *Astrophysics and Space Science* 320, pp. 261–309.

Ceillier, T. et al. (2017). “Surface rotation of Kepler red giant stars.” In: *Astronomy & Astrophysics* 605, A111.

Chaplin, W. J., T. R. Bedding, et al. (2011). “Evidence for the impact of stellar activity on the detectability of solar-like oscillations observed by Kepler.” In: *The Astrophysical Journal Letters* 732.1, L5.

Chaplin, W. J. and A. Miglio (2013). “Asteroseismology of solar-type and red-giant stars.” In: *Annual Review of Astronomy and Astrophysics* 51.1, pp. 353–392.

Charbonnel, C. and S. C. Balachandran (2000). “The Nature of the lithium rich giants. Mixing episodes on the RGB and early-AGB.” In: *Astronomy & Astrophysics* 359, pp. 563–572.

Charbonnel, C. and S. Talon (2005). “Influence of gravity waves on the internal rotation and Li abundance of solar-type stars.” In: *Science* 309.5744, pp. 2189–2191.

Chen, X., P. F. L. Maxted, et al. (2017). “The formation of EL CVn-type binaries.” In: *Monthly Notices of the Royal Astronomical Society* 467.2, pp. 1874–1889.

Chen, Z.-Y. and D.-R. Lü (2009). “On the calculation of Hough functions for resolving atmospheric thermal tidal structure.” In: *Chinese Journal of Geophysics* 52.3, pp. 547–554.

Christensen-Dalsgaard, J. (2008). “Lecture notes on stellar structure and evolution.” Aarhus Universitet. Institute for Fysik og Astronomi.

Christensen-Dalsgaard, J. (2012). “Stellar model fits and inversions.” In: *Astronomische Nachrichten* 333.10, pp. 914–925.

Cieza, L. A. (2015). “The Structure and Evolution of Protoplanetary Disks: an infrared and submillimeter view.” In: *Proceedings of the International Astronomical Union* 10.S314, pp. 128–134.

Clayton, D. (2003). “Handbook of Isotopes in the Cosmos.”

Clayton, G. C. et al. (2007). “Very large excesses of ^{18}O in hydrogen-deficient carbon and R coronae borealis stars: Evidence for white dwarf mergers.” In: *The Astrophysical Journal* 662.2, 1220.

Constantino, T. et al. (2015). “The treatment of mixing in core helium burning models— I. Implications for asteroseismology.” In: *Monthly Notices of the Royal Astronomical Society* 452.1, pp. 123–145.

Corsaro, E. et al. (2012). “Asteroseismology of the open clusters NGC 6791, NGC 6811, and NGC 6819 from 19 months of Kepler photometry.” In: *The Astrophysical Journal* 757.2, 190.

Córsico, A. H. et al. (2019). “Pulsating white dwarfs: new insights.” In: *The Astronomy and Astrophysics Review* 27.1, 7.

Cox, J. P. (1963). “On Second Helium Ionization as a Cause of Pulsational Instability in Stars.” In: *The Astrophysical Journal* 138, 487.

Cox, J. P. and R. T. Giuli (1968). “Principles of Stellar Structure: Physical Principles.” Vol. 1. 0. Gordon and Breach.

Cuadrado, R. A. et al. (2004). “Discovery of kilogauss magnetic fields in three DA white dwarfs.” In: *Astronomy & Astrophysics* 423.3, pp. 1081–1094.

Cunha, M. S., P. P. Avelino, and W. J. Chaplin (2020). “From solar-like to mira stars: a unifying description of stellar pulsators in the presence of stochastic noise.” In: *Monthly Notices of the Royal Astronomical Society* 499.4, pp. 4687–4697.

Cunha, M. S., D. Stello, et al. (2015). “Structural glitches near the cores of red giants revealed by oscillations in g-mode period spacings from stellar models.” In: *The Astrophysical Journal* 805.2, 127.

Curd, B. et al. (2017). “Four new massive pulsating white dwarfs including an ultramassive DAV.” In: *Monthly Notices of the Royal Astronomical Society* 468.1, pp. 239–249.

Dalessio, J. et al. (2013). “Periodic Variations in the $O - C$ Diagrams of Five Pulsation Frequencies of the DB White Dwarf EC 20058-5234.” In: *The Astrophysical Journal* 765.1, 5.

Das, S. B., L. Einramhof, and L. Bugnet (2024). “Unveiling complex magnetic field configurations in red giant stars.” In: *Astronomy & Astrophysics* 690, A217.

De Gerónimo, F. C. et al. (2019). “Pulsation properties of ultra-massive DA white dwarf stars with ONe cores.” In: *Astronomy & Astrophysics* 621, A100.

Deepak and D. L. Lambert (2021). “Lithium in red giants: the roles of the He-core flash and the luminosity bump.” In: *Monthly Notices of the Royal Astronomical Society* 507.1, pp. 205–224.

Deheuvels, S., J. Ballot, P. Eggenberger, et al. (2020). “Seismic evidence for near solid-body rotation in two Kepler subgiants and implications for angular momentum transport.” In: *Astronomy & Astrophysics* 641, A117.

Deheuvels, S., J. Ballot, C. Gehan, et al. (2022). “Seismic signature of electron degeneracy in the core of red giants: Hints for mass transfer between close red-giant companions.” In: *Astronomy & Astrophysics* 659, A106.

Deheuvels, S., G. Doğan, et al. (2014). “Seismic constraints on the radial dependence of the internal rotation profiles of six Kepler subgiants and young red giants.” In: *Astronomy & Astrophysics* 564, A27.

Deheuvels, S., R. A. Garcia, et al. (2012). “Seismic evidence for a rapidly rotating core in a lower-giant-branch star observed with Kepler.” In: *The Astrophysical Journal* 756.1, 19.

Deheuvels, S., G. Li, et al. (2023). “Strong magnetic fields detected in the cores of 11 red giant stars using gravity-mode period spacings.” In: *Astronomy & Astrophysics* 670, L16.

Deheuvels, S., R.-M. Ouazzani, and S. Basu (2017). “Near-degeneracy effects on the frequencies of rotationally-split mixed modes in red giants.” In: *Astronomy & Astrophysics* 605, A75.

Denissenkov, P. A. and A. Weiss (2000). “Episodic lithium production by extra-mixing in red giants.” In: *Astronomy & Astrophysics* 358, pp. L49–L52.

Deubner, F.-L. and D. Gough (1984). “Helioseismology: Oscillations as a diagnostic of the solar interior.” In: *Annual Review of Astronomy and Astrophysics* 22, pp. 593–619.

Dewberry, J. W. et al. (2021). “Constraining Saturn’s interior with ring seismology: effects of differential rotation and stable stratification.” In: *The Planetary Science Journal* 2.5, 198.

Dhanpal, S. et al. (2023). “Inferring Coupling Strengths of Mixed-mode Oscillations in Red Giant Stars Using Deep Learning.” In: *The Astrophysical Journal* 958.1, 63.

Dhouib, H., S. Mathis, et al. (2022). “Detecting deep axisymmetric toroidal magnetic fields in stars-The traditional approximation of rotation for differentially rotating deep spherical shells with a general azimuthal magnetic field.” In: *Astronomy & Astrophysics* 661, A133.

Dhouib, H., V. Prat, et al. (2021a). “The traditional approximation of rotation for rapidly rotating stars and planets - II. Deformation and differential rotation.” In: *Astronomy & Astrophysics* 656, A122.

Dhouib, H., V. Prat, et al. (2021b). “The traditional approximation of rotation for rapidly rotating stars and planets-I. The impact of strong deformation.” In: *Astronomy & Astrophysics* 652, A154.

Dintrans, B. and M. Rieutord (2000). “Oscillations of a rotating star: a non-perturbative theory.” In: *Astronomy and Astrophysics* 354, pp. 86–98.

Dintrans, B., M. Rieutord, and L. Valdettaro (1999). “Gravito-inertial waves in a rotating stratified sphere or spherical shell.” In: *Journal of Fluid Mechanics* 398, pp. 271–297.

Dolez, N. et al. (2006). “Whole Earth telescope observations of the ZZ Ceti star HL Tau 76.” In: *Astronomy & Astrophysics* 446.1, pp. 237–257.

Donati, J. F. and J. D. Landstreet (2009). “Magnetic fields of non-degenerate stars.” In: *Annual Review of Astronomy and Astrophysics* 47.1, pp. 333–370.

Dorsch, M., C. S. Jeffery, et al. (2024). “Discovery of three magnetic He-sdOs with SALT.” In: *Astronomy & Astrophysics* 691, A165.

Dorsch, M., N. Reindl, et al. (2022). “Discovery of a highly magnetic He-sdO star from a double-degenerate binary merger.” In: *Astronomy & Astrophysics* 658, L9.

Drake, N. A. et al. (2002). “Rapidly rotating lithium-rich K giants: The new case of the giant PDS 365.” In: *The Astronomical Journal* 123.5, 2703.

Duan, R. M. et al. (2021). “EPIC 228782059: Asteroseismology of What Could Be the Coolest Pulsating Helium-atmosphere White Dwarf (DBV) Known.” In: *The Astrophysical Journal* 922.1, 2.

Dudorov, A. E. and S. A. Khaibrakhmanov (2015). “Theory of fossil magnetic field.” In: *Advances in Space Research* 55.3, pp. 843–850.

Duez, V. (2011). “Numerical simulations of magnetic relaxation in rotating stellar radiation zones.” In: *Astronomische Nachrichten* 332.9-10, pp. 983–987.

Duez, V. and S. Mathis (2010). “Relaxed equilibrium configurations to model fossil fields-I. A first family.” In: *Astronomy & Astrophysics* 517, A58.

Dufour, P., S. Desharnais, et al. (2010). “Multiwavelength observations of the hot DB star PG 0112+104.” In: *The Astrophysical Journal* 718.2, 647.

Dufour, P., G. Fontaine, et al. (2008). “SDSS J142625.71+575218.3: the first pulsating white dwarf with a large detectable magnetic field.” In: *The Astrophysical Journal* 683.2, L167.

Dupret, M.-A., K. Belkacem, et al. (2009). “Theoretical amplitudes and lifetimes of non-radial solar-like oscillations in red giants.” In: *Astronomy & Astrophysics* 506.1, pp. 57–67.

Dupret, M.-A., A. Grigahcine, et al. (2004). “Theoretical instability strips for δ Scuti and γ Doradus stars.” In: *Astronomy & Astrophysics* 414.2, pp. L17–L20.

Duvall Jr., T. L. and J. W. Harvey (1986). “Solar Doppler shifts: sources of continuous spectra”. In: *Seismology of the Sun and the Distant Stars*. Springer, pp. 105–116.

Dziembowski, W. A. (1971). “Nonradial oscillations of evolved stars. I. Quasiadiabatic approximation.” In: *Acta Astronomica* 21, pp. 289–306.

Dziembowski, W. A. and P. R. Goode (1992). “Effects of differential rotation on stellar oscillations-A second-order theory.” In: *The Astrophysical Journal* 394, pp. 670–687.

Dziembowski, W. A. and P. R. Goode (1996). “Magnetic effects on oscillations in roAp stars.” In: *The Astrophysical Journal* 458, 338.

Dziembowski, W. A., P. Moskalik, and A. A. Pamyatnykh (1993). “The opacity mechanism in B-type stars-II. Excitation of high-order g-modes in main-sequence stars.” In: *Monthly Notices of the Royal Astronomical Society* 265.3, pp. 588–600.

Eckart, C. (1960). “Variation principles of hydrodynamics.” In: *The Physics of Fluids* 3.3, pp. 421–427.

Eggleton, P. P. (1983). “Approximations to the radii of Roche lobes.” In: *The Astrophysical Journal* 268, 368.

Elsasser, W. M. (1956). "Hydromagnetic dynamo theory." In: *Reviews of Modern Physics* 28.2, 135.

Elsworth, Y. et al. (2017). "A new method for the asteroseismic determination of the evolutionary state of red-giant stars." In: *Monthly Notices of the Royal Astronomical Society* 466.3, pp. 3344–3352.

Everitt, W. N., J. Gunson, and A. Zettl (1987). "Some comments on Sturm-Liouville eigenvalue problems with interior singularities." In: *Zeitschrift für angewandte Mathematik und Physik ZAMP* 38.6, pp. 813–838.

Featherstone, N. A. et al. (2009). "Effects of Fossil Magnetic Fields on Convective Core Dynamos in A-type Stars." In: *The Astrophysical Journal* 705.1, pp. 1000–1018.

Federman, A. (1911). "On some general methods of integration of first-order partial differential equations." In: *Proceedings of the Saint-Petersburg Polytechnic Institute. Section of Technology, Natural Science and Mathematics* 16, pp. 97–155.

Ferrario, L., D. de Martino, and B. T. Gänsicke (2015). "Magnetic white dwarfs." In: *Space Science Reviews* 191, pp. 111–169.

Ferrario, L., A. Melatos, and J. Zrake (2015). "Magnetic field generation in stars." In: *Space Science Reviews* 191.1, pp. 77–109.

Ferrario, L., J. E. Pringle, et al. (2009). "The origin of magnetism on the upper main sequence." In: *Monthly Notices of the Royal Astronomical Society: Letters* 400.1, pp. L71–L74.

Fontaine, G. and F. Wesemael (1987). "Recent advances in the theory of white dwarf spectral evolution." In: *IAU Colloq. 95: Second Conference on Faint Blue Stars*, pp. 319–326.

Fu, J.-N. et al. (2007). "Asteroseismology of the PG 1159 star PG 0122+200." In: *Astronomy & Astrophysics* 467.1, pp. 237–248.

Fuentes, J. R., M. Castro-Tapia, and A. Cumming (2024). "A Short Intense Dynamo at the Onset of Crystallization in White Dwarfs." In: *The Astrophysical Journal Letters* 964.1, L15.

Fuller, J. (2017). "Heartbeat stars, tidally excited oscillations and resonance locking." In: *Monthly Notices of the Royal Astronomical Society* 472.2, pp. 1538–1564.

Fuller, J., M. Cantiello, et al. (2015). "Asteroseismology can reveal strong internal magnetic fields in red giant stars." In: *Science* 350.6259, pp. 423–426.

Fuller, J., D. W. Kurtz, et al. (2020). "Tidally trapped pulsations in binary stars." In: *Monthly Notices of the Royal Astronomical Society* 498.4, pp. 5730–5744.

Fuller, J. and D. Lai (2014). "Dynamical tides in compact white dwarf binaries: influence of rotation." In: *Monthly Notices of the Royal Astronomical Society* 444.4, pp. 3488–3500.

Fuller, J., A. L. Piro, and A. S. Jermyn (2019). "Slowing the spins of stellar cores." In: *Monthly Notices of the Royal Astronomical Society* 485.3, pp. 3661–3680.

Fuller, J., S. Rappaport, et al. (2025). “Tidally distorted stars are triaxial pulsators.” In: *The Astrophysical Journal* 979.1, 80.

Gaburov, E., J. C. Lombardi Jr., and S. Portegies Zwart (2008). “Mixing in massive stellar mergers.” In: *Monthly Notices of the Royal Astronomical Society: Letters* 383.1, pp. L5–L9.

Galaktionov, V. A. et al. (2004). “Intermediate asymptotics for inhomogeneous nonlinear heat conduction.” In: *Journal of Mathematical Sciences* 120, pp. 1277–1294.

García, R. A., F. P. Hernández, et al. (2014). “Study of KIC 8561221 observed by Kepler: an early red giant showing depressed dipolar modes.” In: *Astronomy & Astrophysics* 563, A84.

García, R. A., S. Mathur, et al. (2010). “CoRoT reveals a magnetic activity cycle in a Sun-like star.” In: *Science* 329.5995, pp. 1032–1032.

García, R. A., F. Pérez Hernández, et al. (2014). “Study of KIC 8561221 observed by Kepler: an early red giant showing depressed dipolar modes.” In: *Astronomy & Astrophysics* 563, A84.

García-Berro, E. et al. (2012). “Double degenerate mergers as progenitors of high-field magnetic white dwarfs.” In: *The Astrophysical Journal* 749.1, 25.

Gardner, W. (2003). “Measurement of spectral correlation.” In: *IEEE Transactions on Acoustics, Speech, and Signal Processing* 34.5, pp. 1111–1123.

Gaulme, P., J. Jackiewicz, T. Appourchaux, et al. (2014). “Surface activity and oscillation amplitudes of red giants in eclipsing binaries.” In: *The Astrophysical Journal* 785.1, 5.

Gaulme, P., J. Jackiewicz, F. Spada, et al. (2020). “Active red giants: Close binaries versus single rapid rotators.” In: *Astronomy & Astrophysics* 639, A63.

Gautschy, A. and H. Saio (1993). “On non-radial oscillations of B-type stars.” In: *Monthly Notices of the Royal Astronomical Society* 262.1, pp. 213–219.

Gautschy, A., H. Saio, and H. Harzenmoser (1998). “How to drive roAp stars.” In: *Monthly Notices of the Royal Astronomical Society* 301.1, pp. 31–41.

Gehan, C. et al. (2018). “Core rotation braking on the red giant branch for various mass ranges.” In: *Astronomy & Astrophysics* 616, A24.

Gentile Fusillo, N. P. et al. (2021). “A catalogue of white dwarfs in Gaia EDR3.” In: *Monthly Notices of the Royal Astronomical Society* 508.3, pp. 3877–3896.

Gerkema, T. and V. I. Shrira (2005). “Near-inertial waves in the ocean: beyond the ‘traditional approximation’.” In: *Journal of Fluid Mechanics* 529, pp. 195–219.

Gianninas, A., P. Bergeron, and G. Fontaine (2005). “Toward an empirical determination of the ZZ Ceti instability strip.” In: *The Astrophysical Journal* 631.2, 1100.

Gianninas, A., B. Curd, et al. (2016). “Discovery of three pulsating, mixed-atmosphere, extremely low-mass white dwarf precursors.” In: *The Astrophysical Journal Letters* 822.2, L27.

Gianninas, A., M. Kilic, et al. (2015). “The ELM survey. VI. Eleven new double degenerates.” In: *The Astrophysical Journal* 812.2, 167.

Ginzburg, S. et al. (2022). “Slow convection and fast rotation in crystallization-driven white dwarf dynamos.” In: *Monthly Notices of the Royal Astronomical Society* 514.3, pp. 4111–4119.

Gizon, L. and S. K. Solanki (2003). “Determining the inclination of the rotation axis of a Sun-like star.” In: *The Astrophysical Journal* 589.2, 1009.

Glatzel, W. (1994). “On the origin of strange modes and the mechanism of related instabilities.” In: *Monthly Notices of the Royal Astronomical Society* 271.1, pp. 66–74.

Goedbloed, H. and S. Poedts (2004). “Principles of magnetohydrodynamics: with applications to laboratory and astrophysical plasmas.” Cambridge University Press.

Goldreich, P. and Y. Wu (1999). “Gravity modes in ZZ Ceti stars. I. Quasi-adiabatic analysis of over stability.” In: *The Astrophysical Journal* 511.2, 904.

Gomes, P. and I. Lopes (2020). “Core magnetic field imprint in the non-radial oscillations of red giant stars.” In: *Monthly Notices of the Royal Astronomical Society* 496.1, pp. 620–628.

Goossens, M. (1972). “Perturbation of the radial and non-radial oscillations of a star by a magnetic field.” In: *Astrophysics and Space Science* 16.3, pp. 386–404.

Goossens, M. (1976). “Non-radial oscillations and stability of Prendergast’s model.” In: *Astrophysics and Space Science* 43.1, pp. 9–18.

Goossens, M., P. Smeyers, and J. Denis (1976). “Stellar oscillations and magnetic field perturbations of the boundary conditions.” In: *Astrophysics and Space Science* 39.2, pp. 257–272.

Gough, D. O. and A. G. Kosovichev (1993). “Initial asteroseismic inversions.” In: *International Astronomical Union Colloquium*. Vol. 137. Cambridge University Press, pp. 541–543.

Gould, A. et al. (2015). “WFIRST Ultra-Precise Astrometry II: Asteroseismology.” In: *Journal of Korean Astronomical Society* 48.2, pp. 93–104.

Grevesse, N. and A. J. Sauval (1998). “Standard solar composition.” In: *Space Science Reviews* 85, pp. 161–174.

Grosjean, M. et al. (2014). “Theoretical power spectra of mixed modes in low-mass red giant stars.” In: *Astronomy & Astrophysics* 572, A11.

Grunhut, J. H. et al. (2016). “The MiMeS survey of Magnetism in Massive Stars: magnetic analysis of the O-type stars.” In: *Monthly Notices of the Royal Astronomical Society*, pp. 2432–2470.

Gunson, J. (1987). “Perturbation theory for a Sturm-Liouville problem with an interior singularity.” In: *Proceedings of the Royal Society of London. Series A, Containing Papers of a Mathematical and Physical Character* 414.1846, pp. 255–269.

Guzik, J. A., A. B. Kaye, P. A. Bradley, A. N. Cox, and C. Neuforge (2000). “Driving the Gravity-Mode Pulsations in γ Doradus Variables.” In: *The Astrophysical Journal* 542.1, L57.

Guzik, J. A., A. B. Kaye, P. A. Bradley, A. N. Cox, C. Neuforge-Verheecke, et al. (2002). “A Proposed Pulsation Driving Mechanism for γ Doradus Variable Stars.” In: *International Astronomical Union Colloquium*. Vol. 185. Cambridge University Press, pp. 502–505.

Al-Gwaiz, M. A. (2008). “Sturm-Liouville theory and its applications.” Vol. 264. Springer.

Han, Z.-W. et al. (2020). “Binary population synthesis.” In: *Research in Astronomy and Astrophysics* 20.10, 161.

Handler, G. (2012). “Hybrid Pulsators among A/F-type Stars.” In: *Progress in Solar/Stellar Physics with Helio- and Asteroseismology*. Ed. by H Shibahashi, M Takata, and AE Lynas-Gray. Vol. 462. Astronomical Society of the Pacific Conference Series, 111.

Handler, G. et al. (2020). “Tidally trapped pulsations in a close binary star system discovered by TESS.” In: *Nature Astronomy* 4.7, pp. 684–689.

Hatt, E. J. et al. (2024). “Asteroseismic signatures of core magnetism and rotation in hundreds of low-luminosity red giants.” In: *Monthly Notices of the Royal Astronomical Society* 534.2, pp. 1060–1076.

Hayek, M. (2014). “An exact solution for a nonlinear diffusion equation in a radially symmetric inhomogeneous medium.” In: *Computers & Mathematics with Applications* 68.12, pp. 1751–1757.

Hekker, S. et al. (2023). “Low-period spacing core-helium burning giants: ‘hot subdwarf analogues’?.”

Henneco, J., F. R. N. Schneider, S. Hekker, et al. (2024). “Merger seismology: Distinguishing massive merger products from genuine single stars using asteroseismology.” In: *Astronomy & Astrophysics* 690, A65.

Henneco, J., F. R. N. Schneider, M. Heller, et al. (2025). “Asteroseismic predictions for a massive main-sequence merger product.”

Henneco, J., T. Van Reeth, et al. (2021). “The effect of the centrifugal acceleration on period spacings of gravito-inertial modes in intermediate-mass stars.” In: *Astronomy & Astrophysics* 648, A97.

Hermes, J. J., B. T. Gänsicke, A. Bischoff-Kim, et al. (2015). “Insights into internal effects of common-envelope evolution using the extended Kepler mission.” In: *Monthly Notices of the Royal Astronomical Society* 451.2, pp. 1701–1712.

Hermes, J. J., B. T. Gänsicke, S. D. Kawaler, et al. (2017). “White dwarf rotation as a function of mass and a dichotomy of mode line widths: Kepler observations of 27 pulsating DA white dwarfs through K2 campaign 8.” In: *The Astrophysical Journal Supplement Series* 232.2, 23.

Hermes, J. J., S. D. Kawaler, et al. (2017). “A deep test of radial differential rotation in a helium-atmosphere white dwarf. I. Discovery of pulsations in PG 0112+104.” In: *The Astrophysical Journal* 835.2, 277.

Hermes, J. J., S. O. Kepler, et al. (2013). “Discovery of an ultramassive pulsating white dwarf.” In: *The Astrophysical Journal Letters* 771.1, L2.

Hermes, J. J., M. H. Montgomery, A. Gianninas, et al. (2013). “A new class of pulsating white dwarf of extremely low mass: the fourth and fifth members.” In: *Monthly Notices of the Royal Astronomical Society* 436.4, pp. 3573–3580.

Hermes, J. J., M. H. Montgomery, F. Mullally, et al. (2013). “A new timescale for period change in the pulsating DA white dwarf WD 0111+0018.” In: *The Astrophysical Journal* 766.1, 42.

Hermes, J. J., M. H. Montgomery, D. E. Winget, W. R. Brown, A. Gianninas, et al. (2013). “Discovery of pulsations, including possible pressure modes, in two new extremely low mass, He-core white dwarfs.” In: *The Astrophysical Journal* 765.2, 102.

Hermes, J. J., M. H. Montgomery, D. E. Winget, W. R. Brown, M. Kilic, et al. (2012). “SDSS J184037.78+642312.3: the first pulsating extremely low mass white dwarf.” In: *The Astrophysical Journal Letters* 750.2, L28.

Hillman, Y. et al. (2016). “Growing white dwarfs to the Chandrasekhar limit: the parameter space of the single degenerate SN Ia channel.” In: *The Astrophysical Journal* 819.2, 168.

Hills, J. G. and C. A. Day (1976). “Stellar collisions in globular clusters.” In: *Astrophysical Letters* 17, 87.

Homer, M. S. (1990). “Boundary value problems for the Laplace tidal wave equation.” In: *Proceedings of the Royal Society of London. Series A, Containing Papers of a Mathematical and Physical Character* 428.1874, pp. 157–180.

Hon, M., D. Huber, J. S. Kuszlewicz, et al. (2021). “A “Quick Look” at All-sky Galactic Archeology with TESS: 158,000 Oscillating Red Giants from the MIT Quick-look Pipeline.” In: *The Astrophysical Journal* 919.2, 131.

Hon, M., D. Huber, N. Z. Rui, et al. (2023). “A close-in giant planet escapes engulfment by its star.” In: *Nature* 618.7967, pp. 917–920.

Houdek, G., N. J. Balmforth, et al. (1999). “Amplitudes of stochastically excited oscillations in main-sequence stars.” In: *Astronomy & Astrophysics* 351, pp. 582–596.

Houdek, G. and M.-A. Dupret (2015). “Interaction between convection and pulsation.” In: *Living Reviews in Solar Physics* 12, pp. 1–88.

Houdek, G. and D. O. Gough (2007). “An asteroseismic signature of helium ionization.” In: *Monthly Notices of the Royal Astronomical Society* 375.3, pp. 861–880.

Hough, S. S. (1898a). “On the application of harmonic analysis to the dynamical theory of the tides. Part II: On the general integration of Laplace’s dynamical equations.” In: *Proceedings of the Royal Society of London. Series A, Containing Papers of a Mathematical and Physical Character* 191, pp. 139–185.

Hough, S. S. (1898b). “V. On the application of harmonic analysis to the dynamical theory of the tides.—Part II. On the general integration of Laplace’s dynamical equations.” In: *Proceedings of the Royal Society of London. Series A, Containing Papers of a Mathematical and Physical Character* 191, pp. 139–185.

Hoven, M. and Y. Levin (2011). “Magnetar oscillations—I. Strongly coupled dynamics of the crust and the core.” In: *Monthly Notices of the Royal Astronomical Society* 410.2, pp. 1036–1051.

Huber, D. et al. (2023). “Asteroseismology with the Roman Galactic Bulge Time-Domain Survey.”

Hubrig, S. et al. (2004). “New measurements of magnetic fields of roAp stars with FORS 1 at the VLT.” In: *Astronomy & Astrophysics* 415.2, pp. 685–689.

Iben Jr., I. and A. V. Tutukov (1996). “On the evolution of symbiotic stars and other binaries with accreting degenerate dwarfs.” In: *The Astrophysical Journal Supplement Series* 105, 145.

Isern, J. et al. (2017). “A common origin of magnetism from planets to white dwarfs.” In: *The Astrophysical Journal Letters* 836.2, L28.

Ivanova, N., S. Justham, X. Chen, et al. (2013). “Common envelope evolution: where we stand and how we can move forward.” In: *The Astronomy and Astrophysics Review* 21.1, 59.

Ivanova, N., S. Justham, J. L. A. Nandez, et al. (2013). “Identification of the long-sought common-envelope events.” In: *Science* 339.6118, pp. 433–435.

Izzard, R. G., C. S. Jeffery, and J. Lattanzio (2007). “Origin of the early-type R stars: a binary-merger solution to a century-old problem?.” In: *Astronomy & Astrophysics* 470.2, pp. 661–673.

Jayaraman, R. et al. (2022). “Tidally Tilted Pulsations in HD 265435, a Subdwarf B Star with a Close White Dwarf Companion.” In: *The Astrophysical Journal Letters* 928.2, L14.

Jermyn, A. S. et al. (2023). “Modules for experiments in stellar astrophysics (MESA): time-dependent convection, energy conservation, automatic differentiation, and infrastructure.” In: *The Astrophysical Journal Supplement Series* 265.1, 15.

Jiang, C. and J. Christensen-Dalsgaard (2014). “Verification of asymptotic relation for mixed modes in red giant stars.” In: *Monthly Notices of the Royal Astronomical Society* 444.4, pp. 3622–3631.

Jones, P. W. et al. (1989). “On the possibility of detecting weak magnetic fields in variable white dwarfs.” In: *The Astrophysical Journal* 336, pp. 403–408.

Jura, M. (2003). “A flared, orbiting, dusty disk around HD 233517.” In: *The Astrophysical Journal* 582.2, 1032.

Kallinger, T., S. Hekker, et al. (2012). “Evolutionary influences on the structure of red-giant acoustic oscillation spectra from 600d of Kepler observations.” In: *Astronomy & Astrophysics* 541, A51.

Kallinger, T., W. W. Weiss, et al. (2010). “Oscillating red giants in the CoRoT exofield: asteroseismic mass and radius determination.” In: *Astronomy & Astrophysics* 509, A77.

Kamiński, T., M. Schmidt, et al. (2023). “Lithium in red novae and their remnants.” In: *Astronomy & Astrophysics* 672, A196.

Kamiński, T., W. Steffen, et al. (2018). “Submillimeter-wave emission of three Galactic red novae: cool molecular outflows produced by stellar mergers.” In: *Astronomy & Astrophysics* 617, A129.

Kanaan, A. et al. (2005). “Whole Earth Telescope observations of BPM 37093: A seismological test of crystallization theory in white dwarfs.” In: *Astronomy & Astrophysics* 432.1, pp. 219–224.

Karambelkar, V. R. et al. (2021). “Census of R Coronae Borealis Stars. I. Infrared Light Curves from Palomar Gattini IR.” In: *The Astrophysical Journal* 910.2, 132.

Kasliwal, M. M. et al. (2017). “SPIRITS: Uncovering unusual infrared transients with Spitzer.” In: *The Astrophysical Journal* 839.2, 88.

Kato, M., I. Hachisu, and H. Saio (2017). “Recurrent novae and long-term evolution of mass-accreting white dwarfs—toward the accurate mass retention efficiency.” In: *The Golden Age of Cataclysmic Variables and Related Objects IV*, 56.

Kaufman, E. et al. (2022). “The stability of Prendergast magnetic fields.” In: *Monthly Notices of the Royal Astronomical Society* 517.3, pp. 3332–3340.

Kawaler, S. D. (1988). “The hydrogen shell game-pulsational instabilities in hydrogen shell-burning planetary nebula nuclei.” In: *The Astrophysical Journal* 334, pp. 220–228.

Kawaler, S. D. et al. (1995). “Whole earth telescope observations and seismological analysis of the pre-white dwarf PG 2131+066.” In: *The Astrophysical Journal* 450.1, pp. 350–363.

Kepler, S. O. et al. (2013). “Magnetic white dwarf stars in the Sloan Digital Sky Survey.” In: *Monthly Notices of the Royal Astronomical Society* 429.4, pp. 2934–2944.

Keszthelyi, Z. (2023). “Magnetism in High-Mass Stars.” In: *Galaxies* 11.2, 40.

Kilic, M., A. H. Córscico, et al. (2023). “WD J004917.14-252556.81: the most massive pulsating white dwarf.” In: *Monthly Notices of the Royal Astronomical Society* 522.2, pp. 2181–2187.

Kilic, M., A. Gianninas, et al. (2015). “A dark spot on a massive white dwarf.” In: *The Astrophysical Journal Letters* 814.2, L31.

Kilic, M., J. J. Hermes, A. H. Corsico, et al. (2018). “A refined search for pulsations in white dwarf companions to millisecond pulsars.” In: *Monthly Notices of the Royal Astronomical Society* 479.1, pp. 1267–1272.

Kilic, M., J. J. Hermes, A. Gianninas, et al. (2015). “PSR J1738+0333: the first millisecond pulsar + pulsating white dwarf binary.” In: *Monthly Notices of the Royal Astronomical Society: Letters* 446.1, pp. L26–L30.

Kilic, M., A. G. Moss, et al. (2023). “The merger fraction of ultramassive white dwarfs.” In: *Monthly Notices of the Royal Astronomical Society* 518.2, pp. 2341–2353.

Kippenhahn, R. (1981). “On the core mass luminosity relation..” In: *Astronomy & Astrophysics*. 0th ser. 102, pp. 293–295.

Kirch, W. (2008). “Encyclopedia of Public Health: Volume 1: A-H Volume 2: I-Z.” Springer Science & Business Media.

Klion, H. and E. Quataert (2017). “A diagnostic for localizing red giant differential rotation.” In: *Monthly Notices of the Royal Astronomical Society: Letters* 464.1, pp. L16–L20.

Knigge, C. (2011). “The Evolution of Cataclysmic Variables.” In: *Evolution of Compact Binaries*. Ed. by L Schmidtobreick, MR Schreiber, and C Tappert. Vol. 447. Astronomical Society of the Pacific Conference Series, 3.

Kochanek, C. S., S. M. Adams, and K. Belczynski (2014). “Stellar mergers are common.” In: *Monthly Notices of the Royal Astronomical Society* 443.2, pp. 1319–1328.

Kochukhov, O., A. Lundin, et al. (2010). “The extraordinary complex magnetic field of the helium-strong star HD 37776.” In: *The Astrophysical Journal* 726.1, 24.

Kochukhov, O. and G. A. Wade (2016). “Magnetic field topology of τ Scorpii-The uniqueness problem of Stokes V ZDI inversions.” In: *Astronomy & Astrophysics* 586, A30.

Kosakowski, A. et al. (2023). “The ELM Survey South. II. Two Dozen New Low-mass White Dwarf Binaries.” In: *The Astrophysical Journal* 950.2, 141.

Kovetz, A. and D. Prialnik (1994). “Accretion onto a 1.4 solar mass white dwarf: Classical nova, recurrent nova, or supernova?.” In: *The Astrophysical Journal* 424.1, pp. 319–332.

Kress, R. (1989). “Linear integral equations.”

Kroupa, P. (2001). “On the variation of the initial mass function.” In: *Monthly Notices of the Royal Astronomical Society* 322.2, pp. 231–246.

Kroupa, P. and C. Weidner (2003). “Galactic-field initial mass functions of massive stars.” In: *The Astrophysical Journal* 598.2, 1076.

Kulkarni, S. R., E. O. Ofek, et al. (2007). “An unusually brilliant transient in the galaxy M85.” In: *Nature* 447.7143, pp. 458–460.

Kulkarni, S. R. and C. Thompson (1998). “A star powered by magnetism.” In: *Nature* 393.6682, pp. 215–216.

Kumar, Y. B., B. E. Reddy, S. W. Campbell, et al. (2020). “Discovery of ubiquitous lithium production in low-mass stars.” In: *Nature Astronomy* 4.11, pp. 1059–1063.

Kumar, Y. B., B. E. Reddy, and D. L. Lambert (2011). “Origin of lithium enrichment in K giants.” In: *The Astrophysical Journal Letters* 730.1, L12.

Kurtz, D. W. (1982). “Rapidly oscillating Ap stars.” In: *Monthly Notices of the Royal Astronomical Society* 200.3, pp. 807–859.

Kurtz, D. W. et al. (2014). “Asteroseismic measurement of surface-to-core rotation in a main-sequence A star, KIC 11145123.” In: *Monthly Notices of the Royal Astronomical Society* 444.1, pp. 102–116.

Kuszlewicz, J. S., M. Hon, and D. Huber (2023). “Mixed-mode Ensemble Asteroseismology of Low-luminosity Kepler Red Giants.” In: *The Astrophysical Journal* 954.2, 152.

Lagos, F. et al. (2020). “Most EL CVn systems are inner binaries of hierarchical triples.” In: *Monthly Notices of the Royal Astronomical Society: Letters* 499.1, pp. L121–L125.

Landstreet, J. D. (2014). “Basics of spectropolarimetry.” In: *Proceedings of the International Astronomical Union* 9.S307, pp. 311–320.

Lawson, W. A. and D. Kilkenny (1996). “The observational characterization of hydrogen-deficient carbon stars as pulsating stars.” In: *ASP Conf. Ser.* Vol. 96, 349.

Lecocanet, D., D. M. Bowman, and T. Van Reeth (2022). “Asteroseismic inference of the near-core magnetic field strength in the main-sequence B star HD 43317.” In: *Monthly Notices of the Royal Astronomical Society: Letters* 512.1, pp. L16–L20.

Lecocanet, D., G. M. Vasil, et al. (2017). “Conversion of internal gravity waves into magnetic waves.” In: *Monthly Notices of the Royal Astronomical Society* 466.2, pp. 2181–2193.

Ledoux, P. (1951). “The Nonradial Oscillations of Gaseous Stars and the Problem of Beta Canis Majoris..” In: *The Astrophysical Journal* 114.

Lee, U. and H. Saio (1997). “Low-frequency nonradial oscillations in rotating stars. I. Angular dependence.” In: *The Astrophysical Journal* 491.2, 839.

Levin, Y. (2006). “QPOs during magnetar flares are not driven by mechanical normal modes of the crust.” In: *Monthly Notices of the Royal Astronomical Society: Letters* 368.1, pp. L35–L38.

Levin, Y. (2007). “On the theory of magnetar QPOs.” In: *Monthly Notices of the Royal Astronomical Society* 377.1, pp. 159–167.

Li, G., S. Deheuvels, and J. Ballot (2024). “Asteroseismic measurement of core and envelope rotation rates for 2006 red giant branch stars.” In: *Astronomy & Astrophysics* 688, A184.

Li, G., S. Deheuvels, J. Ballot, and F. Lignières (2022). “Magnetic fields of 30 to 100 kG in the cores of red giant stars.” In: *Nature* 610.7930, pp. 43–46.

Li, G., S. Deheuvels, T. Li, et al. (2023). “Internal magnetic fields in 13 red giants detected by asteroseismology.” In: *Astronomy & Astrophysics* 680, A26.

Li, G., T. Van Reeth, et al. (2020). “Gravity-mode period spacings and near-core rotation rates of 611 γ Doradus stars with Kepler.” In: *Monthly Notices of the Royal Astronomical Society* 491.3, pp. 3586–3605.

Li, M. and L. Xiao (2016). “Lifetimes and Accretion Rates of Protoplanetary Disks.” In: *The Astrophysical Journal* 820.1, 36.

Li, T., T. R. Bedding, D. Huber, et al. (2018). “Modelling Kepler red giants in eclipsing binaries: calibrating the mixing-length parameter with asteroseismology.” In: *Monthly Notices of the Royal Astronomical Society* 475.1, pp. 981–998.

Li, Y., T. R. Bedding, S. J. Murphy, et al. (2022). “Discovery of post-mass-transfer helium-burning red giants using asteroseismology.” In: *Nature Astronomy* 6.6, pp. 673–680.

Liebert, J., P. Bergeron, and J. B. Holberg (2003). “The true incidence of magnetism among field white dwarfs.” In: *The Astronomical Journal* 125.1, 348.

Lignières, F., M. Rieutord, and D. Reese (2006). “Acoustic oscillations of rapidly rotating polytropic stars-I. Effects of the centrifugal distortion.” In: *Astronomy & Astrophysics* 455.2, pp. 607–620.

Lindsay, C. J., J. M. J. Ong, and S. Basu (2023). “Near-core Acoustic Glitches Are Not Oscillatory: Consequences for Asteroseismic Probes of Convective Boundary Mixing.” In: *The Astrophysical Journal* 950.1, 19.

Liu, D. and D. Jiang (2021). “The fractions of post-binary-interaction stars and evolved blue straggler stars on the red giant branch of globular clusters.” In: *Research in Astronomy and Astrophysics* 21.9, 223.

Loi, S. T. (2020a). “Effect of a strong magnetic field on gravity-mode period spacings in red giant stars.” In: *Monthly Notices of the Royal Astronomical Society* 496.3, pp. 3829–3840.

Loi, S. T. (2020b). “Effect of a strong magnetic field on gravity-mode period spacings in red giant stars.” In: *Monthly Notices of the Royal Astronomical Society* 496.3, pp. 3829–3840.

Loi, S. T. (2020c). “Magneto-gravity wave packet dynamics in strongly magnetized cores of evolved stars.” In: *Monthly Notices of the Royal Astronomical Society* 493.4, pp. 5726–5742.

Loi, S. T. (2021). “Topology and obliquity of core magnetic fields in shaping seismic properties of slowly rotating evolved stars.” In: *Monthly Notices of the Royal Astronomical Society* 504.3, pp. 3711–3729.

Loi, S. T. and J. C. B. Papaloizou (2017). “Torsional Alfvén resonances as an efficient damping mechanism for non-radial oscillations in red giant stars.” In: *Monthly Notices of the Royal Astronomical Society* 467.3, pp. 3212–3225.

Loi, S. T. and J. C. B. Papaloizou (2018). “Effects of a strong magnetic field on internal gravity waves: trapping, phase mixing, reflection, and dynamical chaos.” In: *Monthly Notices of the Royal Astronomical Society* 477.4, pp. 5338–5357.

Lombardi Jr., J. C. et al. (2002). “Stellar collisions and the interior structure of blue stragglers.” In: *The Astrophysical Journal* 568.2, 939.

Longuet-Higgins, M. S. (1968). “The eigenfunctions of Laplace’s tidal equation over a sphere.” In: *Philosophical Transactions of the Royal Society A* 262.1132, pp. 511–607.

Lopez, I. D. et al. (2021). “Discovery, TESS Characterization, and Modeling of Pulsations in the Extremely Low-mass White Dwarf GD 278.” In: *The Astrophysical Journal* 922.2, 220.

Ma, L., C. Johnston, et al. (2024). “Variability of Blue Supergiants in the LMC with TESS.” In: *The Astrophysical Journal* 966.2, 196.

Ma, X.-Y., W. Zong, et al. (2023). “Amplitude and frequency variations in PG 0101+039 from K2 photometry-A pulsating hot B subdwarf star in an unsynchronized binary system.” In: *Astronomy & Astrophysics* 680, A11.

Maben, S. et al. (2023). “Asteroseismology sheds light on the origin of carbon-deficient red giants: likely merger products and linked to the Li-rich giants.” In: *The Astrophysical Journal* 957.1, 18.

MacGregor, K. B. and T. M. Rogers (2011). “Reflection and ducting of gravity waves inside the Sun.” In: *Solar Physics* 270, pp. 417–436.

MacLeod, M., E. C. Ostriker, and J. M. Stone (2018). “Bound outflows, unbound ejecta, and the shaping of bipolar remnants during stellar coalescence.” In: *The Astrophysical Journal* 868.2, 136.

Maeder, A. and G. Meynet (2005). “Stellar evolution with rotation and magnetic fields-III. The interplay of circulation and dynamo.” In: *Astronomy & Astrophysics* 440.3, pp. 1041–1049.

Mamajek, E. E. (2009). “Initial Conditions of Planet Formation: Lifetimes of Primordial Disks.” In: *AIP Conference Proceedings* 1158.1, pp. 3–10.

Markiel, J. A., J. H. Thomas, and H. M. Van Horn (1994). “Dynamo generation of magnetic field in the white dwarf GD 358.” In: *The Astrophysical Journal* 430, pp. 834–838.

Martell, S. L. et al. (2021a). “The GALAH survey: a census of lithium-rich giant stars.” In: *Monthly Notices of the Royal Astronomical Society* 505.4, pp. 5340–5355.

Martell, S. L. et al. (2021b). “The GALAH survey: a census of lithium-rich giant stars.” In: *Monthly Notices of the Royal Astronomical Society* 505.4, pp. 5340–5355.

Mastrobuono-Battisti, A. et al. (2019). “Mergers, tidal interactions, and mass exchange in a population of disc globular clusters-II. Long-term evolution.” In: *Astronomy & Astrophysics* 622, A86.

Mathieu, É. (1868). “Mémoire sur le mouvement vibratoire d’une membrane de forme elliptique..” In: *Journal de mathématiques pures et appliquées* 13, pp. 137–203.

Mathis, S. (2009). “Transport by gravito-inertial waves in differentially rotating stellar radiation zones-I-Theoretical formulation.” In: *Astronomy & Astrophysics* 506.2, pp. 811–828.

Mathis, S. and N. de Brye (2012). “Low-frequency internal waves in magnetized rotating stellar radiation zones-II. Angular momentum transport with a toroidal field.” In: *Astronomy & Astrophysics* 540, A37.

Mathis, S. and L. Bugnet (2023). “Asymmetries of frequency splittings of dipolar mixed modes: a window on the topology of deep magnetic fields.” In: *Astronomy & Astrophysics* 676, L9.

Mathis, S., L. Bugnet, et al. (2021). “Probing the internal magnetism of stars using asymptotic magneto-asteroseismology.” In: *Astronomy & Astrophysics* 647, A122.

Mathis, S. and N. De Brye (2011). “Low-frequency internal waves in magnetized rotating stellar radiation zones-I. Wave structure modification by a toroidal field.” In: *Astronomy & Astrophysics* 526, A65.

Mathis, S., C. Neiner, and N. T. Minh (2014). “Impact of rotation on stochastic excitation of gravity and gravito-inertial waves in stars.” In: *Astronomy & Astrophysics* 565, A47.

Mathis, S. and V. Prat (2019). “The traditional approximation of rotation, including the centrifugal acceleration for slightly deformed stars.” In: *Astronomy & Astrophysics* 631, A26.

Mathis, S. and J.-P. Zahn (2004). “Transport and mixing in the radiation zones of rotating stars-I. Hydrodynamical processes.” In: *Astronomy & Astrophysics* 425.1, pp. 229–242.

Mathur, S. et al. (2019). “Revisiting the impact of stellar magnetic activity on the detectability of solar-like oscillations by Kepler.” In: *Frontiers in Astronomy and Space Sciences* 6, 46.

Matteuzzi, M. et al. (2023). “Red horizontal branch stars: An asteroseismic perspective.” In: *Astronomy & Astrophysics* 671, A53.

Maxted, P. F. L., S. Bloemen, et al. (2014). “EL CVn-type binaries—discovery of 17 helium white dwarf precursors in bright eclipsing binary star systems.” In: *Monthly Notices of the Royal Astronomical Society* 437.2, pp. 1681–1697.

Maxted, P. F. L., L. Ferrario, et al. (2000). “WD 1953-011: a magnetic white dwarf with peculiar field structure.” In: *Monthly Notices of the Royal Astronomical Society* 315.3, pp. L41–L44.

Maxted, P. F. L., A. M. Serenelli, et al. (2013). “Multi-periodic pulsations of a stripped red-giant star in an eclipsing binary system.” In: *Nature* 498.7455, pp. 463–465.

Medeiros, J. R. de and M. Mayor (1999). “A catalog of rotational and radial velocities for evolved stars.” In: *Astronomy and Astrophysics Supplement Series* 139, pp. 433–460.

Melis, C. (2020). “Rise of the Phoenix Giants: A Rich History of Dusty Post-merger Stellar Remnants.” In: *Research Notes of the AAS* 4.12, 238.

Menon, A. et al. (2013). “Reproducing the Observed Abundances in RCB and HdC Stars with Post-double-degenerate Merger Models—Constraints on Merger and Post-merger Simulations and Physics Processes.” In: *The Astrophysical Journal* 772.1, 59.

Mestel, L. (1950). “On the thermal conductivity in dense stars.” In: 46.2, pp. 331–338.

Mestel, L. (1952). “On the theory of white dwarf stars: I. the energy sources of white dwarfs.” In: *Monthly Notices of the Royal Astronomical Society* 112.6, pp. 583–597.

Mestel, L. (1968). “Magnetic braking by a stellar wind—I.” In: *Monthly Notices of the Royal Astronomical Society* 138.3, pp. 359–391.

Metzger, B. D. and O. Pejcha (2017). “Shock-powered light curves of luminous red novae as signatures of pre-dynamical mass-loss in stellar mergers.” In: *Monthly Notices of the Royal Astronomical Society* 471.3, pp. 3200–3211.

Metzger, B. D., Y. Zenati, et al. (2021). “Transients from the Cataclysmic Deaths of Cataclysmic Variables.” In: *The Astrophysical Journal* 923.1, 100.

Michielsen, M., C. Aerts, and D. M. Bowman (2021). “Probing the temperature gradient in the core boundary layer of stars with gravito-inertial modes-The case of KIC 7760680.” In: *Astronomy & Astrophysics* 650, A175.

Michielsen, M., M. G. Pedersen, et al. (2019). “Probing the shape of the mixing profile and of the thermal structure at the convective core boundary through asteroseismology.” In: *Astronomy & Astrophysics* 628, A76.

Miglio, A., W. J. Chaplin, et al. (2016). “Detection of solar-like oscillations in relics of the Milky Way: asteroseismology of K giants in M4 using data from the NASA K2 mission.” In: *Monthly Notices of the Royal Astronomical Society* 461.1, pp. 760–765.

Miglio, A., L. Girardi, et al. (2021). “HAYDN – High-precision AsteroseismologY of DeNse stellar fields.” In: *Experimental Astronomy* 51.3, pp. 963–1001.

Miglio, A., J. Montalbán, F. Carrier, et al. (2010). “Evidence for a sharp structure variation inside a red-giant star.” In: *Astronomy & Astrophysics* 520, L6.

Miglio, A., J. Montalbán, A. Noels, et al. (2008). “Probing the properties of convective cores through g modes: high-order g modes in SPB and γ Doradus stars.” In: *Monthly Notices of the Royal Astronomical Society* 386.3, pp. 1487–1502.

Mink, S. E. de et al. (2014). “The incidence of stellar mergers and mass gainers among massive stars.” In: *The Astrophysical Journal* 782.1, 7.

Mombarg, J. S. G., A. Dotter, M. Rieutord, et al. (2022). “Predictions for gravity-mode periods and surface abundances in intermediate-mass dwarfs from shear mixing and radiative levitation.” In: *The Astrophysical Journal* 925.2, 154.

Mombarg, J. S. G., A. Dotter, T. Van Reeth, et al. (2020). “Asteroseismic modeling of gravity modes in slowly rotating A/F stars with radiative levitation.” In: *The Astrophysical Journal* 895.1, 51.

Mombarg, J. S. G., M. Rieutord, and F. E. Lara (2023). “The first two-dimensional stellar structure and evolution models of rotating stars-Calibration to β Cephei pulsator HD 192575.” In: *Astronomy & Astrophysics* 677, L5.

Montgomery, M. H., J. J. Hermes, et al. (2020). “Limits on mode coherence in pulsating DA white dwarfs due to a nonstatic convection zone.” In: *The Astrophysical Journal* 890.1, 11.

Montgomery, M. H., J. L. Provencal, et al. (2010). “Evidence for temperature change and oblique pulsation from light curve fits of the pulsating white dwarf GD 358.” In: *The Astrophysical Journal* 716.1, 84.

Mosser, B., C. Barban, et al. (2011). “Mixed modes in red-giant stars observed with CoRoT.” In: *Astronomy & Astrophysics* 532, A86.

Mosser, B., K. Belkacem, et al. (2017). “Dipole modes with depressed amplitudes in red giants are mixed modes.” In: *Astronomy & Astrophysics* 598, A62.

Mosser, B., O. Benomar, et al. (2014). “Mixed modes in red giants: a window on stellar evolution.” In: *Astronomy & Astrophysics* 572, L5.

Mosser, B., Y. Elsworth, et al. (2012). “Characterization of the power excess of solar-like oscillations in red giants with Kepler.” In: *Astronomy & Astrophysics* 537, A30.

Mosser, B., M. J. Goupil, K. Belkacem, J. P. Marques, P. G. Beck, S. Bloemen, J. De Ridder, C. Barban, S. Deheuvels, Y. Elsworth, et al. (2012a). “Spin down of the core rotation in red giants.” In: *Astronomy & Astrophysics* 548, A10.

Mosser, B., M. J. Goupil, K. Belkacem, J. P. Marques, P. G. Beck, S. Bloemen, J. De Ridder, C. Barban, S. Deheuvels, Y. Elsworth, et al. (2012b). “Spin down of the core rotation in red giants.” In: *Astronomy & Astrophysics* 548, A10.

Mosser, B., C. Pinçon, et al. (2017). “Period spacings in red giants-III. Coupling factors of mixed modes.” In: *Astronomy & Astrophysics* 600, A1.

Mosser, B., M. Vrard, et al. (2015). “Period spacings in red giants-I. Disentangling rotation and revealing core structure discontinuities.” In: *Astronomy & Astrophysics* 584, A50.

Müller, J., Q. Coppée, and S. Hekker (2025). “Oscillations of red giant stars with magnetic damping in the core-I. Dissipation of mode energy in dipole-like magnetic fields.” In: *Astronomy & Astrophysics* 696, A134.

Murphy, S. J., T. Li, et al. (2021). “A binary with a δ Scuti star and an oscillating red giant: Orbit and asteroseismology of KIC 9773821.” In: *Monthly Notices of the Royal Astronomical Society*.

Murphy, S. J., H. Saio, et al. (2020). “On the first δ Sct-roAp hybrid pulsator and the stability of p and g modes in chemically peculiar A/F stars.” In: *Monthly Notices of the Royal Astronomical Society* 498.3, pp. 4272–4286.

Neiner, C. et al. (2020). “Transport of angular momentum by stochastically excited waves as an explanation for the outburst of the rapidly rotating Be star HD49330.” In: *Astronomy & Astrophysics* 644, A9.

Newsham, G., S. Starrfield, and F. Timmes (2014). “Evolution of accreting white dwarfs; some of them continue to grow.” In: *Stellar Novae: Past and Future Decades*. Ed. by PA Woudt and VARM Ribeiro. Vol. 490. Astronomical Society of the Pacific Conference Series, 287.

Nitta, A. et al. (2015). “Constraining the physics of carbon crystallization through pulsations of a massive DAV BPM37093.” In: *Proceedings of the International Astronomical Union* 11.A29B, pp. 493–496.

Observatoire de Paris GEPI, E. C. (2006). “Diagramme_HR_Be_star.png.” Wikimedia Commons. URL: https://commons.wikimedia.org/wiki/File:Diagramme_HR_Be_star.png.

Ogilvie, G. I. and D. N. C. Lin (2004). “Tidal dissipation in rotating giant planets.” In: *The Astrophysical Journal* 610.1, 477.

Ong, J. M. J. (2025). “Signatures of Core-envelope Rotational Misalignment in the Mixed-mode Asteroseismology of Kepler-56.” In: *The Astrophysical Journal* 980.1, 40.

Ong, J. M. J. and S. Basu (2019). “Explaining deviations from the scaling relationship of the large frequency separation.” In: *The Astrophysical Journal* 870.1, 41.

Ong, J. M. J. and S. Basu (2020). “Semianalytic Expressions for the Isolation and Coupling of Mixed Modes.” In: *The Astrophysical Journal* 898.2, 127.

Ong, J. M. J., L. Bugnet, and S. Basu (2022). “Mode Mixing and Rotational Splittings. I. Near-degeneracy Effects Revisited.” In: *The Astrophysical Journal* 940.1, 18.

Ong, J. M. J., M. T. Y. Hon, et al. (2024). “The Gasing Pangkah Collaboration: I. Asteroseismic Identification and Characterisation of a Rapidly-Rotating Engulfment Candidate.” In: *The Astrophysical Journal* 966.1, 42.

Østensen, R. H. et al. (2014). “Stochastic pulsations in the subdwarf-B star KIC 2991276.” In: *Astronomy & Astrophysics* 564, L14.

Ouazzani, R.-M., F. Lignières, et al. (2020). “First evidence of inertial modes in γ Doradus stars: The core rotation revealed.” In: *Astronomy & Astrophysics* 640, A49.

Ouazzani, R.-M., S. J. A. J. Salmon, et al. (2017). “A new asteroseismic diagnostic for internal rotation in γ Doradus stars.” In: *Monthly Notices of the Royal Astronomical Society* 465.2, pp. 2294–2309.

Pablo, H. et al. (2012). “Seismic evidence for non-synchronization in two close sdB+dM binaries from Kepler photometry.” In: *Monthly Notices of the Royal Astronomical Society* 422.2, pp. 1343–1351.

Paczynski, B. (1976). “Common envelope binaries.” In: *Symposium-International Astronomical Union*. Vol. 73. Cambridge University Press, pp. 75–80.

Pakmor, R. et al. (2024). “Large-scale ordered magnetic fields generated in mergers of helium white dwarfs.” In.

Pala, A. F. et al. (2022). “Constraining the evolution of cataclysmic variables via the masses and accretion rates of their underlying white dwarfs.” In: *Monthly Notices of the Royal Astronomical Society* 510.4, pp. 6110–6132.

Pápics, P. I. et al. (2017). “Signatures of internal rotation discovered in the Kepler data of five slowly pulsating B stars.” In: *Astronomy & Astrophysics* 598, A74.

Park, J., V. Prat, and S. Mathis (2020). “Horizontal shear instabilities in rotating stellar radiation zones-I. Inflectional and inertial instabilities and the effects of thermal diffusion.” In: *Astronomy & Astrophysics* 635, A133.

Pascal57 (2019). “HR_Diagram_for_pulsating_stars.svg.” Wikimedia Commons. URL: https://commons.wikimedia.org/wiki/File:HR_Diagram_for_pulsating_stars.svg.

Paxton, B., L. Bildsten, et al. (2010). “Modules for experiments in stellar astrophysics (MESA).” In: *The Astrophysical Journal Supplement Series* 192.1, 3.

Paxton, B., M. Cantiello, et al. (2013). “Modules for experiments in stellar astrophysics (MESA): planets, oscillations, rotation, and massive stars.” In: *The Astrophysical Journal Supplement Series* 208.1, 4.

Paxton, B., P. Marchant, et al. (2015). “Modules for experiments in stellar astrophysics (MESA): binaries, pulsations, and explosions.” In: *The Astrophysical Journal Supplement Series* 220.1, 15.

Paxton, B., J. Schwab, et al. (2018). “Modules for experiments in stellar astrophysics (MESA): Convective boundaries, element diffusion, and massive star explosions.” In: *The Astrophysical Journal Supplement Series* 234.2.

Paxton, B., R. Smolec, et al. (2019). “Modules for Experiments in Stellar Astrophysics (MESA): pulsating variable stars, rotation, convective boundaries, and energy conservation.” In: *The Astrophysical Journal Supplement Series* 243.1, 10.

Pedersen, M. G. et al. (2018). “The shape of convective core overshooting from gravity-mode period spacings.” In: *Astronomy & Astrophysics* 614, A128.

Pejcha, O., B. D. Metzger, and K. Tomida (2016). “Binary stellar mergers with marginally bound ejecta: excretion discs, inflated envelopes, outflows, and their luminous transients.” In: *Monthly Notices of the Royal Astronomical Society* 461.3, pp. 2527–2539.

Pelisoli, I., K. J. Bell, et al. (2019). “The sdA problem–III. New extremely low-mass white dwarfs and their precursors from Gaia astrometry.” In: *Monthly Notices of the Royal Astronomical Society* 482.3, pp. 3831–3842.

Pelisoli, I., M. Dorsch, et al. (2022). “Discovery and analysis of three magnetic hot subdwarf stars: evidence for merger-induced magnetic fields.” In: *Monthly Notices of the Royal Astronomical Society* 515.2, pp. 2496–2510.

Pelisoli, I., S. O. Kepler, et al. (2018). “The sdA problem–II. Photometric and spectroscopic follow-up.” In: *Monthly Notices of the Royal Astronomical Society* 478.1, pp. 867–884.

Pichardo Marcano, M., L. E. Rivera Sandoval, et al. (2023). “A candidate magnetic helium-core white dwarf in the globular cluster NGC 6397.” In: *Monthly Notices of the Royal Astronomical Society* 521.4, pp. 5026–5032.

Pichardo Marcano, M., L. E. R. Sandoval, et al. (2025). “A second candidate magnetic helium core white dwarf and 3 other variable white dwarfs in the globular cluster NGC 6397.” In: *The Astrophysical Journal* 979.2, 167.

Piersanti, L. et al. (2000). “Hydrogen-Accreting Carbon-Oxygen White Dwarfs of Low Mass: Thermal and Chemical Behavior of Burning Shells.” In: *The Astrophysical Journal* 535.2, 932.

Pigulski, A. et al. (2024). “OGLE-BLAP-001 and ZGP-BLAP-08: Two possible magnetic blue large-amplitude pulsators.” In: *Astronomy & Astrophysics* 691, A343.

Pinçon, C., K. Belkacem, et al. (2017). “Can plume-induced internal gravity waves regulate the core rotation of subgiant stars?” In: *Astronomy & Astrophysics* 605, A31.

Pinçon, C., M. J. Goupil, and K. Belkacem (2020). “Probing the mid-layer structure of red giants-I. Mixed-mode coupling factor as a seismic diagnosis.” In: *Astronomy & Astrophysics* 634, A68.

Pinçon, C. and M. Takata (2022). “Multi-cavity gravito-acoustic oscillation modes in stars-A general analytical resonance condition.” In: *Astronomy & Astrophysics* 661, A139.

Pintér, B., R. Erdélyi, and M. Goossens (2007). “Global oscillations in a magnetic solar model-II. Oblique propagation.” In: *Astronomy & Astrophysics* 466.1, pp. 377–388.

Poedts, S., D. Hermans, and M. Goossens (1985). “The continuous spectrum of an axisymmetric self-gravitating and static equilibrium with a mixed poloidal and toroidal magnetic field.” In: *Astronomy and Astrophysics* 151, pp. 16–26.

Prat, V., S. Mathis, B. Buyschaert, et al. (2019). “Period spacings of gravity modes in rapidly rotating magnetic stars-I. Axisymmetric fossil field with poloidal and toroidal components.” In: *Astronomy & Astrophysics* 627, A64.

Prat, V., S. Mathis, C. Neiner, et al. (2020a). “Period spacings of gravity modes in rapidly rotating magnetic stars-II. The case of an oblique dipolar fossil magnetic field.” In: *Astronomy & Astrophysics* 636, A100.

Prat, V., S. Mathis, C. Neiner, et al. (2020b). “Period spacings of gravity modes in rapidly rotating magnetic stars-II. The case of an oblique dipolar fossil magnetic field.” In: *Astronomy & Astrophysics* 636, A100.

Prendergast, K. H. (1956). “The Equilibrium of a Self-Gravitating Incompressible Fluid Sphere with a Magnetic Field. I.” In: *The Astrophysical Journal* 123, 498.

Press, W. H. et al. (2007). “Numerical Recipes with Source Code CD-ROM 3rd Edition: The Art of Scientific Computing.” Cambridge University Press.

Price-Whelan, A. M. et al. (2020). “Close Binary Companions to APOGEE DR16 Stars: 20,000 Binary-star Systems Across the Color–Magnitude Diagram.” In: *The Astrophysical Journal* 895.1, 2.

Proctor, M. R. E. and N. O. Weiss (1982). “Magnetohydrodynamic convection.” In: *Reports on Progress in Physics* 45.11, 1317.

Provencal, J. L. et al. (2009). “2006 Whole Earth Telescope observations of GD358: a new look at the prototype DBV.” In: *The Astrophysical Journal* 693.1, 564.

Punzi, K. M. et al. (2017). “Is the Young Star RZ Piscium Consuming Its Own (Planetary) Offspring?” In: *The Astronomical Journal* 155.1, 33.

Raghavan, D. et al. (2010). “A survey of stellar families: multiplicity of solar-type stars.” In: *The Astrophysical Journal Supplement Series* 190.1, 1.

Rauer, H. et al. (2014). “The PLATO 2.0 mission.” In: *Experimental Astronomy* 38, pp. 249–330.

Rauf, S. and J. A. Tataronis (1995). “On the Alfvén resonance and its existence.” In: *Physics of Plasmas* 2.1, pp. 340–342.

Rebull, L. M. et al. (2015). “On Infrared Excesses Associated With Li-Rich K Giants.” In: *The Astronomical Journal* 150.4, 123.

Reddy, B. E. et al. (2002). “Spectroscopic Study of IRAS 19285+0517 (PDS 100): A Rapidly Rotating Li-Rich K Giant.” In: *The Astronomical Journal* 123.4, 1993.

Reed, M. D. et al. (2007). “Follow-up observations of pulsating subdwarf B stars: Multisite campaigns on PG 1618+563B and PG 0048+091.” In: *The Astrophysical Journal* 664.1, 518.

Reese, D., F. Rincon, and M. Rieutord (2004). “Oscillations of magnetic stars-II. Axisymmetric toroidal and non-axisymmetric shear Alfvén modes in a spherical shell.” In: *Astronomy & Astrophysics* 427.1, pp. 279–292.

Refsdal, S. and A. Weigert (1970). “Shell Source Burning Stars with Highly Condensed Cores.” In: *Astronomy & Astrophysics* 6, 426.

Reimers, D. (1975). *Circumstellar absorption lines and mass loss from red giants*. Tech. rep. Univ., Kiel.

Reimers, D. (1977). “On the absolute scale of mass-loss in red giants. I-Circumstellar absorption lines in the spectrum of the visual companion of Alpha-1 HER.” In: *Astronomy and Astrophysics* 61.2, pp. 217–224.

Riabouchinsky, D. (1911). “Methode des variables de dimension zero, et son application en aerodynamique.” In: *L'aérophile* 1, pp. 407–408.

Ricker, G. R. et al. (2015). “Transiting exoplanet survey satellite.” In: *Journal of Astronomical Telescopes, Instruments, and Systems* 1.1, pp. 014003–014003.

Rieutord, M. and L. Valdettaro (1997). “Inertial waves in a rotating spherical shell.” In: *Journal of Fluid Mechanics* 341, pp. 77–99.

Rincon, F. and M. Rieutord (2003). “Oscillations of magnetic stars: I. Axisymmetric shear Alfvén modes of a spherical shell in a dipolar magnetic field.” In: *Astronomy & Astrophysics* 398.2, pp. 663–675.

Roestel, J. van et al. (2018). “Discovery of 36 eclipsing EL CVn binaries found by the Palomar Transient Factory.” In: *Monthly Notices of the Royal Astronomical Society* 475.2, pp. 2560–2590.

Rogers, T. M. (2015). “On the differential rotation of massive main-sequence stars.” In: *The Astrophysical Journal Letters* 815.2, L30.

Rogers, T. M. and K. B. MacGregor (2010). “On the interaction of internal gravity waves with a magnetic field—I. Artificial wave forcing.” In: *Monthly Notices of the Royal Astronomical Society* 401.1, pp. 191–196.

Rose, M. E. (1995). "Elementary theory of angular momentum." Courier Corporation.

Rossem, W. E. van (2023). "Astroseismology in the red clump: mass transfer and merger remnants through mixed modes". PhD thesis. University of Birmingham.

Rowan, D. M. et al. (2019). "Detections and constraints on white dwarf variability from time-series GALEX observations." In: *Monthly Notices of the Royal Astronomical Society* 486.4, pp. 4574–4589.

Rui, N. Z. and J. Fuller (2021a). "Astroseismic fingerprints of stellar mergers." In: *Monthly Notices of the Royal Astronomical Society* 508.2, pp. 1618–1631.

Rui, N. Z. and J. Fuller (2021b). "Astroseismic Signatures of Stellar Mergers." Zenodo. URL: <https://doi.org/10.5281/zenodo.4782723>.

Rui, N. Z. and J. Fuller (2023). "Gravity waves in strong magnetic fields." In: *Monthly Notices of the Royal Astronomical Society* 523.1, pp. 582–602.

Rui, N. Z. and J. Fuller (2024). "Finding the unusual red giant remnants of cataclysmic variable mergers." In: *Open Journal of Astrophysics*.

Rui, N. Z., J. Fuller, and J. J. Hermes (2025). "Supersensitive Seismic Magnetometry of White Dwarfs." In: *The Astrophysical Journal* 981.1, 72.

Rui, N. Z., J. Fuller, and J. M. J. Ong (2025). "It's not just a phase: oblique pulsations in magnetic red giants and other stochastic oscillators." In: *The Astrophysical Journal Letters* 985.2, L39.

Rui, N. Z., J. M. J. Ong, and S. Mathis (2024). "Astroseismic g-mode period spacings in strongly magnetic rotating stars." In: *Monthly Notices of the Royal Astronomical Society* 527.3, pp. 6346–6362.

Rursus (2008). "HR-vartype.svg." Wikimedia Commons. URL: <https://commons.wikimedia.org/wiki/File:HR-vartype.svg>.

Saio, H. and A. Gautschy (2004). "Axisymmetric p-mode pulsations of stars with dipole magnetic fields." In: *Monthly Notices of the Royal Astronomical Society* 350.2, pp. 485–505.

Saio, H., M. Takata, et al. (2021). "Rotation of the convective core in γ Dor stars measured by dips in period spacings of g modes coupled with inertial modes." In: *Monthly Notices of the Royal Astronomical Society* 502.4, pp. 5856–5874.

Salpeter, E. E. (1957). "Nuclear reactions in stars. Buildup from helium." In: *Physical Review* 107.2, 516.

Samadi, R., K. Belkacem, and T. Sonoi (2015). "Stellar oscillations-II-The non-adiabatic case." In: *EAS Publications Series* 73, pp. 111–191.

Sandquist, E. L. et al. (2002). "A critical examination of Li pollution and giant-planet consumption by a host star." In: *The Astrophysical Journal* 572.2, 1012.

Sanjayan, S. et al. (2022). "Pulsating subdwarf B stars in the oldest open cluster NGC 6791." In: *Monthly Notices of the Royal Astronomical Society* 509.1, pp. 763–777.

Schaffenroth, V. et al. (2022). “Hot subdwarfs in close binaries observed from space-I. Orbital, atmospheric, and absolute parameters, and the nature of their companions.” In: *Astronomy & Astrophysics* 666, A182.

Schanze, T. (1995). “Sinc interpolation of discrete periodic signals.” In: *IEEE Transactions on Signal Processing* 43.6, pp. 1502–1503.

Schatzman, E. (1993). “Transport of angular momentum and diffusion by the action of internal waves.” In: *Astronomy & Astrophysics* 279, pp. 431–446.

Schmidt, G. D. and A. D. Grauer (1997). “Upper Limits for Magnetic Fields on Pulsating White Dwarfs.” In: *The Astrophysical Journal* 488.2, 827.

Schneider, F. R. N., S. T. Ohlmann, Ph. Podsiadlowski, F. K. Röpke, S. A. Balbus, and R. Pakmor (2020). “Long-term evolution of a magnetic massive merger product.” In: *Monthly Notices of the Royal Astronomical Society* 495.3, pp. 2796–2812.

Schneider, F. R. N., S. T. Ohlmann, Ph. Podsiadlowski, F. K. Röpke, S. A. Balbus, R. Pakmor, and V. Springel (2019). “Stellar mergers as the origin of magnetic massive stars.” In: *Nature* 574.7777, pp. 211–214.

Schneider, F. R. N., Ph. Podsiadlowski, et al. (2016). “Rejuvenation of stellar mergers and the origin of magnetic fields in massive stars.” In: *Monthly Notices of the Royal Astronomical Society* 457.3, pp. 2355–2365.

Schönberg, M. and S. Chandrasekhar (1942). “On the Evolution of the Main-Sequence Stars..” In: *The Astrophysical Journal* 96, 161.

Schreiber, M. R., D. Belloni, et al. (2021). “The origin and evolution of magnetic white dwarfs in close binary stars.” In: *Nature Astronomy* 5.7, pp. 648–654.

Schreiber, M. R., M. Zorotovic, and T. P. G. Wijnen (2015). “Three in one go: consequential angular momentum loss can solve major problems of CV evolution.” In: *Monthly Notices of the Royal Astronomical Society: Letters* 455.1, pp. L16–L20.

Schwab, J. (2020). “A Helium-flash-induced Mixing Event Can Explain the Lithium Abundances of Red Clump Stars.” In: *The Astrophysical Journal* 901.1, L18.

Shara, M. M., D. Prialnik, and A. Kovetz (1993). “Multiple hydrogen flashes on accreting low-mass white dwarfs-Novae and DAO stars.” In: *The Astrophysical Journal* 406, pp. 220–228.

Shara, M. M., O. Yaron, et al. (2010). “An Extended Grid of Nova Models. III. Very Luminous, Red Novae.” In: *The Astrophysical Journal* 725.1, 831.

Shen, K. J. (2015). “Every interacting double white dwarf binary may merge.” In: *The Astrophysical Journal Letters* 805.1, L6.

Shen, K. J., S. Blouin, and K. Breivik (2023). “The Q Branch Cooling Anomaly Can Be Explained by Mergers of White Dwarfs and Subgiant Stars.” In: *The Astrophysical Journal Letters* 955.2, L33.

Shen, K. J., I. Idan, and L. Bildsten (2009). “Helium Core White Dwarfs in Cataclysmic Variables.” In: *The Astrophysical Journal* 705.1, 693.

Shen, K. J., D. Kasen, et al. (2010). “Thermonuclear Ia supernovae from helium shell detonations: explosion models and observables.” In: *The Astrophysical Journal* 715.2, 767.

Shen, K. J. and E. Quataert (2022). “Binary interaction dominates mass ejection in classical novae.” In: *The Astrophysical Journal* 938.1, 31.

Shibahashi, H. and C. Aerts (2000). “Astroseismology and Oblique Pulsator Model of β Cephei.” In: *The Astrophysical Journal* 531.2, L143.

Shibahashi, H. and M. Takata (1993). “Theory for the distorted dipole modes of the rapidly oscillating Ap stars: A refinement of the oblique pulsator model.” In: *Publications of the Astronomical Society of Japan* 45.4, pp. 617–641.

Shu, F. H. (1991). “The Physics of Astrophysics: Gas Dynamics.” Vol. 2. University Science Books.

Shultz, M. E. et al. (2019). “The magnetic early B-type stars—III. A main-sequence magnetic, rotational, and magnetospheric biography.” In: *Monthly Notices of the Royal Astronomical Society* 490.1, pp. 274–295.

Siess, L. and M. Livio (1999). “The accretion of brown dwarfs and planets by giant stars—II. Solar-mass stars on the red giant branch.” In: *Monthly Notices of the Royal Astronomical Society* 308.4, pp. 1133–1149.

Silvotti, R., P. Németh, et al. (2022). “Filling the gap between synchronized and non-synchronized sdBs in short-period sdBV+dM binaries with TESS: TIC 137608661, a new system with a well-defined rotational splitting.” In: *Monthly Notices of the Royal Astronomical Society* 511.2, pp. 2201–2217.

Silvotti, R., M. Uzundag, et al. (2019). “High-degree gravity modes in the single sdB star HD 4539.” In: *Monthly Notices of the Royal Astronomical Society* 489.4, pp. 4791–4801.

Singh, R. et al. (2021). “Tracking the evolution of lithium in giants using astroseismology: Super-Li-rich stars are almost exclusively young red-clump stars.” In: *The Astrophysical Journal Letters* 913.1, L4.

Soares-Furtado, M. et al. (2021). “Lithium enrichment signatures of planetary engulfment events in evolved stars.” In: *The Astronomical Journal* 162.6, 273.

Soberman, G. E., E. S. Phinney, and E. P. J. van den Heuvel (1997). “Stability criteria for mass transfer in binary stellar evolution..” In: *Astronomy & Astrophysics* 327, pp. 620–635.

Soker, N. and R. Tylenda (2006). “Violent stellar merger model for transient events.” In: *Monthly Notices of the Royal Astronomical Society* 373.2, pp. 733–738.

Soker, N. and R. Tylenda (2007). “Magnetic activity in stellar merger products.” In: *Monthly Notices of the Royal Astronomical Society* 375.3, pp. 909–912.

Sowicka, P. et al. (2023). “The GW Vir Instability Strip in Light of New Observations of PG 1159 Stars: Discovery of Pulsations in the Central Star of A72 and Variability of RX J0122. 9–7521.” In: *The Astrophysical Journal Supplement Series* 269.1, 32.

Spruit, H. C. (2002). “Dynamo action by differential rotation in a stably stratified stellar interior.” In: *Astronomy & Astrophysics* 381.3, pp. 923–932.

Stello, D., M. Cantiello, J. Fuller, R. A. Garcia, et al. (2016). “Suppression of quadrupole and octupole modes in red giants observed by Kepler.” In: *Publications of the Astronomical Society of Australia* 33.

Stello, D., M. Cantiello, J. Fuller, D. Huber, et al. (2016). “A prevalence of dynamo-generated magnetic fields in the cores of intermediate-mass stars.” In: *Nature* 529.7586, pp. 364–367.

Stello, D. and R. L. Gilliland (2009). “Solar-like oscillations in a metal-poor globular cluster with the Hubble Space Telescope.” In: *The Astrophysical Journal* 700.2, 949.

Stello, D., D. Huber, et al. (2013). “Asteroseismic classification of stellar populations among 13,000 red giants observed by Kepler.” In: *The Astrophysical Journal Letters* 765.2, L41.

Stello, D., H. Kjeldsen, et al. (2004). “Simulating stochastically excited oscillations: The mode lifetime of ξ Hya.” In: *Solar Physics* 220.2, pp. 207–228.

Sweigart, A. V. (1997). “Helium mixing in globular cluster stars.” In: *The Third Conference on Faint Blue Stars*. Ed. by AGD Philip et al., 3.

Szary, A. (2013). “Non-dipolar magnetic field at the polar cap of neutron stars and the physics of pulsar radiation.”

Takata, M. (2016a). “Asymptotic analysis of dipolar mixed modes of oscillations in red giant stars.” In: *Publications of the Astronomical Society of Japan*, 109.

Takata, M. (2016b). “Physical formulation of mixed modes of stellar oscillations.” In: *Publications of the Astronomical Society of Japan* 68.6, 91.

Takata, M. (2018). “Asymptotic view of oscillations of red giant stars.” In: *PHysics of Oscillating STars*, 39.

Takata, M. and H. Saio (2013). “Rosette Modes of Oscillations of Rotating Stars Caused by Close Degeneracies. I. Axisymmetric Modes.” In: *Publications of the Astronomical Society of Japan* 65.3.

Talon, S. et al. (1997). “Rotational mixing in early-type stars: the main-sequence evolution of a $9M_{\odot}$ star.” In: *Astronomy & Astrophysics* 322, pp. 209–217.

Tassoul, M. (1980). “Asymptotic approximations for stellar nonradial pulsations.” In: *The Astrophysical Journal Supplement Series* 43, pp. 469–490.

Tayar, J., T. Ceillier, et al. (2015). “Rapid rotation of low-mass red giants using APOKASC: A measure of interaction rates on the post-main-sequence.” In: *The Astrophysical Journal* 807.1, 82.

Tayar, J., F. D. Moyano, et al. (2022). “Spinning up the Surface: Evidence for Planetary En-gulfment or Unexpected Angular Momentum Transport?.” In: *The Astrophysical Journal* 940.1, 23.

Telting, J., R. Östensen, et al. (2014). “Low-Resolution Radial-Velocity Monitoring of Pulsating sdBs in the Kepler Field.” In: *6th Meeting on Hot Subdwarf Stars and Related Objects*. Vol. 481, 287.

Telting, J. H., C. Aerts, and P. Mathias (1997). “A period analysis of the optical line variability of beta Cephei: evidence for multi-mode pulsation and rotational modulation.” In: *Astronomy and Astrophysics* 322, pp. 493–506.

Thomas, H.-C. (1967). “Sternentwicklung VIII. Der Helium-Flash bei einem Stern von 1. 3 Sonnenmassen.” In: *Zeitschrift für Astrophysik* 67, 420.

Thompson, C. and R. C. Duncan (1993). “Neutron star dynamos and the origins of pulsar magnetism.” In: *The Astrophysical Journal* 408, pp. 194–217.

Tokuno, T. and M. Takata (2022). “Astroseismology of the dip structure in period-spacings of rapidly rotating γ Doradus stars caused by the coupling between core and envelope oscillations.” In: *Monthly Notices of the Royal Astronomical Society* 514.3, pp. 4140–4159.

Toonen, S. and G. Nelemans (2013). “The effect of common-envelope evolution on the visible population of post-common-envelope binaries.” In: *Astronomy & Astrophysics* 557, A87.

Tout, C. A., D. T. Wickramasinghe, and L. Ferrario (2004). “Magnetic fields in white dwarfs and stellar evolution.” In: *Monthly Notices of the Royal Astronomical Society* 355.3, pp. L13–L16.

Tout, C. A., D. T. Wickramasinghe, J. Liebert, et al. (2008). “Binary star origin of high field magnetic white dwarfs.” In: *Monthly Notices of the Royal Astronomical Society* 387.2, pp. 897–901.

Townsend, R. H. D. (2003). “Asymptotic expressions for the angular dependence of low-frequency pulsation modes in rotating stars.” In: *Monthly Notices of the Royal Astronomical Society* 340.3, pp. 1020–1030.

Townsend, R. H. D. (2020). “Improved asymptotic expressions for the eigenvalues of Laplace’s tidal equations.” In: *Monthly Notices of the Royal Astronomical Society* 497.3, pp. 2670–2679.

Townsend, R. H. D. and S. A. Teitler (2013). “GYRE: an open-source stellar oscillation code based on a new Magnus Multiple Shooting scheme.” In: *Monthly Notices of the Royal Astronomical Society* 435.4, pp. 3406–3418.

Tremblay, P.-E., G. Fontaine, et al. (2015). “On the evolution of magnetic white dwarfs.” In: *The Astrophysical Journal* 812.1, 19.

Tremblay, P.-E., A. Gianninas, et al. (2015). “3D model atmospheres for extremely low-mass white dwarfs.” In: *The Astrophysical Journal* 809.2, 148.

Tremblay, P.-E., H.-G. Ludwig, et al. (2015). “Calibration of the mixing-length theory for convective white dwarf envelopes.” In: *The Astrophysical Journal* 799.2, 142.

Tutukov, A. V. and A. V. Fedorova (2010). “Possible scenarios for the formation of Ap/Bp stars.” In: *Astronomy Reports* 54.2, pp. 156–162.

Tylenda, R., M. Hajduk, et al. (2011). “V1309 Scorpii: merger of a contact binary.” In: *Astronomy & Astrophysics* 528, A114.

Tylenda, R., T. Kamiński, and R. Smolec (2024). “Nova 1670 (CK Vulpeculae) was a merger of a red giant with a helium white dwarf.” In: *Astronomy & Astrophysics* 685, A49.

Tylenda, R. and N. Soker (2006). “Eruptions of the V838 Mon type: stellar merger versus nuclear outburst models.” In: *Astronomy & Astrophysics* 451.1, pp. 223–236.

Ulrich, R. K. (1986). “Determination of stellar ages from asteroseismology.” In: *The Astrophysical Journal Letters* 306, pp. L37–L40.

Unno, W., Y. Osaki, H. Ando, H. Saio, et al. (1989). “Nonradial oscillations of stars, 2e.” Tokyo: University of Tokyo Press.

Unno, W., Y. Osaki, H. Ando, and H. Shibahashi (1979). “Nonradial oscillations of stars.” Tokyo: University of Tokyo Press.

Vallastro (2022). “Variable_stars_in_the_HRD.svg.” Wikimedia Commons. URL: https://commons.wikimedia.org/wiki/File:Variable_stars_in_the_HRD.svg.

Valyavin, G. et al. (2006). “A search for kilogauss magnetic fields in white dwarfs and hot subdwarf stars.” In: *The Astrophysical Journal* 648.1, 559.

Van Beeck, J. et al. (2020). “Detecting axisymmetric magnetic fields using gravity modes in intermediate-mass stars.” In: *Astronomy & Astrophysics* 638, A149.

Van Grootel, V. et al. (2012). “The newly discovered pulsating low-mass white dwarfs: an extension of the ZZ Ceti instability strip.” In: *The Astrophysical Journal* 762.1, 57.

Van Reeth, T., J. S. G. Mombarg, et al. (2018). “Sensitivity of gravito-inertial modes to differential rotation in intermediate-mass main-sequence stars.” In: *Astronomy & Astrophysics* 618, A24.

Van Reeth, T., A. Tkachenko, and C. Aerts (2016). “Interior rotation of a sample of γ Doradus stars from ensemble modelling of their gravity-mode period spacings.” In: *Astronomy & Astrophysics* 593, A120.

Van Reeth, T., A. Tkachenko, C. Aerts, et al. (2015). “Detecting non-uniform period spacings in the Kepler photometry of γ Doradus stars: methodology and case studies.” In: *Astronomy & Astrophysics* 574, A17.

Van Zyl, L. et al. (2004). “The non-radially pulsating primary of the cataclysmic variable GW Librae.” In: *Monthly Notices of the Royal Astronomical Society* 350.1, pp. 307–316.

Vanlaer, V. et al. (2023). “On the feasibility of structure inversions for gravity-mode pulsators.” In: *Astronomy & Astrophysics* 675, A17.

Vaschy, A. (1892). "Sur les lois de similitude en physique." In: *Annales télégraphiques*. Vol. 19, pp. 25–28.

Vauclair, G. et al. (2002). "Astroseismology of RXJ 2117+3412, the hottest pulsating PG 1159 star." In: *Astronomy & Astrophysics* 381.1, pp. 122–150.

Viani, L. S. et al. (2017). "Changing the ν_{\max} Scaling Relation: The Need For a Mean Molecular Weight Term." In: *The Astrophysical Journal* 843.1, 11.

Vidotto, A. A. et al. (2014). "Stellar magnetism: empirical trends with age and rotation." In: *Monthly Notices of the Royal Astronomical Society* 441.3, pp. 2361–2374.

Vincent, O., P. Bergeron, and D. Lafrenière (2020). "Searching for ZZ Ceti white dwarfs in the Gaia survey." In: *The Astronomical Journal* 160.6, 252.

Vrard, M., M. S. Cunha, et al. (2022a). "Evidence of structural discontinuities in the inner core of red-giant stars." In: *Nature Communications* 13, 7553.

Vrard, M., M. S. Cunha, et al. (2022b). "Evidence of structural discontinuities in the inner core of red-giant stars." In: *Nature Communications* 13.1, 7553.

Vrard, M., B. Mosser, and R. Samadi (2016). "Period spacings in red giants-II. Automated measurement." In: *Astronomy & Astrophysics* 588, A87.

Wagg, T. et al. (2024). "The asteroseismic imprints of mass transfer-A case study of a binary mass-gainer in the SPB instability strip." In: *Astronomy & Astrophysics* 687, A222.

Wang, B. (2018). "Mass-accreting white dwarfs and type Ia supernovae." In: *Research in Astronomy and Astrophysics* 18.5, 049.

Wang, H., J. P. Boyd, and R. A. Akmaev (2016). "On computation of Hough functions." In: *Geoscientific Model Development* 9.4, pp. 1477–1488.

Wang, K., P. Németh, et al. (2022). "Extremely low-mass white dwarf stars observed in Gaia DR2 and LAMOST DR8." In: *The Astrophysical Journal* 936.1, 5.

Wang, K., X. Zhang, and M. Dai (2020). "Discovery of two pulsating extremely low-mass pre-white dwarf candidates in the TESS eclipsing binaries." In: *The Astrophysical Journal* 888.1, 49.

Wang, L., P. Kroupa, et al. (2020). "The possible role of stellar mergers for the formation of multiple stellar populations in globular clusters." In: *Monthly Notices of the Royal Astronomical Society* 491.1, pp. 440–454.

Wanner, G. and E. Hairer (1996). "Solving ordinary differential equations II." Vol. 375. Springer Berlin Heidelberg New York.

Warrickball (2023). "Astroseismic_HR_diagram.svg." Wikimedia Commons. URL: https://commons.wikimedia.org/wiki/File:Astroseismic_HR_diagram.svg.

Whittaker, E. T. (1903). "An expression of certain known functions as generalized hypergeometric functions." In: *Bulletin of the American Mathematical Society* 10.3, pp. 125–134.

Wickramasinghe, D. T. and L. Ferrario (2000). “Magnetism in isolated and binary white dwarfs.” In: *Publications of the Astronomical Society of the Pacific* 112.773, 873.

Wickramasinghe, D. T., C. A. Tout, and L. Ferrario (2014). “The most magnetic stars.” In: *Monthly Notices of the Royal Astronomical Society* 437.1, pp. 675–681.

Widdowson, S., O. A. Hurricane, and S. C. Cowley (1998). “The continuum of unstable magnetohydrodynamic modes in a simple magnetized atmosphere.” In: *Physics of Plasmas* 5.5, pp. 1259–1264.

Williams, K. A. et al. (2016). “Variability in hot carbon-dominated atmosphere (hot DQ) white dwarfs: rapid rotation?.” In: *The Astrophysical Journal* 817.1, 27.

Winget, D. E., C. J. Hansen, et al. (1991). “Asteroseismology of the DOV star PG 1159-035 with the Whole Earth Telescope.” In: *The Astrophysical Journal* 378.1, pp. 326–346.

Winget, D. E., R. E. Nather, et al. (1994). “Whole earth telescope observations of the DBV white dwarf GD 358.” In: *The Astrophysical Journal* 430.2, pp. 839–849.

Witelski, T. P. and A. J. Bernoff (1998). “Self-similar asymptotics for linear and nonlinear diffusion equations.” In: *Studies in Applied Mathematics* 100.2, pp. 153–193.

Wolf, W. M. et al. (2013). “Hydrogen burning on accreting white dwarfs: stability, recurrent novae, and the post-nova supersoft phase.” In: *The Astrophysical Journal* 777.2, 136.

Wong, T. L. S. and L. Bildsten (2024). “The Asteroseismological Richness of RCB and dLHdC Stars.” In: *The Astrophysical Journal* 962.1, 20.

Woodard, M. F. (1985). “Short-Period Oscillations in the Total Solar Irradiance”. PhD thesis. University of California, San Diego.

Yan, H.-L. et al. (2021). “Most lithium-rich low-mass evolved stars revealed as red clump stars by asteroseismology and spectroscopy.” In: *Nature Astronomy* 5.1, pp. 86–93.

Yu, J. et al. (2018). “Asteroseismology of 16,000 Kepler red giants: global oscillation parameters, masses, and radii.” In: *The Astrophysical Journal Supplement Series* 236.2, 42.

Zahn, J.-P. (1994). “Rotation and lithium depletion in late-type binaries.” In: *Astronomy and Astrophysics* 288, pp. 829–841.

Zahn, J.-P. (1997). “Rotation and angular momentum transport.” In: *SCORe'96 : Solar Convection and Oscillations and their Relationship*. Ed. by FP Pijpers, J Christensen-Dalsgaard, and CS Rosenthal. Vol. 225. Astrophysics and Space Science Library, pp. 187–200.

Zahn, J.-P. (2010). “Rapid rotation and mixing in active OB stars–Physical processes.” In: *Proceedings of the International Astronomical Union* 6.S272, pp. 14–25.

Zhang, X., P. D. Hall, et al. (2017). “Evolution models of helium white dwarf–main-sequence star merger remnants.” In: *The Astrophysical Journal* 835.2, 242.

Zhang, X., P. D. Hall, et al. (2018). “Evolution models of helium white dwarf–main-sequence star merger remnants: the mass distribution of single low-mass white dwarfs.” In: *Monthly Notices of the Royal Astronomical Society* 474.1, pp. 427–432.

Zhang, X. and C. S. Jeffery (2013). “White dwarf–red giant mergers, early-type R stars, J stars and lithium.” In: *Monthly Notices of the Royal Astronomical Society* 430.3, pp. 2113–2120.

Zhang, X., C. S. Jeffery, Y. Li, et al. (2020). “Population synthesis of helium white dwarf–red giant star mergers and the formation of lithium-rich giants and carbon stars.” In: *The Astrophysical Journal* 889.1, 33.

Zhang, X., C. S. Jeffery, J. Su, et al. (2023). “The formation of blue large-amplitude pulsators from white-dwarf main-sequence star mergers.” In: *The Astrophysical Journal* 959.1, 24.

Zhou, Y. et al. (2024). “Does the Scaling Relation Depend on Metallicity? Insights from 3D Convection Simulations.” In: *The Astrophysical Journal* 962.2, 118.

Zong, W. et al. (2016). “Amplitude and frequency variations of oscillation modes in the pulsating DB white dwarf star KIC 08626021-The likely signature of nonlinear resonant mode coupling.” In: *Astronomy & Astrophysics* 585, A22.

Zorotovic, M. and M. Schreiber (2022). “Close detached white dwarf + brown dwarf binaries: further evidence for low values of the common envelope efficiency.” In: *Monthly Notices of the Royal Astronomical Society* 513.3, pp. 3587–3595.

Zorotovic, M. and M. R. Schreiber (2017). “The origin of single low-mass WDs: another problem that consequential angular momentum loss in CVs might solve.” In: *Monthly Notices of the Royal Astronomical Society: Letters* 466.1, pp. L63–L67.

Zorotovic, M. and M. R. Schreiber (2020). “Cataclysmic variable evolution and the white dwarf mass problem: A Review.” In: *Advances in Space Research* 66.5, pp. 1080–1089.

Zorotovic, M., M. R. Schreiber, and B. T. Gänsicke (2011). “Post common envelope binaries from SDSS-XI. The white dwarf mass distributions of CVs and pre-CVs.” In: *Astronomy & Astrophysics* 536, A42.